NORTHWESTERN UNIVERSITY

In Situ X-ray Scattering Studies of Flow-Induced Crystallization in Polymer Melts under Uniaxial Extensional Flow

A DISSERTATION

SUBMITTED TO THE GRADUATE SCHOOL
IN PARTIAL FULFILLMENT OF THE REQUIREMENT

for the degree

DOCTOR OF PHILOSOPHY

Field of Chemical Engineering

By
Mu Sung Kweon

EVANSTON, ILLINOIS
March 2019

Abstract

In Situ X-ray Scattering Studies of Flow-Induced Crystallization in Polymer Melts under Uniaxial Extensional Flow

Mu Sung Kweon

Polymers permeate almost all facets of modern life. For end use applications, these materials are typically processed into products at elevated temperatures under which molten polymers are subjected to flow. Particular interest lies in the flow-induced crystallization behavior of polymer melts under extensional flow, which is a flow type dominant in many important polymer processing operations but has received less attention due to challenges associated with producing a well-defined extensional flow.

This thesis presents a systematic study on flow-induced crystallization of polymer melts under uniaxial extensional flow that aims to quantify the effect of flow on the subsequent crystallization process. The work described here utilizes a custom instrumentation that consists of a Sentmanat Extensional Rheometer housed in a convection oven designed to facilitate x-ray access. Simultaneous extensional rheometry and *in situ* x-ray scattering measurements are performed to characterize the nonlinear rheology and to elucidate the underlying molecular mechanism of the complicated phenomenon. Two different flow protocols are employed to monitor the isothermal crystallization behavior during flow inception and following flow cessation.

Extensional flow-induced crystallization experiments are performed on a wide variety of semi-crystalline polymers. *In situ* structural characterization during flow-induced crystallization of poly(lactic acid) under extensional flow is reported for the first time in literature. Unusual effects of flow are observed in the crystallization behavior under intermediate flow conditions, but the overall crystallization kinetics are associated with the orientation distribution of crystallites. Experiments designed to produce similar enhancements in nucleation under combinations of various extension rates and Hencky strains are performed on poly(1-butene) to directly test the underlying hypothesis in existing flow-induced crystallization models that molecular orientation leads to enhanced nucleation. The impact of crystallization initiated during as well as following the application of flow on the induced microstructure during isothermal crystallization is explored using low-density polyethylene and high-density polyethylene. A wide range of lamellar-scale morphologies is observed across various semi-crystalline polymers. The comprehensive experimental studies coordinated with computational modeling have the potential to positively contribute to the rational design of polymer processing operations.

Acknowledgments

My sincerest gratitude goes to my advisor, Wes Burghardt, for his support and guidance. Wes has always been an inspiration to me for his creativity in approaching problems from different angles and for his positive attitude towards research. Working with Wes felt as if there was no such thing as a failed experiment; he always drew valuable insights and transformed every conversation into a tremendous learning opportunity for me. For this, I am grateful to Wes for always being in the moment during discussions, and for teaching me integrity, hard work, and dedication. I would also like to thank Wes for being my conference travel partner and volunteering for early morning shifts and for food runs at Argonne. Most importantly, I truly appreciate his exceptional patience and understanding, especially during my final years of graduate studies that became convoluted with important life events.

I would also like to thank my thesis committee, Professor Linda Broadbelt, Professor Ken Shull, and Professor John Torkelson, for their valuable feedback and for working me into their schedules. I especially appreciate the challenging questions and thoughtful discussions that prompted me to reflect on my thesis and think more critically while adhering to the fundamentals. I would also like to take this opportunity to sincerely thank the staff at DND-CAT: Steve Weigand and Denis Keane. All of the work presented in this thesis would not have been possible without their incredible help and effort.

I would like to express my sincere gratitude to the outstanding professors from Harvey Mudd College who trained me as a well-rounded engineer and prepared me for graduate studies. Special thanks to Professor Nancy Lape, who introduced me to chemical engineering research and served as my academic & research advisor all throughout college. Thanks to Professor Mary Cardenas and Professor Erik Spjut, who have provided me with opportunities to become more equipped with knowledge in chemical engineering.

To my labmates, Erica McCready and Binbin Luo—my time in the group was truly enjoyable thanks to your company. Thank you for the fruitful discussions on research problems (and random conversations on life in general). Erica, I especially want to thank you for putting in the extra hours to train me when I first joined the research group, letting me tag along with you to your Argonne trip, and simply being an amazing friend that made me feel excited to come to work every day. Binbin, thank you so much for being my fellow international student that I could always talk to and relate to.

My time at Northwestern would have been unbearable without the support of many friends that I made here. A huge gratitude goes to my Korean peers: Sol Ahn, Dongjoon Rhee, June Lee, Ha-Kyung Kwon, Gyeongwon Kang, and Ki-Hee Song. Thank you for always looking out for me. Our lunch breaks and coffee chats will be dearly missed. A special shout out to Bisola Bruno, David Chen, and Graham Spicer for all the fun associated with working out, playing intramural sports, grabbing junk food, and moving my furniture from apartment to apartment. I would also like to thank for my Chicago friends—Eddie Ha, Jiwon Ha, John Lee, and Chelsey Park. Thank you for being there when I needed time away from Evanston and Northwestern to inhale more of the chilly air (and perhaps nice summer breezes) in downtown Chicago.

I also would not have been able to endure the lonesome feeling upon moving to Evanston from sunny California without the emotional support of my dear friends from Mudd—Kyle

Carbon, Richard Hsieh, Monica Hwang, Suzy Kim, Lisa Lam, and Edward Ruan. You all have a special place in my heart, and I am truly grateful to have such amazing friends like you guys. Thanks for checking in on me all the time, making the time to drive/fly out to come visit me, and letting me crash at your places. To my “A. N. Fam” in Korea, thank you all for your friendship and support throughout these past 14 years. You guys always made me feel like I’m home whenever I visited Korea.

I would not be who I am today if it weren’t for my family. Mom and dad, thank you for raising me the way I am. Although at times I can be persistent and stubborn, you have always embraced me and shown nothing but unconditional love. I couldn’t be prouder to be your son. To my brother—I hope you know that I always look up to you. Thank you for being a huge support simply by being there for me.

Lastly but most importantly, I express my ineffable gratitude to my beloved wife, Yeon Ji Park. I cannot thank you enough for joining me on this tough ride and being by my side to support me throughout my graduate studies. Even at times I wouldn’t believe in myself, you always believed in me. Your unwavering love, support, and encouragement have been my source of strength. You are a constant reminder of how happy my life can be.

List of Abbreviations

HDPE – high-density polyethylene

LDPE – low-density polyethylene

iPP – isotactic polypropylene

iPB – poly(1-butene)

PET – poly(ethylene terephthalate)

PLA – poly(lactic acid)

FIC – flow-induced crystallization

LVE – linear viscoelasticity

SER – Sentmanat Extensional Rheometer

WAXS – wide-angle x-ray scattering

SAXS – small-angle x-ray scattering

Table of Contents

List of Figures

List of Tables

Chapter 1

Introduction and Background

1.1 Introduction

Over the past half century, polymers have been vastly incorporated into products that play a ubiquitous role in our daily lives. On a global scale, the annual production of polymer resin and fiber has exceeded 380 million metric tons in 2015;[1] in the United States, the total production of thermoplastic polymer resins reached nearly 44 million metric tons in 2017.[2] Nearly all of these thermoplastics are processed at elevated temperatures in the presence of flow, under which molten polymers are formed into desired shapes and transformed into products for end use applications. Among these materials, more than 60% are classified as semi-crystalline polymers, as they solidify into their final form via crystallization from the melt. These include polyolefins that are widely produced in the industrial scale such as high- and low-density polyethylene (HDPE and LDPE, respectively), isotactic polypropylene (iPP), and isotactic poly(1-butene) (iPB) as well as synthetic polyesters such as poly(ethylene terephthalate) (PET) and those that are bio-based and biodegradable such as poly(lactic acid) (PLA).

Essentially all semi-crystalline polymer melts subjected to deformation during manufacturing operations experience flow-induced crystallization (FIC), in which the application of flow enhances crystallization kinetics by orders of magnitude, allowing crystallization to proceed at temperatures where it occurs on extremely long time scales or is even kinetically prohibited. FIC also frequently leads to highly oriented crystalline structures and morphologies, which have a significant impact on the final material properties.[3] This processing-structure-properties relationship has thus provided a strong impetus for elucidating the underlying mechanism of this complex phenomenon.

From researchers in the fields of rheology and polymer physics to scientists in the plastics industry, it has been of intrinsic importance to gain a comprehensive understanding of the microstructural dynamics and viscoelastic behavior of polymers affected by flow-induced crystallization during various processing conditions as well as during more idealized flows of different types. In particular, x-ray scattering has shown to be an extremely effective tool for studying the structural development of polymers under flow, as it directly probes the relevant morphological factors in semi-crystalline polymers. Works that employ x-ray scattering methods, however, have been primarily limited to studies under shear flow, since shearing flows can be produced with relative ease and are industrially relevant to polymer processing operations such as extrusion and injection molding. While many other processing applications such as blow molding, film blowing, and fiber spinning are dominated by elongational deformation, extensional flows have historically been difficult to generate. Consequently, relatively few studies on extensional rheological characterization are available. Experimental capabilities in flow-induced crystallization studies under extensional flow have been recently expanded with advances in instrumentation that led to the development of various elongational flow devices that reliably produce well-defined extensional flows. Nonetheless, there are only few studies that involve any structural characterization using *in situ* techniques.

This thesis presents a systematic study of flow-induced crystallization employing x-ray scattering methods to directly probe the structural changes in polymer melts subjected to uniaxial extensional flow. The work described here utilizes a custom-built instrument that has been recently developed in this research group and has successfully demonstrated its capability to conduct *in situ* x-ray scattering measurements during well-defined extensional flow experiments.[4–6] The application of powerful *in situ* x-ray techniques offers valuable insight into the crystallization kinetics, evolving crystallinity, and development of microstructural state and orientation of morphological factors in polymers capable of crystallizing. Experimental findings reported in this thesis cover a wide range of semi-crystalline polymers under extensional flow, providing a deeper and richer understanding of flow-induced crystallization that is immediately relevant to processing operations primarily involving extensional deformations. These studies, coordinated with computational modeling to directly test the central link between induced molecular orientation and enhanced nucleation, serve as a strong basis for the rational design of multiscale models that draw on molecular insights while retaining descriptions applicable to industrial process modeling.

1.2 Rheology of Polymers

Polymer processing typically involves the application of flow, under which polymer chains can orient, stretch, or rotate. The molecular or microstructural anisotropy induced by applied flow fields gives rise to interesting yet complicated viscoelastic properties in polymeric systems. Unlike Newtonian fluids that exhibit linear proportionality between the instantaneous rate of deformation and the viscous stresses, polymers are non-Newtonian fluids that often show nonlinear stress dependence upon applied deformation rate. As polymers encounter flow fields at elevated temperatures during processing, molten chains are particularly susceptible to be perturbed and are often entangled, both of which are characteristics that contribute to the non-

Newtonian behavior in the bulk fluid. For this reason, there has been a profound scientific and technological interest in the rheology—the study of deformation and flow—of entangled polymer melts and in characterizing their rheological properties that are strongly connected to the underlying molecular alignment.

1.2.1 Linear Viscoelastic Characterization

Under small deformations or deformation rates, polymers frequently exhibit stress response that is a linear function of both strain and instantaneous rate of deformation, which gives rise to their linear viscoelastic (LVE) properties. The material response from this linear regime is often characterized under simple shear due to the relative ease of producing a homogeneous shear flow and because fluid elements undergo the same deformation history. In Cartesian coordinates, simple shear flow is defined as

$$v_1 = \dot{\gamma} x_2 \tag{1.1}$$

$$v_2 = v_3 = 0. \tag{1.2}$$

Here, $\dot{\gamma}$ is the shear rate, and “1”, “2”, and “3” respectively denote the flow, gradient, and vorticity directions; the product of shear rate and time is the shear strain. Well-defined shear flows are conveniently generated using torsional flow between disks. Hence, rotational rheometers that employ parallel plate or cone and plate fixtures are commonly used to characterize the linear rheology of polymer melts.

Among the different shear material functions (e.g. transient shear viscosity, stress relaxation modulus) that describe the linear response of viscoelastic materials, the storage modulus (*G'*) and loss modulus (*G''*) are useful quantities that deliver information on their elastic and viscous behavior, respectively. These measurements are performed by applying a small amplitude oscillatory shear to the sample and tracking the in-phase (solid-like) and out-of-phase (liquid-like) components of the stress response with respect to the sinusoidal strain input. For polymer melts, these measurements are usually obtained over a wide range of temperatures, and the data are shifted onto a master curve at a reference temperature using time-temperature superposition. This principle is particularly useful for characterizing the LVE response of polydisperse entangled polymer melts, as they exhibit a wide distribution of relaxation times that does not change shape but only *shifts* with changes in temperature. Therefore, time-temperature shift factors (a_T) carry information about the temperature sensitivity of material functions. These shift factors obtained from polymers melts at elevated temperatures far from their glass transition temperature typically follow an Arrhenius relationship:

$$a_T = \exp\left[\frac{E_a}{R}\left(\frac{1}{T} - \frac{1}{T_{ref}}\right)\right] \tag{1.3}$$

where E_a is the activation energy, R is the universal gas constant, T is temperature, and T_{ref} is the reference temperature to which the LVE data are shifted.

To capture the comprehensive elastic and viscous behavior that spans a wide range of time scales separated by orders of magnitude, a multimode Maxwell model is fit to the master curve:

$$G'(\omega) = \sum_{k=1}^{N} \frac{G_k(\lambda_k\omega)^2}{1 + (\lambda_k\omega)^2} \tag{1.4}$$

$$G"(\omega) = \sum_{k=1}^{N} \frac{G_k \lambda_k \omega}{1 + (\lambda_k \omega)^2} \tag{1.5}$$

where ω is frequency, G is the dynamic modulus, and λ is the relaxation time. The fitting strategy involves using a discrete relaxation spectrum composed of N relaxation modes of λ_k and corresponding values of G_k in each mode to accurately describe the actual distribution of relaxation times in the polymer. Once the model fits the data well, the fitting parameters G_k and λ_k can be used to predict other LVE material functions as needed.

1.2.2 Entangled Polymer Melts

Entangled polymer melts exhibit relaxation processes that are fundamentally different from those of dilute polymer solutions or low molecular weight polymers melts, in which polymer molecules act as individual hydrodynamic units since they are separated and disengaged from each other.[7] In entangled polymers melts, the entanglements behave as “physical” crosslinks that are analogous to the chemical bonds in cross-linked rubber. While chains in a cross-linked rubber form a permanent network, the network created by entangled polymer melt molecules is non-permanent, such that the entanglements give rise to both elastic response on short time scales under rapid deformation (e.g. step strain) and liquid-like response on long time scales that are sufficient for chains to disentangle and relax.

The major breakthrough in describing the dynamics of entangled polymers was achieved with the introduction of the “tube model” in 1967 by Edwards, who proposed that the motion of a polymer chain is restricted by the topological constraint formed by its surrounding.[8] In 1971, de Gennes proposed the idea of “reptation” which describes that a polymer chain can diffuse out of its confining tube along the chain axis, even though its lateral motion is hindered by the topological constraints.[9] The concept was further refined by Doi and Edwards and formulated as a theory that describes the slow and fast relaxation processes of entangled polymer melts.[10] The slow chain relaxation process is described by reptation theory, which states that polymer chains are constrained in a temporary network of entanglements that restricts tangential movement (Figure 1.1a), and this mesh of topological constraints effectively confines a polymer chain to a tube-like region (Figure 1.1b). A polymer molecule relaxes by sliding along its chain axis through a “snake-like” motion (i.e. reptation) to “escape” from its confining tube. As the chain moves back and forth along the contour path, it forgets the sections of the original tube that are vacated (Figure 1.1c). The time it takes for the chain to diffuse out of the tube is characterized as the reptation time (λ_{rep}).

Doi and Edwards noted that for entangled polymer melts subjected to step strain, the tube as well as the chain it contains stretch affinely.[10] In contrast to the slow relaxation process in which stress relaxes by reptation motion of the chain out of the stretched tube, a faster relaxation process known as retraction takes place. During retraction, the chain quickly withdraws itself within the deformed tube back to its equilibrium length. The time it takes for the chain to retract is commonly associated with the Rouse time (λ_R), which is related to λ_{rep} by

$$\lambda_R = \frac{\lambda_{rep}}{3Z} \tag{1.6}$$

where Z is the average number of chain entanglements taken as the ratio between the weight-averaged molecular weight (M_w) and entanglement molecular weight (M_e). This distinction between the Rouse and reptation times leads to differences between the role of chain stretching

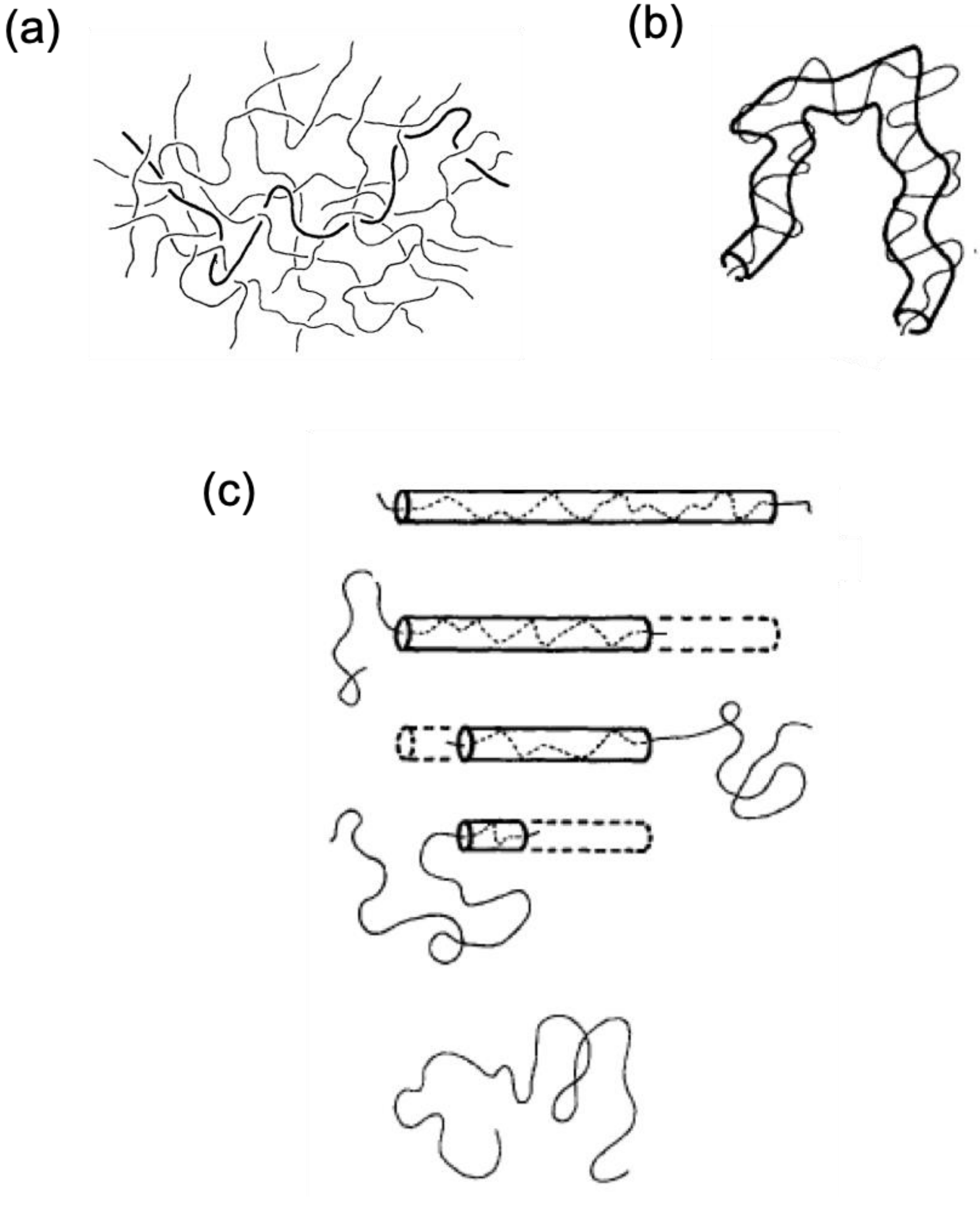

Figure 1.1: A polymer chain (a) entangled in a network of neighboring chains, (b) confined in a tube-like region, and (c) escaping its tube (represented as straight cylinder for visualization aid purposes) via reptation motion. Figures adapted from R. G. Larson, "The Structure and Rheology of Complex Fluids" *Oxford University Press* (1999).[11]

within the tube and orientation of tube segments.

1.2.3 Extensional Rheometry

Contrary to simple shear under which fluid elements undergo linear stretching and solid body rotation, those subjected to extensional flow experience pure exponential stretching/compression (Figure 1.2). However, extensional flows have deserved far less attention than the commonly studied shear flow, since homogenous extension is difficult to generate. Given that extensional flows are dominant flow fields in many polymer processing operations and are highly effective at inducing strong molecular alignment that often result in nonlinear rheological properties, studying the extensional rheology of polymers is a highly sought-after research direction with significant industrial relevance and scientific merit.

Of particular interest to the work presented in this thesis is uniaxial extensional flow, which is defined as

$$v_1 = \dot{\varepsilon} x_1 \tag{1.7}$$

$$v_2 = -\frac{\dot{\varepsilon}}{2} x_2 \tag{1.8}$$

$$v_3 = -\frac{\dot{\varepsilon}}{2} x_3 \tag{1.9}$$

where $\dot{\varepsilon}$ is the extension rate. In uniaxial extension, a fluid element stretches at an exponentially increasing rate, so it is appropriate to describe the elongational strain (derived from the instantaneous incremental deformation experienced by the material) as the true strain or Hencky strain (ε_H):

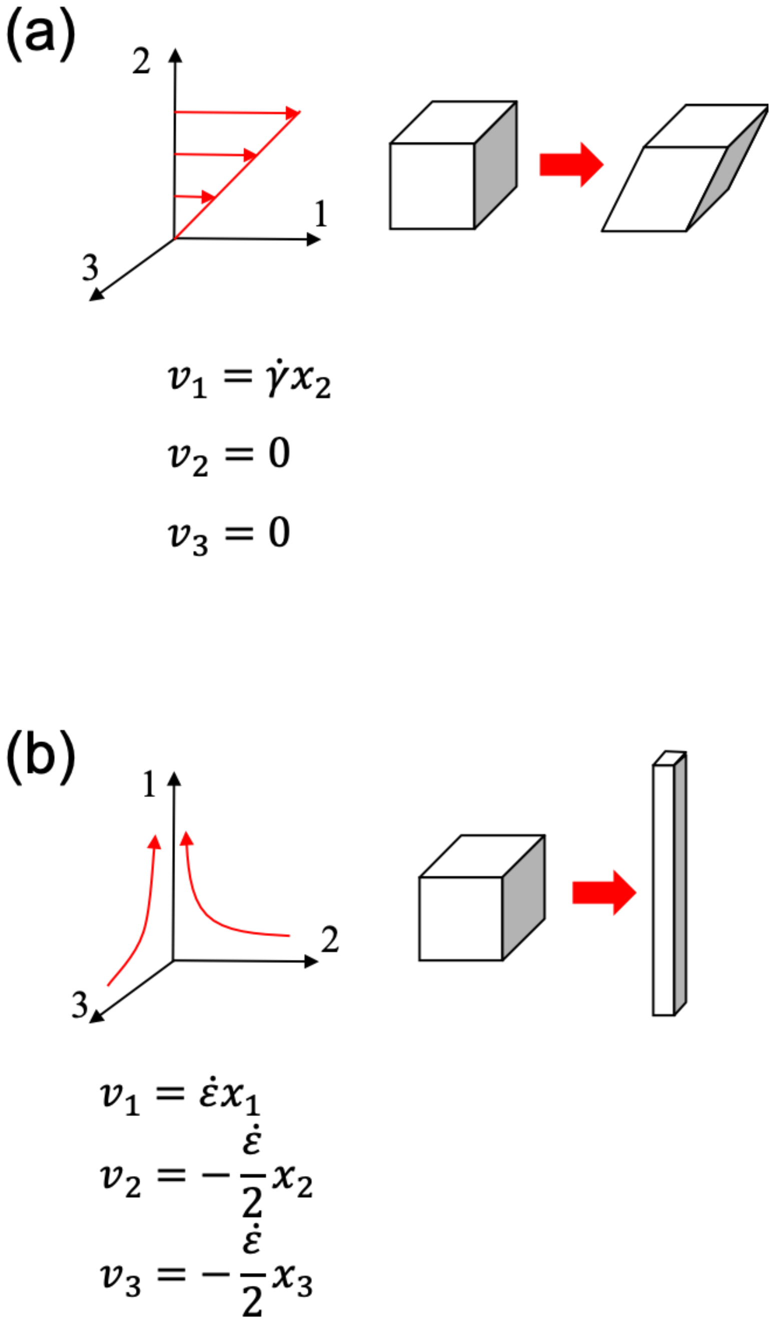

$$v_1 = \dot{\gamma} x_2$$
$$v_2 = 0$$
$$v_3 = 0$$

$$v_1 = \dot{\varepsilon} x_1$$
$$v_2 = -\frac{\dot{\varepsilon}}{2} x_2$$
$$v_3 = -\frac{\dot{\varepsilon}}{2} x_3$$

Figure 1.2: Comparison between the kinematics of shear flow (a) and of uniaxial extensional flow (b).

$$\varepsilon_H \equiv \dot{\varepsilon}t \tag{1.10}$$

$$\varepsilon_H = \ln\left(\frac{l}{l_0}\right) \tag{1.11}$$

where t is time, l is the final length, and l_0 is the initial length of the material along the direction of elongation.

The earliest efforts on experimental methods that employ uniaxial extension date back to 1969.[12] Meissner demonstrated that uniaxial extensional flow can be applied using rotating clamps (Figure 1.3a), and this setup was used to characterize the extensional rheology of a branched polyethylene melt. This original design was improved by using silicone oil as a buoyancy bath to prevent sag in the LDPE melt,[13] and further upgrades led to extensional rheometry on various polymer melts stretched up to Hencky strains of 7.[14] A different extensional rheometer that was designed to vertically suspend the sample in an oil bath was developed by Münstedt (Figure 1.3b), who reported measurements on polystyrene that was stretched to Hencky strains up to 3.9.[15] Further advance in the development of extensional rheometers led to the emergence of filament stretching rheometers that were found suitable for measuring the extensional properties of Newtonian and viscoelastic liquids[16] as well as polymer solutions (Figure 1.3c).[17,18] More recently, the filament stretching rheometer was modified by Hassager *et al.* to facilitate extensional rheometry on branched polymer.[19] The Sentmant Extensional Rheometer (SER) is also a recently developed apparatus that allows reliable measurements on the extensional rheological properties of polymer melts.[20] The design adopts that of a Meissner-type rheometer, but the main difference is in that the SER drums are vertically oriented (Figure 1.3d). The main advantage of this flow fixture is in its easy integration into commercial rotational rheometers to perform uniaxial measurements, but the device is limited to a maximum Hencky strain of 4.3 that may be applied to samples.

While each extensional rheometry device has its own advantage relative to that of others, it is most vital to provide reliable measurements on desired materials. This is crucial when it comes to characterizing the rheology of polymers under shear and extension, since the two flow fields are inherently different and thus lead to radically dissimilar rheological response.[21] For instance, as the shear/extension rate increases, the steady shear viscosity typically exhibits shear thinning while the uniaxial extensional viscosity shows strain hardening. In the low rate limit ($\dot{\gamma}, \dot{\varepsilon} \rightarrow 0$), on the other hand, the viscosity under uniaxial extension is greater than zero-shear viscosity by a factor of 3, known as Trouton's ratio.[22] Under transient flow, the shear viscosity shows negative deviations from the low $\dot{\gamma}$ limit, while the transient extensional viscosity is characterized by positive deviations from the low $\dot{\varepsilon}$ limit. Given these characteristics in the linear viscoelastic regime (small $\dot{\gamma}$ and $\dot{\varepsilon}$), the transient extensional viscosity $\eta_u^+(t)$ can be predicted using a generalized Maxwell model:

$$\eta_u^+(t) = 3\eta^+(t) \tag{1.12}$$

$$\eta^+(t) = \sum_{k=1}^{N} G_k \lambda_k \left(1 - e^{t/\lambda_k}\right) \tag{1.13}$$

where $\eta^+(t)$ is the LVE prediction of transient shear viscosity and the factor of 3 in Eq. (1.12) is the canonical Trouton value that is universal for uniaxial deformations in the linear regime.

The conventional melt strain hardening described above is often more pronounced in branched polymers such as LDPE,[19] as it is believed that long chain branching introduces

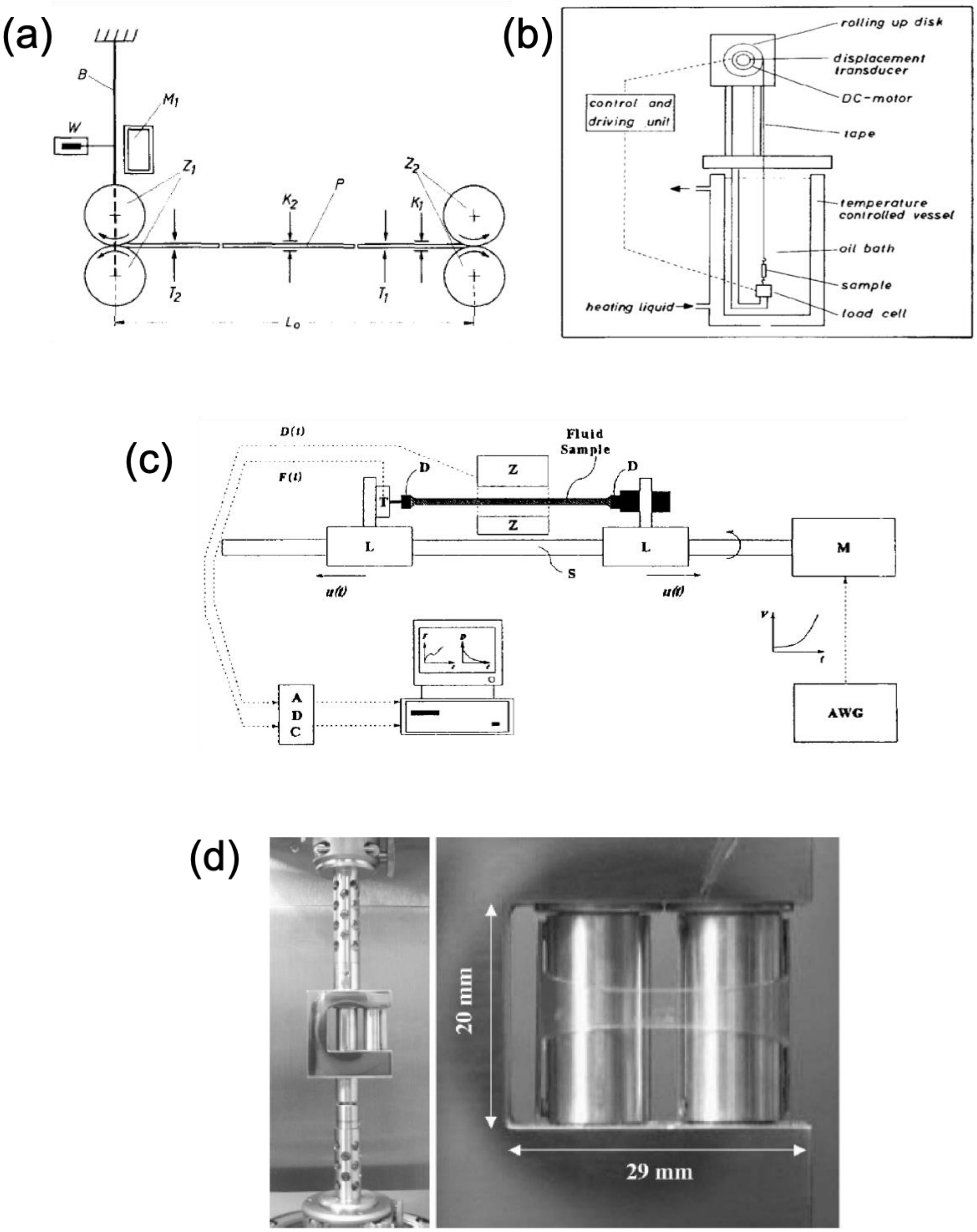

Figure 1.3 Various experimental apparatus for uniaxial extensional rheometry. (a) Original design of Meissner-type rheometer. (b) Original design of Münstedt-type rheometer. (c) Example of a filament stretching rheometer. (d) First version of the Sentmanat Extensional Rheometer integrated into a commercially available rotational rheometer.

resistance to retraction.[23,24] This argument is based on the idea that branches at exterior portions of the chain architecture can relax and retract such that there is negligible effect on the extensional rheology, while the polymer strands between branch points cannot easily retract and thus lead to the possibility of strain hardening. A broad molecular weight distribution is also known to have a similar effect as branching does on extension hardening.[25] HDPE, the linear analogue of LDPE, also exhibits strong extension hardening. Based on the Doi-Edwards formalisms of reptation theory, models fail to simultaneously predict strong extension hardening and shear thinning. Thus, the upturn in extensional viscosity in HDPE has often been attributed to the developing crystallinity during extension,[26] but this cannot be verified without any *in situ* characterization. Therefore, to bridge the gap between the nonlinear rheological response of entangled polymers and the stretching of chains under extensional flow, it is highly desirable to monitor the structural evolution in polymers *in situ* during extensional flow.

1.3 Polymer Crystallization and the Effect of Flow

Flow-induced crystallization is a phenomenon that affects practical manufacturing processes of all thermoplastic polymers that are semi-crystalline. The kinetics of polymer crystallization depends on temperature, rate of cooling, pressure, and applied flow field. Researchers are particularly interested in studying the effect of flow on polymer processing, as flow causes crystallization to proceed in polymer melts at temperatures where crystallization is kinetically suppressed or occurs at an extremely slow rate. In addition, the application of flow often leads to induced molecular orientation that may result in favorable consequences such as enhancement in stiffness and impact strength of the final product, or unfavorable outcomes such as warping in injection-molded polymer products due to differences in modulus at different layers.[27] As flow complicates the crystallization process, it would be prudent to first review the fundamentals of polymer crystallization and then proceed to discussing the effects of flow on crystallization.

1.3.1 Structure and Morphology

Semi-crystalline polymers form ordered structures that span a wide range of length scales. While polymer chains above their melting temperature are distributed in random coils (Figure 1.4a), periodic ordering can occur upon cooling. At the molecular level, polymer chains pack into unit cells that are ~0.1 – 1 nm in size and contain relatively few monomers (Figure 1.4b). Individual polymer chains participate in many unit cells and these chains are typically in extended conformations, where the crystallographic direction parallel to the molecular chains is conventionally defined as the c-axis. The unit cells possess periodicity typical of crystalline materials, which allows for the application of wide-angle x-ray scattering (WAXS) to obtain diffraction peaks that contain information on the size and shape of the crystal unit cell (see Section 2.1 for details).

On a larger length scale, unit cells pack into thin sheets called lamellae, which are typically 10 – 50 nm thick and ~10 microns wide (Figure 1.4c). The lamella is a thin ribbon-like collection of crystalline polymers radiating from a nucleation site, which is where crystallization is initiated. In quiescent crystallization, these lamellae growing from the nucleation site splay, bend, and branch to form three-dimensional structures known as spherulites (Figure 1.4d). Owing to the periodic stacking of lamellae, structural details on this level can be obtained from

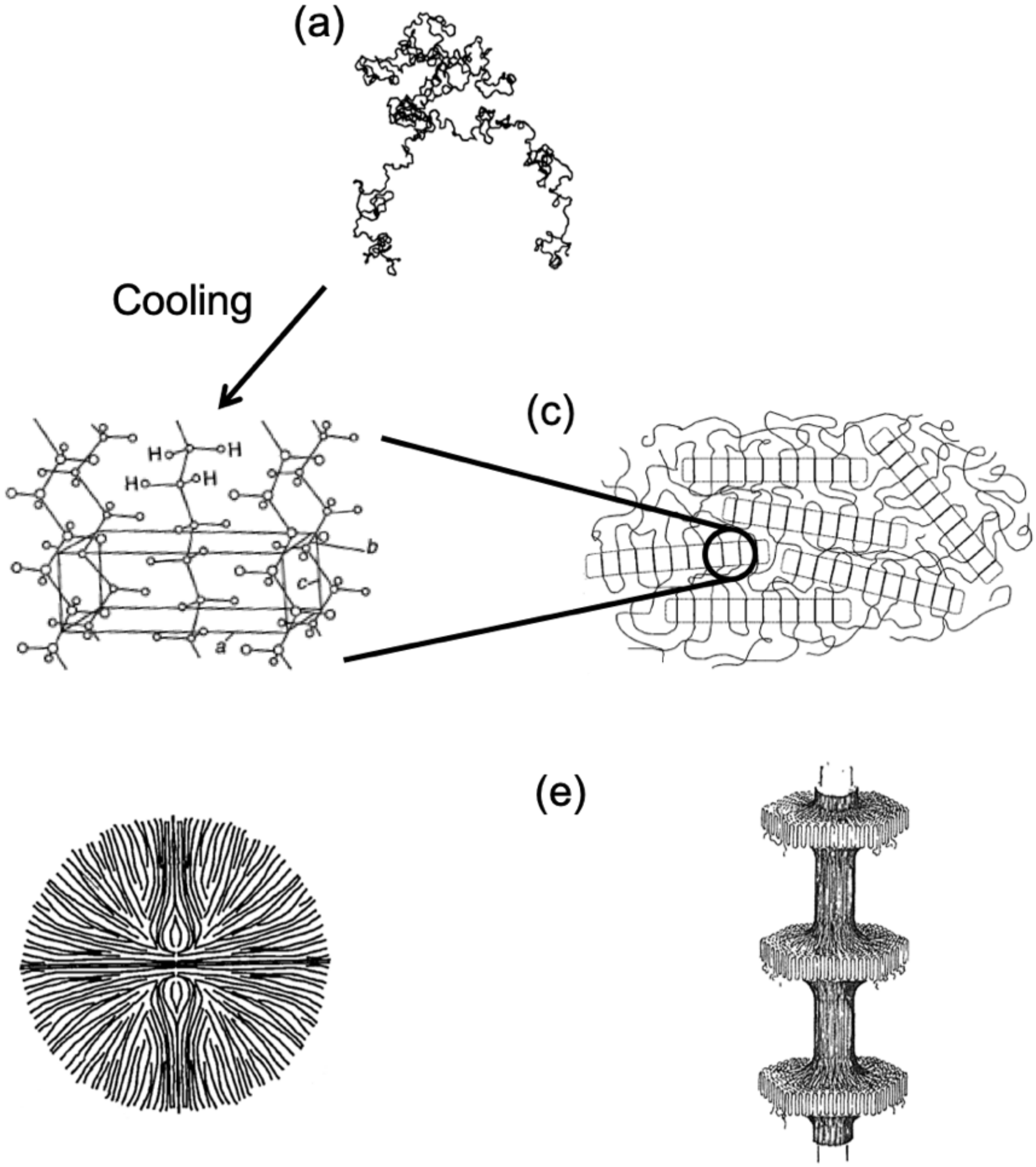

Figure 1.4: Hierarchical structures of semi-crystalline polymers at multiple length scales. At elevated temperatures, polymer chains adopt random coil conformations (a), and pack into unit cells (with c-axis along the chain axis) upon cooling (b), to form lamellae (indicated by rectangular groupings) on larger length scales (c). These lamellae can form three-dimensional structures such as spherulites in quiescent conditions (d) and shish-kebab morphology under sufficiently strong flow (e). Figures adapted from R. G. Larson, “The Structure and Rheology of Complex Fluids” *Oxford University Press* (1999);[11] P. C. Heimenz and T. P. Lodge, “Polymer Chemistry” *CRC Press* (2007)[28].

small-angle x-ray scattering (SAXS) measurements (see Section 2.1 for details).

Spherulites can be ~10 – 100 microns across or exceed millimeters in size, and will grow until they impinge on other spherulites. Within spherulites, the region between lamellae that remains uncrystallized is filled with amorphous materials. The presence of crystalline and amorphous domains allows for characterizing semi-crystalline polymers via the degree of crystallinity, a useful and practical quantity indicating the mass or volume fraction of crystalline matter.[29]

Crystallization under sufficiently strong flow produces a different characteristic morphology known as shish-kebab structures. These consist of lamellae laterally growing outward from a core spine made from highly extended polymer chains (Figure 1.4e). This type of crystal morphology was first observed using electron microscopy in a linear polyethylene crystallized from dilute solution.[30] Typically, the formation of shish-kebab morphology requires very strong flow conditions that sufficiently stretch and align polymer chains to allow the nucleation of thread-like precursors and subsequent lamellar growth.[31]

1.3.2 Crystal Nucleation and Growth

In the absence of flow, crystallization of polymers melts is initiated by nucleation—the formation of crystallites—where temperature plays a key role. The possibility of nuclei formation is governed by thermodynamics, in which the net change in Gibbs free energy (i.e., driving force for phase change) involves a tradeoff between the free energy gain associated with crystallization, which scales with volume, and the free energy penalty associated with solid surface formation, which scales with surface area. Subcooling below the equilibrium melting temperature provides a sufficient thermodynamic driving force to overcome the kinetic barrier for solidification, and spontaneous nucleus growth occurs once the size of the nucleus exceeds a critical value beyond which the overall change in free energy decreases.[32] However, quiescent crystallization rarely occurs via homogeneous nucleation, in which nuclei consisting of nascent polymer crystals form randomly in time and space. Rather, it usually predominantly proceeds via heterogeneous nucleation, in which impurities such as catalyst residuals or foreign particles in the polymer melt lower the surface energy cost for nuclei formation.

The rate at which nucleation and crystal growth occur is determined by two factors: thermodynamic driving force (as described above) and diffusion of amorphous material to crystalline mass. As the temperature decreases from the equilibrium melting temperature, the driving force increases while diffusion becomes slower. Combination of these two effects leads to nucleation and crystal growth rates that increase with undercooling and reaches a maximum.[29] It is evident that the overall crystallization process and its kinetics are both highly temperature-dependent, which is why polymer melts are supercooled to temperatures well below the equilibrium melting temperature for crystallization to be measurable.

1.3.3 Flow-Induced Crystallization

The application of flow on undercooled polymer melts drastically speeds up the crystallization process. This allows crystallization to be observable at reasonable time scales,[33] or even occur at temperatures where there would normally be insufficient thermodynamic driving force to overcome the kinetic barrier for crystallization.[34] Knowing that flow causes polymer chains to stretch and orient, researchers believe that this particularly leads to increase in the number density of nuclei and enhancement in nucleation rates. Morphological investigations show increase in the nucleation density under the influence of shear, where more crystallites smaller in size nucleate with increasing shear rates.[35,36] Evidence from recent studies shows that high molecular weight species and chain orientation in the melt state are particularly sensitive to flow and thus are the key factors that give rise to accelerated nucleation.[35–40]

Other studies[41,42] have also shown that the activation of flow effects on crystallization can be characterized by the Weissenberg number (Wi), the product of deformation rate and characteristic relaxation time. In the flow-induced crystallization literature, flow regimes are generally classified into three categories using Wi based on reptation and Rouse times (described in Section 1.2.2).[41,43] Under flow conditions where $Wi_{rep} < 1$ and $Wi_R < 1$, flow is expected to have little or no effects on the crystallization kinetics as polymer chains are able to relax flow-induced chain stretching quickly; the rheology reverts to Newtonian behavior. For $Wi_{rep} > 1$ and $Wi_R < 1$, polymer chains can align but do not stretch, and the applied flow enhances crystallization kinetics to result in more numerous, smaller spherulitic structures; under sufficiently strong flow conditions ($Wi_{rep} > 1$ and $Wi_R > 1$), extreme morphologies (e.g. rods and shish-kebabs) can develop since polymer chains stretch as well as align.

1.4 Experimental Studies of Flow-Induced Crystallization

Since the first evidence of flow effects on the morphology and crystallization behavior in a polymer solution,[30] researchers have directed their attention to flow-induced crystallization in polymers. Early investigations on the consequences of flow-induced crystallization under process-type flows (e.g. injection molding) were examined using *ex situ* measurements,[44,45] which made it inherently difficult to explore the fundamental details that underlie the phenomenon without real-time or *in situ* monitoring, especially under the conditions where flow is complex or poorly defined. To overcome this challenge, researchers have sought to design simple test protocols in which a well-defined flow field is applied at a constant temperature at which quiescent crystallization is suppressed. Early efforts led to a flow protocol that heated the polymer well into its melt state, cooled it to a desired test temperature, initiated shear flow at a constant rate, and measured the crystallization onset time based on the increase in viscosity.[33] This "continuous" flow protocol was improved by decoupling the effect of flow on crystallization kinetics by applying a short pulse of shear ("short-term" flow) and then monitoring the subsequent accelerated crystallization behavior.[46]

Studies employing either the short-term or continuous flow protocol have used various experimental techniques to monitor flow-induced crystallization. Sharp increase in viscosity was used as an indicator of crystallinity in studies that involve continuous deformation,[26,43,47] while growth of elastic modulus in oscillatory shear was used to monitor crystallization in studies using the pulse flow protocol.[35,48–50] Other works used optical methods such as optical microscopy[42,45,51] to visualize the flow-induced structure or determine nucleation density, turbidity[52–54] to detect the onset of crystallization, and birefringence[37,55] to monitor the evolution of crystallite orientation and growth in crystallinity. Among these monitoring techniques, *in situ* x-ray scattering in particular has found widespread application to study flow-induced crystallization, as SAXS directly probes larger scale structures such as lamellae or shish-kebabs, and WAXS determines crystal structure resulting from the ordering of polymer chains on the unit cell level.

While most existing flow-induced crystallization studies using *in situ* x-ray scattering methods primarily involve shear,[37–39,56–59] recent development of devices that produce well-defined uniaxial extensional flow has allowed more reliable extensional flow-induced crystallization studies. An example of such apparatus is the filament stretch rheometer, with which Hassager *et al.* measured the transient elongational viscosity in various polymer melts.[19,60,61] Rothstein *et al.* took this one step further to use it in extensional flow-induced crystallization studies of iPB[62] and iPP melts.[63] Another device that allows for extensional flow-induced crystallization studies is the SER,[20] which was used to investigate the flow-induced crystallization behavior of iPB,[47] ethylene-butane plastomer,[64] and HDPE melts.[26] However, these extensional flow studies lack *in situ* insight into the evolving structure, crystallite orientation, and extent of crystallization; they rather rely on the upturn in transient viscosity to detect the onset of crystallization or *ex situ* methods such as differential scanning calorimetry, microscopy, and x-ray scattering on already stretched samples.

Li *et al.* remain as the only group that has demonstrated *in situ* x-ray scattering measurements coordinated with simultaneous extensional rheometry during extensional flow-induced crystallization experiments. They have successfully conducted experiments on a large selection of semi-crystalline polymers—HDPE,[65] polyethylene oxide,[66] iPP,[67] cross-linked HDPE,[68–71] and iPB[72]—using an instrumentation very similar to that employed in the studies presented in this dissertation (see Section 2.3). Most of the studies by Li are step strain experiments at very high extension rates. Due to insufficient time resolution to probe the structural evolution during flow inception, *in situ* monitoring of structural changes immediately following deformation is reported. However, some of their work show signs if crystallinity initiated during the application of flow, indicating that the effect of flow and subsequent crystallization are not decoupled.

1.5 Computational Modeling of Flow-Induced Crystallization

Motivated by the impact of deformation history on the rheological properties and structure of semi-crystalline polymers during processing, researchers have devoted significant efforts to develop models to help understand and predict the flow-induced crystallization process. Modeling approaches include kinetic models[73] and molecular dynamics,[74–76] which provide details of the kinetics of polymer crystallization but not of process applications. As it is desirable to formulate models that are applicable to process modeling, researchers have proposed flow-induced crystallization models that include various descriptions of how crystallization and nucleation are affected by applied deformation. These models typically consist of hierarchical descriptions on the melt rheology, nucleation, and crystal growth, where the flow history imposed on the polymer melt impacts the nucleation process, and the subsequent nucleation affects the crystallization kinetics.

At the core lies the crystallization model that captures the details of crystallization kinetics and crystal growth. Descriptions are typically in the form of the Avrami equation[77–79] or a set of rate equations[73] that account for the geometry of the crystal, growth dimensionality, and the growth kinetics.[32] Other models describe how the crystallization process is affected by polymer orientation in the presence of flow, where flow creates a nucleation process that otherwise does not exist prior to its application.[80,81] As it is assumed that crystal growth rate is independent of flow once nucleated, the flow dependence of the rate of nucleation is captured in nucleation model. The driving force that leads to flow-enhanced nucleation is usually in some measurable macroscopic parameter (e.g. deformation rate, strain, work input). For example, Eder *et al.* postulated a shear rate dependent probability function for the presence of flow-induced nuclei that leads to crystallization.[81] However, the model is phenomenological and lacks any dependence on polymer structure or properties. In fact, this is the case for various descriptions of flow-enhanced nucleation, which vary in detail across models.[81–84]

More recent models sought to link the nucleation process to descriptions of melt viscoelasticity through the melt flow model. For instance, Zuidema *et al*. modified the Eder model by adding a viscoelastic model to account for flow-induced orientation and stretch of molecules (i.e. chain conformation) that contribute to enhanced nucleation.[85] In particular, the molecular configuration state was calculated from the invariants of the Finger strain tensor related to the slowest relaxation mode in a Leonov model description of the molten phase. In addition, Coppola *et al.* developed a model that uses the disengagement time and average orientation distribution as the critical parameters that drive the crystallization process.[86] Interestingly, van Meerveld *et al.* point out that the models formulated by both Zuidema *et al.* and Coppola *et al.* can successfully predict the experimental results obtained by Lagasse and Maxwell,[33] although they are radically different in detail.[41] This raises an important point that it is most critical to verify how the flow applied to the polymer in the melt enhances the nucleation process, and subsequently, accelerates crystallization.

In the past two decades, Peters and his group at Eindhoven have played a leading role in developing flow-induced crystallization models that describe the details of how constitutive equations are coupled to nucleation and crystallization models.[41,85,87–93] These models are based on a core assumption that the high molecular weight chains (often represented in the modeling framework by the slowest relaxation mode) are responsible for enhanced nucleation through the formation of regions with highly aligned chains that promote shish nucleation under strong flow conditions. Earlier works by Peters and co-workers attribute recoverable strain of the longest chains to the driving force for flow-induced oriented precursors.[85,87] More recent models use a molecular stretch parameter as a means to quantify the effect of flow on the creation of elongated precursors.[89–93] The stretch parameter is a quantity calculated from a reptation-based constitutive equation that describes the macroscopic melt flow model, where the slowest relaxation time is considered as the reptation time, which in turn in related to the Rouse time through reptation theory. Thus, formulating an accurate flow-induced crystallization model requires information on not only the polymer sample's relaxation spectrum but also its material properties such as the weight-averaged molecular weight, entanglement molecular weight, and average chain entanglement.

1.6 Objectives and Thesis Outline

Semi-crystalline polymers are substantially affected by flow-induced crystallization, in which applied flow fields not only accelerate the crystallization kinetics but also can significantly affect the final properties of the polymer product due to induced molecular orientation. Unfortunately, most existing flow-induced crystallization studies reported in the literature employ shearing flows, since they are relatively easier to produce compared to the kinematically stronger extensional flows, which govern many important polymer processing operations. To this end, the primary motivation of this thesis is to (1) more fully explore the complicated FIC phenomenon in semi-crystalline polymers under well-defined extensional flow, (2) characterize the crystallization behavior using time-resolved x-ray scattering methods, and (3) introduce experimental design strategies that test the formulation of recent FIC models at their core on how induced molecular orientation/stretching in the polymer melt leads to flow-enhanced nucleation (and subsequent accelerated crystallization).

Recent studies in our research group have successfully demonstrated our capability to perform various uniaxial extensional flow experiments by use of a custom-designed instrument that allows x-ray scattering measurements.[94,95] These research efforts have provided a strong foundation to extend FIC studies to extensional flow, which is highly effective at promoting orientation of polymer chains and microstructures. As the formation of crystallites often occurs during or following flow, *in situ* x-ray scattering is a powerful tool that provides direct evidence of the evolving crystallinity and developing microstructural orientation in real time. Such *in situ* structural characterization, coordinated with simultaneous measurements of the bulk rheological response, offers a comprehensive understanding of the effect of extensional flow on polymer crystallization and on the mechanical properties.

This thesis is organized as follows: Chapter 1 has provided an introduction on the linear and nonlinear rheology of polymers, with a particular focus on entangled melts. Following an overview of polymer crystallization and the effect of flow on crystallization, a literature review of experimental and modeling studies of flow-induced crystallization has been presented.

Chapter 2 describes the experimental principles and methods applied to the work presented in this thesis. The chapter begins with the fundamentals on x-ray scattering and discusses the advantages of using x-ray scattering techniques on studies of flow-induced crystallization in polymers. A brief description on the instrumentation used for x-ray scattering studies under extensional flow is given. This chapter closes with the details of the analysis procedures for quantifying the extent of crystallization and the state of molecular/microstructural orientation.

Our experimental capability to perform *in situ* x-ray scattering measurements on elongational flow-induced crystallization in polymer melts is first demonstrated in Chapter 3. This chapter reports findings on the crystallization behavior of branched PLA under uniaxial extensional flow. The chain architecture of linear PLA is modified by inducing long chain branching to provide sufficient melt strength for extensional flow-induced crystallization experiments. This study employs a short-term flow protocol to explore the effect of rate and strain on subsequent crystallization following flow. To the best of our knowledge, *in situ* SAXS and WAXS measurements on flow-induced crystallization of PLA subjected to extensional flow are the very first of their kind and thus have tremendous scientific significance and technological relevance.

Chapter 4 presents experimental studies designed using the modeling framework described by Roozemond and Peters[90] to test a key assumption in most current flow-induced crystallization models that flow-induced molecular orientation leads to enhanced nucleation rate, which in turn leads to accelerated crystallization kinetics. This underlying hypothesis is directly tested by subjecting iPB to various extension rates and Hencky strains that result in similar predicted number density of flow-induced nuclei, calculated from the molecular stretch parameter during extensional flow and relaxation, as predicted by a simplified Rolie-Poly model. *In situ* SAXS is employed under the short-term flow protocol to investigate the crystallization behavior from experimental conditions that are expected to result in similar degrees and kinetics of crystallization as well as final orientation states.

In Chapter 5, flow-induced crystallization of LDPE subjected to uniaxial extension flow is studied using *in situ* x-ray scattering. The extent of crystallization and orientation of crystallites are monitored using SAXS and WAXS measurements. This chapter discusses the difference between the results from experiments where the polymer crystallizes isothermally *after* the application of flow under various extension rates and Hencky strains, and those from studies in which samples crystallize at desired temperatures *during* the application of flow under multiple extension rates. The effect of moderate changes in temperature and applied strain manifested in dramatic differences in morphology is also discussed. The chapter concludes by introducing a hypothesis based on overall observations, and further speculation continues in the following chapter.

Chapter 6 expands upon earlier flow-induced crystallization studies on HDPE reported in a previous thesis to further explore the details of the hypothesis introduced at the end of Chapter 5. *In situ* x-ray scattering measurements are conducted on samples under similar experimental protocols as those employed by McCready and Burghardt.[95] A range of Hencky strains is applied at a fixed extension rate to examine flow conditions that suppress crystallization during flow as well as those that would lead to crystallization during flow. Results are compared to those from all other flow-induced crystallization experiments presented in this thesis to gain a comprehensive insight into the range of morphologies induced by extensional deformation in various polymers that undergo flow-induced crystallization.

Finally, Chapter 7 recapitulates the key findings of the work presented in this thesis and suggests possible directions for further research in the field. Appendix A describes preliminary work on flow-induced crystallization in iPB subjected to simple shear that has set the stage for FIC studies employing uniaxial extensional flow. Additional work revolving the theme of exploiting *in situ* techniques to bridge the gap between rheology and microstructural response to flow is presented in Appendix B, which demonstrates the use of x-ray photon correlation spectroscopy to probe the onset of microscopic structural irreversibility in a colloidal gel under oscillatory shear.

Chapter 2

Experimental Techniques and Analysis Methods

2.1 X-ray Scattering in Polymer Crystallization

X-ray scattering methods are non-destructive and powerful tools that deliver structural information of materials, especially for ordered systems. Under the influence of flow, polymer chains align to form ordered structures, which makes x-ray scattering applied to polymers during flow an extremely effective technique to gain insight into the microstructural dynamics that leads to their complex flow behavior. The purpose of this section is to describe the fundamental principles behind x-ray scattering and its applications in polymer crystallization.

X-rays are electromagnetic radiation that interact with the electrical charges in matter. The interaction may be in the form of absorption or scattering, in which the former event leads to conversion of energy from the incident beam into other forms, while the latter is characterized by the change in direction of propagation of the radiation. In the scattering process, when the oscillating electromagnetic wave of the incident beam induces oscillation in the electrons of the sample at the same frequency, there is no loss in kinetic energy and elastic scattering occurs. In contrast, inelastic scattering occurs when the scattered x-rays do not retain the same wavelength (or energy) as that of the incident beam as a result of energy and momentum transfer between the photon of the incident x-ray and the electron initially at rest. While this may provide information on the electronic motion in atoms, inelastically scattered x-rays possess a range of energies that inherently do not carry any information on the structure of the sample. As the analysis of structure relies on interference among scattered x-rays from different positions in sample space, elastic scattering will be the focus when discussing x-ray scattering techniques for structural characterization.

In principle, two essential phenomena contribute to the determination of structure: *scattering* and *diffraction*.[96] As introduced earlier, (elastic) scattering is described by the interaction of the incident x-ray with the sample in which the wavelength of the redirected electromagnetic radiation remains the same. Diffraction involves the interference of scattered waves, in which constructive interference arises from the superposition of waves that are in phase with each other, while destructive inference leads to a decrease in the wave amplitude as a result of the waves being out of phase. Constructive interference from periodic internal structures that leads to diffraction peaks can be described by Bragg's Law:

$$2d\sin\theta = n\lambda \tag{2.1}$$

where d is the interplanar distance, 2θ is the scattering angle, n is an integer, and λ is the wavelength of the x-ray beam (Figure 2.1).

While "scattering" and "diffraction" may be accorded precise definitions relating to fundamentally different phenomena as described above, there is wide variance is common usage, and, indeed, these words are often used interchangeably (including in this thesis). The word "diffraction" is frequently associated with experiments on samples that are highly ordered and periodic, such that the scattered x-rays are primarily redirected in a particular direction, while "scattering" is more often associated with experiments on weakly ordered or disordered materials, or experiments conducted at small angles (one seldom hears the phrase "small-angle x-ray diffraction", for instance, even in materials like ordered block copolymers that show classic Bragg peaks associated with a wide range of long-range ordered structures).

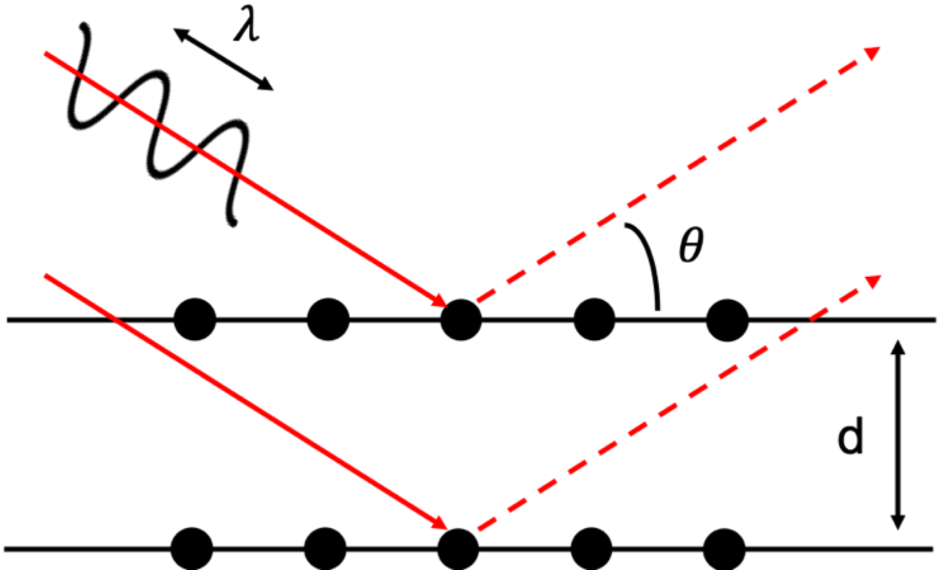

Figure 2.1: Schematic illustration of Bragg’s Law.

Regardless of terminology, information about microscopic structural information is always revealed as a result of interference between/among scattered x-rays, which, in materials lacking precise long-range order, need not lead to sharp diffraction peaks according to Bragg's law. Figure 2.2 illustrates the interference between two scatterers separated by distance $\boldsymbol{r}$, which can then be expanded to describe the interference among scatterers in all sample space. Since x-rays are electromagnetic waves, it is convenient to use the path difference between the two scatterers to describe the phase difference ($\Delta\phi$):

$$\Delta\phi = -\frac{2\pi}{\lambda}(\boldsymbol{S} - \boldsymbol{S_0}) \cdot \boldsymbol{r} \tag{2.2}$$

where $\boldsymbol{S}$ and $\boldsymbol{S_0}$ are the unit vectors in the direction to the observer (detector) and along the direction of incident plane wave, respectively. The scattering vector $\boldsymbol{q}$ is then defined as:

$$\boldsymbol{q} = \frac{2\pi}{\lambda}(\boldsymbol{S} - \boldsymbol{S_0}) \tag{2.3}$$

such that $\boldsymbol{q}$ is a wave vector that bisects the angle between incident and scattered x-rays. By geometry, the magnitude of $\boldsymbol{q}$ is given by

$$q = |\boldsymbol{q}| = \frac{4\pi}{\lambda}\sin\theta. \tag{2.4}$$

The scattering contributions from each part of the sample can then be added by generalizing the effects of interference from two scatterers to a continuous distribution of electrons over the entire scattering space (*V*):

$$A(\boldsymbol{q}) = \int_V \rho(\boldsymbol{r}) e^{-i\boldsymbol{q}\cdot\boldsymbol{r}} d\boldsymbol{r} \tag{2.5}$$

where $A(\boldsymbol{q})$ is the scattered amplitude measured at the detector, $\rho(\boldsymbol{r})$ is the electron density distribution, and $e^{-i\boldsymbol{q}\cdot\boldsymbol{r}}$ is a factor that encodes information about the relative phase of scattered

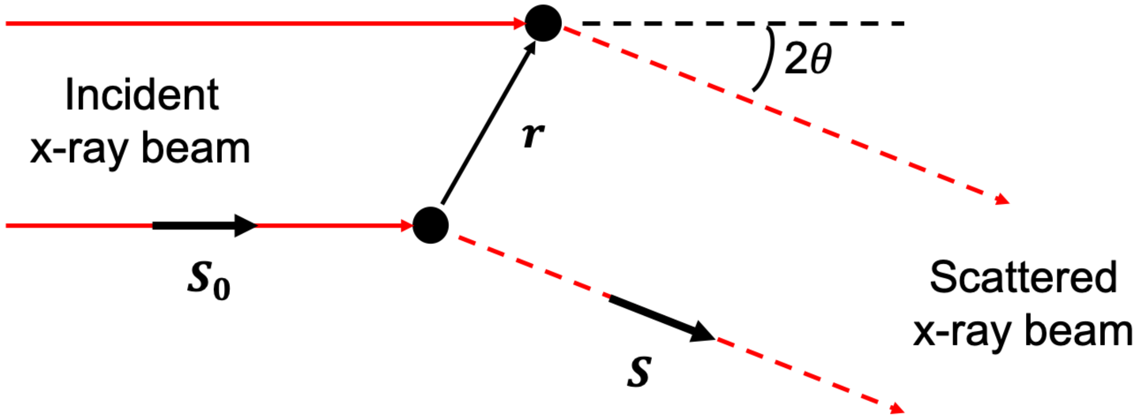

Figure 2.2: Schematic of interference between two scatterers.

x-rays from each position in space. Mathematically, $A(\boldsymbol{q})$ is the three-dimensional (3D) Fourier transform of $\rho(\boldsymbol{r})$, which effectively contain the same information. That is, if it is possible to measure the scattered amplitude in 3D reciprocal space, the inverse Fourier transform would provide full information on the structure in real space. However, the quantity measured at detectors is the flux (intensity) of the scattered amplitude, or equivalently, the magnitude: $I(\boldsymbol{q}) = |A(\boldsymbol{q})|^{\mathbf{2}}$. This leads to the "phase problem" in which information on the phases of scattered waves in real space is lost when the intensity is evaluated.

More of a practical concern is understanding how 3D reciprocal space is probed by x-ray scattering methods. When an x-ray beam is incident on a sample, x-rays scatter in all directions, but the associated scattering vectors correspond to only particular locations within the 3D reciprocal space. As the scattering angle 2θ changes, the tip of the scattering vector $\boldsymbol{q}$ maps a spherical surface with a radius $2\pi/\lambda$, commonly known as the Ewald sphere (Figure 2.3). Since this sphere is tangent to the origin of reciprocal space, it is difficult to fully characterize $I(\boldsymbol{q})$ unless the sample is rotated (to probe different points on the Ewald sphere that satisfy the Bragg condition) or the beam wavelength is varied. In typical x-ray scattering experiments under flow, only a small slice of the Ewald sphere is measured by the detector. For a scattering feature of interest located at a particular value of $\boldsymbol{q}$ (e.g. crystalline Bragg peak), the two-dimensional (2D) scattering patterns display the cross-section between the Ewald sphere a spherical surface a distance $\boldsymbol{q}$ from the origin of reciprocal space. For studies of polymers subjected to uniaxial flow, the distribution of scattered intensity in reciprocal space as a function of polar angle φ is a key indicator of the orientation distribution of the corresponding morphological features in real space. In Figure 2.3, it is evident that the polar angle φ measured away from the axis of symmetry (i.e. flow axis) differs from the apparent azimuthal angle φ' measured by the detector. This is particularly true for scattering images collected at wide angles, such that a geometric correction is necessary:

$$\cos\varphi = \cos\theta\cos\varphi' \tag{2.6}$$

For data collected at small angles, the correction is not necessary because the curvature of the Ewald sphere is negligible.

Bragg's law (Eq. (2.1)) is characterized by an inverse relationship between scattering angle and the corresponding real-space length scale. Small- and wide-angle x-ray scattering (SAXS and WAXS, respectively) are classic techniques for probing polymer structure, and are particular under flow where microstructures are oriented. SAXS and WAXS probe structural features at length scales on the order of 10 – 100 nm and 0.1 – 1 nm, respectively, which are the relevant scales of morphological factors in semi-crystalline polymers as reviewed in Section 1.3.1. Schematics of typical scattering features observed in semi-crystalline polymers are presented in Figure 2.4. Under quiescent conditions, the lamellae and c-axes of unit cells show random distributions, which leads to isotropic intensity distributions in reciprocal space, and hence in the corresponding SAXS and WAXS images (Figure 2.4a and d). Under conditions where flow induces molecular alignment, oriented crystallization leads to lamellar stacks with normals preferentially oriented in the direction of flow. The SAXS patterns from these oriented crystallites are characterized by an anisotropic intensity distribution that is concentrated along the flow direction (Figure 2.4b). When the flow is sufficiently strong, shish-kebab superstructures are produced, and this extreme morphology is manifested as a sharp streak and concentrated lobes of intensities parallel to flow in SAXS (Figure 2.4c). In WAXS, flow-induced

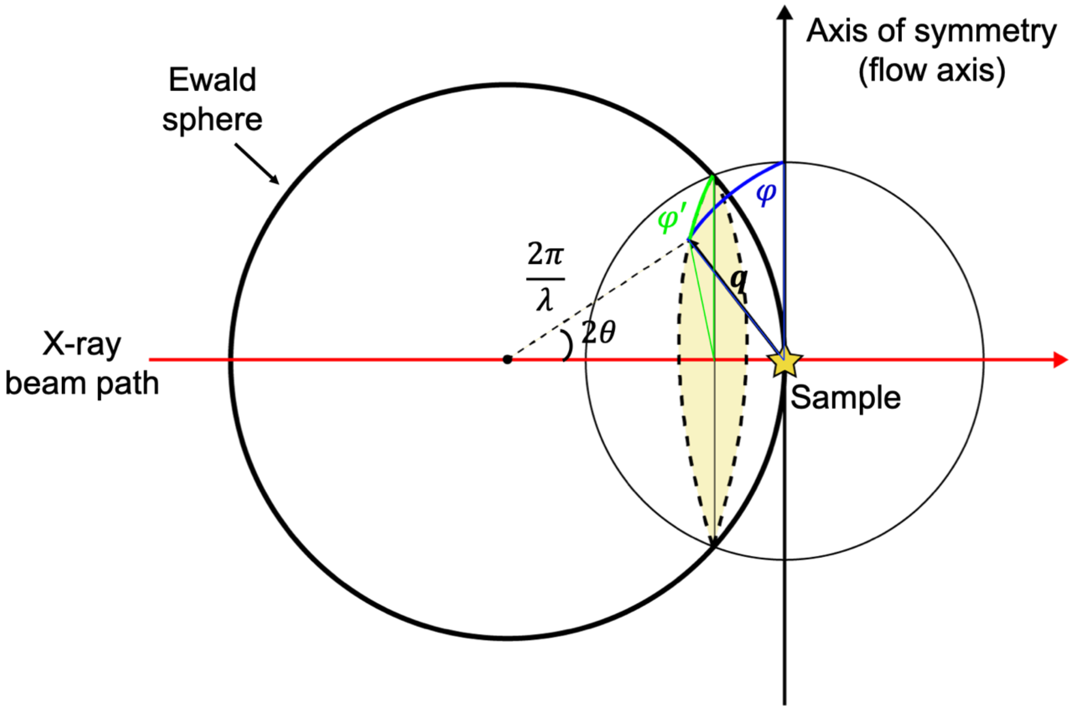

Figure 2.3: Illustration of Ewald sphere construction in 3D reciprocal space. The shaded region in yellow is the scattering intensity measured by the detector. The apparent angle φ' on the detector actually corresponds to the true angle φ in reciprocal space, such that a geometric correction is needed due to the curvature of the Ewald sphere.

polymer orientation results in crystallites in which the c-axis is preferentially oriented along the flow direction. This is reflected by an anisotropic distribution in the diffracted intensity that, for reflections from crystal planes that are parallel to the c-axis, is strongly concentrated transverse to flow. (Diffraction peaks from other crystal reflections may be characterized by different characteristic orientations relative to the flow direction; however, the diffraction peaks selected for detailed analysis in each of the materials studied in this thesis naturally adopt the transverse orientation relationship illustrated schematically in Figure 2.4e.) In particular, the WAXS pattern associated with a shish-kebab structure typically shows extremely concentrated diffraction peaks.

2.2 Experimental Apparatus for Synchrotron Studies

The major components of the experimental platform for simultaneous extensional rheometry and *in situ* x-ray scattering experiments are a Sentmanat Extensional Rheometer (SER) flow fixture, stepper motor, torque transducer, oven with slidable walls, and temperature control system. Details of the initial design[94] and recent applications[95] of the instrument are described elsewhere; here, a brief description will be given.

Uniaxial extensional flow is produced using the SER Universal Testing Platform (Xpansion Instruments LLC), model SER-HV-A01.[97] The flow device consists of two counter-rotating cylindrical drums with radius R, separated by a fixed distance L between the centerlines of the cylinders. A stepper motor connected to the SER drive shaft turns the drums at a constant rotation rate Ω, such that a well-defined extensional flow is applied to the mounted sample at a constant extension rate $\dot{\varepsilon}$ of $2\Omega R/L$..

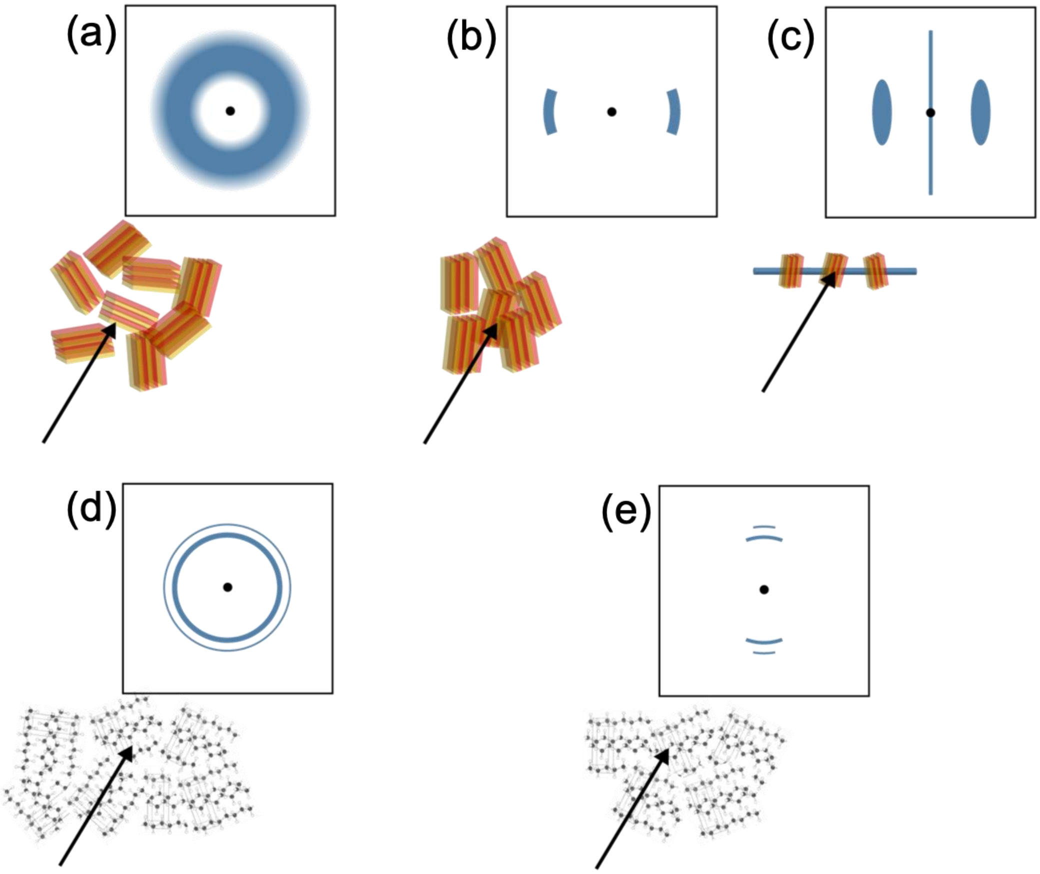

Figure 2.4: Illustrations of representative SAXS (a, b, c) and WAXS (d, e) patterns observed in semi-crystalline polymers. (a) and (d) are SAXS and WAXS images under quiescent conditions, respectively. The flow direction is horizontal in (b), (c), and (e).

The instrumentation also features a torque transducer that is attached to the torque shaft of the SER to record the mechanical response of the deforming sample. The measured torque $\mathcal{T}$ is related to the tensile force F exerted by the sample on the drums:

$$\mathcal{T}(t) = 2RF(t). \tag{2.7}$$

As the sample undergoes exponential stretching over the fixed length L, its cross-sectional area A decreases exponentially with time:

$$A(t) = A_0 \left(\frac{\rho_S}{\rho_M}\right)^{2/3} e^{-\dot{\varepsilon}t} \tag{2.8}$$

where A_0 is the initial cross-sectional area of the sample measured in the solid state, and ρ_S and ρ_M are respectively the solid and melt densities of the polymer. The transient extensional viscosity of a polymer melt can then be determined by:

$$\eta_u^+(t) = \frac{F(t)}{\dot{\varepsilon}A(t)}. \tag{2.9}$$

For extensional flow-induced crystallization experiments, a rectangular strip of polymer (approximately 25 mm in length, 9 mm in width, and 0.7 mm in thickness) sample is attached to the SER drums. A custom-built convection oven surrounds the SER fixture, and includes windows to allow the incident x-ray beam to pass through the center of the polymer sample and scattered x-rays to leave the oven (Figure 2.5a). This instrument is installed at the beam line at the synchrotron facility (Sector 5ID-D of the Advanced Photon Source at Argonne National Laboratory) for *in situ* x-ray scattering experiments. The high brilliance and flux of the synchrotron radiation enable high quality images to be collected with short exposure times, facilitating time-resolved measurements of structural evolution. The overall setup enables coordination of x-ray scattering pattern collection and torque measurement as the sample undergoes deformation, such that parallel measurements of transient extensional viscosity and flow-induced structural evolution can be obtained (Figure 2.5b).

2.3 Experimental Flow Protocol

Flow-induced crystallization experiments most generally follow two different flow protocols: short-term and continuous. Both methods involve heating the sample to a temperature well above its melting point to erase any thermal history and cooling it down to a constant crystallization temperature (T_c), upon which simultaneous SAXS/WAXS measurements are performed. The key difference between the two protocols is in when the onset of crystallization is first detected upon deformation.

In short-term flow, the sample is subjected to a short "pulse" of flow (~10^0 – 10^1 s) and the subsequent crystallization behavior is monitored for a long time (~10^3 s). This protocol decouples the effect of flow on crystallization, where flow is either applied at a constant crystallization temperature,[46] or at an elevated temperature followed by quenching the sample and allowing it to isothermally crystallize.[49] In fact, short-term flow protocol has been widely employed by flow-induced crystallization studies under shear[38,40,52,56,59,98] and extensional flows.[62,63,99] Of particular relevance to the work presented here are extensional flow-induced crystallization studies by Li and coworkers, who employed the short-term flow protocol and performed *in situ* x-ray scattering measurements using a test platform with a flow fixture similar to the SER.[65–68] For the work presented in this thesis, all short-term flow experiments employ a temperature protocol where the sample is first heated above its melting temperature (to erase

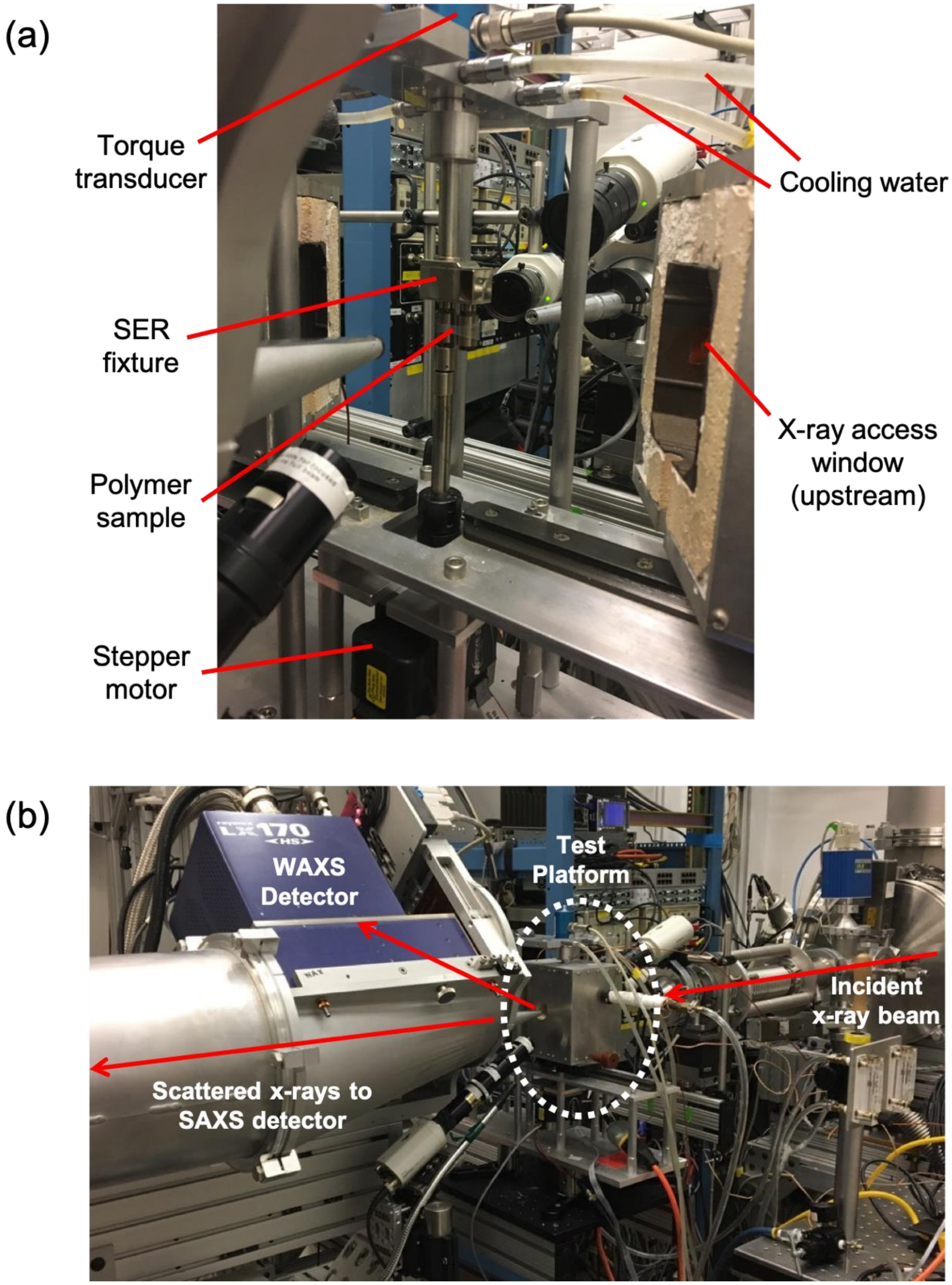

Figure 2.5: Instrumentation integrated into the beam line at DND-CAT Sector 5ID-D of the Advanced Photon Source at Argonne National Laboratory. (a) Individual components of the test platform. (b) Illustration of the experimental setup at the synchrotron facility.

existing crystallites), and then cooled to and equilibrated at a desired crystallization temperature, at which flow is applied and subsequent crystallization is monitored using SAXS and WAXS measurements (Figure 2.6a).

In continuous flow (Figure 2.6b), crystallization occurs during the application of flow. However, other than the few studies by Li *et al.*,[69,70] existing continuous flow-induced crystallization studies under extensional flow have typically relied on the upturn in extensional viscosity, as opposed to *in situ* structural characterization, to indicate the onset of crystallization.[26,47,64,100] Given the lack of *in situ* structural information on the flow-induced crystallization behavior of polymer melts, all experiments in this work significantly contribute to the very small pool of existing knowledge base.

2.4 Data Analysis Procedures

2.4.1 Analysis of 2D Scattering Patterns

A quantitative analysis is performed on the 2D x-ray scattering images to allow comparison across experiments based on absolute quantities. First, the raw intensity (I_{raw}) from the scattering data measured by the detector in each 2D image is extracted as a function of scattering vector q ($q = 4\pi \sin\theta / \lambda$, where 2θ is the scattering angle) and azimuthal angle φ' (at 1° increments) measured away from the flow direction. The extracted intensity is converted to intensity in absolute units ($I_{absolute}$) by accounting for the transmitted intensity (TI) measured at the beamstop, sample thickness (thk), and a calibration factor (CF) determined using a glassy carbon calibration standard:

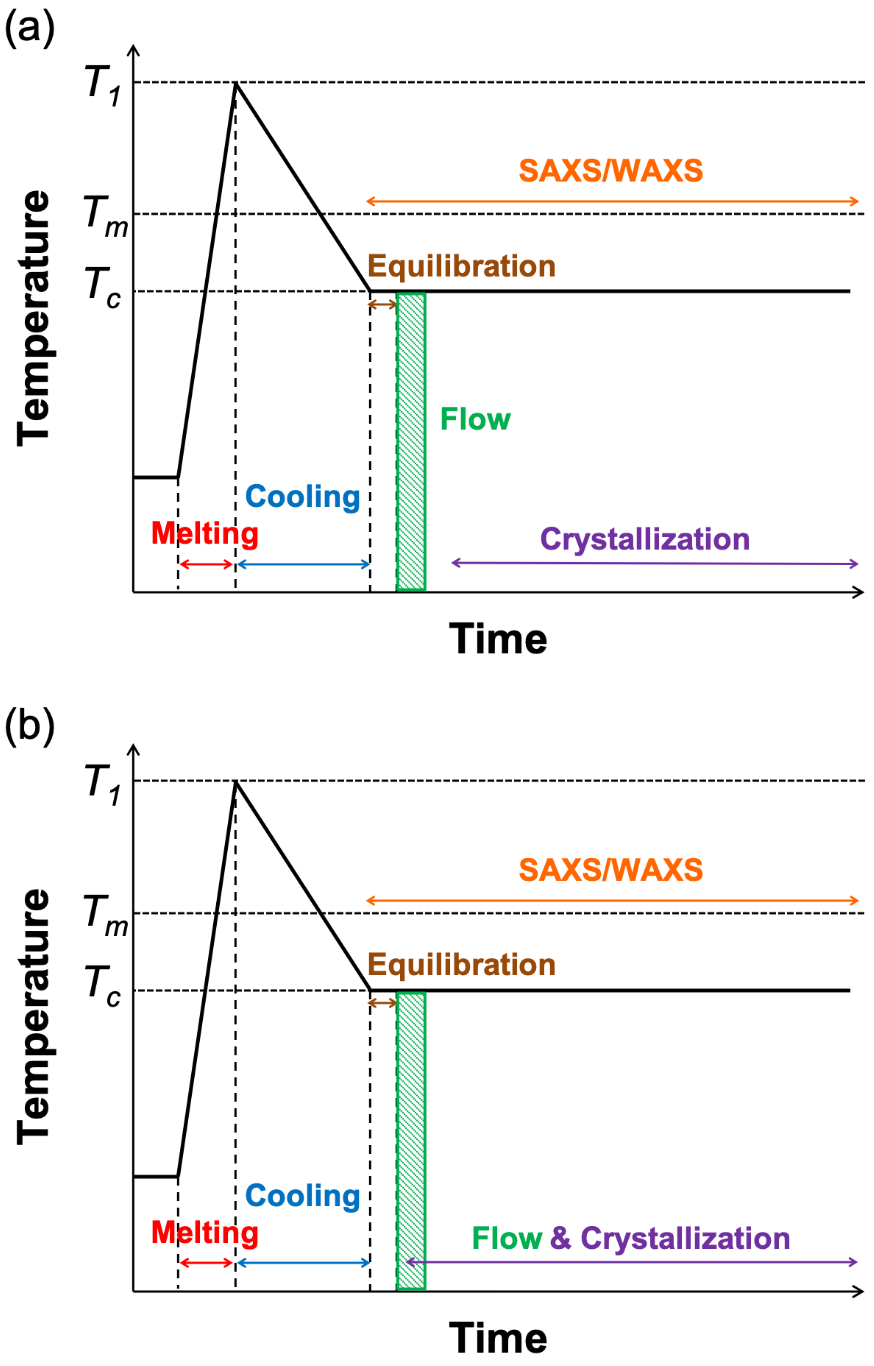

Figure 2.6: Comparison between short-term (a) and continuous (b) flow protocols. In short-term flow, crystallization occurs after a pulse of flow; in continuous flow, crystallization occurs during flow.

$$I_{absolute}(k) = \left(\frac{I_{raw}(k) - 10}{TI(k) - TD}\right)\left(\frac{CF}{thk}\right). \tag{2.10}$$

Here, k denotes the image number and TD is the transmitted intensity measured on the beamstop when no beam is present, which can be considered as a baseline signal. In the expression above, the raw intensity in the numerator is subtracted by 10 to similarly account for the baseline measured by the detector in the absence of scattering.

The intensity data are also corrected for background scattering. For SAXS measurements obtained from short-term flow experiments, the intensity of the image immediately after flow is subtracted from all subsequent images in order to highlight growth of SAXS intensity above the background observed in the amorphous sample. This is facilitated by the fact that the thickness of the sample remains constant with very modest changes as the polymer crystallizes. On the other hand, the background subtraction process for SAXS data from continuous flow experiments is more complicated due to the change in thickness as crystallization is initiated during flow. As this concern is specific to experiments presented in Chapter 5, the background correction for SAXS date measured during flow will be discussed in detail in Section 5.2.4. For WAXS, the scattering pattern from an empty oven is treated as the background and subtracted from the total scattering intensity to eliminate the scattering contributions arising from air as well as the instrument itself. Additional steps are taken to subtract the amorphous halo to isolate the intensity of crystalline diffraction peaks; this must be undertaken on an image-by-image basis, because the intensity of the amorphous background decreases while crystallization proceeds. The background subtraction process described here is relevant to qualitative analyses on SAXS/WAXS images, in which the growth of intensity can be directly related to the development of ordered microstructures, as well as quantitative analyses for characterizing the degree of crystallinity and state of crystallite orientation.

To quantify the extent of crystallization and crystallite orientation distribution, the 2D intensity data are extrapolated to 3D scattering intensity distributions in reciprocal space assuming uniaxial symmetry about the flow axis (Figure 2.3). This assumption is appropriate as the imposed deformation on the sample is a uniaxial extensional flow. The construction of 3D intensity distribution from 2D data requires a geometric correction due to the curvature of the Ewald sphere, as the polar angle measured away the axis of symmetry (i.e. flow axis) in 3D reciprocal space differs from the apparent azimuthal angle (φ') on 2D patterns. This correction becomes necessary for data measured at wide angles while it is negligible for small angles, as described in Section 2.1.

2.4.2 Extent of Crystallization

2.4.2.1 SAXS Invariant

By definition, the SAXS invariant (Q) is the total scattering power in reciprocal space and increases as crystallization proceeds. Therefore, it serves as an indicator of the growth of crystalline lamellae. As the measured intensity takes into account the beam width and the thickness of the sample, it is useful to evaluate the SAXS invariant weighted by the scattering volume (V):

$$Q/V = \frac{1}{(2\pi)^3}\int I(\boldsymbol{q})d\boldsymbol{q}. \tag{2.11}$$

Assuming uniaxial symmetry about the flow axis, Eq. (2.11) becomes

$$Q/V = \frac{1}{(2\pi)^2} \int_0^{\pi} \int_0^{\infty} I(q,\varphi)\, q^2 \sin\varphi \, dq \, d\varphi. \tag{2.12}$$

Owing to practical limitations, the integration in Eq. (2.12) is actually performed over a finite q range. In the work presented here, the low q limit is always set to 0.005 Å^{-1} to avoid any parasitic scattering effects from near the beam stop from being included in the calculation. The upper q-limit varies for each experiment, but is selected based on three practical considerations: (1) a full 360-degree scan of SAXS data is available up to this q value, (2) the intensity beyond the SAXS peak sharply decreases and approaches 0 near this q value, and (3) the intensity fluctuation at higher q leads to an incorrect calculation of Q/V as the noise is amplified from the presence of the q^2 term in Eq. (2.12).

2.4.2.2 WAXS Integrated Peak Area

Here we focus on the WAXS data collected from short-term flow experiments, as the observation time window (~10^3 s) provides sufficient time for the development of appreciable crystallinity. (Experiments using the continuous flow protocol occur over relatively short times, and the crystalline WAXS peaks are thus less pronounced.) In WAXS, the entire area under the diffraction peaks serves as a measure of the total extent of crystallization. The total area under the diffraction peak scales with each diffraction peak, so it is convenient to evaluate the integrated area under the primary crystalline peak that exhibits the strongest diffraction intensity. The intensity contribution only from the primary peak $I_{(\mathrm{abc})}$ with miller indices (abc) is isolated by subtracting the intensity of the underlying amorphous background from the total intensity for each image, because the intensity arising from the amorphous halo becomes suppressed as crystallization proceeds, while the SAXS background intensity does not change. The amorphous background intensity is obtained by fitting a polynomial to the amorphous intensity measured over the q range spanning the location of the primary peak. After subtracting the amorphous contribution, the extent of crystallization from WAXS is computed from the integrated crystalline peak area:

$$A_{(\mathrm{abc})} = \int_0^{\pi} \int_{q_{\mathrm{low}}}^{q_{\mathrm{high}}} I_{(\mathrm{abc})}(q,\varphi)\, q^2 \sin\varphi \, dq \, d\varphi \tag{2.13}$$

where q_{low} and q_{high} define the q range at which the primary peak occurs.

2.4.3 Crystallite Orientation Distribution

Molecular orientation distribution of uniaxial systems is commonly characterized using the Hermans orientation parameter

$$\langle P_2 \rangle = \frac{3\langle \cos^2\varphi \rangle - 1}{2} \tag{2.14}$$

where $\langle \cos^2\varphi \rangle$ is given as

$$\langle \cos^2\varphi \rangle = \frac{\int_0^{\pi} I(\varphi)\cos^2\varphi \sin\varphi \, d\varphi}{\int_0^{\pi} I(\varphi)\sin\varphi \, d\varphi}. \tag{2.15}$$

The angled brackets represent an average cosine squared weighted by the azimuthal intensity distribution $I(\varphi)$. In the work described here, the azimuthal scattering intensity distribution is obtained by radially integrating the corrected absolute intensity (as outlined in Section 2.4.1) over the q-range of interest in SAXS and WAXS.

As it is appropriate to assume uniaxial symmetry for analyzing the data collected from studies pursued in this thesis, $\langle P_2 \rangle$ is a valuable measure of the average distribution of crystallite orientation in polymers with structures induced by uniaxial extensional flow. The values of the orientation factor range from -0.5 to 1, where 0 indicates random distribution of microstructures, and the low and high extremes respectively correspond to perfect orientation orthogonal to and parallel to the direction of orientation. In the analysis of SAXS and WAXS patterns, the images are always configured in a consistent manner in which the stretching direction is presented in the horizontal direction. As it is useful to characterize the orientation distribution with respect to the direction of perfect alignment, the values of $\langle P_2 \rangle$ calculated from Eq. (2.14) are normalized by the $\langle P_2 \rangle$ value for perfect alignment. For a perfectly orientated sample, lamellae diffraction occurs along the axis of the lamellar normal (φ = 0° in SAXS), while diffraction from the primary crystalline peak is always orthogonal to the polymer chain axis (φ = 90° in WAXS). Defined in this way, the normalized $\langle P_2 \rangle$ values in both SAXS and WAXS always range between -0.5 and 1, where $\langle P_2 \rangle$ = 0 indicates random distribution of lamellae and polymer crystals, while $\langle P_2 \rangle$ = -0.5 and 1 respectively indicate perfect alignment of both the lamellar normal and c-axes of unit cells perpendicular to and parallel to the stretching direction.

Chapter 3

Flow-Induced Crystallization of Branched Poly(lactic acid)

3.1 Introduction

Poly(lactic acid) (PLA), a semi-crystalline thermoplastic that can be derived from renewable sources, has attracted attention over the past decade as a possible replacement for petroleum-based polymers. Owing to its high tensile strength and good transparency, PLA has been widely used as a packaging material for food and beverage containers, thermoform packaging, and paper coating.[101] The biocompatibility and bioresorbability of PLA have also extended its applications to pharmaceutical and biomedical fields as drug delivery systems[102] and bioresorbable vascular scaffolds.[103] However, PLA exhibits poor thermal resistance due to its low glass transition temperature (T_g ~ 60-65 °C) and is limited to applications at low temperatures unless its crystallinity is enhanced. In addition, the intrinsically slow crystallization kinetics has presented challenges in typical melt processing operations that produce PLA-based polymer products.[104]

Consequently, researchers have studied the flow-induced crystallization behavior of PLA as the application of flow not only leads to accelerated crystallization kinetics but produces oriented structures that enhance the mechanical properties of the final product. To examine the effect of temperature and flow on PLA crystallization, studies in the current literature employ techniques such as optical microscopy and rotational rheometry.[105–108] More recent studies exploit x-ray scattering methods to probe the structural changes induced by deformation but are limited to *ex situ* characterization of quenched samples.[109–111] A few studies have performed *in* *situ* x-ray scattering measurements under shear.[112,113] A recent study has considered elongational flow,[114] but only under conditions relevant to solid processing—at temperatures between T_g and the melting temperature.

It is important to understand the flow-induced crystallization behavior of PLA under extensional flow, as it is a dominant flow field in processing applications such as melt spinning and blow molding. Unfortunately, there is a conspicuous absence of studies in the current literature that involve *in situ* structural characterization of PLA crystallization under extensional flow. Due to its relative ease of implementation in the melt, shear flow is widely used in existing flow-induced crystallization studies. The low melt viscosity of the material also hinders the capability of conducting extensional flow-induced crystallization experiments. To enhance the melt strength of PLA, researchers explored methods such as adding nucleating agents and plasticizers[115] or increasing the molecular weight.[108] In particular, Nofar *et al.* demonstrated that branched structure is particularly effective in promoting crystallization since branched chains act as nucleating sites.[116] Shear-induced crystallization studies on linear and branched PLA also showed that long chain branching significantly enhanced the nucleation density.[117] Wang *et al.* further revealed that increasing the degree of long chain branching leads to an increased nucleation density.[105] While these studies allude to the possibility of using branched PLA to conduct extensional flow-induced crystallization experiments, none has been reported to the best of our knowledge.

In this chapter, we explore crystallization in a branched PLA subjected to uniaxial elongational flow. The modified architecture provides sufficient melt strength for extensional flow-induced crystallization experiments. *In situ* x-ray scattering measurements are performed to probe the structural evolution as the polymer crystallizes. A range of extension rates and Hencky strains are applied to explore the effect of rate and strain on the crystallization behavior. X-ray scattering data are analyzed quantitatively to reveal the extent of crystallization and state of crystallite orientation during the crystallization process. Monitoring the structural response in real time during crystallization offers deeper insights into the structure and morphology induced from extensional flow as well as its impact on crystallization kinetics.

3.2 Material and Experimental Methods

3.2.1 Material Processing and Characterization

The poly(lactic acid) studied in this work is a semi-crystalline grade (Ingeo 4032D) supplied by NatureWorks with a 2% *D*-lactic acid content. Its chain architecture was modified via melt compounding of the polymer with 2,5-bis(*tert*-butylperoxy)-2,5-dimethylhexane used as a chain extender. Resins of the neat polymer were dried overnight in a vacuum oven at 40 °C to prevent hydrolysis at elevated temperatures during compounding. The dried pellets were melt-blended with 0.5 wt% chain extender in a Readco Kurimoto RK1 Lab Size Continuous Processor at 180 °C. Mixing was performed at a rotation speed of 100 rpm for 10 min. The extruded branched PLA was pelletized and dried in a vacuum oven at 40 °C for 24 h prior to compression molding at 180 °C into 1.5 mm disks for linear viscoelastic (LVE) characterization conducted in a Rheometrics Scientific ARES rheometer using 25 mm diameter parallel plate fixtures. Figure 3.1 displays the melt linear viscoelasticity of the polymer measured at 180 °C, well above its melting point. A response typical of a polydisperse melt is found, reflected in the higher loss modulus compared to the storage modulus. Owing to long chain branching, the zero-shear melt viscosity of the branched PLA was shown to be increased by a factor of 1.5 compared to that of the linear counterpart.[118] Also, branching resulted in a large enhancement in the elastic characteristics. As an extra cautionary measure to avoid hydrolytic degradation, trial experiments were performed in an inert environment. However, rheological measurements under N_2 and compressed air revealed identical behavior. Thus, air was used for all experiments conducted in this work.

3.2.2 In Situ X-ray Scattering Experiments

Samples for extensional flow-induced crystallization experiments were prepared by compression molding the vacuum-dried pellets into thin sheets that were cut into rectangular strips of 25 mm x 11 mm x 0.7 mm in size. Uniaxial extensional flow was applied using an SER fixture that was incorporated into a custom-built convection oven with windows designed to facilitate x-ray access for *in situ* x-ray scattering measurements. A short-term flow protocol was applied to decouple the effect of flow on subsequent crystallization.[46] Samples were heated to 180 °C to erase existing crystallites and cooled to a desired crystallization temperature (T_c) of 148 °C. This particular temperature was selected for two reasons. First, T_c was high enough that no crystallization was detected prior to and during flow. At the same time, T_c was selected to be as low as possible in an attempt to reduce sagging in the sample due to its low melt viscosity. Nevertheless, given the time spent at elevated temperatures during the thermal clearing and during cooling to and equilibration at T_c (~9 min in total), significant sag of the molten sample strip was unavoidable due to the modest viscosity of this polymer, even in its branched form (Figure 3.2a). Once the undercooled melt equilibrated at T_c for 1 min, extensional flow

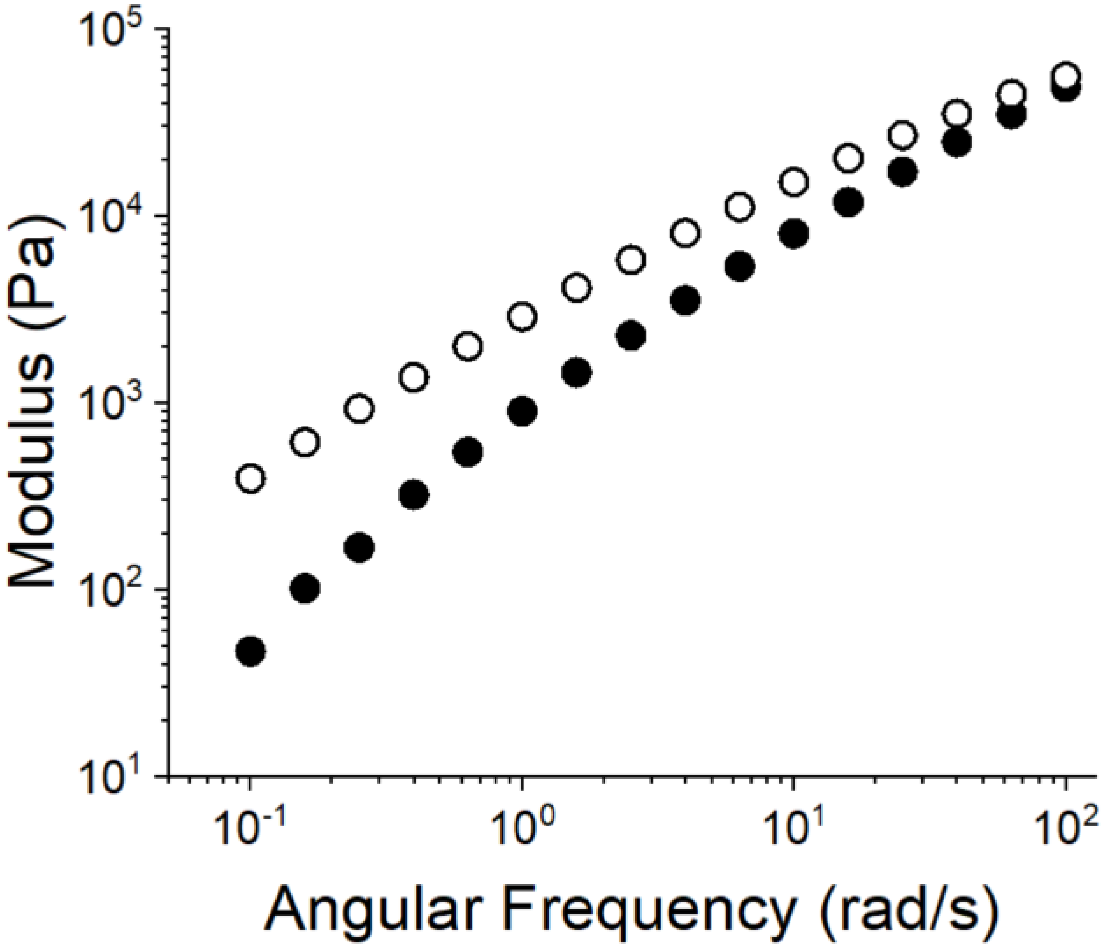

Figure 3.1: Melt rheology of branched PLA at 180 °C. The loss modulus (○) dominates the storage modulus (●), indicating that the material is well in its molten state at this temperature.

was applied at extension rates ranging from 0.1 s^{-1} to 3 s^{-1} and at Hencky strains between 1 and 3. Deformation under these flow conditions produced fully stretched samples that, with only minor deviations, demonstrated changes in width and thickness expected for uniaxial extension to the given strain (Figure 3.2b). While the final shape and dimensions of the sample are encouraging, the extent of sag in the sample prior to flow is obviously nonideal. Despite the viscosity enhancement produced by branching in the PLA, these experiments are just at the edge of feasibility, and certainly would not be possible using the original parent linear PLA sample due to the significant amount of sag found in samples when multiple attempts were made to characterize the extensional viscosity at elevated temperatures.

Simultaneous small- and wide-angle x-ray scattering (SAXS and WAXS, respectively) measurements were used to monitor the structural response of the stretched polymer in real time as it crystallized isothermally following uniaxial deformation. Synchrotron x-ray scattering experiments were conducted at DND-CAT (Sector 5ID-D) of the Advanced Photon Source at Argonne National Laboratory. A beam energy of 17 keV (wavelength λ = 0.729 Å) was selected. The incoming x-ray beam was incident on the sample after it traveled between the SER drums. Scattered x-rays were collected downstream on Rayonix WAXS and SAXS detectors positioned at a sample-to-detector distance of 0.21 m and 8.5 m, respectively. The detectors had a resolution of 1920 x 3840 pixels (WAXS) and 3840 x 3840 pixels (SAXS) and images were collected using 2 x 2 pixel binning to reduce noise and size of image data files. Depending on the applied flow condition, two different image collection methods were employed to capture the structural evolution in the sample accordingly at appropriate time points. For experiments at low strains ($\varepsilon_H \leq 1.5$) or slow extension rates ($\dot{\varepsilon} \leq 0.1$ s^{-1}), the initial 29 images were collected at a 15-

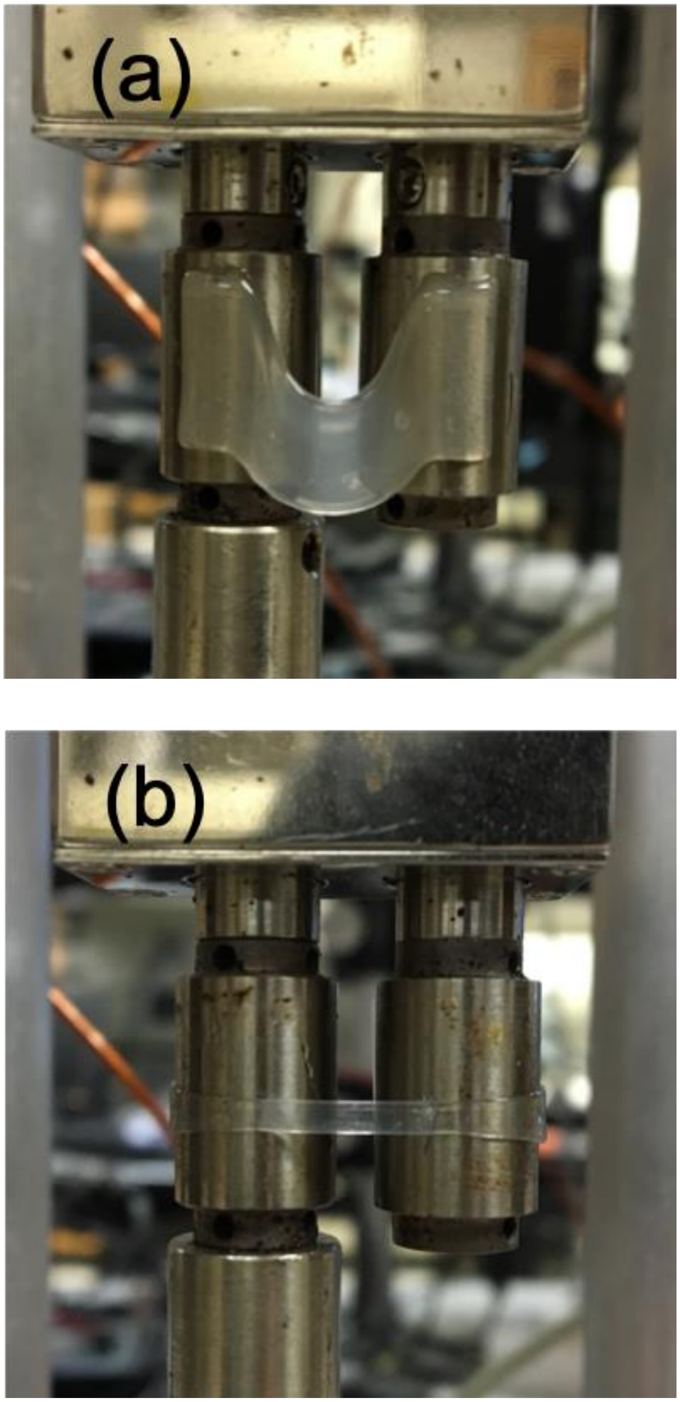

Figure 3.2: PLA sample at T_c = 148 °C (a) prior to and (b) following deformation to a Hencky strain of 3. (a) The sample sags during the heating and cooling steps before flow is applied. (b) Despite the presence of sag, uniaxial extensional flow fully stretches the sample.

second interval. As crystallization proceeded more slowly at later times, the interval was increased to 60 s for the next 10 images, and 120 s for the final 15 images. The exposure time of each image was set to 0.3 s. For experiments that involved stronger flow conditions, faster data acquisition intervals of 5 s, 20 s, 60 s, and 120 s were used to collect 24, 18, 12, and 10 images, respectively. The exposure time was reduced to 0.25 s to conserve the total integrated exposure to the incident x-ray beam.

3.2.3 Data Analysis Procedures

Quantitative analyses are performed on the collected x-ray scattering data for direct comparison across experiments based on an absolute intensity scale. Following the procedures outlined in Section 2.4, geometric correction and background subtraction are performed as necessary.

Two key quantities are calculated from the x-ray scattering data to quantify the extent of crystallization and the state of crystallite orientation. For SAXS data, an indicator of the total extent of crystallization is determined by calculating the volume-weighted scattering invariant (Q/V):

$$Q/V = \frac{1}{(2\pi)^3}\int I(\boldsymbol{q})d\boldsymbol{q}. \tag{2.11}$$

Assuming uniaxial symmetry about the flow axis, Eq. (2.11) becomes

$$Q/V = \frac{1}{(2\pi)^2}\int_0^{\pi}\int_0^{\infty} I(q,\varphi)\, q^2 \sin\varphi\, dq\, d\varphi. \tag{2.12}$$

In practice, the integration over scattering vector is performed over a finite range, using limits q_1 = 0.005 Å^{-1} and q_2 = 0.045 Å^{-1} selected to avoid any undesirable contribution of stray background scattering at small q as well as amplified noise from the q^2 weighting at large q on the invariant calculation (Figure 3.3a). From WAXS data, we focus on the (110)/(200) peak, as it is the strongest diffraction peak (Figure 3.3b). To obtain the intensity contribution only from this crystalline peak ($I_{(110)/(200)}$), the amorphous background (fit as a polynomial) in every image is subtracted from the total intensity. This is because the amorphous background intensity in WAXS becomes more suppressed as crystallization proceeds (Figure 3.3b), unlike the SAXS background scattering that remains unchanged over the course of crystallization. Thus, the extent of crystallization from WAXS is obtained by calculating the (110)/(200) crystalline peak area ($A_{(110)/(200)}$):

$$A_{(110)/(200)} = \int_0^{\pi} \int_{q_3}^{q_4} I_{(110)/(200)}(q, \varphi)\, q^2 \sin\varphi \, dq \, d\varphi \tag{3.1}$$

where q_3 = 1.13 Å^{-1} and q_4 = 1.22 Å^{-1}.

To characterize the average distribution of crystallite orientation in polymers with structures induced by uniaxial extensional flow, we use the Hermans order parameter $\langle P_2 \rangle$:

$$\langle P_2 \rangle = \frac{3\langle \cos^2 \varphi \rangle - 1}{2} \tag{2.14}$$

where $\langle \cos^2 \varphi \rangle$ is given as

$$\langle \cos^2 \varphi \rangle = \frac{\int_0^{\pi} I(\varphi) \cos^2 \varphi \sin\varphi \, d\varphi}{\int_0^{\pi} I(\varphi) \sin\varphi \, d\varphi}. \tag{2.15}$$

As discussed in Section 2.4.3, $\langle P_2 \rangle$ values are normalized with respect to the angle of perfect alignment such that $\langle P_2 \rangle$ = 0 indicates random distribution, while values of -0.5 and 1 respectively indicate perfect orientation of structures perpendicular to and parallel to the flow direction.

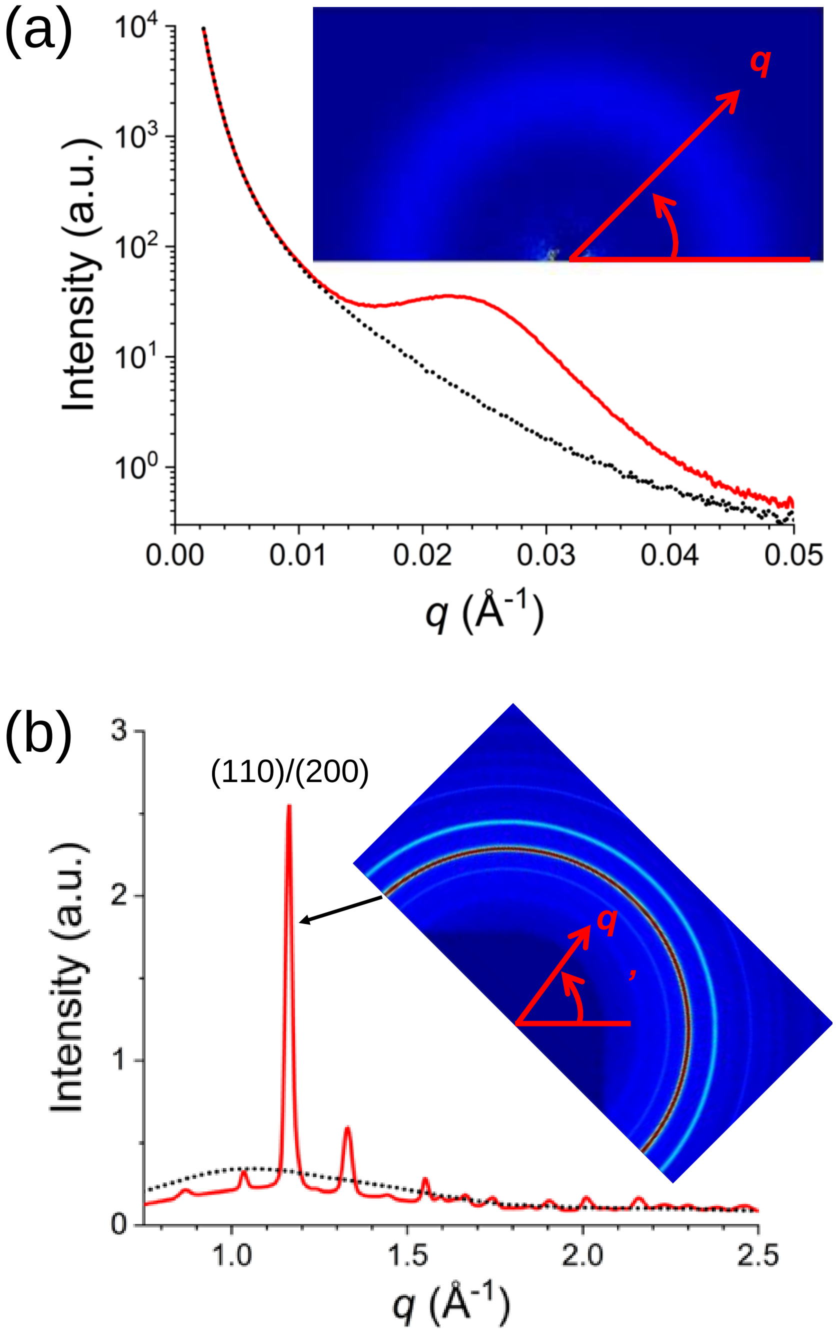

Figure 3.3: Azimuthally averaged intensity profiles (red solid line) extracted from (a) small- and (b) wide-angle x-ray scattering images when crystallization is completed under quiescent conditions. The black dotted line is the scattering intensity of the first SAXS and WAXS images collected after application of flow. In the case of SAXS (a), this image is treated as a background, subtracted from all subsequent images during the quantitative analysis.

3.3 Results and Discussion

3.3.1 SAXS/WAXS Image Analysis: Effect of Rate and Strain

Representative SAXS and WAXS patterns (Figure 3.4) reveal the structural evolution of samples stretched under various extension rates to a final Hencky strain of 3. In all experiments, $t = 0$ min is defined as the time point that corresponds to the image collected immediately following flow. The background subtraction process described in Section 2.4.1 is applied to all images such that the growth of intensity in SAXS and WAXS patterns is a direct sign of crystallization. In the absence of flow, the SAXS intensity increases over time and shows an isotropic distribution, indicating that crystalline lamellae grow outward in all directions. Similarly, isotropic growth of the (110)/(200) peak intensity in WAXS demonstrates that the c-axis of the polymer crystal unit cell is oriented in all directions during quiescent crystallization.

In the presence of flow, a transition in the orientation of crystallites occurs. Focusing on the final SAXS patterns when crystallization is completed at $t \sim 24$ min, we observe an anisotropic distribution in the scattering intensity, where spots of intensity become increasingly concentrated along the flow direction. The azimuthal dependence of the SAXS peak upon the application of flow reflects the orientation distribution of lamellae, in which the lamellar normals preferentially orient along the flow as the extension rate increases. This observation is in accordance with experimental evidence of oriented crystallites seen in branched PLA during shear-induced crystallization[105]. However, what is striking is the emergence of a bimodal distribution in the scattering intensity under lower extension rates ($\dot{\varepsilon} = 0.1$ s^{-1} and 0.3 s^{-1}). In these experiments, the presence of equatorial and meridional SAXS peaks suggests a coexistence of lamellar structure with the normal direction parallel to and perpendicular to flow, respectively.

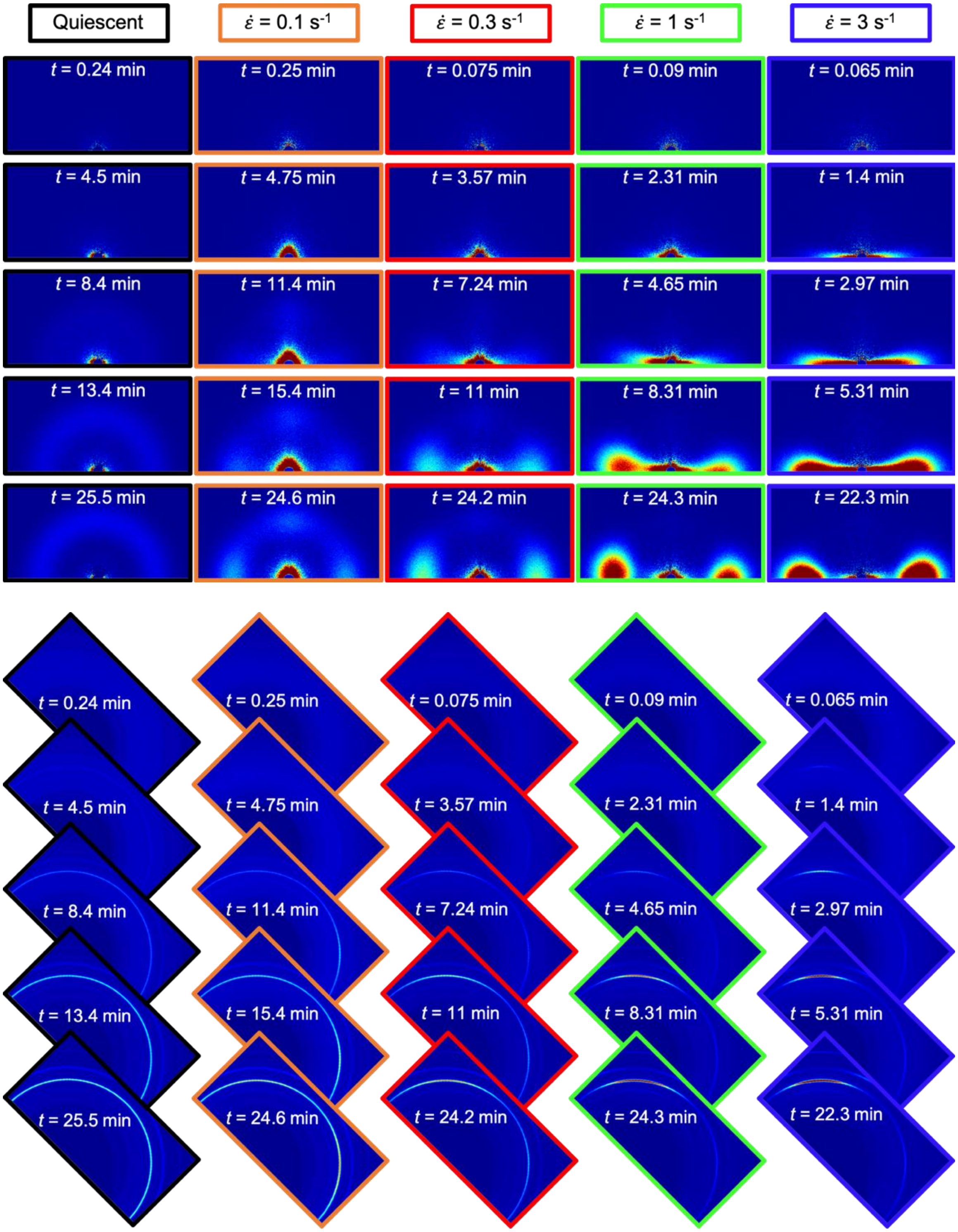

Figure 3.4: Time evolution of SAXS (above) and WAXS (below) patterns at a Hencky strain of 3 under various extension rates (indicated using color-coded borders). Flow direction is horizontal.

Radial scans of intensity along φ = 0° and φ = 90° reveal that the SAXS peak in both azimuthal directions appears at q = 0.024 Å^{-1}, corroborating that the structure induced under intermediate flow conditions is fundamentally the same lamellar packing. This unusual behavior at $\dot{\varepsilon}$ = 0.1 and 0.3 s^{-1} is consistent with observations from the corresponding WAXS patterns at the end of crystallization (Figure 3.4). The diffraction peak shows a similar bimodal azimuthal dependence, with concentrated intensity both perpendicular to and parallel to flow, indicating that the c-axis of the unit cell is preferentially oriented in both the flow and transverse directions, respectively. At higher extension rates ($\dot{\varepsilon}$ = 1 s^{-1} and 3 s^{-1}), the diffraction from the (110)/(200) peak becomes strongly concentrated perpendicular to flow, reflecting increasingly strong alignment of c-axis of the crystal unit cell along the flow. The overall observations in SAXS and WAXS—aside from the unexpected structural response under intermediate flow conditions—are in close agreement with the fact that polymer chains aligning during flow lead to subsequent orientation of crystallites.

Figure 3.5 displays the progression of crystallization over time that is reflected in the increase in SAXS and WAXS intensities from experiments performed at a constant extension rate of 1 s^{-1} and various Hencky strains. In SAXS, the lowest applied strain (ε_H = 1) leads to an anisotropic distribution in the scattering intensity that is concentrated in the direction perpendicular to flow. When the strain is increased to ε_H = 1.5, a bimodal distribution of intensity appears in the SAXS pattern. Higher applied strains (ε_H = 2, 2.5, and 3) result in spots of intensity that are highly concentrated along the direction of flow while the SAXS peak along the meridian is suppressed. The strain dependence in these observations is indicative of a transition in the lamellar structure with the normal directions oriented preferentially perpendicular to, both perpendicular and parallel to, and predominantly parallel to the flow direction as the applied strain increases. WAXS data at the smaller Hencky strains (1 and 1.5) give a consistent picture of this unexpected crystallite orientation based on measurements at the unit-cell level. In WAXS, the diffraction from the (110)/(200) peak is more intense along the flow than the transverse direction at ε_H = 1, indicating that the c-axis of the unit cell is preferentially aligned perpendicular to flow. At ε_H = 1.5, a bimodal distribution in the (110)/(200) diffraction emerges, implying the presence of unit cells with c-axes pointing both perpendicular and parallel to flow. As the applied strain increases to ε_H = 2, 2.5, and 3, the diffraction peak becomes more intense along the meridian, which is indicative of the c-axis preferentially oriented parallel to flow as expected for strong flow conditions. The unexpected behavior in the lamellae orientation resulting from intermediate strains is similar to the that from lower extension rates in Figure 3.4.

Kornfield *et al.* reported superficially similar bimodal distributions in SAXS intensity in poly L-lactide during a predominantly biaxial elongation.[114] The authors postulate that the oriented SAXS patterns reflect the presence of a shish-kebab morphology with shish and growth of oriented kebabs along the elongational direction, but the details of the scattering features are rather different from typical SAXS images of a shish-kebab superstructure (sharp streaks perpendicular to flow and lobes of intensity parallel to flow).[109] In our experiments, such an explanation for bimodal SAXS patterns does not seem plausible. First, they are observed under conditions of moderate deformation or deformation rate, while shish-kebabs are classically associated with strong flow conditions. The *q*-dependence of SAXS intensity is identical in both directions, which would not be the case for traditional shish-kebab SAXS features. Further, our

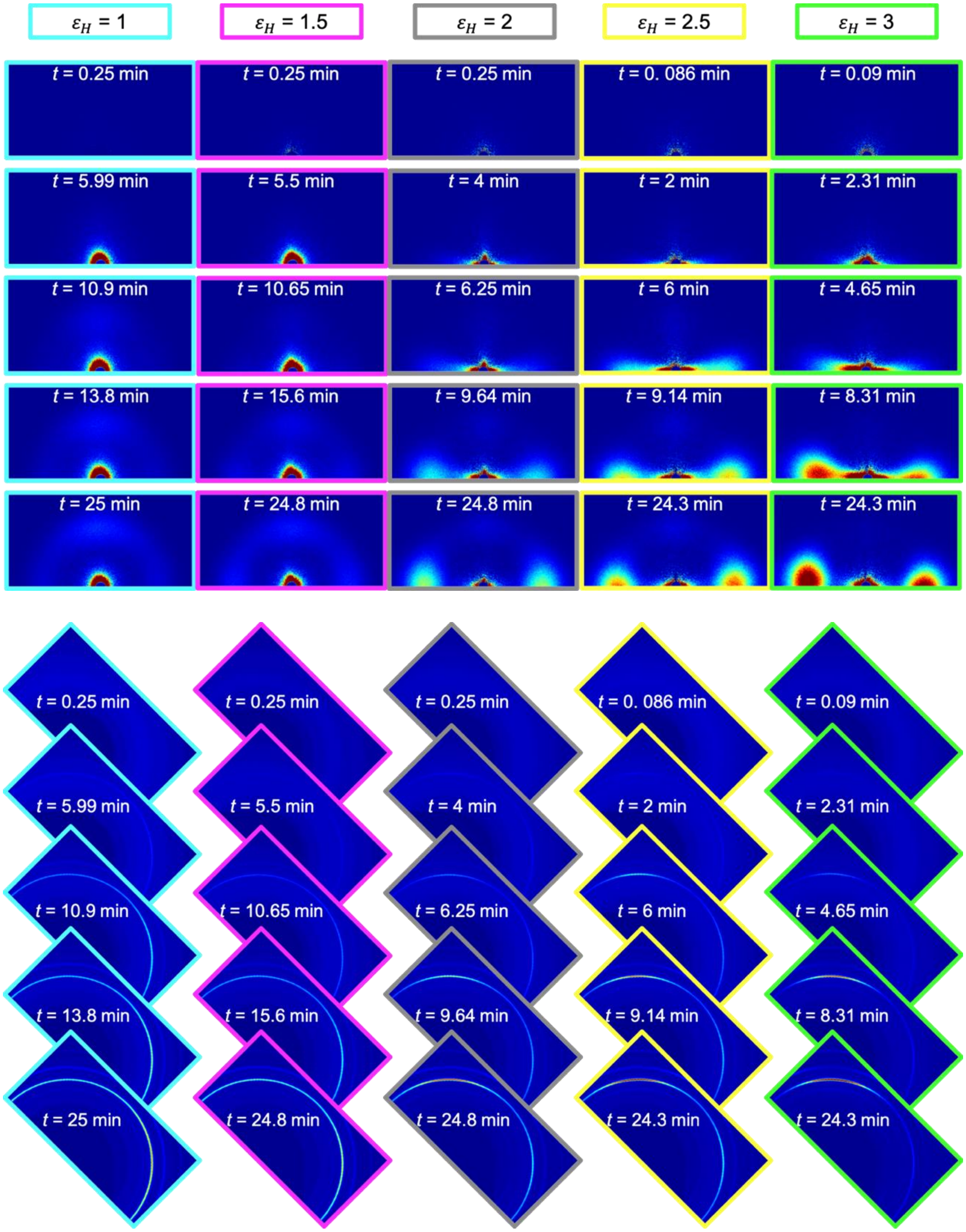

Figure 3.5: Time evolution of SAXS (above) and WAXS (below) patterns at a constant extension rate of 1 s^{-1} under various applied Hencky strains (indicated using color-coded borders). Flow direction is horizontal.

WAXS data confirm corresponding bimodal distributions of c-axis orientation, which certainly would not occur in shish-kebabs. It is not clear whether the unexpected orientation states observed here are representative of the true morphology produced in PLA crystallization under weak uniaxial extensional flow, or whether this results from artifacts stemming from the complicated deformation history induced during stretching of a sagged sample. The sagging itself does not appear to have a direct impact on the crystallization: SAXS and WAXS patterns in quiescent crystallization experiments are perfectly isotropic, with no preferred crystallite orientation. However, sag induces an odd shape in the undercooled melt (Figure 3.2a) such that the early stages of flow in these experiments must be kinematically more complicated than the sought-for ideal uniaxial flow. This, in turn, may produce populations of crystallites with orientation transverse to expectations, and what is indeed observed under stronger flow conditions. Any such artifacts would naturally be most pronounced at small strains, as seen in Figure 3.5. In this light it is harder to explain why they would be present at low rates in Figure 3.4, where samples have been stretched to Hencky strains of 3 (stretch ratio = 20).

3.3.2 Quantifying the Crystallization Behavior

To quantify the effect of flow on the degree of crystallization and crystallization kinetics, we monitor the evolution of SAXS invariant and WAXS (110)/(200) peak area. Figure 3.6 illustrates that all experiments show growth of Q/V and $A_{(110)/(200)}$ during the 25-minute experimental time frame, both in the absence and presence of flow. Specifically, for experiments at different extension rates, Q/V reaches similar final values with the exception of two experiments (Figure 3.6a). Similarly, $A_{(110)/(200)}$ reaches comparable final values with small deviations (Figure 3.6b). Experiments with higher final Q/V values were scrutinized to identify the cause of this discrepancy. Specifically, thickness measurements were repeatedly examined to ensure consistency, various q_2 values for the integration in Eq. (2.12) were explored to evaluate Q/V, and the slight misalignment in the SAXS image (Figure 3.4; $\dot{\varepsilon}$ = 1 s^{-1}) was corrected for using a tilt angle with respect to the flow axis, but the results were unaffected in any significant way. Setting aside the quantitative discrepancies, Q/V and $A_{(110)/(200)}$ are in qualitative agreement and demonstrate comparable rate dependence in the crystallization kinetics. In general, higher extension rate accelerates crystallization kinetics, as reflected in the faster growth of Q/V and $A_{(110)/(200)}$. Interestingly, the onset of growth of Q/V and $A_{(110)/(200)}$ is later at $\dot{\varepsilon}$ = 0.1 s^{-1} than that found in the absence of flow although the quiescent condition is expected to lead to the slowest crystallization kinetics. Similar decelerated crystallization is observed under intermediate conditions in experiments at different applied strains, where the rate of growth of Q/V (Figure 3.6c) and $A_{(110)/(200)}$ (Figure 3.6d) becomes increasingly suppressed as ε_H increases from 0 (i.e. quiescent condition) to 1.5. At larger strains ($\varepsilon_H > 1.5$), faster kinetics is achieved with increasing applied strain as expected.

SAXS and WAXS patterns were also analyzed according to Eqs. (2.14) and (2.15) to quantify the state of orientation of crystallites as crystallization proceeds (Figure 3.7). Under quiescent conditions, $\langle P_2 \rangle$ remains at 0 during the entire experiment, indicating the isotropic orientation of lamellae and c-axes of unit cells. In the presence of flow, the values of $\langle P_2 \rangle$ initially change over time and reach a constant final value at the point where data in Figure 3.6 indicate that crystallization has completed. Comparisons of Figure 3.7a to Figure 3.7b, and Figure 3.7c to Figure 3.7d reveal strong agreement between the orientation distribution of

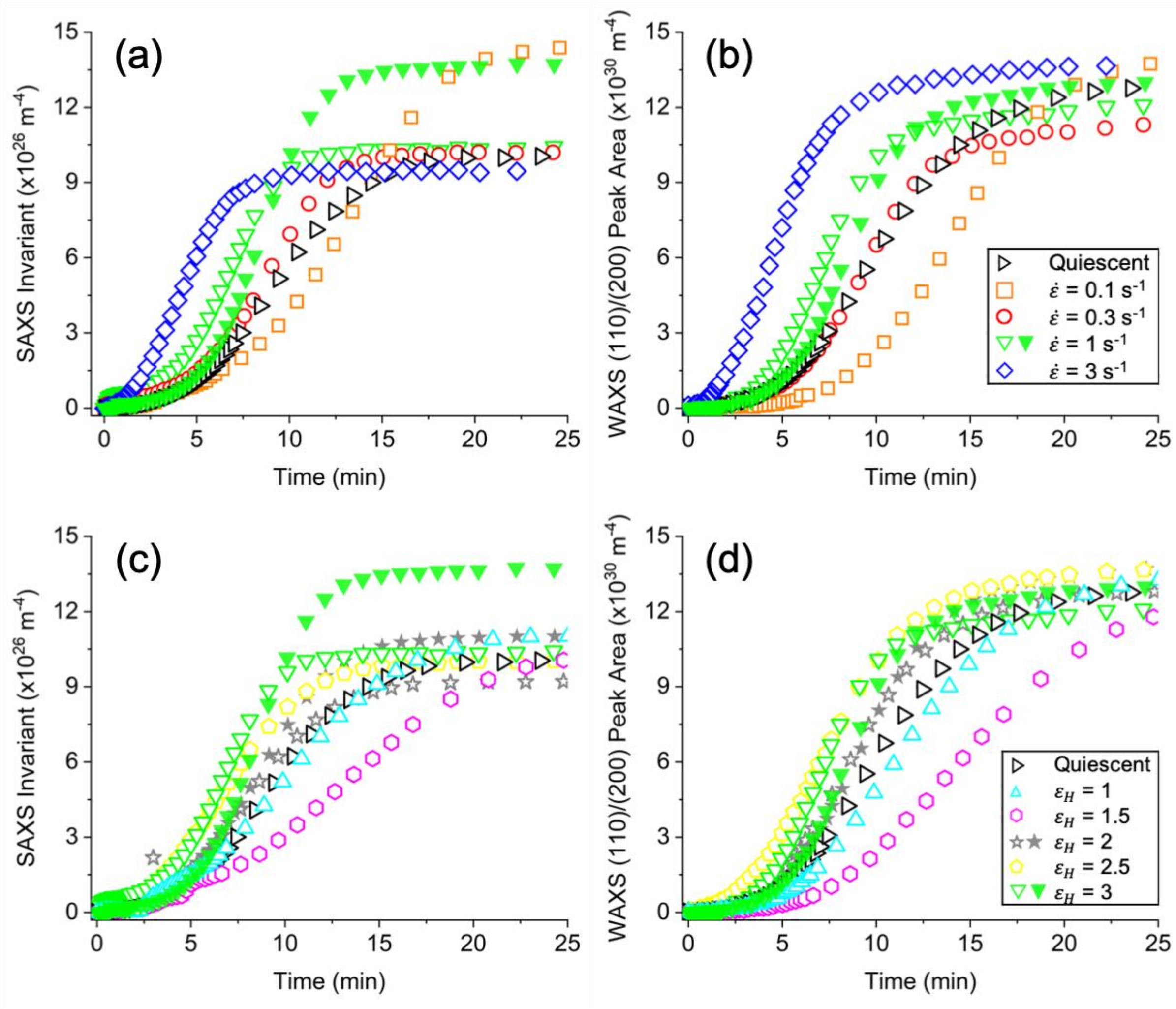

Figure 3.6: The extent of crystallization calculated from experiments at a range of extension rates at $\varepsilon_H = 3$ (a) & (b) and at a range of applied strains at $\dot{\varepsilon} = 1$ s^{-1} (c) & (d). In general, similar final values of Q/V and $A_{(110)/(200)}$ are reached in SAXS and WAXS when crystallization is completed. Crystallization kinetics is generally accelerated with increasing extension rate or Hencky strain, while it is slowed down under intermediate conditions. The overall crystallization behavior observed in SAXS and WAXS is consistent with each other.

lamellae and unit cells. When varying extension rate at fixed strain, $\langle P_2 \rangle$ values generally start off higher at higher extension rates and reach higher final values. This observation implies that the initial structures crystallizing upon the application of flow are increasingly oriented as the extension rate increases, and that the behavior continues towards the end of crystallization. However, the evolution of $\langle P_2 \rangle$ at $\dot{\varepsilon}$ = 0.1 s^{-1} disagrees with this overall trend, as the $\langle P_2 \rangle$ values in SAXS and WAXS are initially negative and slowly reach 0 over time. This suggests the initial formation of crystallites with lamellar normals and unit cell c-axes more preferentially aligned perpendicular to flow at short times. Over the course of crystallization, lamellae and crystalline unit cells with their normal and c-axis pointing along the flow direction become more present such that the negative $\langle P_2 \rangle$ value increases to 0. At this point, there is 'balance' between the two populations of orientation revealed in final SAXS and WAXS patterns at $\dot{\varepsilon}$ = 0.1 s^{-1} (Figure 3.4). The evolution of $\langle P_2 \rangle$ under various Hencky strains also reflect the unusual behavior found at small applied strains (ε_H = 1 and 1.5) in Figure 3.5. $\langle P_2 \rangle$ values derived from SAXS and WAXS data illustrate that the average distribution of crystallite orientation is biased with lamellar normal and unit cell c-axes preferentially oriented perpendicular to flow, as the values are negative throughout the entire experiment. Data at higher strains (ε_H = 2, 2.5, and 3) demonstrate the expected trend of larger applied strains producing higher degrees of orientation along the stretching direction.

Comparing the crystallization kinetics and crystallite orientation indicates strong correlation between the two, in which the unusual effect of flow under weaker flow conditions is manifested in a similar way (Figure 3.8). Crystallization half-time is used as a measure to describe the kinetics and obtained by determining the time at which the extent of crystallization

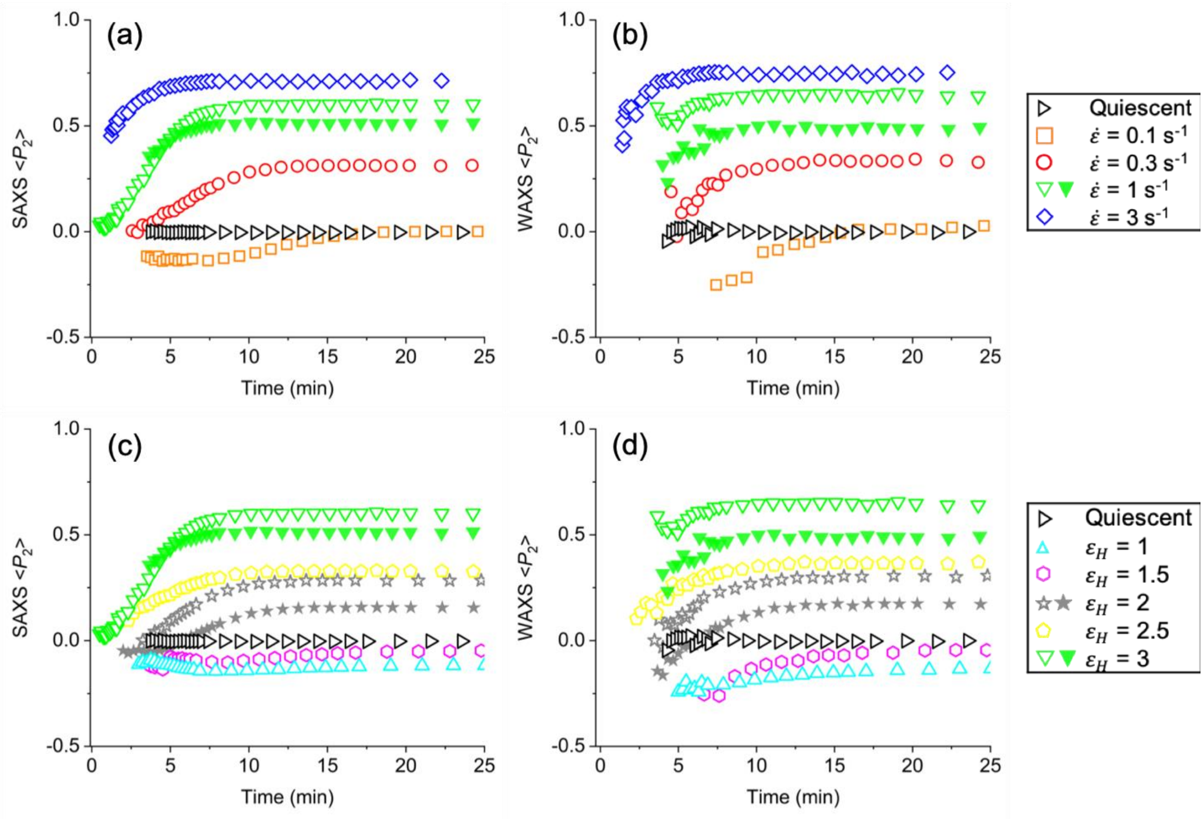

Figure 3.7: Time evolution of the orientation distribution of crystallites demonstrating rate (a) & (b) and strain (c) & (d) dependence. In general, higher degrees of orientation along the flow is achieved with increasing rate/strain, as reflected in the final $\langle P_2 \rangle$ values at the end of crystallization.

reaches half of its maximum value. The final $\langle P_2 \rangle$ value of each experiment is extracted to summarize the overall rate and strain dependence of the crystallite orientation state. Under various extension rates, the generally positive trend in both plots of inverse crystallization half-time and final $\langle P_2 \rangle$ value implies that faster flow leads to faster kinetics and higher final degree of orientation (Figure 3.8a and c). However, data collected $\dot{\varepsilon}$ = 0.1 s^{-1} show anomalous orientation, and retarded kinetics. Similarly, at higher applied strains, the overall trend in the crystallization kinetics and state of orientation is positive, with anomalous results for both kinetics and orientation observed at intermediate strains of ε_H = 1 and 1.5 (Figure 3.8b and d).

Interestingly, the observed half-times for crystallization detected by SAXS are systematically shorter than those detected by WAXS (Figure 3.8a and b). We believe this reflects the fact that the SAXS invariant is not directly proportional to the degree of crystallinity; rather according to the classic two-phase model of small-angle scattering, $Q \propto \phi_c(1 - \phi_c)$ where ϕ_c is the volume fraction of crystallinity.[96] Conversely, the integrated WAXS peak area should scale directly with ϕ_c, since it simply tracks the total amount of crystalline material in the illuminated sample. If data from Figure 3.6a and b were scaled to have identical short-time behavior, the SAXS invariant would be expected to end up at a lower final value owing to its nonlinear, concave-downward dependence on ϕ_c. This, in turn, would lead to a systematically smaller half-time for crystallization, as seen here.

While it is plausible that complicated deformation during the early stages of stretching of sagging samples could produce the unexpected orientation behavior—with bimodal orientation states and, in some circumstances, a bias in orientation actually transverse to the stretching direction—it is harder to explain why this would be associated with a *retardation* of

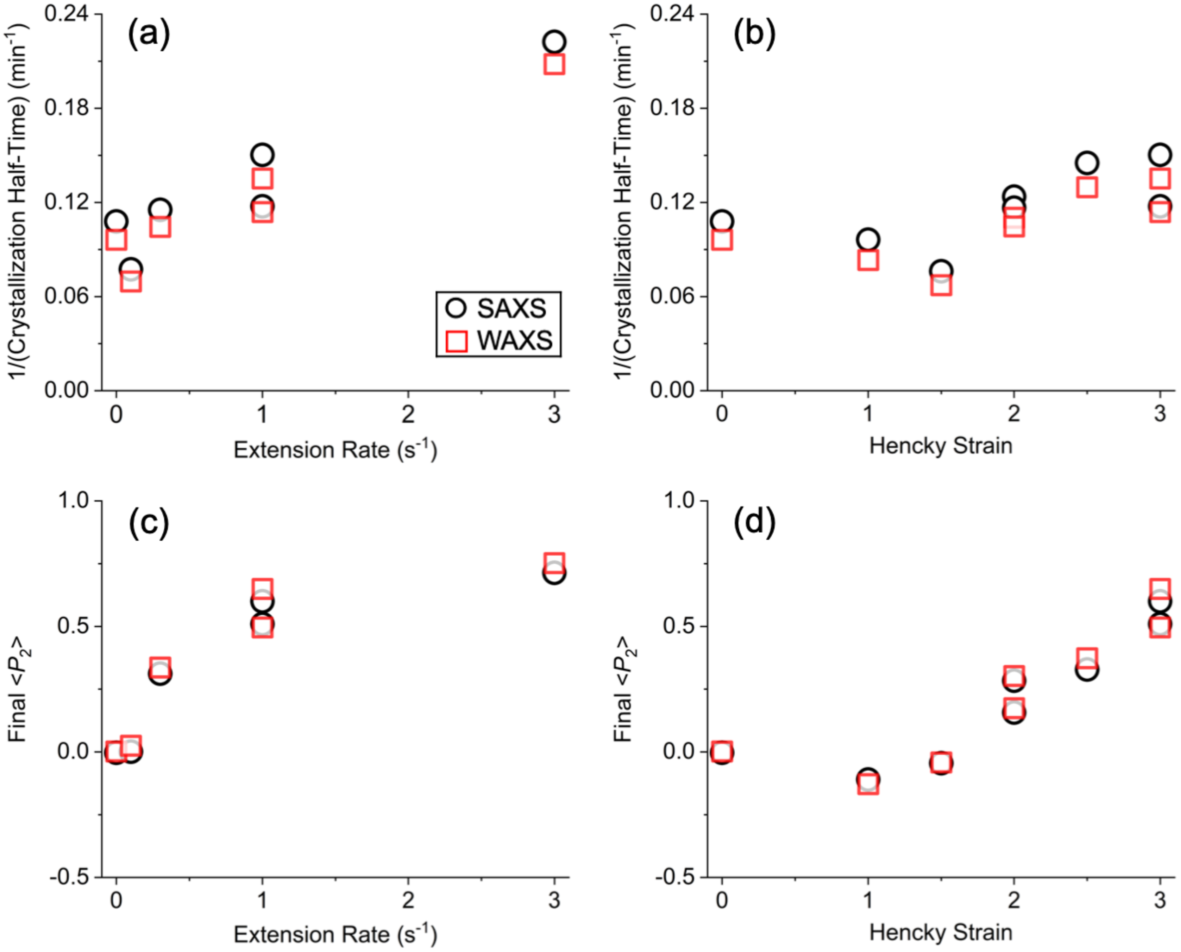

Figure 3.8: Inverse crystallization half-time (a) & (b) and final $\langle P_2 \rangle$ value (c) & (d) plotted against extension rate (a) & (c) and Hencky strain (b) & (d) for all experiments. Similar qualitative rate and strain dependence is reflected in the crystallization kinetics and crystallite orientation.

crystallization kinetics. Even though the resulting orientation is weak in a qualitative sense, SAXS and WAXS patterns show clear signs of induced anisotropy. While one may reasonably expect negligible enhancement in kinetics when flow conditions are weak, it is counter-intuitive that flow would ever inhibit crystallization. Due to limitations in available sample and available beam time, only a single quiescent experiment was undertaken. Repeats of experiments under selected conditions (open and closed symbols in Figure 3.6 and Figure 3.7) showed generally consistent results. However, it is possible that the single quiescent data set shows anomalously fast crystallization kinetics due to some experimental nonideality. Even with the viscosity enhancement produced in the branched PLA sample used here, these extensional flow-induced crystallization experiments are only just feasible.

While questions of detail remain, observations from all experiments, summarized in Figure 3.9, illustrate certain robust trends. First, faster crystallization kinetics is associated with higher final state of crystallite orientation, consistent with qualitative expectations with any mechanism of flow-induced crystallization. Second, there is remarkable quantitative agreement between the degree of crystallite orientation inferred from either the orientation of unit cell c-axes (WAXS) or crystalline lamellae (SAXS), indicating a relationship of unusually high fidelity between measurements reflecting length scales differing by nearly two orders of magnitude.

3.4 Conclusion

We have expanded upon previous extensional flow-induced crystallization studies using *in situ* SAXS and WAXS to demonstrate the capability of conducting extensional flow-induced crystallization experiments on PLA. To the best of our knowledge, this is the first time the

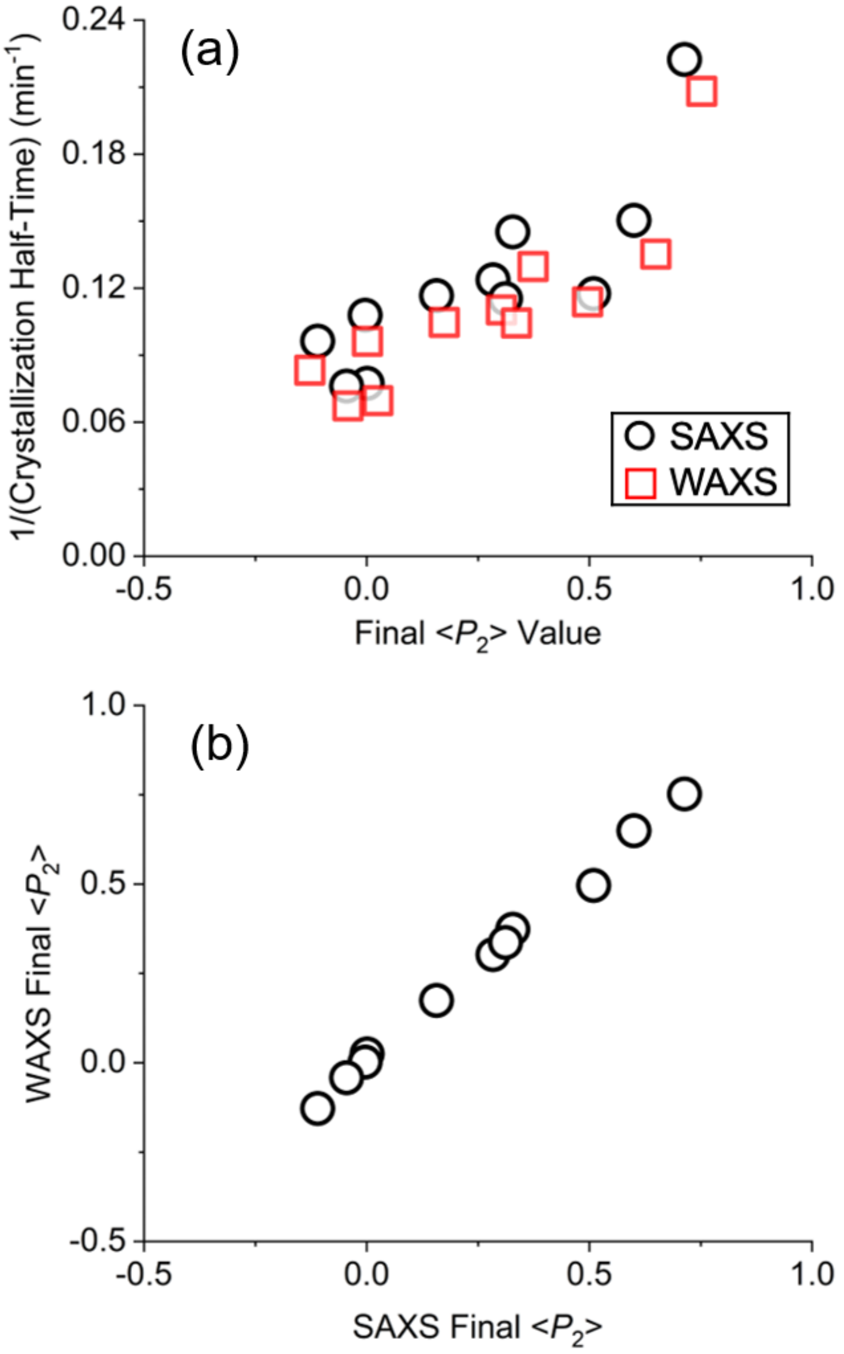

Figure 3.9: (a) Inverse crystallization half-time plotted against final $\langle P_2 \rangle$ value. (b) Cross plot of final SAXS and WAXS degrees of orientation. Across all experiments, accelerated crystallization kinetics is associated with higher degree of crystallite orientation. Also, polymer chain alignment down at the molecular level gives rise to oriented lamellae being formed on a larger length scale.

structural evolution during PLA crystallization following a uniaxial extension flow has been reported. Applying flow at various extension rates at a fixed strain as well as various strains at a fixed extension rate induces oriented crystallization that undergoes complex transition in the structure and morphology as the flow condition changes. In general, crystallization kinetics is accelerated with faster extension rates and higher Hencky strains. Stronger flow conditions also lead to higher final degrees of crystallite orientation. Unusual behavior in the crystallization kinetics and crystallite orientation distribution is observed under intermediate flow conditions, where the kinetics is slowed down and a bimodal distribution in SAXS and WAXS intensities arise. Despite the unexpected crystallization behavior, the overall crystallization kinetics is associated with the orientation distribution of crystallites, where oriented polymer chains at the molecular level consistently lead to oriented lamellae at larger length scales.

Chapter 4

Model-Guided Experimental Design of Flow-Induced Crystallization in Poly(1-butene)

4.1 Introduction

The crystallization kinetics and morphology of polymer products are profoundly affected by flow fields encountered during processing. To better understand flow-induced crystallization (FIC) in polymers, researchers have sought to quantify the impact of deformation history on crystallization as well as to model the nucleation and crystallization kinetics in relation to the rheological properties of the polymer in its molten state. These efforts have led to the development of predictive models that span large length and time scales. At the microscopic level, molecular dynamics and lattice Monte Carlo simulations have been performed to investigate the underlying mechanism of polymer crystallization kinetics in the absence or presence of flow.[74,75,119–123] However, while these models describe the details of flow-induced crystallization at the molecular level, the small length scales and short time scales inherently limit them from being feasible for industrial process simulations.

In recent years, multiscale models that draw upon molecular underpinnings while retaining descriptions applicable to process modeling have been proposed. These models consist of hierarchically interrelated elements that describe how crystals nucleate and grow into three-dimensional structures, how the applied flow promotes enhanced nucleation and impacts the melt rheology, and how the evolving crystallinity affects the mechanical properties during the solidification process. However, models formulated by fundamentally different descriptions of the link between elements at different levels have shown to lead to similar predictions of the same experiment.[41] This suggests the possibility of designing and conducting experiments to specifically test how various descriptions of molecular orientation induced by flow is related to the enhancement in nucleation, and consequently, accelerates the crystallization kinetics.

As reviewed in Section 1.5, Peters and colleagues have extensively studied and formulated flow-induced crystallization models that adopt a viewpoint that molecular orientation induced by flow is directly related to enhanced nucleation.[41,85,87–93] In fact, this family of models has shown good agreement with experimental data from shear and extensional flow-induced crystallization studies. However, the predictive capability depends on adjustable parameters and specific formulations of how the stretch parameter is incorporated into the nucleation model. Therefore, it is essential to conduct experiments that test and verify how flow-induced chain alignment and stretching leads to enhanced nucleation. Unfortunately, complete flow-induced crystallization models need to be formulated in great detail and require full-scale simulations that are cumbersome for verification.

Motivated by this practical difficulty, we report *in situ* x-ray scattering studies of flow-induced crystallization of poly(1-butene) (iPB) under extensional flow that directly test the role of molecular stretch in enhancing nucleation as described in the work by Roozemond and Peters.[90] *In situ* x-ray scattering has found widespread application for flow-induced crystallization studies as it offers comprehensive details on the phenomenon. Recent work by McCready and Burghardt[95] demonstrated real-time monitoring of flow-induced crystallization in iPB under uniaxial extensional flow using *in situ* small- and wide-angle x-ray scattering (SAXS and WAXS, respectively) measurements, which provided insight into the evolution of lamellar-scale morphologies and of unit cell-level structures, respectively. We explored how varying extension rate under a constant Hencky strain impacted the onset kinetics of crystallization and the orientation of crystallites, which were both observed to occur at earlier times with increasing extension rates. In fact, this work has shown great promise to directly test the core mechanism of existing flow-induced crystallization models through *in situ* structural characterization.

4.2 Material and Experimental Methods

4.2.1 Material and Characterization

Experiments were conducted on an isotactic poly(1-butene), grade PB0110M, provided by LyondellBasell. The material is reported to have a nominal melting temperature of 124 °C.[124] For linear viscoelastic (LVE) measurements, the polymer was compression molded into 1.5 mm disks and loaded onto 25 mm parallel plate fixtures in an ARES (Rheometrics Scientific) controlled-strain rheometer. A series of frequency sweeps at 5% strain were performed at temperatures ranging from 120 to 200 °C. Time-temperature superposition was applied to shift the collected LVE data to a reference temperature (T_{ref}) of 160 °C; the shift factors (a_T) followed an Arrhenius relation with an activation energy of 51 kJ/mol. As illustrated in Figure 4.1, the linear viscoelasticity is characterized by a broad distribution of relaxation times, typical of a polydisperse polymer melt.

A generalized multimode Maxwell model was fit to the shifted data using Eqs. (1.4) and (1.5) to obtain the relaxation spectrum. Following the approach described by Roozemond and Peters,[90] the slowest Maxwell mode was taken to be indicative of the reptation time (λ_{rep}), and

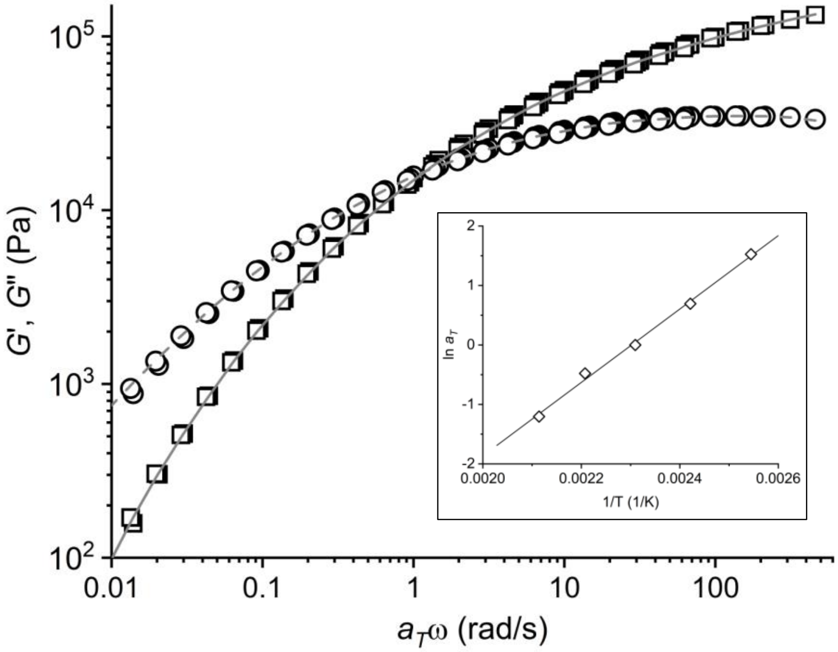

Figure 4.1: LVE measurement of isotactic poly(1-butene) melt at a reference temperature of 160 °C. A multimode Maxwell model fit to the measured G' (☐) and $G"$ (○) data are indicated as solid and dotted lines, respectively. The inset shows that the shift factors (◇) follow an Arrhenius relation (fit in solid line).

the Rouse time (λ_R) was calculated using[10]

$$\lambda_R = \frac{\lambda_{rep}}{3Z} \tag{1.6}$$

where Z is the average number of entanglements determined from molecular properties of the polymer (Table 4.1). The estimated λ_{rep} and λ_R at T_{ref} = 160 °C were shifted to their respective values at 100 °C, the crystallization temperature (T_{c}) used in flow-induced crystallization experiments. A summary of the estimated relaxation times at T_{ref} = 160 °C and T_{c} = 100 °C are presented in Table 4.2, along with the range of reptation- and Rouse-based Weissenberg numbers (*Wi*) spanned by the range of extension rates used in the FIC experiments.

4.2.2 Model-Guided Design of Experiments

As mentioned in Section 1.5, recent FIC models developed by Peters *et al*. utilize chain stretch in the slowest relaxing mode (as calculated from a molecularly-inspired nonlinear rheological model) as the driving force when modeling accelerated nucleation[88–90,92,93], which, in turn, drives accelerated crystallization kinetics. This modeling approach implies that any flow history resulting in similar degrees of stretch in the highest molecular weight chains should lead to similar rates of flow-enhanced nucleation and subsequent crystallization behavior. Therefore, once the melt rheology is described by an appropriate constitutive equation, it is possible to directly test how molecular stretch promotes enhanced nucleation through tailored FIC experiments subjected to various combinations of rates and strains that produce comparable enhancements in nucleation. Under these conditions, the overall crystallization process is expected to be similar.

Table 4.1: Molecular properties of isotactic poly(1-butene) used in calculating the Rouse time from the estimated reptation time. M_w is the weight average molecular weight,[124] M_e is the molecular weight between entanglements,[90] and Z is the number of entanglements per chain.

M_w (kg/mol)	M_e (kg/mol)	$Z = M_w/M_e$
711	18	40

Table 4.2: Estimated reptation and Rouse times. The relaxation times at 160 °C are shifted to 100 °C using a shift factor of 10.4 extrapolated from the Arrhenius relationship in Figure 4.1.

Relaxation Time (s)	T_{ref} = 160 °C	T_c = 100 °C	Wi Range at T_c ($\dot{\varepsilon} = 0.023 – 0.5\ s^{-1}$)
λ_{rep}	50	520	12 – 260
λ_R	0.42	4.4	0.1 – 2.2

To design such experiments, we closely followed the modeling framework outlined in Roozemond and Peters,[90] in which the simulation results were compared with experimental data from existing FIC studies on poly(1-butene). The melt rheology was described using a Rolie-Poly model,[125] which accounts for both flow-induced orientation and relaxation mechanisms, and therefore has built-in capabilities of capturing both orientation and stretch of polymer chains. The model was simplified by removing the effect of convective constraint release, as this modification was shown to result in good agreement with transient shear data[125] and extensional viscosity measurements[89,90] in other studies. The simplified Rolie-Poly model is given as

$$\frac{d\boldsymbol{B}_e}{dt} = \boldsymbol{L} \cdot \boldsymbol{B}_e + \boldsymbol{B}_e \cdot \boldsymbol{L}^T - \frac{1}{\lambda_{rep}}(\boldsymbol{B}_e - \boldsymbol{I}) - \frac{1}{\lambda_R}\left(1 - \frac{1}{\Lambda}\right)\boldsymbol{B}_e \tag{4.1}$$

where $\boldsymbol{L}$ is the rate of deformation tensor, $\boldsymbol{B}_e$ is the elastic tensor that can be related to the stress tensor, and Λ is the stretch parameter defined as

$$\Lambda = \sqrt{\frac{\mathrm{tr}(\boldsymbol{B}_e)}{3}}. \tag{4.2}$$

The connection between chain stretch induced during polymer melt flow and enhanced nucleation rate is based on the assumption that regions with highly stretched polymer chains serve as nucleation sites. In particular, chain stretch in the slowest relaxing mode (indicative of the highest molecular weight species) is coupled to the rate of creation of flow-induced nuclei through

$$\frac{dN_f}{dt} = g_n(T, P)[\Lambda^4(t) - 1] \tag{4.3}$$

where N_f is the number density of flow-induced nuclei and $g_n(T, P)$ is a scaling parameter that depends on temperature (T) and pressure (P). This specific formulation of Λ raised to the fourth power was reported to show closest agreement with experimental results[89] and therefore was used to describe the rate of flow-enhanced nucleation.

Crystallization following the pulse flow protocol employed in this work (see Section 4.2.3 below) occurred under constant temperature and pressure. This allows us to treat $g_n(T,P)$ as a constant, while N_f is determined by simply integrating Eq. (4.3) over time. One subtle but crucial point in calculating N_f in this manner is to account for the evolution of the stretch parameter both during and after the pulse of extensional flow. That is, it is necessary to account for enhanced nucleation that was still being driven by Λ during relaxation after flow. As long as the time it takes for Λ to relax was short compared to the time scale during which crystallization takes place, this captures the total integrated enhancement in nucleation that then drives subsequent accelerated crystallization kinetics. Calculations of $\Lambda^4(t)$ at various flow conditions show that stretch relaxation occurs at a shorter time scale than that during which crystallization proceeded in experiments. Hence, the entire area under the stretch curve during and following flow is evaluated (Figure 4.2).

This integration was performed over a range of rates and strains to compute N_f as a function of extension rate for multiple Hencky strains (Figure 4.3a). Combinations of rates and strains that resulted in similar N_f values were identified by drawing a horizontal line across the N_f curves such that flow-induced crystallization experiments executed under these flow conditions sould exhibit similar crystallization behavior. All experiments in this work were conducted under flow conditions corresponding to the points along the contours shown in Figure 4.3b, which displays the selected combination of rates and strains that led to similar N_f values of

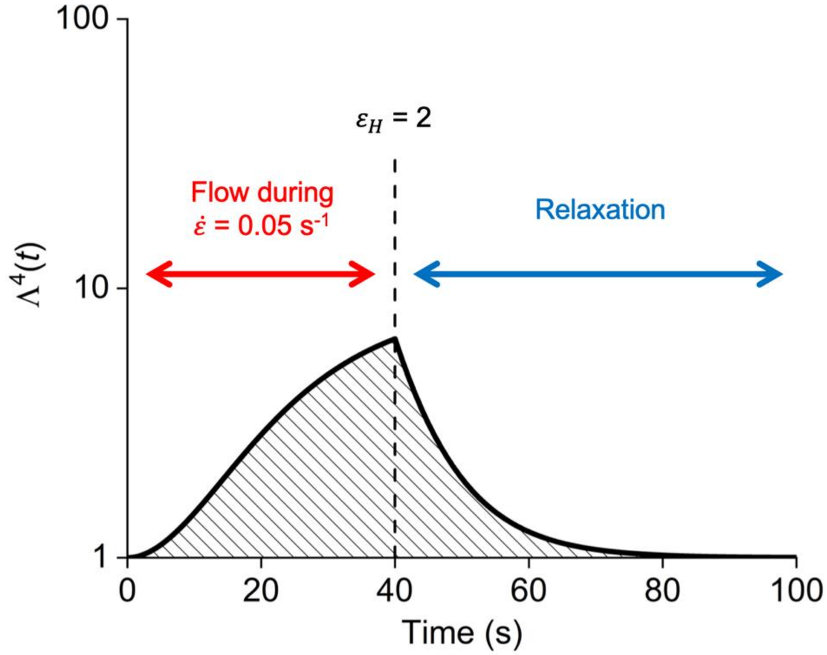

Figure 4.2: Stretch history during flow inception and following cessation, as calculated by Eqs. (4.1), (4.2), and (4.3) using parameters appropriate for the experimental T_c = 100 °C. The area under the curve corresponds to the number density of flow-induced nuclei resulting from flow at an extension rate of 0.05 s^{-1} and ε_H = 2. The same calculation can be performed using any combination of extension rate and Hencky strain to evaluate the N_f value for a given flow history.

115 and 250. In addition, a more conventional series of experiments under various extension rates at a fixed Hencky strain of 1.5 were performed to explore the effect of rate.

4.2.3 In Situ X-ray Scattering Experiments

In situ x-ray scattering was employed to monitor the crystallization kinetics and morphological evolution of poly(1-butene) following a well-defined uniaxial extensional flow. Extensional flow was produced using an SER fixture, onto which a rectangular strip of sample (approximately 25 x 9 x 0.7 mm) was mounted. The SER is housed in a home-built convection oven with access windows for incident and scattered x-ray beams. Time-resolved synchrotron SAXS measurements were performed at DND-CAT beam line 5ID-D of the Advanced Photon Source at Argonne National Laboratory. Images were collected using Rayonix detectors with a resolution of 3840 x 3840 pixels with a 2 x 2 binning, placed at a sample-to-detector distance of 8.5 m. The x-ray beam energy was set to 17 keV, equivalent to a wavelength of λ = 0.729 Å. Two different data acquisition methods were used to accommodate the crystallization behavior that proceeded at different rates depending on the applied flow condition. For experiments where samples deformed to Hencky strains below 1.5, SAXS patterns were initially acquired at intervals of 15 s between each frame. The image collection interval increased to 60 s and then to 120 s as crystallization progressed at a slower rate with time. The exposure time was set to 0.5 s per image and a total of 54 images were collected for these experiments (i.e., 27 s of total exposure per experiment). For larger strain experiments, initial images were collected at a shorter interval of 8 s between each frame to accurately capture the rapid crystallization kinetics immediately following flow. Subsequent images were then collected at 18 s, 30 s, 60 s, and 120 s

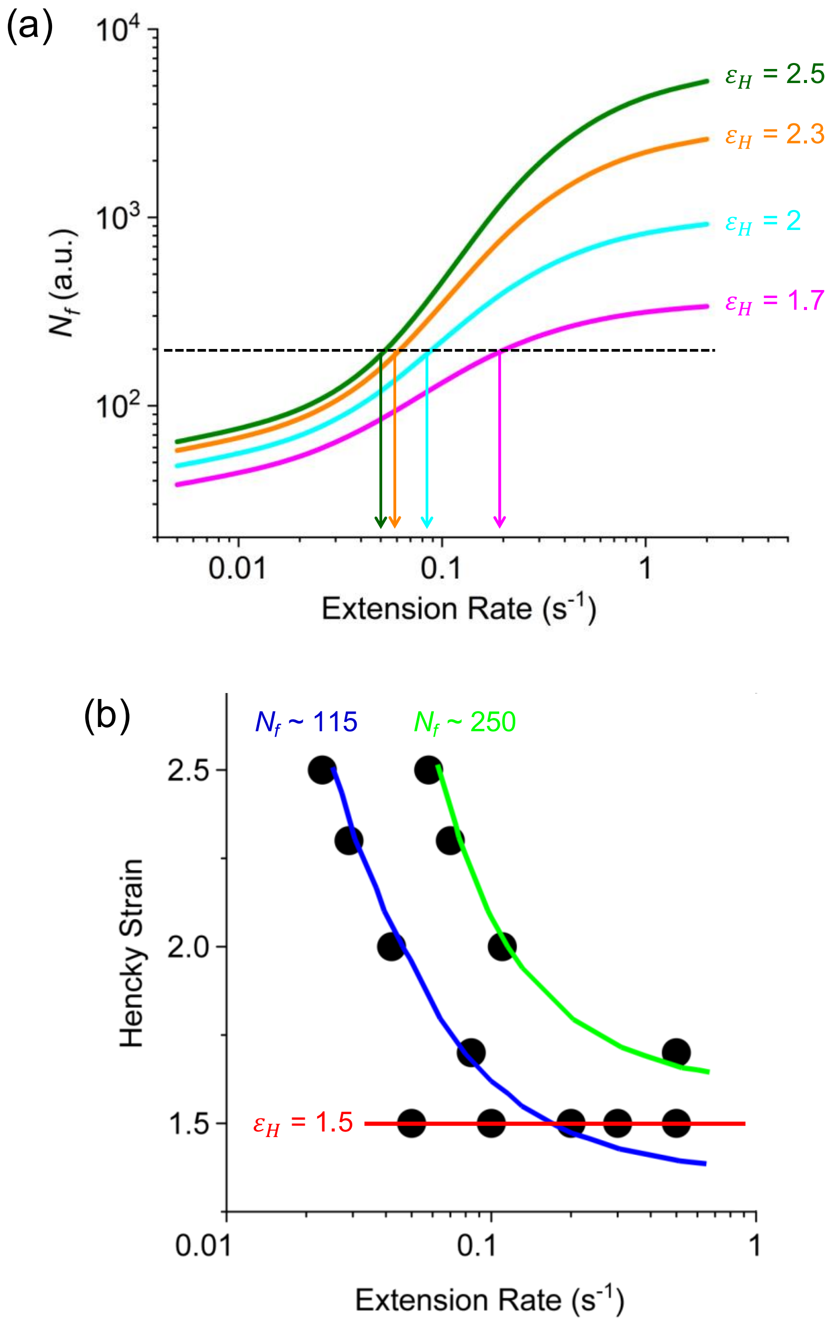

Figure 4.3: Model-assisted design of experimental flow conditions. Each of the curves in part (a) is the predicted N_f as a function of extension rate at a given Hencky strain. The points where the curves intersect with a horizontal line (i.e. constant N_f) correspond to flow conditions that would produce similar N_f values. Part (b) displays the flow conditions that resulted in N_f ~ 115 (blue line) and N_f ~ 250 (green line) as well as those under a fixed Hencky strain of 1.5 (red line).

intervals. For these experiments, a shorter exposure time of 0.4 s was selected, and 68 images were collected such that the total sample exposure to the x-ray beam was conserved.

A short-term flow protocol was employed to decouple the effect of flow from subsequent crystallization. The sample was heated to 180 °C—beyond its melting temperature of 124 °C — to erase its thermo-mechanical history and then immediately cooled to T_c = 100 °C. Once the sample equilibrated at this desired test temperature, a short burst of extensional flow was applied, and subsequent crystallization was probed by SAXS. No signs of crystallinity were observed prior to and during flow for all experiments, ensuring that the applied flow, rather than temperature variations or existing crystallites, was responsible for accelerating the crystallization kinetics or inducing structural changes.

4.3 Results

4.3.1 SAXS Image Analysis

The typical progression of crystallization observed in this study is presented in Figure 4.4, which displays a series of SAXS patterns from an experiment conducted at T_c = 100 °C, $\dot{\varepsilon}$ = 0.023 s^{-1}, and ε_H = 2.5. The first image (Figure 4.4a) collected immediately after the application of flow is defined as the point at which t = 0 min and is treated as a background frame. This frame is subtracted from all subsequent images to remove the scattering contribution that is unrelated to crystallization, such as air scattering or stray scattering surrounding the beam stop. At very short times at t = 0.25 min (Figure 4.4b), no signs of crystallinity are observed as expected from the short-term flow protocol. As time progresses, crystallization is manifested in the growth of anisotropic SAXS intensity that is concentrated along the horizontal direction shown in Figure 4.4c. The intensity increases and broadens azimuthally until the later stages of the experiment, where crystallization is completed, as reflected in the qualitative similarity between images Figure 4.4d and Figure 4.4e. The concentration of intensity along the flow direction arises from the periodicity in the lamellar structure and indicates preferential orientation of lamellae with the normal parallel to the flow direction. This overall observation is consistent with the fact that polymer chain alignment during flow leads to subsequent orientation of crystallites, and in accordance with results from previous studies conducted in our research group. [95]

4.3.2 Extent of Crystallization and Crystallization Kinetics

SAXS data were converted to an absolute intensity scale (see Section 2.4.1) and assuming uniaxial symmetry, the volume-weighted SAXS invariant (*Q/V*) was used to quantify the extent of crystallization to allow quantitative comparison across all experiments. Owing to practical limitations described in Section 2.4.2.1, the integration in Eq. (2.12) was performed, over a finite q-range of 0.005 $\mathrm{\AA}^{-1}$ to 0.034 $\mathrm{\AA}^{-1}$, which is the interval that contains the SAXS peak.

Figure 4.5a depicts the evolution of *Q/V* over time for samples deformed to ε_H = 1.5 at various extension rates. Repeated experiments under identical flow conditions are labeled with closed symbols. The dotted line indicates a threshold *Q/V* value beyond which crystallization has developed sufficiently to support reliable measurements of lamellar orientation (see below) and corresponds to 5% of the average of the final *Q/V* values from all experiments. In the absence of flow, crystallization proceeds at a slow rate and appreciable crystallization does not occur until

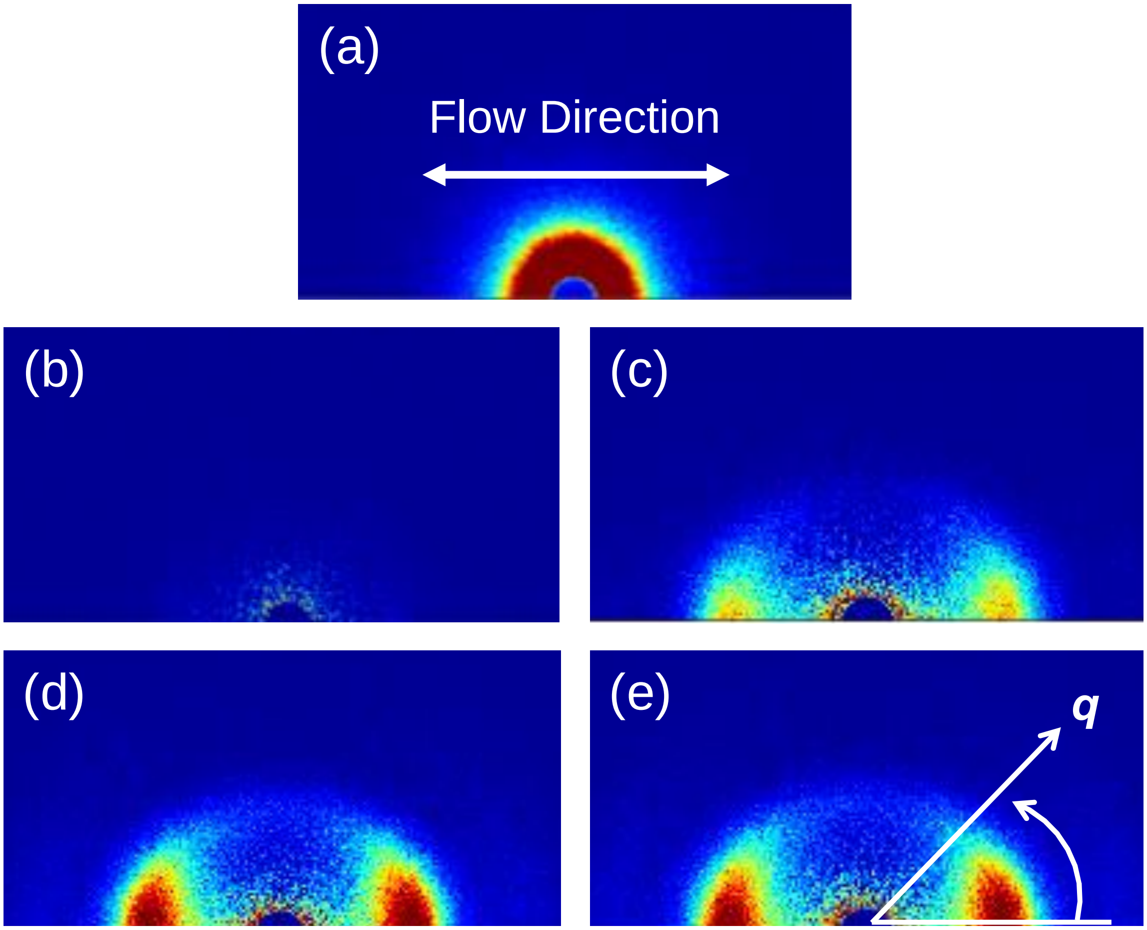

Figure 4.4: Representative SAXS patterns following $\dot{\varepsilon}$ = 0.023 s^{-1} and ε_H = 2.5 at 100 °C. The first image (a) is the frame immediately following flow and taken as the background frame (t = 0 min). This frame is subtracted from all subsequent images. The following images are at t = 0.25 min (b), t = 3 min (c), t = 9 min (d), and t = 43 min (e) following flow.

approximately 20 minutes. In all flow experiments, the impact of flow on crystallization is clearly reflected in the departure of *Q/V* from the quiescent crystallization behavior. At early times (<5 min), *Q/V* upon flow grows at a steeper slope compared to that under no flow. Towards the end of crystallization at later times, *Q/V* from all flow experiments reach a similar plateau value (Figure 4.5b). Some variability seems to exist among the final invariant values, but it is difficult to attribute such minor difference to flow dependence. What is evident is that increasing the extension rate accelerates the crystallization kinetics, as revealed in the positive trend in the inverse of the crystallization half-time ($t_{1/2}$) plotted against extension rate (Figure 4.5c).

Data in Figure 4.5 show the expected increase in kinetics with increasing deformation rate. Of particular interest in this work, however, is examining crystallization kinetics under flow conditions designed to produce equal degrees of nucleation enhancement. Based on the modeling assumptions used above, the crystallization kinetics should be comparable and independent of applied flow under extension rates and Hencky strains that lead to a constant N_f ~ 115. However, the crystallization behavior under these flow conditions show considerable variability (Figure 4.6). While the final degree of crystallization achieved in these experiments at late times is similar, the invariants grow at distinctly different rates. The two lowest extension rates (or equivalently the two highest Hencky strains) lead to the most highly accelerated crystallization kinetics. At the other end, the slowest crystallization kinetics is observed under intermediate flow conditions ($\dot{\varepsilon} = 0.084$ s^{-1} and $\varepsilon_H = 1.7$, $\dot{\varepsilon} = 0.042$ s^{-1} and $\varepsilon_H = 2$). The crystallization behavior that lies between the two extremes is seen at the highest extension rate (or equivalently the lowest applied strain). Figure 4.6b displays the inverse crystallization half-time plotted as a

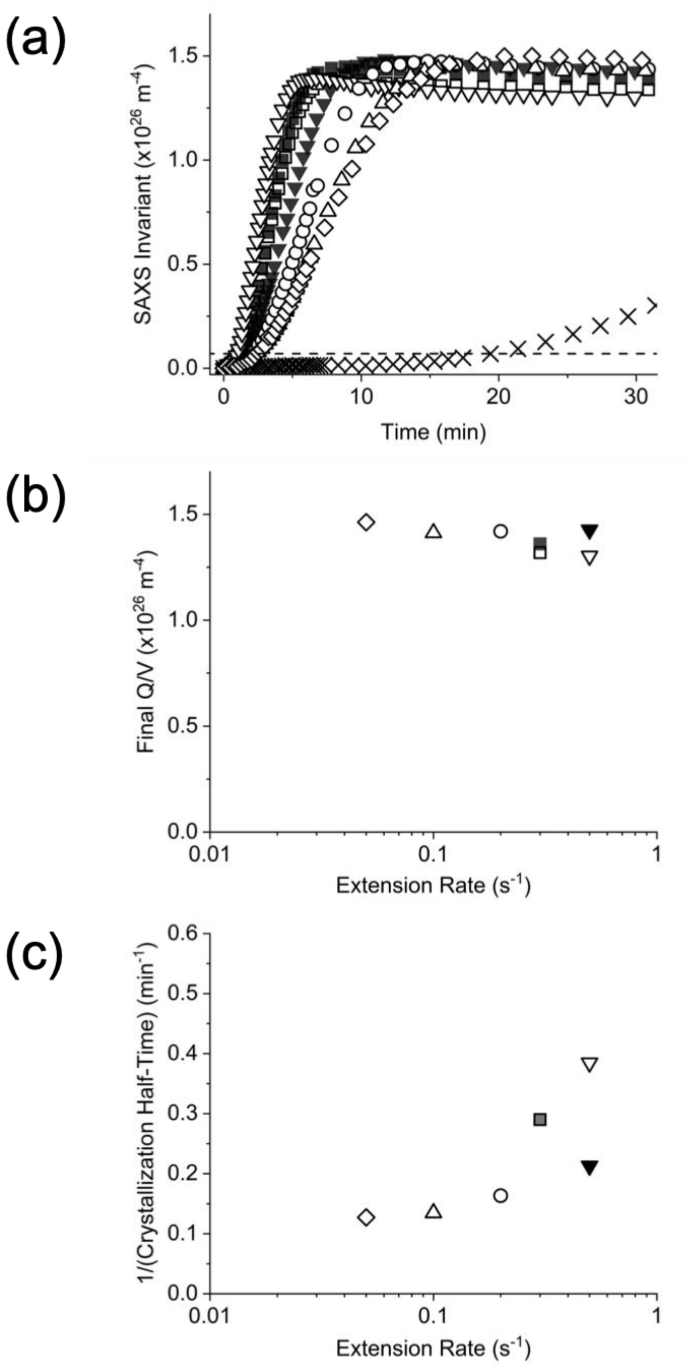

Figure 4.5: Rate dependence of SAXS invariant (a), final SAXS invariant (b), and inverse crystallization half-time (c) for experiments conducted at a constant Hencky strain of 1.5. Symbols denote extension rate: quiescent (×), $\dot{\varepsilon} = 0.05$ s^{-1} (◇), 0.1 s^{-1} (△), 0.2 s^{-1} (○), 0.3 s^{-1} (□,■), and 0.5 s^{-1} (▽,▼). The dotted line corresponds to the minimum invariant value that indicates the onset of crystallization.

function of extension rate to illustrate the variability in the crystallization kinetics described here. For experiments subjected to rates and strains that produce N_f ~ 250, the overall crystallization kinetics is enhanced compared to the results from N_f ~ 115, as expected with a larger number density of flow-induced nuclei based on the stronger flow conditions. However, the details of the evolution of *Q/V* once again vary across flow conditions (Figure 4.6c). The highest extension rate causes the fastest growth of *Q/V* while the other flow conditions lead to comparable crystallization behavior, which is reflected as the difference among the crystallization half-times in Figure 4.6d.

4.3.3 Orientation Distribution of Crystallites

We also quantify the state of crystallite orientation over the course of crystallization using the Hermans order parameter $\langle P_2 \rangle$:

$$\langle P_2 \rangle = \frac{3\langle \cos^2 \varphi \rangle - 1}{2} \tag{2.14}$$

where $\langle \cos^2 \varphi \rangle$ is given as

$$\langle \cos^2 \varphi \rangle = \frac{\int_0^\pi I(\varphi) \cos^2 \varphi \sin \varphi \, d\varphi}{\int_0^\pi I(\varphi) \sin \varphi \ \ d\varphi}. \tag{2.15}$$

In the expression above, the angled brackets represent an average weighted by the azimuthal intensity distribution $I(\varphi)$ that is obtained from integrating the corrected 2D intensity in absolute units over the *q*-range defined earlier. At early time frames when crystallization has not taken place, intensity fluctuations that arise from background subtraction or noise lead to unreliable calculations of $\langle P_2 \rangle$. Therefore, we use the threshold *Q/V* described in Figure 4.5a as an indicator

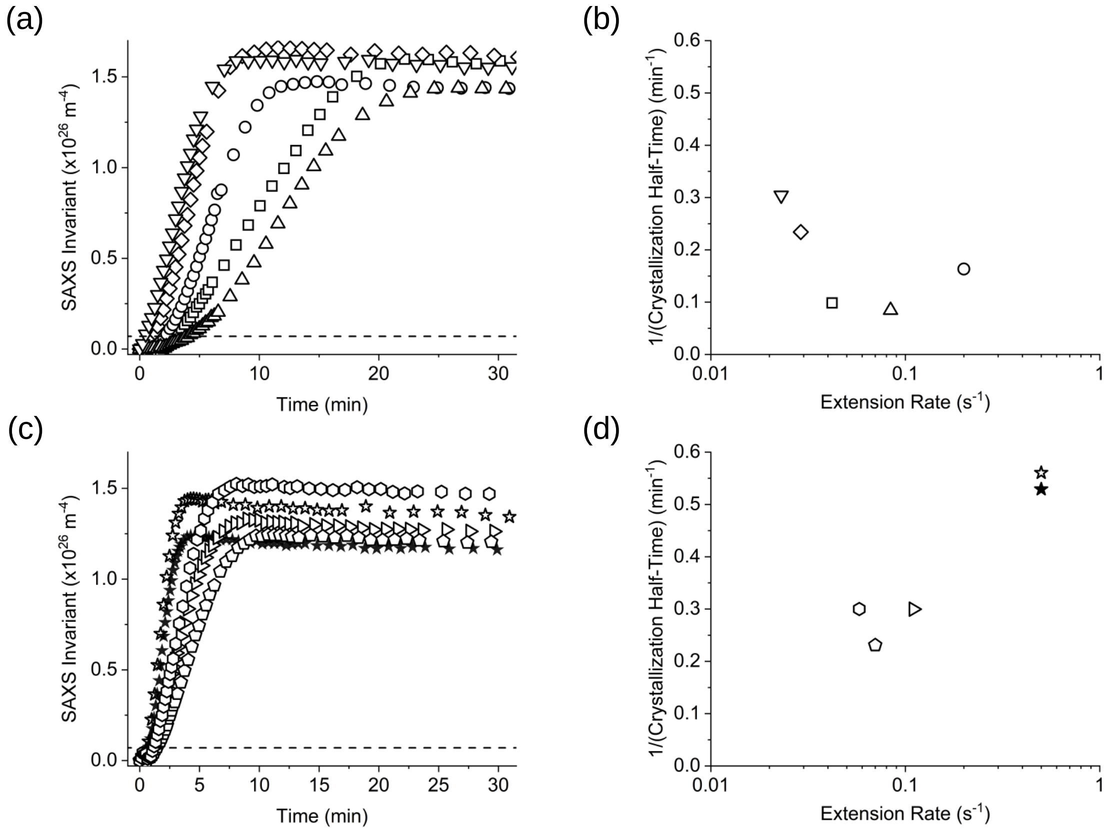

Figure 4.6: Crystallization resulting from experiments that lead to similar number density of flow-induced nuclei. For N_f ~ 115, the invariants grow at different rates (a) and this discrepancy is reflected in the variability in the crystallization half-time (b). Similar disagreement in the evolution of *Q/V* (c) and crystallization kinetics (d) is observed in experiments that lead to N_f ~ 250. Symbols denote specific combinations of extension rate and Hencky strain: $(\dot{\varepsilon}, \varepsilon_H)$ = (0.2 s^{-1}, 0.5) ○; (0.084 s^{-1}, 1.7) △; (0.042 s^{-1}, 2.0) □; (0.029 s^{-1}, 2.3) ◇; (0.023 s^{-1}, 2.5) ▽; (0.5 s^{-1}, 1.7) ☆★; (0.11 s^{-1}, 2.0) ▷; (0.07 s^{-1}, 2.3) ⬠; and (0.058 s^{-1}, 2.5) ⬡.

of the time frame at which there is sufficient growth in $I(\varphi)$ to result in a reliable $\langle P_2 \rangle$ value. $\langle P_2 \rangle$ serves as a valuable measure of the average distribution of lamellae orientation induced by flow, where $\langle P_2 \rangle$ = 0 is when the distribution is isotropic while $\langle P_2 \rangle$ = 1 indicates perfect alignment of the lamellae normal along the flow direction.

Figure 4.7a displays the evolution of $\langle P_2 \rangle$ over time for experiments conducted under various extension rates and at a constant Hencky strain of 1.5. At early times (< 5 min), the degrees of orientation are higher than those at later times for all flow conditions. This implies that the initial structures that crystallize are highly aligned and the observation is consistent with the scattering patterns in Figure 4.4c where the intensity is strongly concentrated along the flow. As the scattering intensity becomes stronger and broadens over time, the overall $\langle P_2 \rangle$ values for all experiments decrease and reach a plateau value. Focusing on the final $\langle P_2 \rangle$ values when crystallization is completed, we observe that increasing the extension rate leads to higher final degrees of lamellar orientation as demonstrated in Figure 4.7b.

Under rate-strain combinations designed to produce similar N_f, the state of orientation is expected to be comparable across experiments. However, different degrees of orientation are achieved at the end of crystallization in experiments at N_f ~ 115, as shown in Figure 4.8. Similar to the observations made regarding crystallization kinetics (Figure 4.6b), the intermediate flow conditions result in relatively lower final $\langle P_2 \rangle$ values compared to those from the slowest or fastest extension rates. When N_f is increased to 250, the final $\langle P_2 \rangle$ values are generally higher than those at N_f ~ 115, which is consistent with the idea that a higher N_f leads to a more pronounced effect of flow on subsequent crystallization. However, discrepancy in the final state

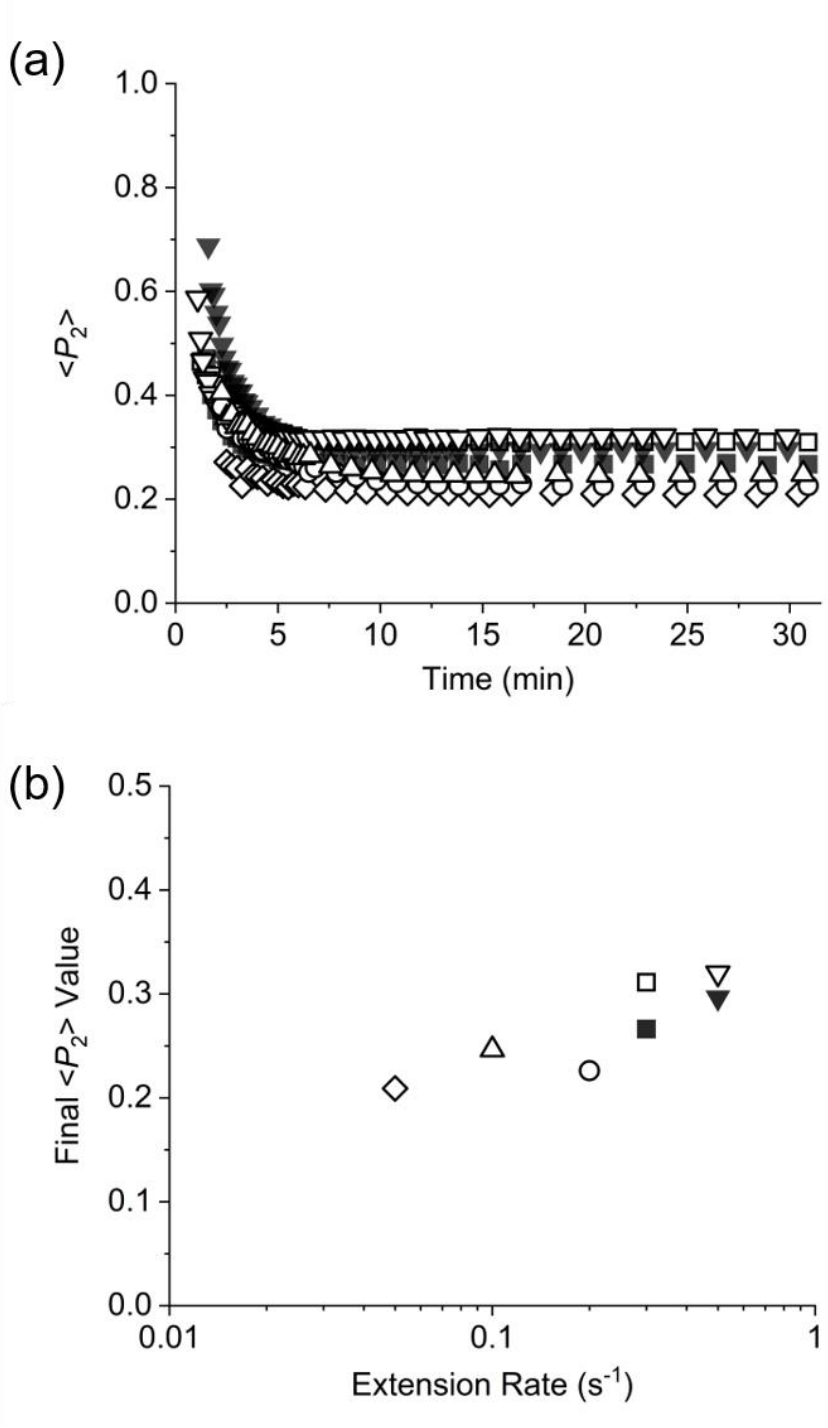

Figure 4.7: (a) Evolution of molecular orientation and (b) final degree of orientation for various extension rates at a fixed Hencky strain of 1.5. In general, increasing the extension rate leads to a higher final degree of lamellar orientation. Symbols denote extension rate: $\dot{\varepsilon} =$ 0.05 s^{-1} (◇), 0.1 s^{-1} (△), 0.2 s^{-1} (○), 0.3 s^{-1} (□,■), and 0.5 s^{-1} (▽,▼).

of orientation exists as well. At N_f ~ 250, it appears that increasing the extension rate leads to a higher final degree of orientation, although the orientation should be independent of applied flow.

4.4 Discussion

Overall, we observe that faster crystallization kinetics is generally associated with higher degree of lamellar orientation (Figure 4.9). The inverse of the crystallization half-time is positively correlated with the final $\langle P_2 \rangle$ value, ensuring that the experiments reliably demonstrate what is expected from flow-induced crystallization tests. However, flow conditions that are expected to lead to similar flow-enhanced nucleation and subsequent crystallization behavior have shown to result in experimental data that disagree with modeling predictions. This mismatch is illustrated in Figure 4.10, where the crystallization half-times from experiments at similar N_f values show variability and deviate from the contours along the 3D surface plot of predicted N_f values in the parameter space. This naturally brings us to a critical assessment of the discrepancy between the experimental and modeling results. It is worthwhile to revisit the assumptions that went into the strategy of experimental design using modeling predictions: (1) a single "reptation time" was used for a polydisperse sample, in which the slowest Maxwell mode was taken to represent the population of chains relevant for flow-enhanced nucleation; (2) a modified Rolie-Poly model was used to describe the melt rheology, while the model itself is a simplified version of sophisticated reptation concepts; and (3) chain stretch was identified as the appropriate variable to link melt rheology and enhanced nucleation, using a specific functional form of $N_f = N_f(\Lambda^4)$.

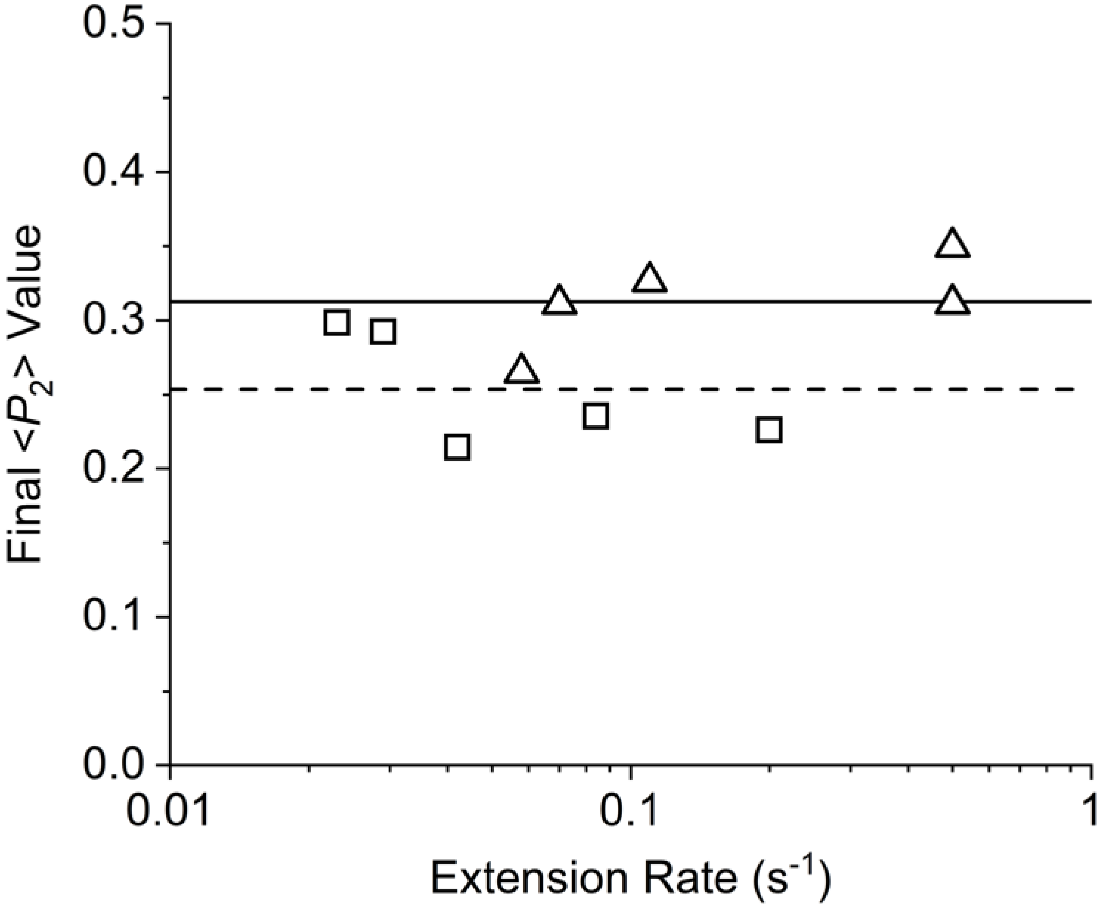

Figure 4.8: Final degree of orientation as a function of extension rate conditions that lead to N_f ~ 115 (□) and N_f ~ 250 (△). Dotted and solid lines indicate the average of the final $\langle P_2 \rangle$ values for each case.

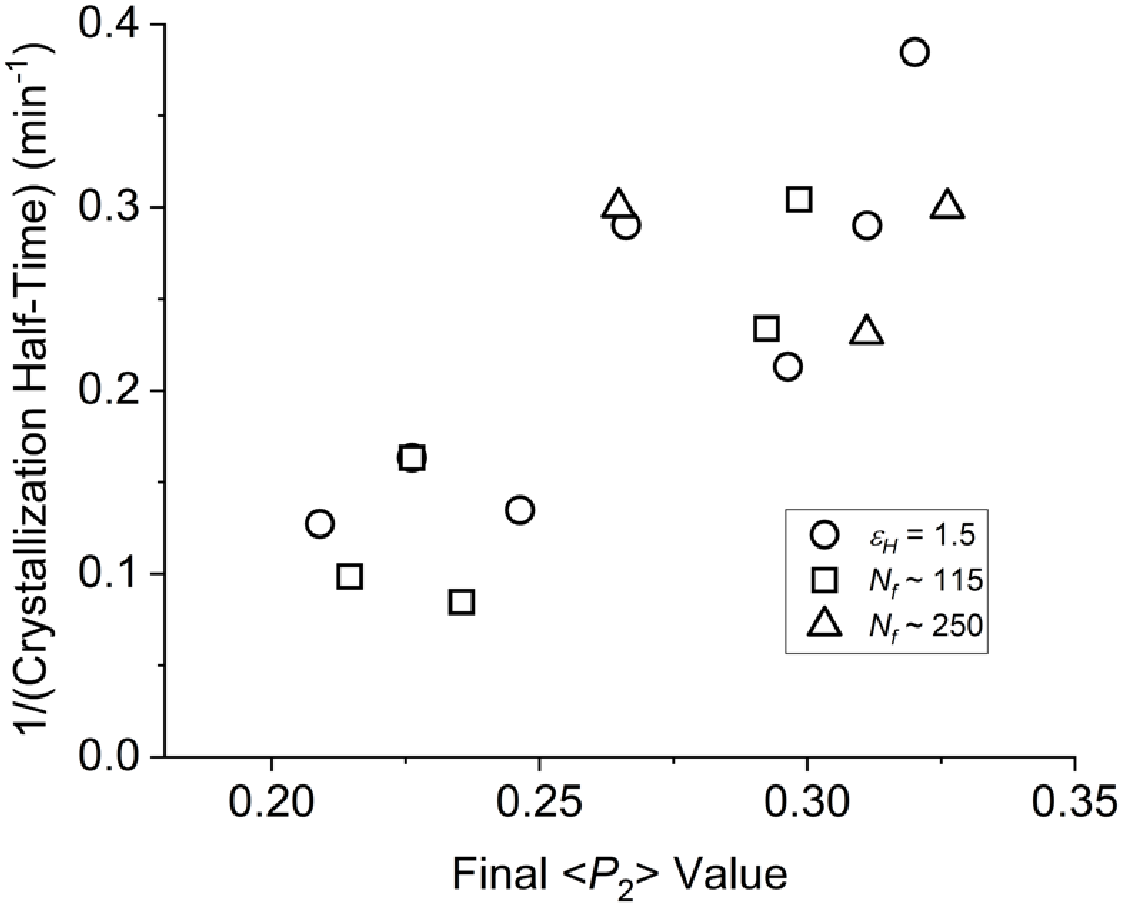

Figure 4.9: Cross-plot of the inverse of the crystallization half-time versus the final degree of orientation for all experiments. The data demonstrate that faster crystallization kinetics is generally associated with higher molecular orientation.

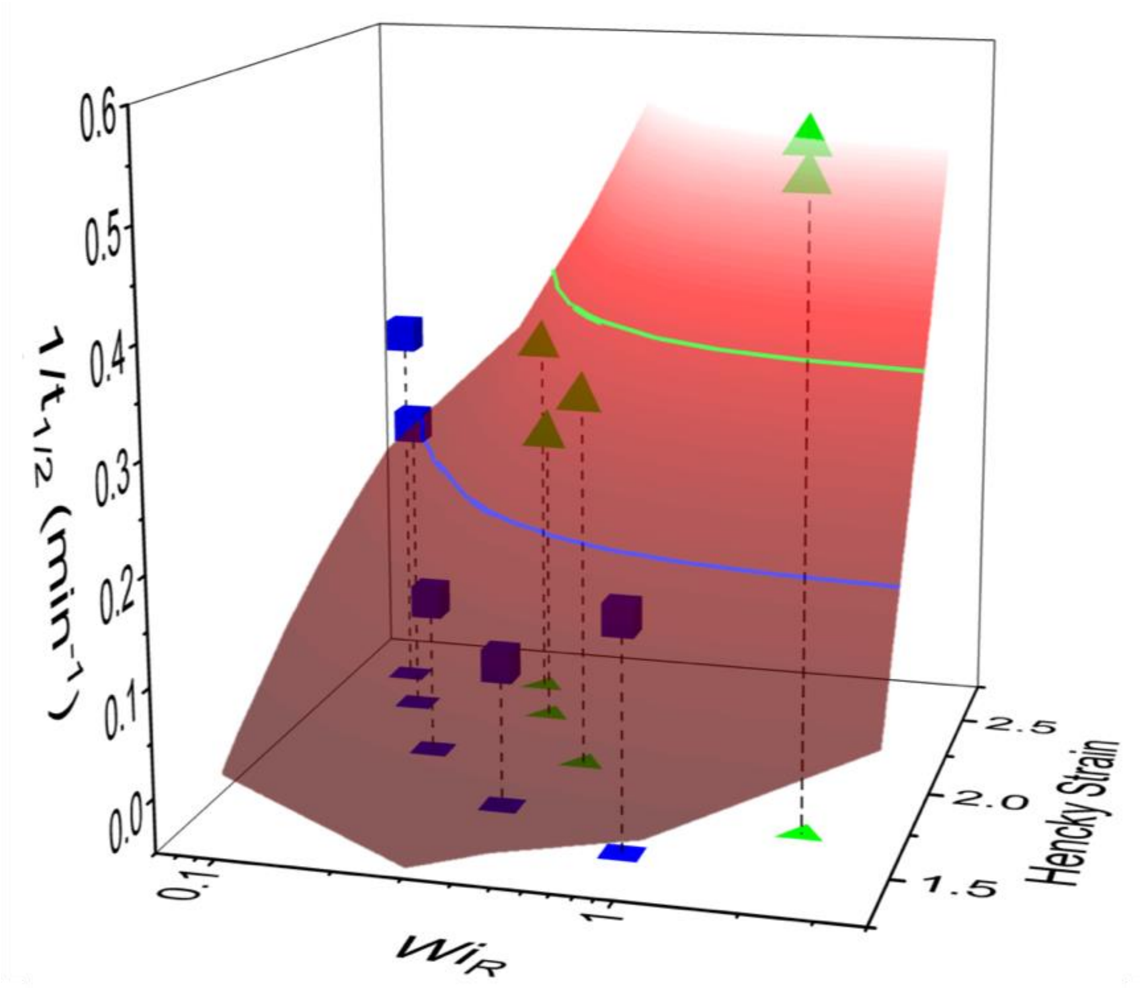

Figure 4.10: Summary of experimental and modeling results. Crystallization half-times from experiments that lead to N_f ~ 115 (blue □) and N_f ~ 250 (green △) show variability, as illustrated in their mismatch with the contours (blue and green lines) along the 3D surface plot of predicted N_f (red) in the Wi-strain space.

First and foremost, the notion of a single “reptation time” may be too simplistic for a polydisperse sample. It is possible that lower molecular weight chains, in addition to the higher molecular weight components, contribute to producing stretch and to the formation of crystalline structure. Kornfield and co-workers used small-angle neutron scattering (SANS) with deuterium labeling of isotactic polypropylene chains with different lengths and observed that short and medium length chains are included in the shish.[126] In fact, the concentration and long chains in the shish was found to match that in the surrounding melt, indicating that chains of all lengths are included in the shish as it propagates. Similar experimental observations were made by Kanaya and co-workers, who used SAXS and SANS to find that more low molecular weight chains than long-chain segments were incorporated in the shish during the drawing of polyethylene.[127] Thus, a more accurate way to calculate the total amount of stretch produced in the melt would be to consider the entire molecular weight distribution (i.e., the entire relaxation spectrum) as opposed to only the highest molecular weight species (represented in this modeling strategy by the slowest mode).

It is also possible that the Rolie-Poly model may not be the most appropriate constitutive equation to describe the polymer melt rheology. The model itself is a simplified version of the Graham-Likhtman and Milner-McLeish (GLaMM) model[128]—a refined version of the tube model of reptation that comprehensively describes entangled linear polymers under linear to nonlinear shear and extensional flows, but is computationally expensive. As described previously, the Rolie-Poly equation was further simplified by removing the effect of convective constraint release, and although justified, this simplification may not hold as the main mechanism of stress relaxation is convective constrain release in nonlinear flow experiments.[129]

In fact, Likhtman and Graham note that the Rolie-Poly equation has three relaxation regimes with the convective constrain release regime falling between the regimes where relaxation is dominated by reptation and retraction.[125] Of course, the Rolie-Poly model itself is a rather simple implementation of reptation concepts.

In addition, the creation rate of flow-induced nuclei is a phenomenological function of the stretch parameter, where the relation $N_f \propto \Lambda^4 - 1$ was empirically determined as it resulted in the best fit. This suggests that other formulations of the stretch parameter can be related to flow-induced nucleation. For example, other incarnations of the FIC models developed by Peters and co-workers use $\Lambda^2 - 1$ to link molecular stretch to enhanced nucleation.[93] On a larger scope—beyond the specific functional form of how N_f is related to Λ—the modeling approach used here starts with an assumption that chain stretch is the appropriate link between melt rheology and enhanced nucleation. Alternate constitutive equations may be used to describe the melt rheology, with alternative links to the nucleation process. For instance, the Giesekus model is used to represent the melt rheology in the model of Doufas *et al.*,[130] where the conformation tensor is coupled to the overall crystallization kinetics. Similarly, a multimode Giesekus model can be used to determine the principal stress difference, and flow protocols can be designed based on the amount of stress imposed on the polymer melt.

We have specifically subjected the model developed by Roozemond and Peters[90] to a meticulous test in this present work. Considering the assumptions and simplifications involved in describing the complexities of flow-induced crystallization, it is difficult to say that the model formulation is incorrect; rather, it is a difficult task to design models capable of withstanding such a stringent test of their predictions. However, we feel that the general approach adopted in this work, which allows direct testing of critical elements in a more comprehensive modeling strategy, offers advantages over tests based on full simulation of the entire crystallization process in which even more factors and assumptions are embedded. This general approach can be extended to using similar design strategies in different types of flow, such as monitoring the crystallization under shear and extensional flow conditions that produce similar enhanced crystallization behavior and revisiting the strategy as necessary.

4.5 Conclusion

We directly tested how molecular stretch leads to flow-enhanced nucleation through flow-induced crystallization experiments of poly(1-butene) subjected to various extension rates and Hencky strain that produce similar number density of flow-induced nuclei. The N_f values were calculated from the degree of stretch during extensional flow and relaxation, as predicted by a simplified Rolie-Poly model. For experimental conditions that are expected to result in similar crystallization kinetics and degree of crystallite orientation, both the SAXS invariants and final $\langle P_2 \rangle$ values generally do not show agreement, as revealed by *in situ* SAXS data. Experiments at a higher N_f value generally result in faster kinetics and higher degrees final of lamellae orientation, and accelerated crystallization kinetics is generally associated with higher degree of orientation. The discrepancy between experimental data and modeling predictions do not necessary suggest that the model formulation is invalid, as simplifications and assumptions involved in the modeling framework make it difficult to accurately predict FIC.

Chapter 5

Short-Term and Continuous Flow-induced Crystallization in Low-Density Polyethylene

5.1 Introduction

In a recent study, Wingstrand and colleagues studied the influence of stress overshoot in the melt on the final morphology of low-density polyethylene (LDPE) by following a procedure similar to the short-term flow protocol.[131] After erasing the thermal history in the LDPE at an elevated temperature above its melting point, the sample was cooled to a selected temperature at which extensional flow was applied using a filament stretch rheometer to induce different levels of stresses in the polymer melt. The stretched sample was rapidly quenched to room temperature to induce crystallization, and *ex situ* small- and wide-angle x-ray scattering (SAXS and WAXS, respectively) measurements were performed to reveal that the final morphology was dictated by the stress at quench, rather than the final Hencky strain at quench. Motivated by the feasibility of extensional flow-induced crystallization experiments on this material, we use a different approach to explore the crystallization behavior in LDPE subjected to uniaxial extensional flow. Rather than applying flow and inducing crystallization during quench, we study the immediate effect of flow on the structural evolution during *isothermal* crystallization.

In this chapter, we employ *in situ* SAXS and WAXS measurements in real time to probe the structural evolution as the polymer crystallizes. Extensional flow-induced crystallization experiments are conducted at a range of crystallization temperatures, extension rates, and applied

Hencky strains under short-term and continuous flow protocols. In fact, only modest changes in experimental conditions determine whether crystallization occurs subsequent to, or during the applied flow. Crystallization behavior under the two different protocols is compared based on the extent of crystallization and state of crystallite orientation quantified from the measured x-ray scattering data, which are complemented by simultaneous measurements of the extensional viscosity. Fundamentally different morphologies are found depending on whether or not crystallization is initiated during the flow.

5.2 Material and Experimental Methods

5.2.1 Material of Study

The material used in this study is a commercial long-chain branched polymer (Lupolen 3020D from BASF). LDPE pellets were generously donated by Sara Wingstrand and Ole Hassager from the Technical University of Denmark, who explored the impact of stress overshoot in the LDPE melt on its final morphology.[131] The sample has a peak melting temperature (T_m) of 114 °C, a weight-averaged molecular weight (M_w) of 300,000 g/mol, and a polydispersity index of 8. Consequently, the linear viscoelasticity of the material is characterized by a broad distribution of relaxation times.[132]

5.2.2 In Situ X-ray Scattering Experiments

Extensional flow-induced crystallization experiments were performed using the custom-built instrument employing an SER extensional flow fixture. Samples were prepared by compression molding LDPE pellets at 180 °C into thin sheets that were cut into rectangular strips with a length of 22 mm, width of 11 mm, and thickness of 0.8 mm. For time-resolved SAXS and WAXS measurements, the instrument was integrated into the beam line at Sector 5ID-D of the Advanced Photon Source at Argonne National Laboratory. An x-ray beam energy of 17 keV (wavelength $\lambda = 0.729$ Å) was selected to collect images on Rayonix detectors with pixel sizes 3840 x 3840 (SAXS) and 1920 x 3840 (WAXS), placed at a sample-to-detector distance of 8.5 m and 0.21 m, respectively. Depending on the flow protocol, a 2 x 2 binning (short-term flow) or 6 x 6 binning (continuous flow) was used. The two flow protocols are distinguished based on whether the onset of crystallization is first detected only after flow (short-term flow-induced crystallization) or during flow (continuous flow-induced crystallization). In both cases, the sample was first heated to 150 °C to erase its thermo-mechanical history, then cooled to and equilibrated at a desired crystallization temperature (T_c). In short-term flow experiments, a brief pulse of extensional flow was applied to the undercooled melt, and crystallization following flow was monitored for 30 – 45 min using SAXS/WAXS measurements. X-ray images were collected using exposure times of 0.25 – 0.3 s at intervals of 5 – 120 s between each frame. No signs of crystallization were observed during extension, ensuring that the effect of flow was decoupled from subsequent crystallization. In continuous flow experiments, crystallization occurred during the application of flow and thus required faster acquisition of data. X-ray data collection was initiated 2 s prior to flow inception, and continued during flow and then 20 s after flow cessation, using a minimum of 0.1 s per frame with an exposure time of 60 ms.

5.2.3 Experimental Conditions

Short-term flow experiments were conducted at three crystallization temperatures, under which no crystallization was detected prior to or during flow. The effect of extension rate and Hencky strain was explored using rates ranging from 0.1 to 3 s^{-1} and applied strains ranging from 1 to 2 (corresponding to melt stretch ratios of 2.7 to 7.4). At the highest crystallization temperature (T_c = 114 °C), no crystallization was observed within the experimental time frame under any but the most extreme flow conditions. At the intermediate temperature (T_c = 112 °C), crystallization under quiescent conditions occurred towards the end of the experimental time frame used in these experiments, and all flow conditions led to detectable and accelerated crystallization. At the lowest crystallization temperature (T_c = 110 °C), the crystallization behavior was qualitatively similar to that at T_c = 112 °C, while the crystallization kinetics were further accelerated. These observations will be described more in detail in Section 5.3. Subjecting the sample to stronger flow conditions by increasing the applied strain led to one of two outcomes: at T_c = 112 °C and 114 °C, Hencky strains greater than 2 resulted in necking failure due to non-uniform deformation of the sample; at T_c = 110 °C, an additional unit of Hencky strain ($\varepsilon_H = 3$) led to crystallization *during* flow. Based on this observation, the continuous flow data acquisition protocol was applied for experiments conducted at T_c = 110 °C with samples stretched to $\varepsilon_H = 3$ under various extension rates up to 3 s^{-1}. While attempts were made to extend the range of temperatures to T_c = 108 °C, no flow-induced crystallization experiments were performed at this temperature as crystallinity was detected during the equilibration step prior to applying deformation. Rather modest changes in temperature were thus found to have a significant impact on the observed crystallization behavior.

5.2.4 SAXS/WAXS Data Analysis

Based on the procedures outlined in Section 2.4.1, intensities from SAXS and WAXS images are converted to an absolute intensity scale to make direct, quantitative comparisons across all experiments. This process includes making an axial symmetry assumption along the direction of extension (applicable for uniaxial extensional flow) as well as performing a geometric correction.

A background subtraction is also performed to isolate the scattering contribution arising only from crystallization. For SAXS measurements under the short-term flow protocol, the image immediately following flow is treated as a background frame and subtracted from all subsequent patterns; for WAXS data, the intensity from the primary crystalline peak is extracted by subtracting the underlying amorphous background intensity that is fit as a polynomial in each frame.

The background subtraction process for data collected under the continuous flow protocol requires more treatment because the thickness of the sample decreases in each image collected during the application of flow. To account for the relative change in thickness, we track the peak height of the amorphous background in each WAXS pattern, since the raw scattered intensity should be proportional to the sample thickness (x-ray absorption is negligible at the relatively high x-ray energy used in these experiments).[95] The amorphous peak height is determined from a radial scan along $\varphi' = 30°$ (a region where no crystalline peaks appear), and the average value of the amorphous peak height prior to flow is scaled to the initially measured sample thickness. This scaled quantity is used as a surrogate for the apparent sample thickness, which not only accurately captures the changing sample thickness during flow but also exhibits an exponential decrease with time during the flow, confirming expectations for an ideal uniaxial extensional deformation (Figure 5.1). The background subtraction for SAXS measurements from continuous flow experiments then involves subtraction of the thickness-corrected image at the very beginning of flow (t = 0 min) from all subsequent thickness-corrected patterns.

The corrected absolute intensity data are used to quantify the extent of crystallization. In SAXS, the evolving degree of crystallinity is reflected in the volume-weighted scattering invariant (Q/V), calculated using Eq. (2.12). Owing to a cutoff at low q (due to stray background scattering surrounding the beam stop), and a desire to suppress noise amplified by the q^2 factor at high q where the SAXS intensity vanishes, the integration in Eq. (2.12) is actually evaluated over a finite q range between 0.005 Å^{-1} and 0.07 Å^{-1}. In WAXS, the area under the (110) crystalline peak serves as a measure of the extent of crystallization. As mentioned earlier, the intensity from this primary peak (I_{110}) is obtained by subtracting an amorphous background intensity in every image to account for the suppression of the amorphous background as the sample crystallizes over time. The area under the (110) crystalline peak (A_{110}) is then calculated from

$$A_{110} = \int_0^{\pi} \int_{q_1}^{q_2} I_{110}(q, \varphi)\, q^2 \sin\varphi \, dq \, d\varphi \tag{5.1}$$

where q_1 = 1.49 Å^{-1} and q_2 = 1.57 Å^{-1}.

As the applied flow naturally leads to a uniaxially symmetric orientation distribution, the orientation of crystallites is characterized using the Hermans order parameter $\langle P_2 \rangle$:

$$\langle P_2 \rangle = \frac{3\langle \cos^2 \varphi \rangle - 1}{2}. \tag{2.14}$$

In Eq. (2.14), $\langle \cos^2 \varphi \rangle$ is the average of $\cos^2 \varphi$ weighted by the azimuthal intensity distribution $I(\varphi)$ and given as

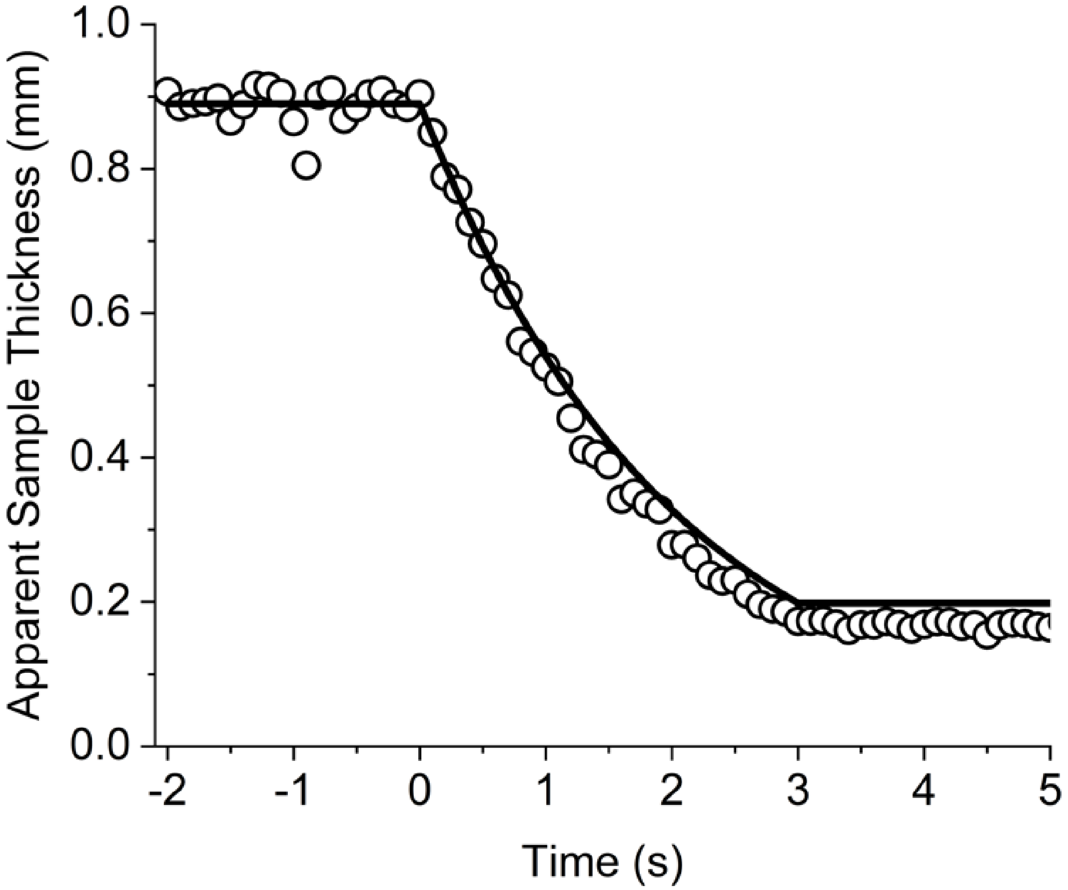

Figure 5.1: Apparent sample thickness in continuous flow experiments. The change in amorphous peak height from raw WAXS patterns is converted to the relative sample thickness prior to, during, and following flow based on the measured initial sample thickness. The apparent sample thickness calculated in this way follows a uniaxial extension prediction (solid line).

$$\langle \cos^2 \varphi \rangle = \frac{\int_0^{\pi} I(\varphi) \cos^2 \varphi \sin \varphi \, d\varphi}{\int_0^{\pi} I(\varphi) \sin \varphi \, \, d\varphi}. \tag{2.15}$$

$\langle P_2 \rangle$ is normalized by its value along the angle of perfect alignment, as this allows the values of $\langle P_2 \rangle$ to always range between -0.5 and 1. For a perfectly oriented sample along the flow direction, the normal direction of the expected chain-folded lamellae is parallel to flow, such that lamellae diffraction appears in the flow direction (φ = 0° in SAXS). In this chapter, we present orientation factor analyses derived from SAXS data only. With the $\langle P_2 \rangle$ values normalized in this manner, the orientation of crystallites is always analyzed with respect to the flow direction, where $\langle P_2 \rangle$ = 0 indicates random distribution, $\langle P_2 \rangle$ = -0.5 indicates perfect orientation of crystallites perpendicular to flow, and $\langle P_2 \rangle$ = 1 indicates perfect orientation of crystallites parallel to flow.

5.3 Results and Discussion

5.3.1 Short-term Flow

Short-term flow experiments conducted at T_c = 112 °C and ε_H = 2 subjected to various extension rates exhibit rate dependence in the crystallization behavior (Figure 5.2). Quiescent crystallization is much slower than crystallization upon the application of flow, under which the onset of growth in Q/V and A_{110} occurs at earlier times. The steeper slopes of Q/V and A_{110} at higher extension rates confirm that crystallization kinetics is substantially accelerated with increasing flow strength. These observations are consistent with results from previous flow-induced crystallization experiments (Chapters 3 and 4), which generally show similar rate dependence in the crystallization kinetics. However, unlike the results from previous studies where similar final extent of crystallization was achieved at the end of crystallization under different extension rates, higher extension rates in this study lead to higher degrees of crystallization at the end of the experimental time frame. Specifically, Q/V and A_{110} monotonically increase throughout the experimental observation window, indicating the continued progression of crystallization. Such behavior is also seen in experiments at a fixed extension rate and various applied strains (Figure 5.3), where the extent of crystallization found at the end of our observation window exhibits strong strain dependence. In both cases of varied rate and strain, calculations of the extent of crystallization from SAXS and WAXS data show strong qualitative agreement.

While the evolution of crystallinity observed at T_c = 112 °C follows expected trends, quantitative measurements of crystallite orientation, as characterized by $\langle P_2 \rangle$ extracted from SAXS data, show an unexpected complex evolution of morphology during crystallization induced by varying extension rates (Figure 5.4). At the lowest extension rate of 0.1 s^{-1}, the first crystalline structures detected by SAXS at t ~ 10 min are characterized by a negative $\langle P_2 \rangle$ value. Interpreting the SAXS in terms of conventional lamellar semi-crystalline morphologies would thus indicate that the lamellar normals are preferentially oriented *perpendicular* to flow, counter to expectations for oriented crystallization under flow. As time progresses, $\langle P_2 \rangle$ increases to positive values, more in keeping with expectations. Increasing the extension rate to 0.3 s^{-1} leads to a drastically different behavior in the evolution of $\langle P_2 \rangle$. The microstructures that crystallize at early times (t ~ 5 min) lead to a nonnegative $\langle P_2 \rangle$ value; $\langle P_2 \rangle$ then decreases to negative values, again suggesting the growth of subsequent crystallites with lamellar normal orthogonal to flow. The transient $\langle P_2 \rangle$ at higher extension rates of 1 s^{-1} and 3 s^{-1} is more akin to the evolution of $\langle P_2 \rangle$

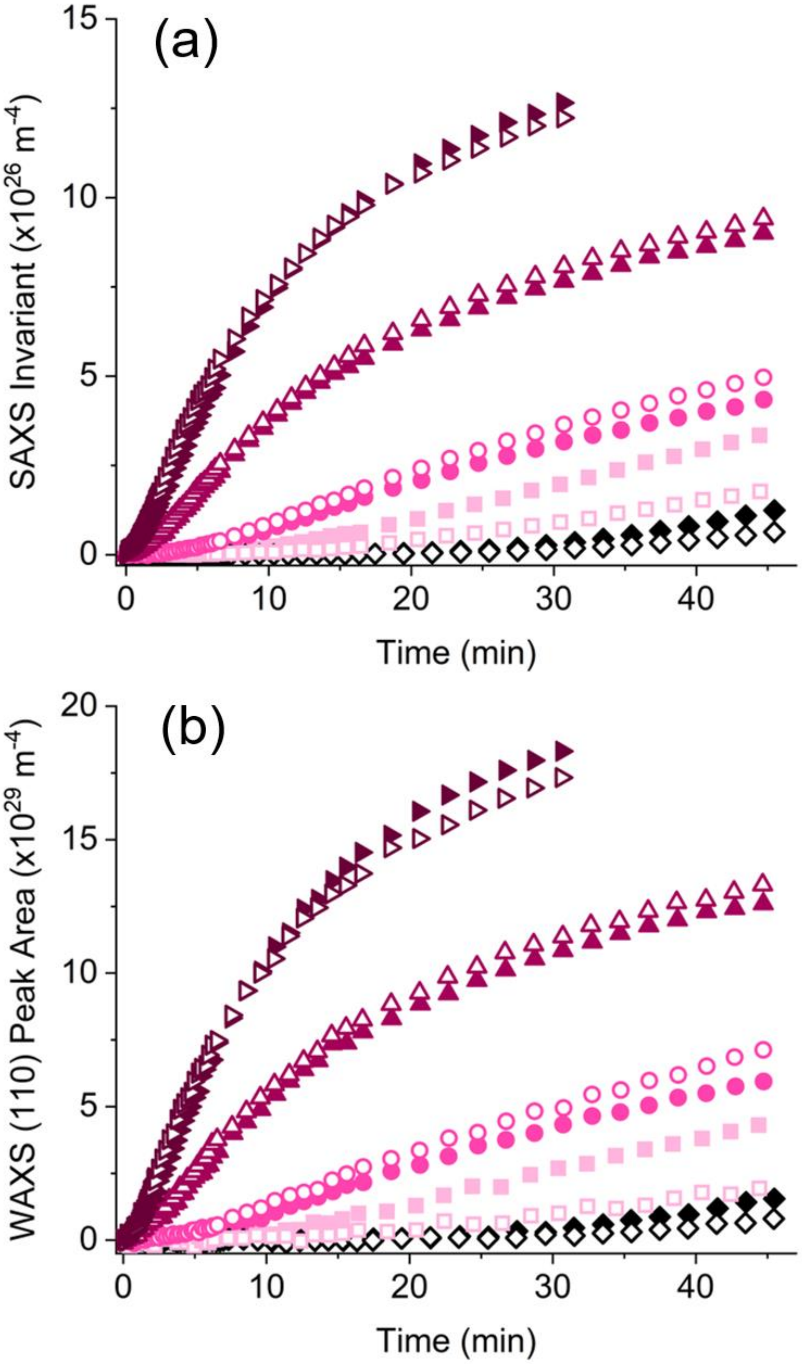

Figure 5.2: SAXS invariant (a) and WAXS (110) peak area (b) at T_c = 112 °C and ε_H = 2 for multiple extension rates: quiescent (◇), $\dot{\varepsilon}$ = 0.1 s^{-1} (□), $\dot{\varepsilon}$ = 0.3 s^{-1} (○), $\dot{\varepsilon}$ = 1 s^{-1} (△), $\dot{\varepsilon}$ = 3 s^{-1} (▷) (extension rates are color-coded in a consistent manner for all short-term flow experiments). In all Figures, open and closed symbols denote repeated experiments at the same flow condition.

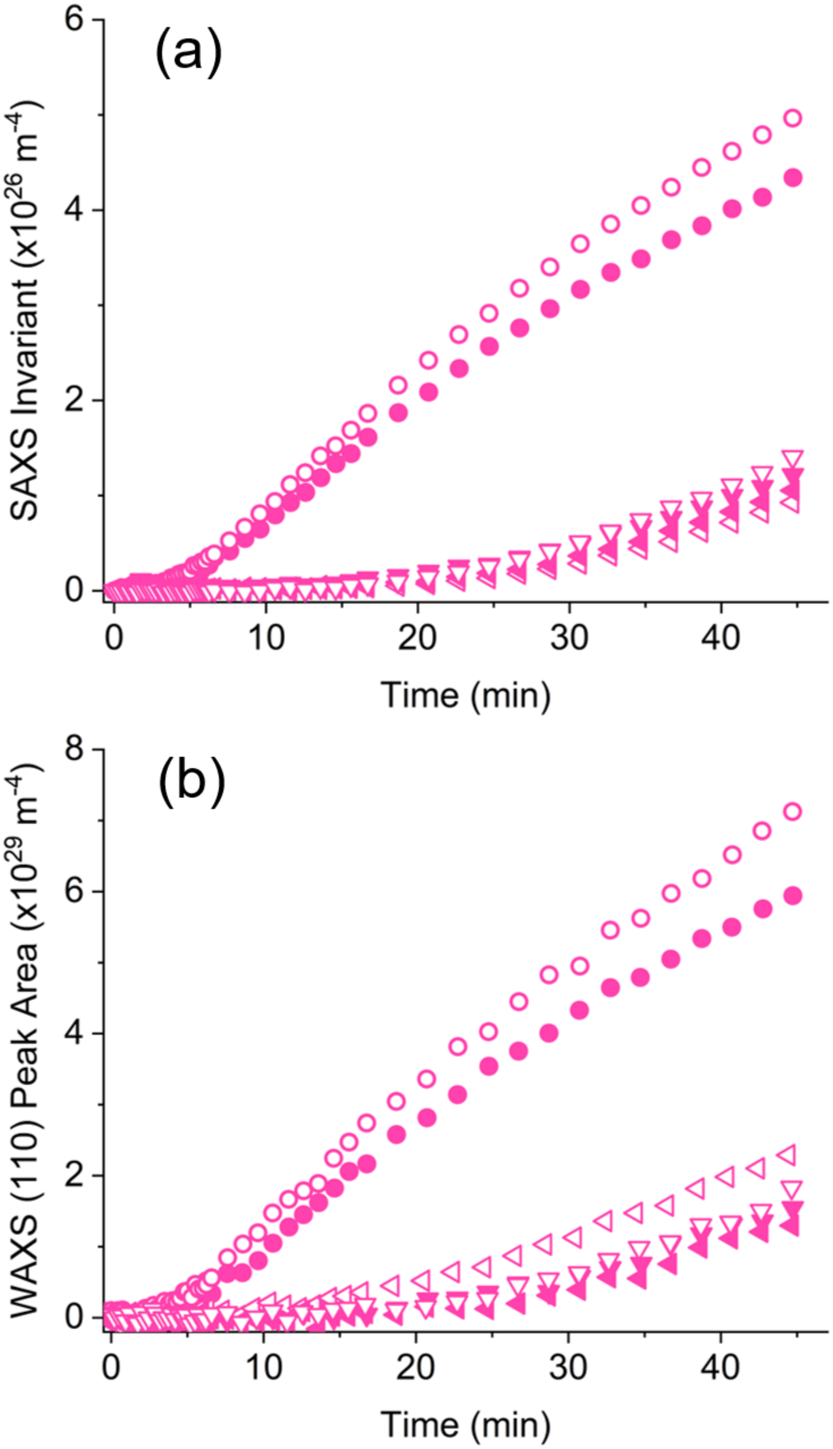

Figure 5.3: SAXS invariant (a) and WAXS (110) peak area (b) at T_c = 112 °C and $\dot{\varepsilon}$ = 0.3 s^{-1} for different Hencky strains: ε_H = 1 (◁), 1.5 (▽), 2 (○). Open and closed symbols denote repeated experiments at the same flow condition.

seen in previous studies (Chapter 4).[95] The high $\langle P_2 \rangle$ values at early times indicate that initial crystallites are highly aligned, and subsequent crystallization leads to a decrease in the overall $\langle P_2 \rangle$. In all flow conditions, the final degrees of orientation at the end of the experiment do not reach a steady value, implying that structures continue to evolve with varying orientation state as crystallization proceeds. Despite the stark differences and unexpected behavior found in transient $\langle P_2 \rangle$ across various extension rates, repeated experiments under identical conditions show remarkable reproducibility.

Figure 5.5a presents SAXS patterns from experiments at T_c = 112 °C and ε_H = 2 that reveal the zoology of lamellar-scale structures resulting from different extension rates, as previewed in the complicated evolution of $\langle P_2 \rangle$ in Figure 5.4. In all experiments, crystallization is manifested in the growth of anisotropic SAXS intensity over time. At the slowest flow condition ($\dot{\varepsilon}$ = 0.1 s^{-1}), the intensity becomes increasingly concentrated in the flow direction over time, indicating the growth of crystallites that are elongated transverse to the flow direction. Conversely, at $\dot{\varepsilon}$ = 0.3 s^{-1}, the intensity grows in the transverse direction indicating anisotropic structures oriented along the flow direction. At an extension rate of 1 s^{-1}, strong signs of oriented crystallization are observed at early times (t = 2.5 min) where the SAXS intensity is concentrated parallel to flow; this is more in keeping with expectations for lamellar crystallization with normal along the flow direction. As crystallization proceeds, however, a scattering pattern characterized by a bimodal azimuthal intensity distribution emerges, in which the SAXS peaks appear at an intermediate angle with respect to the flow axis. Similar unusual features characterized by “four-point”[133–137] or “x-shaped”[69] patterns have been reported in samples stretched in the solid state, and are classically attributed to tilted lamellae resulting from interlamellar shear. However, these

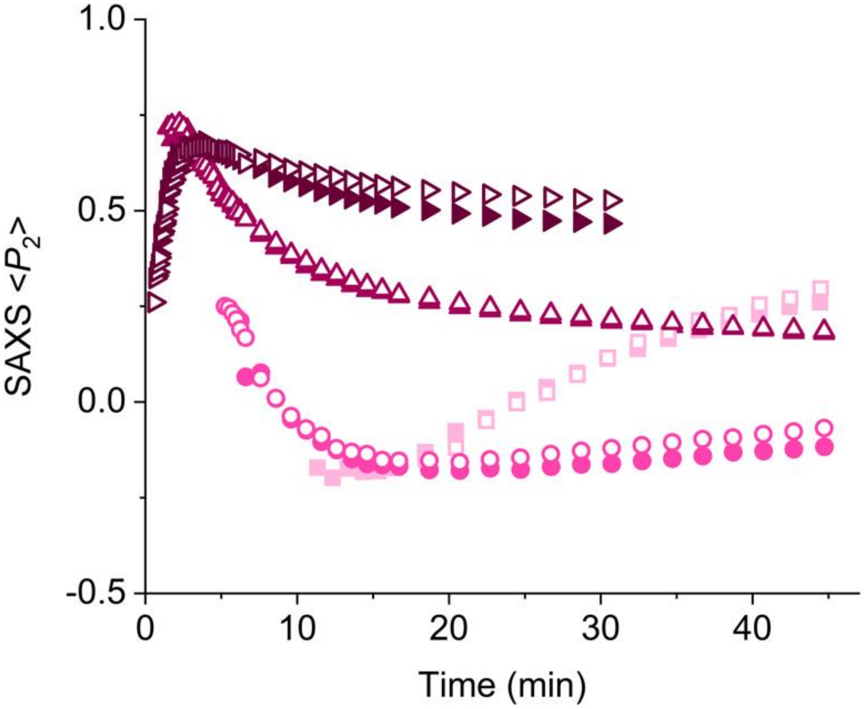

Figure 5.4: Evolution of $\langle P_2 \rangle$ calculated from SAXS data at T_c = 112 °C and ε_H = 2 for multiple extension rates: $\dot{\varepsilon}$ = 0.1 s^{-1} (□), 0.3 s^{-1} (○), 1 s^{-1} (△), 3 s^{-1} (▷). Open and closed symbols denote repeated experiments at the same flow condition.

studies involve stretching of a sample at room temperature or annealing of a sample stretched to extremely large deformations, which are very different from the temperature and flow conditions used in our experiments. In addition, the SAXS patterns from cold drawn samples have very distinct four-point features associated with clear peaks in scattered intensity as a function of scattering vector, while the x-shaped pattern at $\dot{\varepsilon}$ = 1 s^{-1} in our experiments extends from the center of the image with no obvious peak. Indeed, none of these patterns exhibit a peak in $I(q)$ that is the usual indicator of lamellae alternating with amorphous regions (Figure 5.5b). At the highest extension rate of 3 s^{-1}, yet another radically different pattern appears towards the end of the experiment, which is depicted by a broadly concentrated SAXS intensity parallel to the flow direction.

A series of SAXS patterns from similar short-term flow experiments at T_c = 110 °C with samples stretched to ε_H = 2 at different extension rates also demonstrate that modest changes in flow conditions lead to diverse and complex evolution of lamellar-scale morphologies (Figure 5.6a). At the lowest extension rate of 0.1 s^{-1}, the SAXS intensity initially (t = 5.5 min) shows growth in the direction orthogonal to flow; as time progresses, the growth is primarily in the flow direction. The SAXS pattern associated with the earliest signs of crystallinity at an extension rate of 0.3 s^{-1} is also rather unusual, where the SAXS intensity initially shows a bimodal distribution at t = 2.2 min, then grows in the transverse direction at t = 5.6 min, and ultimately becomes increasingly concentrated along the direction of flow towards the end of the experiment. At the highest extension rate of 1 s^{-1}, crystallization is detected at very early times (t = 0.67 min). Interestingly, a unimodal intensity distribution with SAXS peaks along the flow direction at early times evolves into a distinct bimodal distribution with peaks at an angle away from the flow axis,

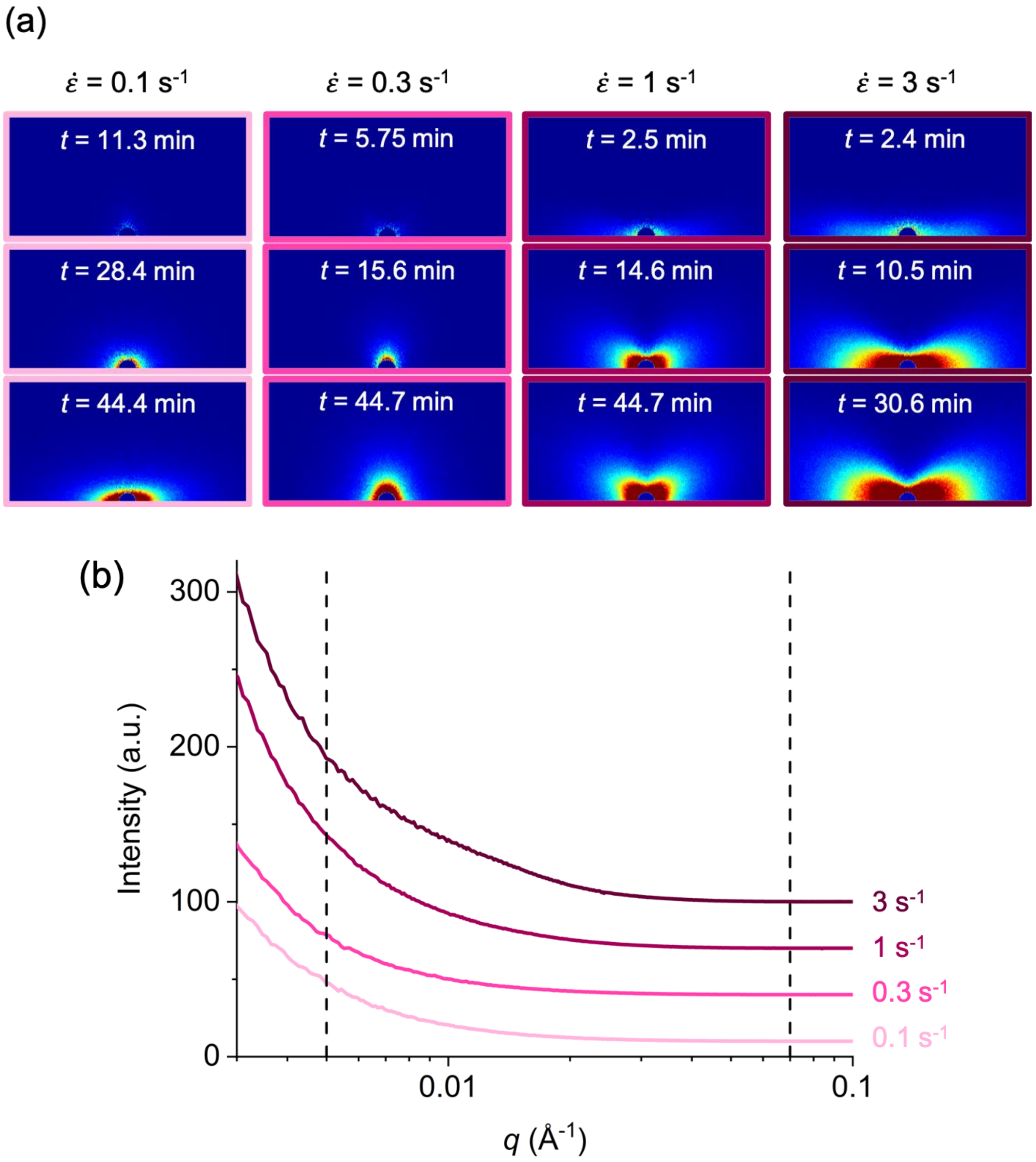

Figure 5.5: (a) Representative SAXS patterns from experiments at T_c = 112 °C and ε_H = 2 under multiple extension rates. Flow direction is horizontal. (b) Azimuthally averaged scattering intensity as a function of scattering vector, extracted from images at the end of the experiment. Dotted lines indicate the low and high q cutoffs (0.005 Å^{-1} and 0.07 Å^{-1}, respectively) used in the SAXS invariant calculation.

analogous to the experiment at T_c = 112 °C at 1 s^{-1} (Figure 5.5a). Similar to the general behavior seen in experiments at T_c = 112 °C, the complicated evolution of crystallite morphology under different flow conditions at T_c = 110 °C is reflected in the corresponding transient $\langle P_2 \rangle$ (Figure 5.6b).

The extent of crystallization calculated from SAXS and WAXS data at T_c = 110 °C Figure 5.7 shows similar rate-dependence to the observations from experiments at T_c = 112 °C (Figure 5.2). Increasing the extension rate accelerates the crystallization kinetics and leads to higher degrees of crystallinity. More noteworthy is that lowering the crystallization temperature from 112 °C to 110 °C drastically enhances the extent of crystallization. Comparing the extent of crystallization at the same extension rate at the two crystallization temperatures shows that the values of Q/V and A_{110} at T_c = 110 °C are greater than those at T_c = 112 °C by a factor of 3 – 6 at t ~ 30 min. From a rheological perspective, the effect of temperature may be assessed through the use of appropriate time-temperature shift factors. However, a 2 °C difference is small enough that there should only be a minor difference in polymer relaxation time scale between these temperatures (shift factors for Lupolen 3020D reported by Wingstrand *et al*. indicate only a 10% difference in relaxation time between 110 °C and 112 °C).[131] Thus, there is expected to be only a very slight difference in flow strength, characterized for instance by Weissenberg number, between experiments conducted at the same rate at these two temperatures. On this basis, we attribute the faster kinetics seen at 110 °C to the strong temperature dependence generally seen in polymer crystallization, associated with barriers to both primary and secondary crystal nucleation.

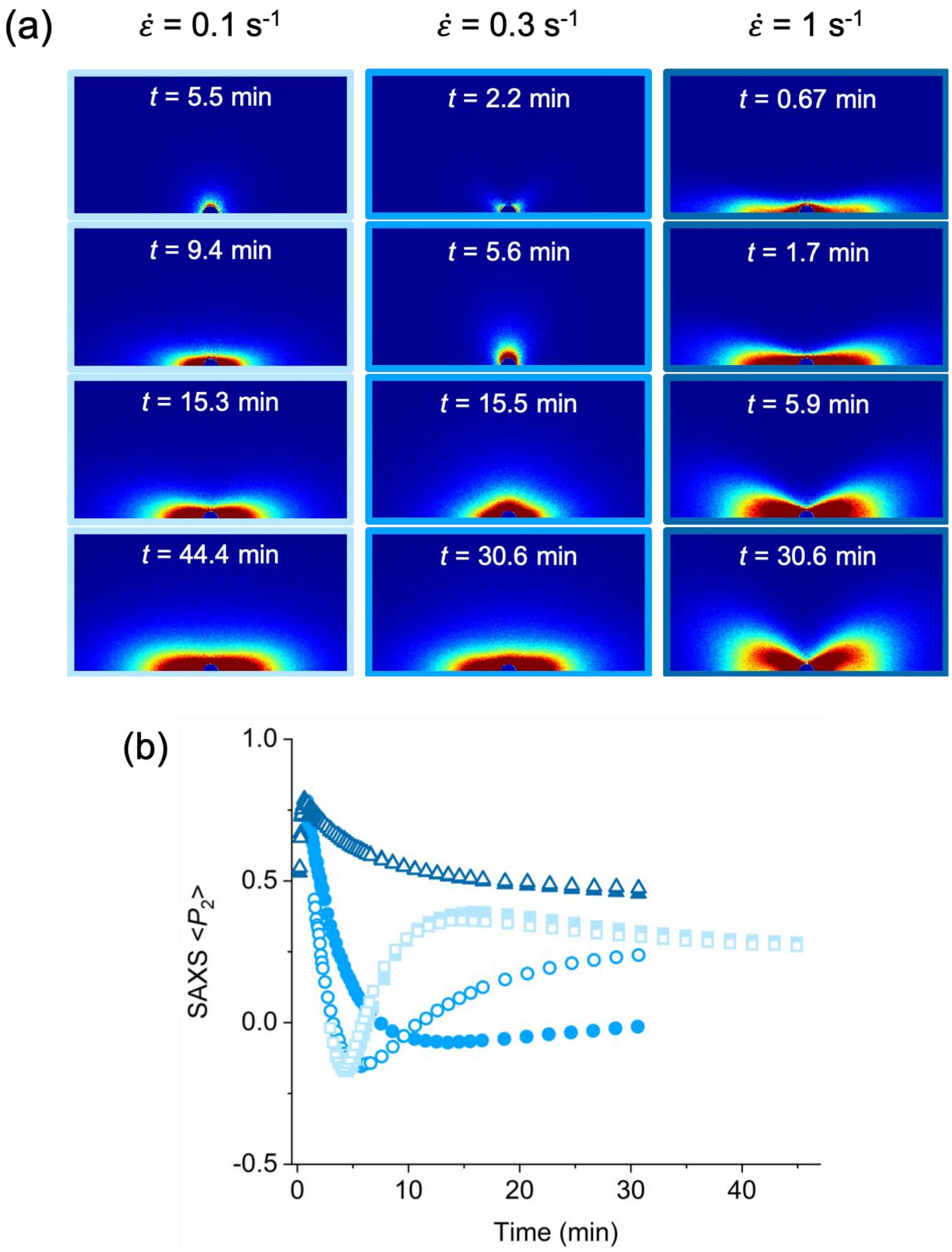

Figure 5.6: Representative SAXS images (a) at T_c = 110 °C and ε_H = 2 and the corresponding transient $\langle P_2 \rangle$ (b) reflecting the complicated evolution of lamellae under different extension rates: $\dot{\varepsilon}$ = 0.1 s^{-1} (☐), 0.3 s^{-1} (○), and 1 s^{-1} (△). Flow direction is horizontal in the scattering patterns. Open and closed symbols denote repeated experiments at the same flow condition.

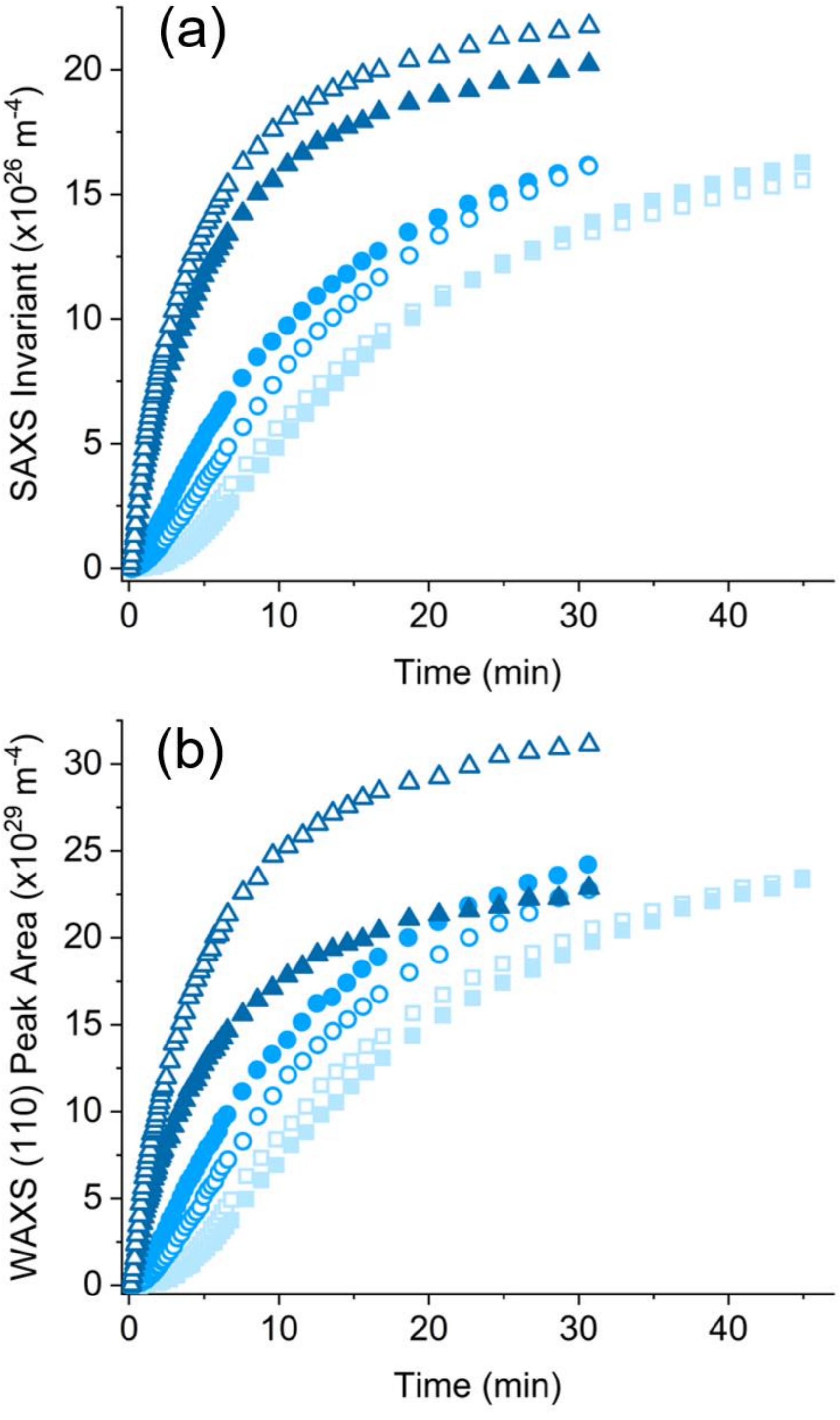

Figure 5.7: SAXS invariant (a) and WAXS (110) peak area (b) at T_c = 110 °C and ε_H = 2 for multiple extension rates: $\dot{\varepsilon}$ = 0.1 s^{-1} (□), 0.3 s^{-1} (○), and 1 s^{-1} (△). Open and closed symbols denote repeated experiments at the same flow condition.

Given that the flow strength should be comparable between experiments conducted at equivalent extension rates at 110 °C and 112 °C, one can speculate that the flow conditions might set up a particular morphological "trajectory" that is simply followed at different rates depending on the intrinsic temperature-dependent rate of crystallization. In Figure 5.8, SAXS $\langle P_2 \rangle$ data are replotted as a function of SAXS invariant rather than time. This presentation highlights strong underlying similarities in how morphology evolves as a function of crystallinity, reflected in the shape of the $\langle P_2 \rangle$-invariant profiles, depending on different flow conditions. The correspondence is not perfect; for instance, strong similarity is found between the trajectory observed at T_c = 112 °C, $\dot{\varepsilon}$ = 3 s^{-1} and T_c = 110 °C, $\dot{\varepsilon}$ = 1 s^{-1}, but not between the trajectories for 1 s^{-1} at both temperatures. Closer resemblance is found at the lower rates, as can be more clearly seen in Figure 5.9, which presents a side-by-side comparison of representative SAXS patterns at T_c = 110 °C and 112 °C along with $\langle P_2 \rangle$ plotted at selected SAXS invariant values. When the extent of crystallization induced in the sample is comparable, we observe similar features appear on the SAXS images and in the trends of the $\langle P_2 \rangle$-invariant profiles. Based on this observation, it may be reasonable to extrapolate the expected morphology in experiments at T_c = 112 °C beyond the available time frame, such that the SAXS patterns at T_c = 112 °C would be expected to evolve with further crystallization along the lines seen at T_c = 110 °C for larger Q/V values.

In contrast to the highly unconventional SAXS images observed in these short-term flow experiments, the corresponding WAXS patterns show no signs of unexpected orientation behavior. Figure 5.10 presents WAXS patterns observed at the end of these experiments; patterns at intermediate times show similar qualitative features, with only an increase of diffracted

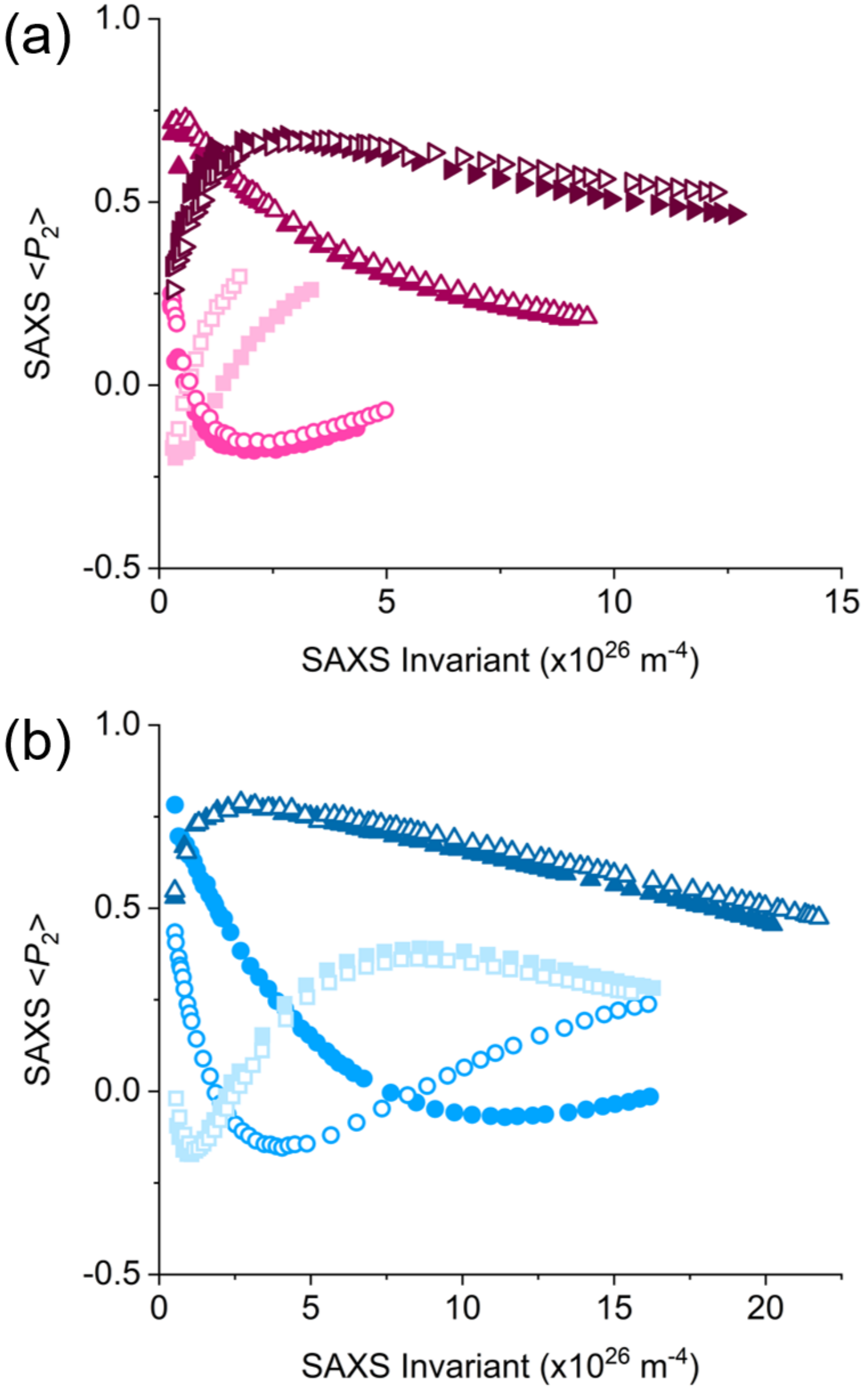

Figure 5.8: Change in SAXS ⟨P_2⟩ as monitored as a function of the SAXS invariant from experiments at T_c = 112 °C (a) and T_c = 110 °C (b) for different extension rates: $\dot{\varepsilon}$ = 0.1 s^{-1} (□), 0.3 s^{-1} (○), 1 s^{-1} (△), and 3 s^{-1} (▷). Open and closed symbols denote repeated experiments at the same flow condition.

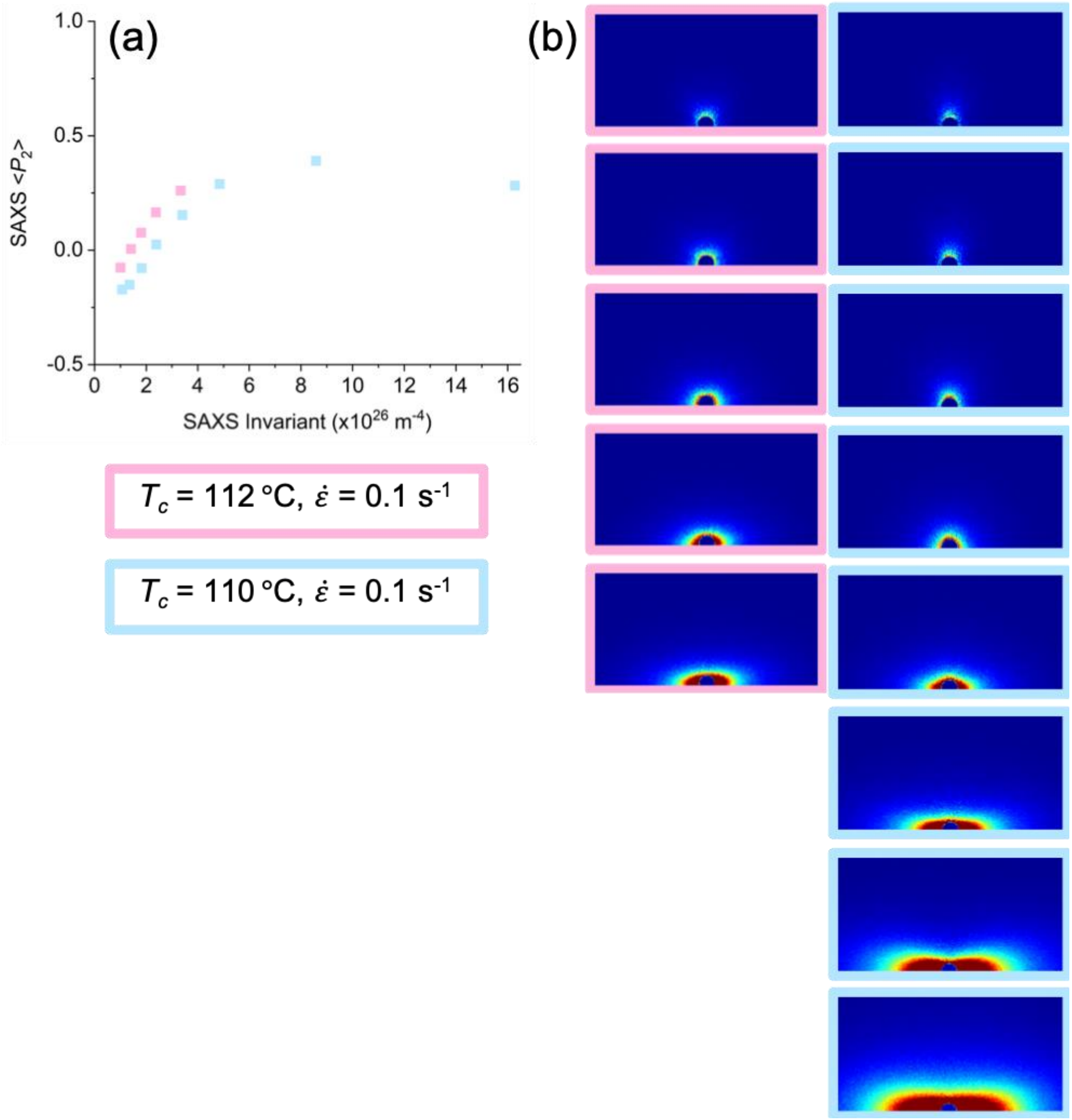
(a)
1.0
0.5
0.0
-0.5
SAXS <P_2>
0
2
4
6
8
10
12
14
16
SAXS Invariant (x10^{26} m^{-4})
T_c = 112 °C, $\dot{\varepsilon}$ = 0.1 s^{-1}
T_c = 110 °C, $\dot{\varepsilon}$ = 0.1 s^{-1}
(b)

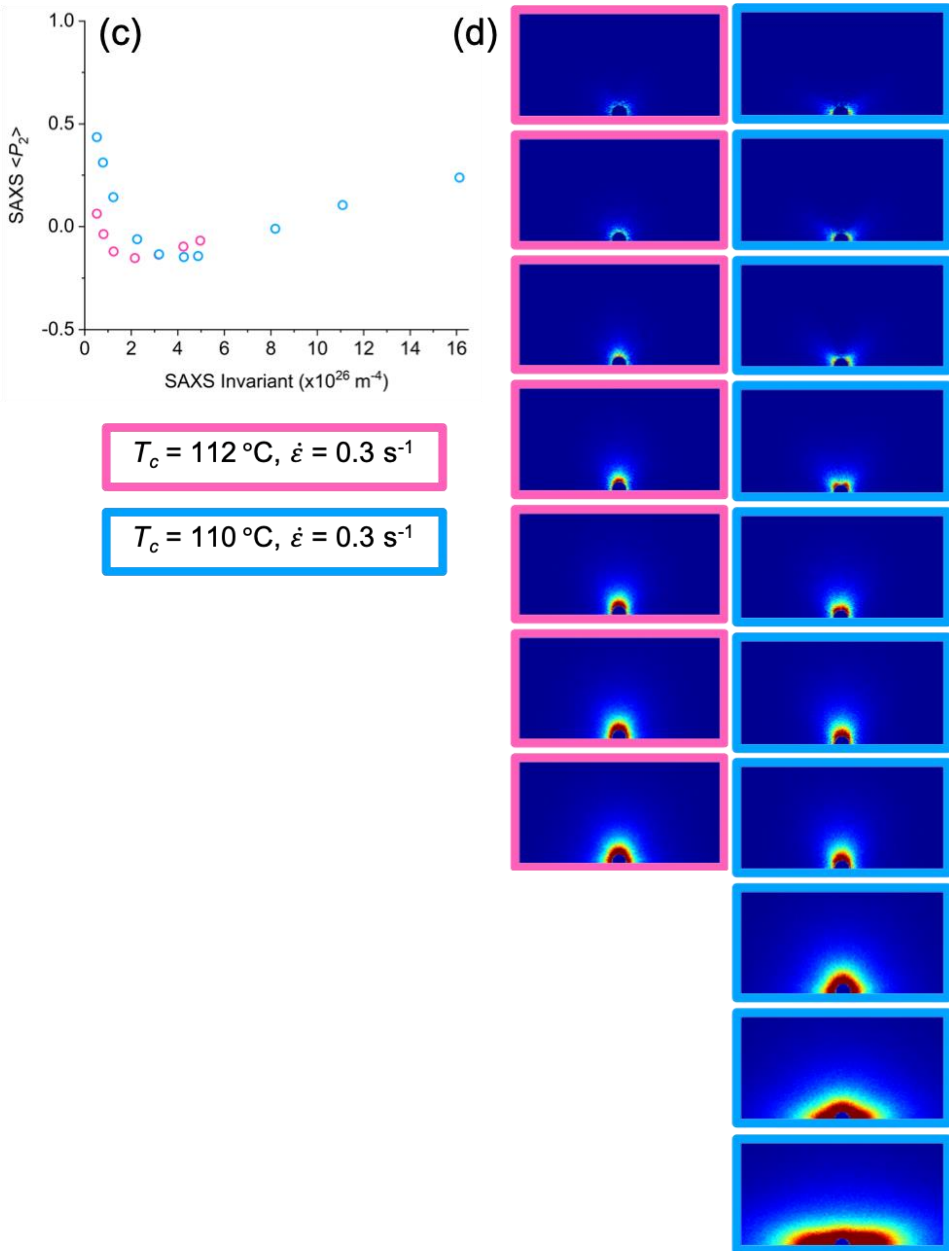
(c)
(d)
SAXS <P2>
1.0
0.5
0.0
-0.5
0
2
4
6
8
10
12
14
16
SAXS Invariant (x10^26 m^-4)
Tc = 112 °C, ε̇ = 0.3 s^-1
Tc = 110 °C, ε̇ = 0.3 s^-1

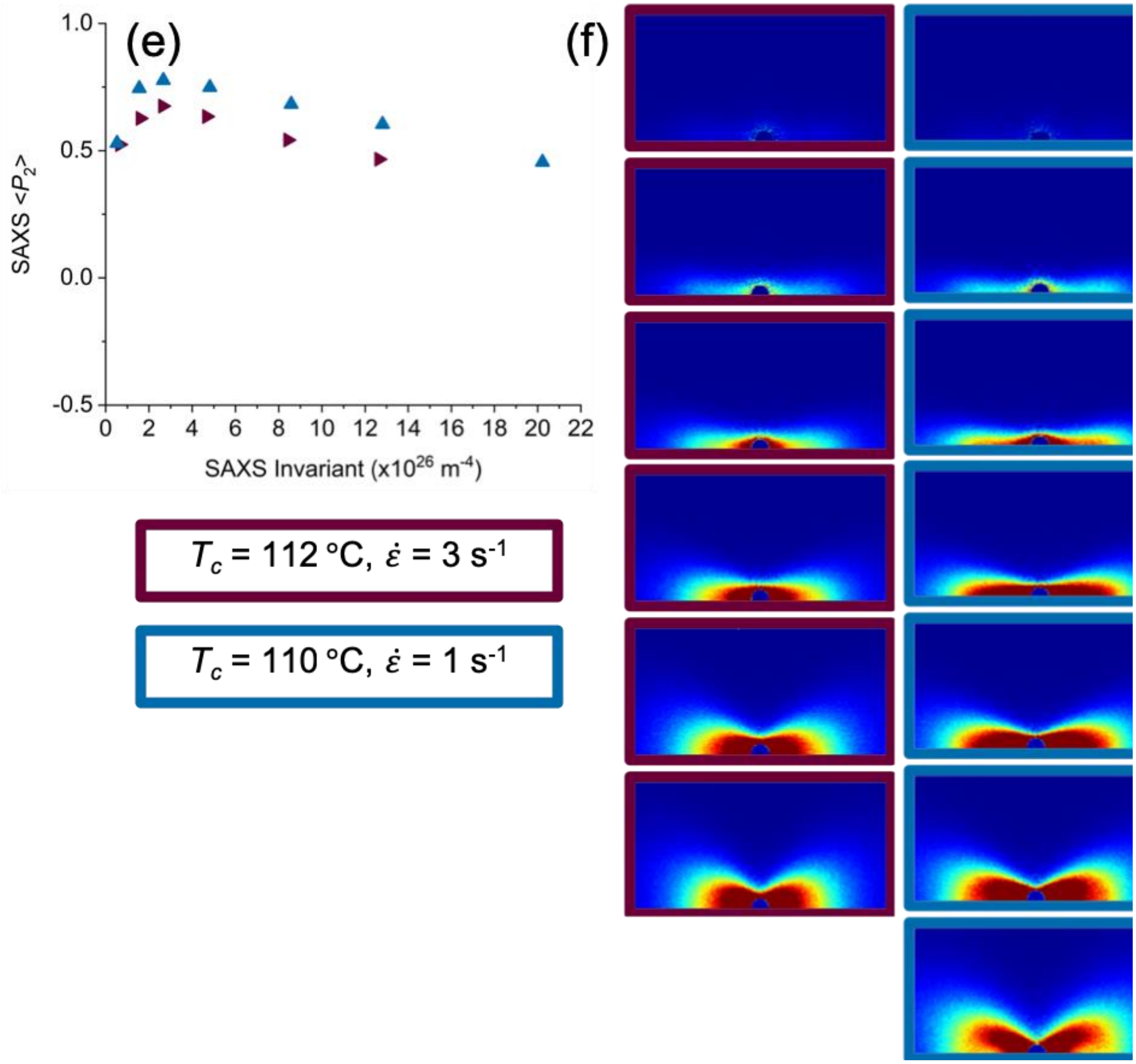

Figure 5.9: Selected values of $\langle P_2 \rangle$ at similar SAXS invariant values from experiments at T_c = 110 °C and 112 °C (a), (c), and (e) and the respective SAXS patterns (b), (d), and (f).

intensity from the developing crystalline phase. Diffraction from the (110) and (200) crystalline peaks becomes stronger, and the amorphous halo is suppressed as the extension rate increases, reflecting the higher final degree of crystallinity reflected in Figure 5.2 and Figure 5.7. For all flow conditions, the strong (110) diffraction in the transverse direction confirms that that c-axis of the crystal unit cell is aligned along the flow direction, indicative of the expected chain alignment/stretching along the flow direction. At extension rates above 1 s^{-1}, the splitting in the (110) diffraction peak provides evidence of lamellae twisting as they grow outwards.[138] These observations, including a transition to twisted lamellae under stronger flow conditions, are in accordance with those seen by Wingstrand *et al.* in their study of LDPE crystallization upon quenching after application of uniaxial flow. They found a strong correlation between anisotropy in *ex situ* patterns and the stress at quench of LDPE filaments.[131] In their work, however, the SAXS patterns consistently show strong indication of oriented crystallization that is populated by lamellae with the normal direction parallel to the direction of elongation. At higher applied stresses, the SAXS patterns are characterized by a “tear drop” shape that indicate the presence of intertwined lamellae resulting from interlocking of side branches.[139] The twisted lamellae structure was further supported by the corresponding WAXS pattern that displayed split (110) peaks concentrated in the direction parallel to flow.

What accounts for the unusual morphological features reflected in the SAXS patterns observed in these short-term flow/isothermal crystallization experiments? Noting that certain features in some of these patterns (specifically bimodal populations of crystallite orientation) resemble observations found in polymers deformed in the solid state, we have considered the possibility that the morphological evolution during crystallization is affected by additional

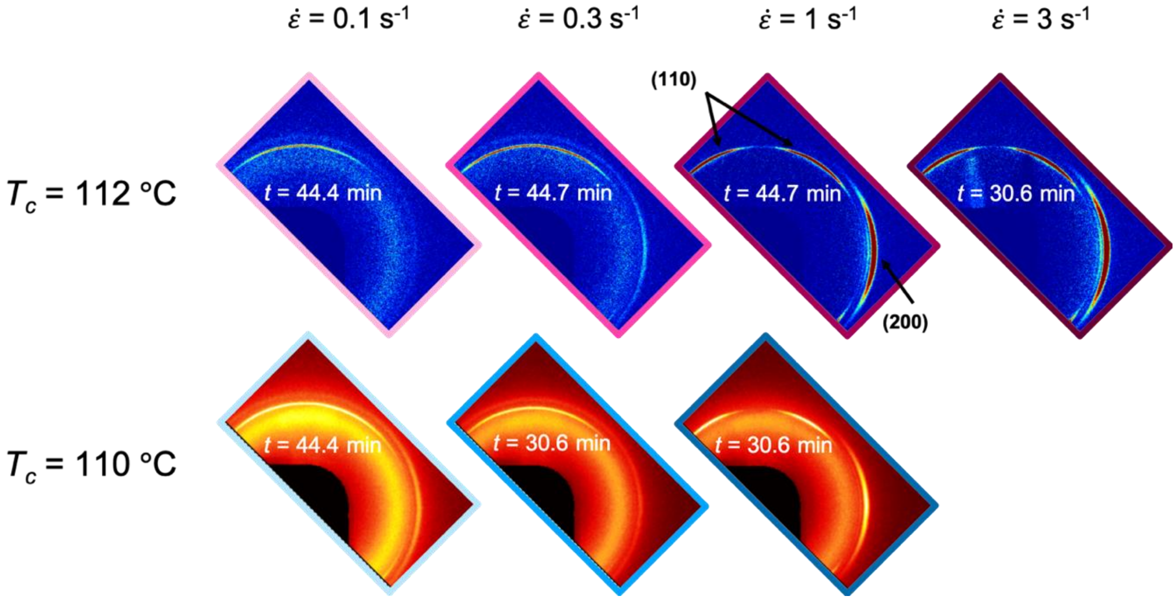

Figure 5.10: Final WAXS patterns at the end of experiments at T_c = 112 °C and 110 °C at ε_H = 2 under multiple extension rates. Flow direction is horizontal.

deformation due to volume change as crystallization proceeds in a sample constrained to have a fixed length. However, this explanation is not satisfactory on several fronts. First, the volume change during crystallization is quite small, so that any effect of these lines should involve only small strains. Solid state deformation conditions that lead to bimodal SAXS patterns should also be manifested in WAXS observations, while here we observe highly conventional behavior in WAXS. Finally, prior flow-induced crystallization studies on other polymers using similar methods have never revealed SAXS behavior of this sort (Chapters 3 and 4).[95] Instead, it appears that the nature of early stage crystallites in these experiments is fundamentally different from the chain-folded lamellar morphologies typically associated with crystallization. This is illustrated in Figure 5.11, which demonstrates that microstructures that form during isothermal crystallization at 112 °C occur on different length scales than those of crystallites in quenched samples. *Ex situ* SAXS patterns show clear indication of lamellar diffraction that arises due to periodicity in lamellar structures. In addition, samples that are quenched ~45 min after isothermal crystallization upon deformation (Figure 5.11b) and immediately following flow cessation (Figure 5.11c) show similar anisotropic SAXS peaks, but the intensity in the former is more broadly distributed relative to that in the latter. This suggests that the crystallization behavior in the melt, given sufficient time to crystallize isothermally, is convoluted by the interplay between orientation of chains due to flow and relaxation of short chains. This may also reflect the fact that crystallization in branched polymers is complicated by frustration associated with chain branching. It is likely that crystallites formed at high temperatures in these isothermal experiments preferentially incorporate sections of molecules that are free from branching.

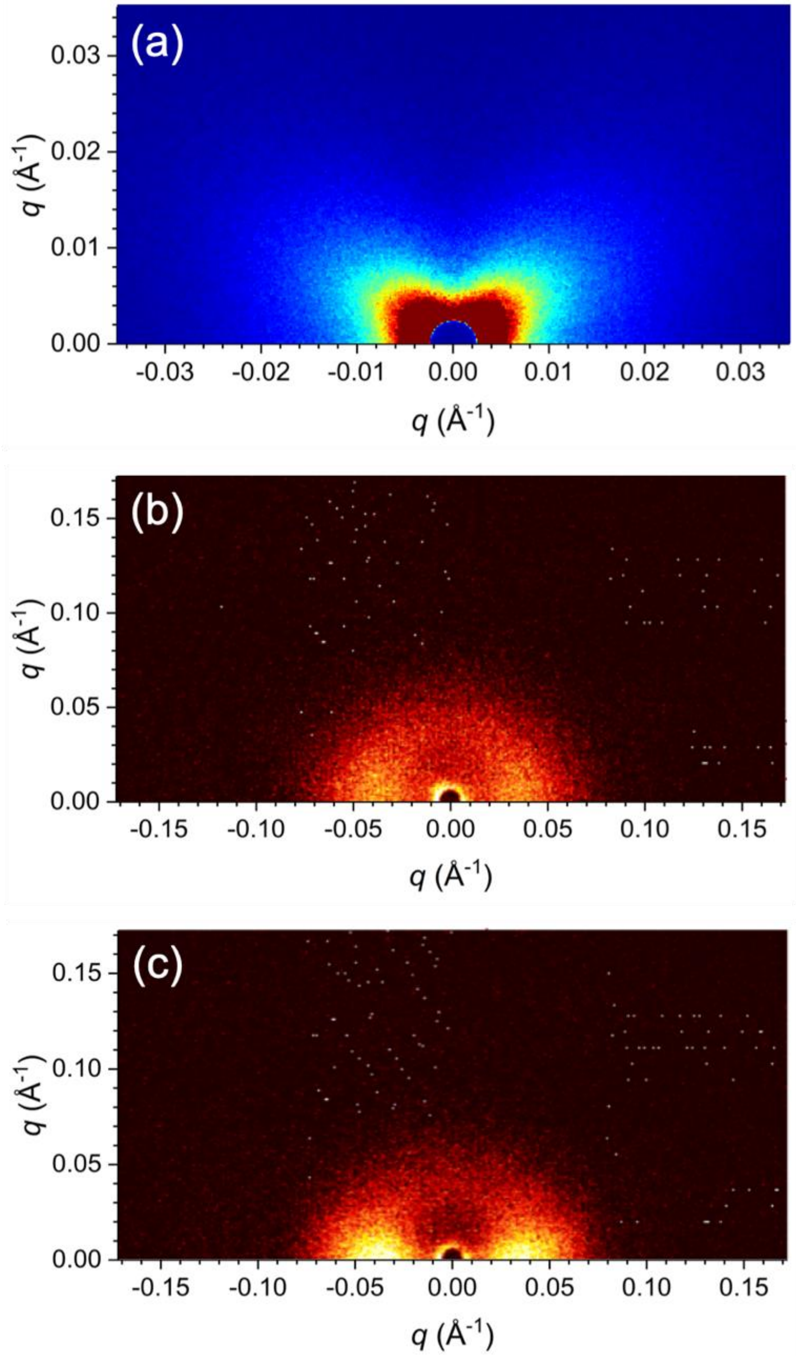

Figure 5.11: SAXS patterns (with q scale bars) from experiments conducted at T_c = 112 °C, $\dot{\varepsilon}$ = 1 s^{-1}, and ε_H = 2. Applied flow is in the horizontal direction. The sample at the end (t ~ 45 min) of isothermal crystallization at 112 °C (a) is quenched to ambient temperature by opening the oven for *ex situ* SAXS measurements (b). The image in (c) is from a quenched sample that is cooled immediately after the application of flow.

5.3.2 Continuous Flow

All results presented to this point have involved Hencky strains no larger than 2. As noted in Section 5.2.3, attempts to access higher strains in experiments at 112 °C all failed, owing to necking in the sample that led to its rupture. However, higher strain experiments were possible at 110 °C, where it was observed that crystallization had already been initiated prior to the conclusion of the flow. To explore these phenomena, a different "continuous flow" protocol was used with much more rapid data acquisition, to characterize structure development during and immediately following flow. The observed SAXS and WAXS patterns reveal radically different morphology from that observed following short-term flow. Figure 5.12 illustrates the structural evolution of a sample during flow and up to 20 s after flow from an experiment at T_c = 110 °C, ε_H = 3, and $\dot{\varepsilon}$ = 3 s^{-1}. At the beginning of flow (ε_H = 0), the null scattering pattern in SAXS results from the background subtraction, while the WAXS pattern is characterized by an isotropic amorphous scattering halo. At 0.93 s after flow (ε_H = 2.8), the first sign of shish appears in SAXS as a vertical streak. This is accompanied by a weak but clear (110) diffraction in WAXS that is highly concentrated in the direction perpendicular to flow, indicating a strong preferential alignment of the c-axis along the flow direction. After the application of flow, subsequent growth of kebabs is manifested as the growth in SAXS intensity concentrated in the flow direction; in WAXS, the (110) diffraction becomes stronger, accompanied by the (200) reflection that is also highly concentrated perpendicular to the flow axis.

Similar patterns indicative of a shish-kebab morphology are consistently produced during experiments at extension rates ranging from 0.15 s^{-1} to 3 s^{-1}. Only at the lowest rate studied (0.1 s^{-1}) was no crystallization detected during flow. Where crystallization occurs, the first

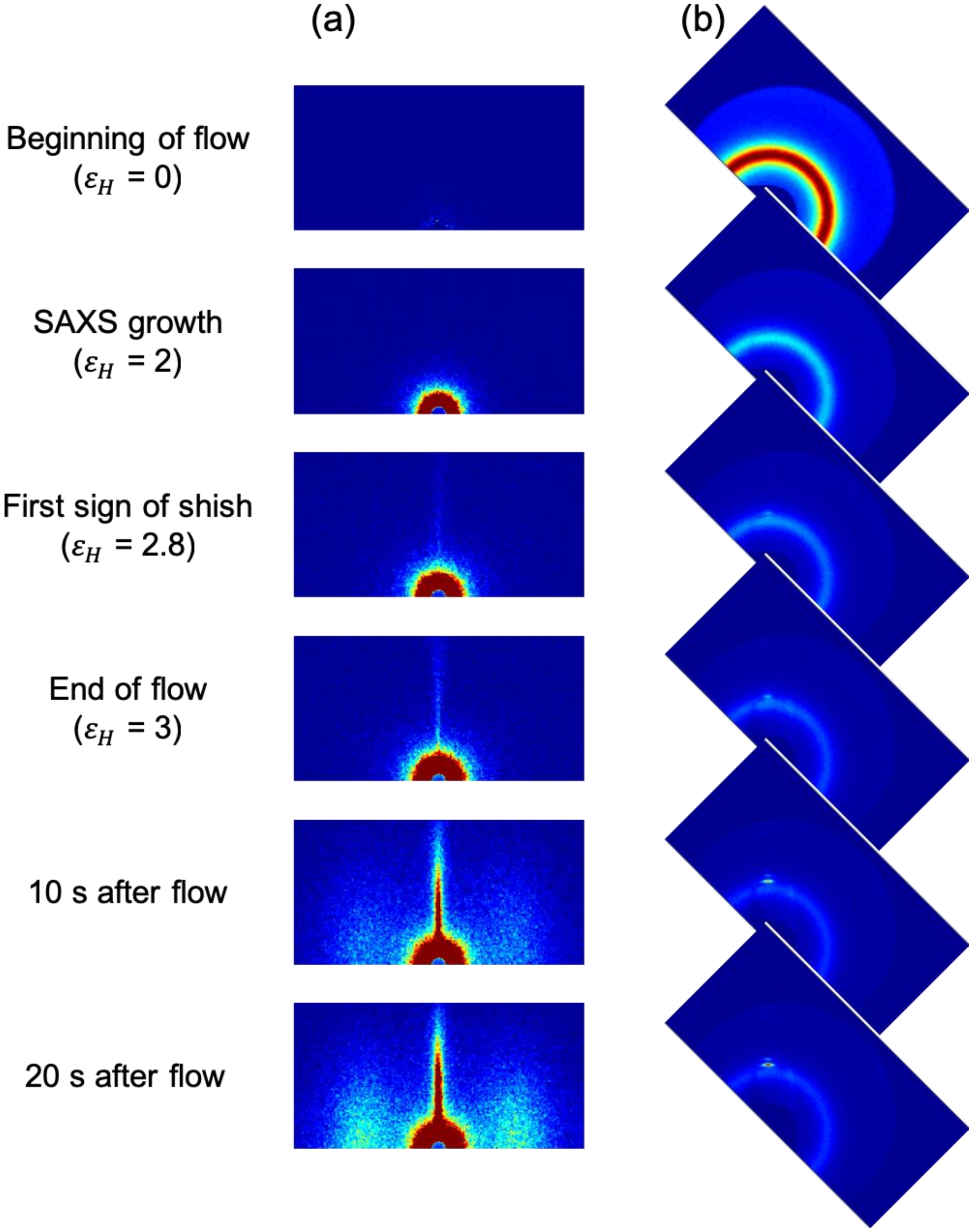

Figure 5.12: Representative SAXS (a) and WAXS (b) patterns from continuous flow experiment at T_c = 110 °C, $\varepsilon_H = 3$, and $\dot{\varepsilon} = 3\ s^{-1}$. Flow direction is horizontal. SAXS patterns are background-subtracted using the image taken immediately prior to flow inception adjusted for change of sample thickness during flow. WAXS patterns are background-corrected by subtracting scattering contributions from air and from the instrument without any sample. The decreasing sample thickness during flow leads to an overall decrease in scattered intensity.

appearance of shish similarly occurs only towards the end of flow at $\varepsilon_H \geq 2.8$. The onset strain at which the first signs of shish are detected is indicated in a plot of transient extensional viscosity measured simultaneously during the application uniaxial extension in these experiments (Figure 5.13). Well before the onset of detectable crystallinity, the extensional viscosity departs from the linear viscoelastic prediction (obtained using the relaxation spectrum and time-temperature shift factors provided by Huang *et al*.[132] The LDPE melt shows significant strain hardening under all extension rates explored in this work, even at the lowest rate of 0.1 s^{-1} where no crystallization during flow was detected. This is typical of LDPE, in which it is broadly understood that the branched chain architecture is responsible for the strain hardening behavior. Although a sharp increase in extensional viscosity has been used to determine the onset of crystallization in some flow-induced crystallization studies,[26,43,47] such an upturn may not necessarily be a reliable indicator of crystallinity during flow depending on the polymer. And, in the present case, the detectable onset of crystallization late in the flow is not accompanied by any discernable change in behavior of the associated mechanical response.

It is quite striking that subtle differences in flow conditions in these experiments lead to distinct dissimilarities in the final morphology. Lowering the temperature by two degrees to T_c = 110 °C is sufficient to allow successful experiments to higher strains (Hencky strain of 3 rather than 2), which, in turn, leads to the onset of crystallization *during* flow with the associate transformation to highly characteristic shish-kebab morphologies. Indeed, we speculate that the *lack* of any crystallization during flow in experiments to higher strains at the slightly higher temperature of 112 °C is responsible for the necking failure of the stretched sample. That is, we believe that mechanical reinforcement associated with the developing crystallinity stabilizes the

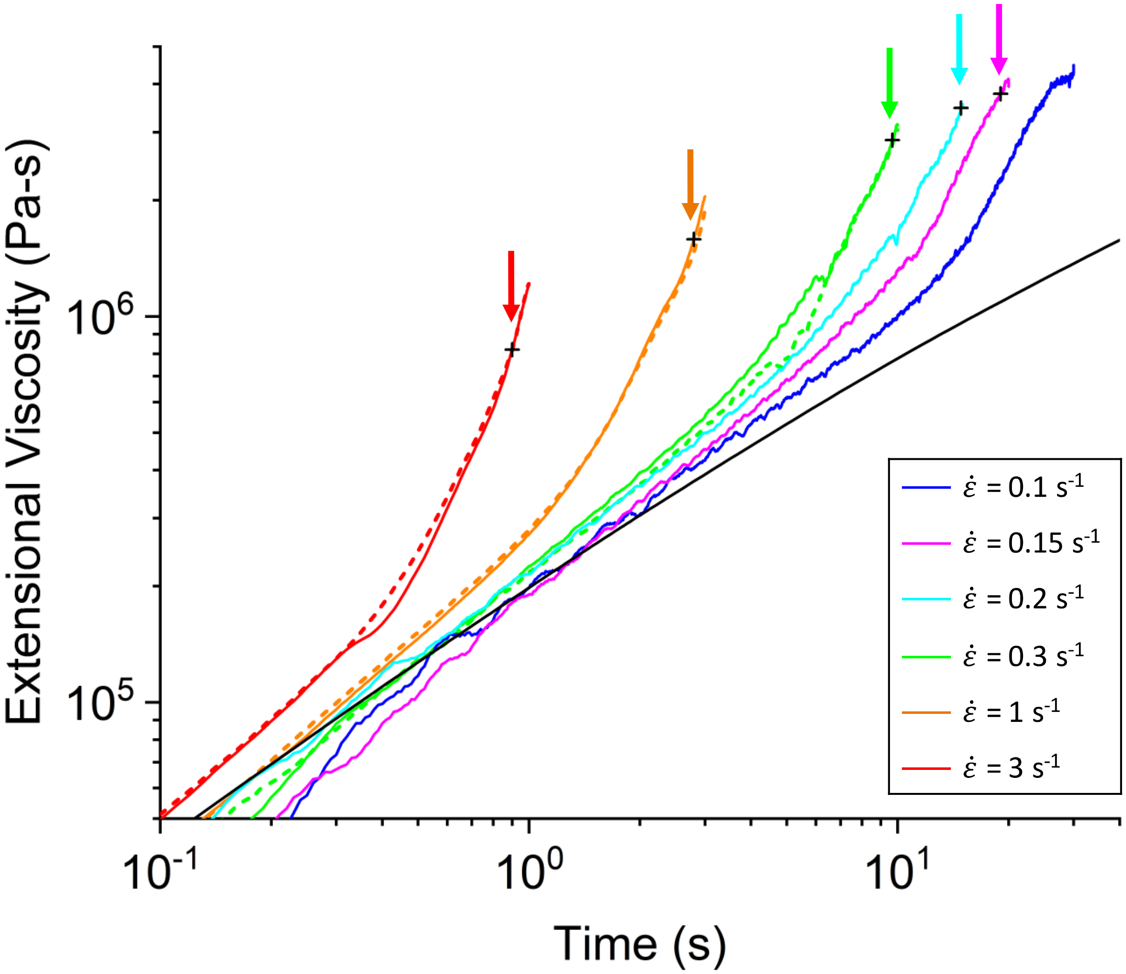

Figure 5.13: Transient extensional viscosity of LDPE at T_c = 110 °C under various extension rates. Solid and dotted lines indicate repeated experiments. The symbol (+) refers to the time point which the first sign of shish is detected in SAXS.

sample in higher strain experiments at 110 °C. The drastic differences in crystallization behavior resulting from such narrow parameter space are summarized in Figure 5.14, where the extent of crystallization developed during flow in the experiment at $\varepsilon_H = 3$ is significantly higher than the degrees of crystallinity from short-term flow experiments at early times. Also, the *Q/V* values at 20 s after flow ($t = 0.33$ min) from continuous flow experiments are reached in short-term flow experiments at much later times separated by orders of magnitude.

Figure 5.14 also shows the profound morphological transition found when crystallization is initiated during the flow. We hypothesize that a shish-kebab morphology may in fact be an indicator that crystallization occurs during flow. In other words, under short-term flow conditions where crystallization is not detected during the application of flow, it may not be possible to observe such extreme morphology. Certainly, the range of SAXS and WAXS behavior found here under short-term flow conditions do not resemble that associated with highly aligned shish-kebab morphologies at all. Earlier studies of flow-induced crystallization monitored using *in situ* x-ray scattering methods following a pulse flow protocol reported evidence of shish-kebab morphology after the cessation of intense shear.[57,58,140] However, the large time resolution window of the employed scattering methods relative to the short shear duration imposes practical limitations to probe the structural change *during* the application of flow. This implies that the shish-kebab features reflected in SAXS and WAXS patterns may have been nucleated during the application of shear rather than following deformation. More recent experimental studies that report direct evidence of shish-kebab morphology using SAXS/WAXS measurements show that such extreme morphology is developed only when crystallization is induced during flow.[59,70,72] To further test the hypothesis of whether shish-kebab structures can

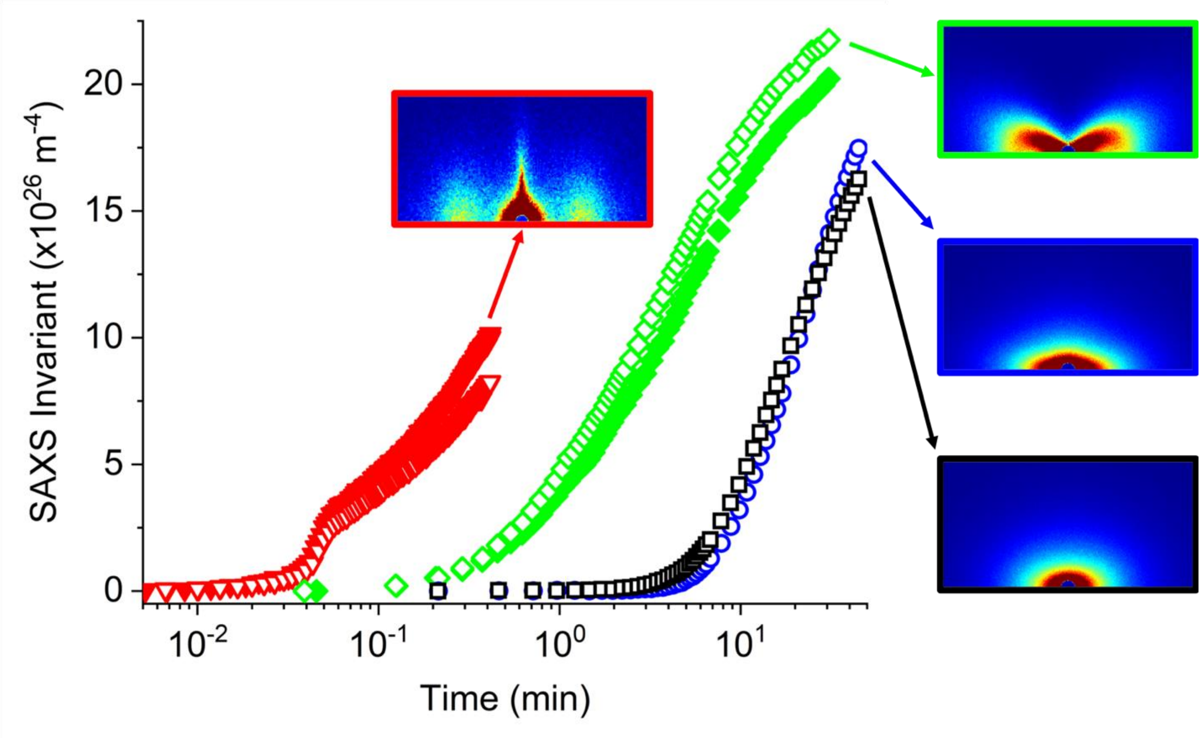

Figure 5.14: SAXS invariant over time from short-term and continuous flow experiments at T_c = 110 °C and $\dot{\varepsilon}$ = 1 s^{-1} stretched to different Hencky strains: ε_H = 1 (□), 1.5 (○), 2 (◇), and 3 (▽). Open and closed symbols denote repeated experiments at the same flow condition.

be induced only when crystallization occurs during flow, it would be necessary to conduct similar experiments under temperatures and flow conditions spanning a wider range, as will be discussed in the following chapter.

5.4 Conclusion

In summary, we employed *in situ* SAXS and WAXS measurements to probe the crystallization behavior of LDPE under two different flow protocols. Under the short-term flow protocol, in which no crystallization is detected during flow, SAXS images from samples subjected to various extension rates at $\varepsilon_H = 2$ revealed a diverse and complex evolution in the crystallite morphology and orientation, while WAXS patterns showed conventional features indicative of oriented crystallization, including their rate dependence. Increasing the applied strain to $\varepsilon_H = 3$ led to initiation of crystallization during the flow, and produced fundamentally different SAXS patterns reflecting a shish-kebab morphology and WAXS patterns that showed extreme alignment of the c-axis along the direction of extension. A rigorous quantitative analysis was performed to quantify the extent of crystallization and orientation distribution of crystallites. Analyzing the orientation distribution as a result of the crystallization induced by flow at different temperatures offered insight into anticipating the morphological evolution beyond the experimental time frame. A direct comparison between the crystallization behavior from short-term and continuous flow experiments demonstrated that the extent of crystallization produced from crystallization during flow is significantly higher than that in short-term flow experiments at early times. Further, we hypothesize that shish-kebab morphology can be formed only when crystallization is induced during flow; otherwise the absence of crystallinity during the application of flow leads to various unusual crystallite morphologies that are manifested quite differently than anisotropic SAXS peaks associated with stacked semi-crystalline lamellae.

Chapter 6

Flow-Induced Crystallization of High-Density Polyethylene and Beyond: Reflections and Outlook on FIC

6.1 Introduction

In Chapter 5, we found that crystallinity induced during flow in an undercooled low-density polyethylene (LDPE) melt resulted in a radically different morphology and orientation state compared to when crystallization occurred following flow. Earlier chapters on poly(lactic acid) (PLA) and isotactic poly(1-butene) (iPB), where crystallization only occurred after flow, do not show shish-kebab features in their scattering behavior. Based on these observations, we postulate that the presence of a shish-kebab structure may serve as a reliable indicator of crystallization induced *during* flow. Under this premise, flow-induced crystallization experiments conducted under the short-term flow protocol should lead to oriented crystallization with an anisotropic distribution of unit cell and lamellar orientation, reflecting flow-induced chain orientation along the flow direction, but not the distinctive morphological features in small- and wide-angle x-ray scattering (SAXS and WAXS) patterns traditionally associated with shish-kebab morphologies. This hypothesis motivates further flow-induced crystallization studies of polymer melts designed to promote crystallization either during or following flow on the same polymer.

An earlier extensional flow-induced crystallization study on high-density polyethylene (HDPE) using SAXS and WAXS measurements demonstrated that the polymer crystallizes during flow and results in a shish-kebab morphology.[95] In this work, samples were stretched to applied Hencky strain (ε_H) of 3 at various rates to explore the effect of rate on the crystallization behavior. The experimental results revealed that the onset strain at which crystallization was detected in SAXS and WAXS decreases slightly with increasing extension rate. Over a range of extension rates that spans nearly two orders of magnitude, the largest decrease in onset strain was found to be ~0.4 Hencky strain units, while the agreement in the onset strain for the first detection of crystallinity from SAXS and WAXS data at each extension rate was within ε_H ~ 0.2. In HDPE, onset strains were roughly around 2, which is significantly lower than the value of 2.8 seen in Chapter 5 for LDPE, perhaps reflecting the fact that LDPE is intrinsically more difficult to crystallize owing to its branched-chain architecture.

Using the work by McCready[95] as a foundation, here we explore crystallization in HDPE subjected to uniaxial extensional flow. *In situ* x-ray scattering measurements are conducted on samples using the same thermal history protocol as employed by McCready and Burghardt to ensure repeatability. A range of Hencky strains are applied at a fixed extension rate in an attempt to span the onset of crystallization during flow. These results are also compared to those from other flow-induced crystallization experiments to gain deeper insight into the range of crystallization behavior of a wide variety of semi-crystalline polymers subjected to extensional flow.

6.2 Experimental Methods

The material used in this work is an HDPE, grade AL55, donated by ExxonMobil. This polymer was previously studied in our group and demonstrated the capability to crystallize during uniaxial elongation. [95] For extensional flow-induced crystallization studies, pellets were compression molded into thin sheets at 180 °C for 10 minutes, then cut into rectangular strips of approximately 22 mm in length, 11 mm in width, and 0.7 mm in thickness. The linear viscoelasticity is characterized by a broad spectrum of relaxation times, reflecting the high polydispersity in the sample (data presented in Figure 7.1 of McCready Thesis[95]). The peak melting temperature (T_m) is 144 °C, as determined from a Mettler Toledo 882e differential scanning calorimeter at a heating rate of 40 °C/min.

In situ synchrotron studies were conducted using a custom instrument that has been used for a number of similar flow-induced crystallization experiments. The test platform consists of a convection oven with windows that allows x-ray access and an SER encased in the oven for applying uniaxial extensional flow. The fixture is driven by a stepper motor and is also attached to a torque transducer that collects the torque response from the material during extension, which can be related to the tensile stress in the deforming filament, and, in turn, transient extensional viscosity. For simultaneous measurement of extensional viscosity and collection of SAXS/WAXS images, this instrument was installed at the beamline at DND-CAT Sector 5ID-D of the Advanced Photon Source at Argonne National Laboratory. The energy of the incident x-ray beam was set to 17 keV, corresponding to a wavelength (λ) of 0.729 Å. Scattered x-rays were collected on Rayonix WAXS and SAXS detectors placed at a sample-to-detector distance of 0.21 m and 8.5 m, respectively. The detectors have a full resolution of 1920 x 3840 pixels (WAXS) and 3840 x 3840 pixels (SAXS), but a 2 x 2 (slow mode) or 6 x 6 binning (fast mode) was used to reduce the image size and readout time as well as to improve the signal-to-noise ratio. In the slow mode setting, 24, 18, 12, and 10 scattering images were collected at intervals of

5, 20, 60, and 120 s per frame, respectively. This operation mode was used to monitor the transient crystallization behavior in the sample following deformation, mainly in short-term flow experiments where the polymer did not crystallize during the application of flow, but also in some experiments to probe the structural evolution at extended times in samples that crystallized during flow. The exposure time was set to 0.25 s in these experiments. For samples that crystallized during the application of flow, a faster data acquisition was necessary to resolve the rapid phase transformation. To accommodate this, an exposure time of 60 ms was selected to acquire x-ray scattering patterns 2 s prior to, during, and 2 s following flow at a rate of 10 frames per second.

Short-term and continuous flow protocols were employed in this study. In both protocols, a strip of polymer was loaded onto the SER and heated to 180 °C, well above its T_m to melt crystallites and erase prior processing history. Then the sample was cooled to and equilibrated at a crystallization temperature (T_c) of 127. 5 °C, after which flow was applied. This temperature was found to yield behavior in continuous flow experiments conducted out to a strain of 3 that was comparable to behavior found by McCready at T_c = 128. 5 °C.[95] We speculate that small errors and differences in oven temperature calibration between these experiments—conducted 3 years apart—account for this difference. In short-term flow experiments, a brief pulse of extension was imposed to the undercooled melt, and subsequent crystallization was monitored using SAXS/WAXS measurements. Continuous flow experiments involved the acquisition of SAXS/WAXS patterns primarily during the application flow as the sample crystallized, in addition to before and after flow. In all experiments, flow was applied at an extension rate of 1 s^{-1} to various Hencky strains up to 3.

6.3 Results

6.3.1 Transient Extensional Viscosity

Figure 6.1 presents transient extensional viscosity measurements obtained during flow-induced crystallization experiments. The elongational viscosity under all strains overlap very well with each other, as expected for experiments conducted at the same extension rate of 1 s^{-1}. Some deviation is observed at very short times (as is often the case) in one experiment, which may be due to imperfections in sample loading or sag resulting from the long thermal history, but the data agree well after 1 s into the application of flow. Viscosity measurements from experiments at higher applied strains of 2.3 and 3 show strong strain hardening behavior that may be observed in linear, polydisperse polyolefins.[26,43,47,63] In some studies, the upturn in extensional viscosity has been used as an indicator for the onset of crystallization. While there is evidence that the viscosity upturn may indicate crystallization onset, McCready and Burghardt used simultaneous *in situ* structural characterization to demonstrate that the crystallization onset time must be assigned with caution, as extensional viscosity measurements may be complicated by nonidealities and possible experimental artifacts. [95] They did, however, document that the extent of strain hardening found in the presence of continuous flow-induced crystallization is *higher* than that found under dynamically equivalent testing (e.g. identical Weissenberg number, after time-temperature shifting) performed in the melt at higher temperatures.

6.3.2 SAXS/WAXS Image Analysis

Flow-induced crystallization experiments conducted at T_c = 127.5 °C, $\dot{\varepsilon}$ = 1 s^{-1}, and ε_H = 3 reveal that crystallization during flow leads to a shish-kebab morphology. Figure 6.2 presents a

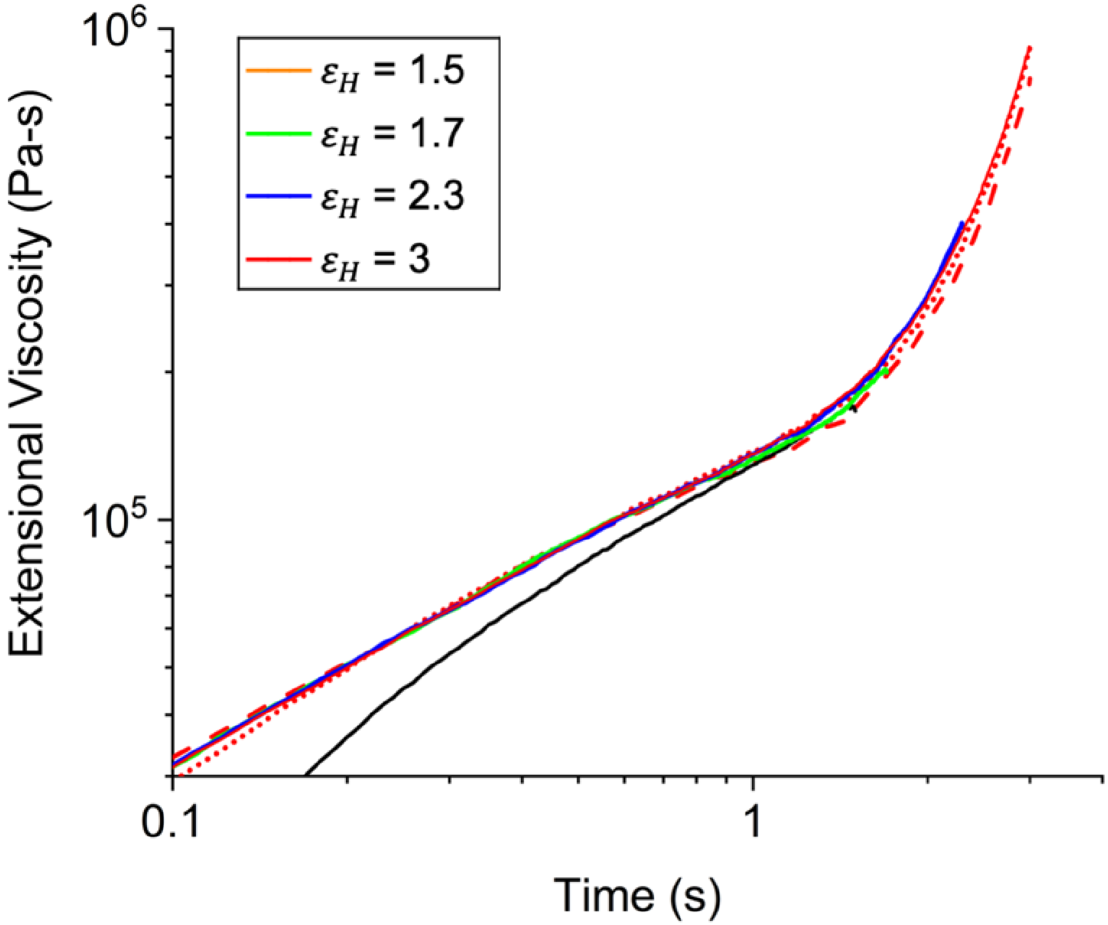

Figure 6.1: Extensional viscosity as a function of time for experiments conducted at T_c = 127.5 °C, $\dot{\varepsilon}$ = 1 s^{-1} and various Hencky strains (dotted and dashed lines indicate repeated experiments at the same flow condition)

series of representative SAXS patterns (corrected for background scattering using the method described in Chapter 5), where the first sign of a streak perpendicular to flow occurs at t = 2.01 s (t = 0 is defined here as the beginning of flow) and continues to grow both during and after the remaining flow. Such streaks in SAXS patterns are attributed to “shish” features. By ~2 s after flow (t = 5.11 s), the SAXS pattern also shows clear evidence of peaks along the stretching direction indicative of “kebabs” nucleated off of the shish structures. McCready found that the growth of this peak intensity actually begins nearly simultaneously with the growth of the streak transverse to flow.[95] The progression of SAXS patterns in Figure 2 is in qualitative agreement with those from previous continuous flow-induced crystallization experiments on the same material. In particular, the onset of crystallization at an applied strain of ε_H ~ 2, agrees with the earlier study, although it is significantly earlier than found in LDPE, described in the preceding chapter.

For experiments conducted at lower strains, below ε_H ~ 2, no crystallization is observed in the immediate aftermath of flow, so it is necessary to study behavior at longer times to explore the nature of crystallization under weaker flow conditions. Evidence of oriented crystallization due to the application of flow under various applied strains is demonstrated in SAXS and WAXS images collected towards the end (~38 min) of experiments at T_c = 127.5 °C (Figure 6.3). Under quiescent conditions, SAXS and WAXS intensities show a perfectly isotropic distribution, indicating the growth of crystalline lamellae and c-axis of the unit cell in all directions, respectively. Compared with patterns obtained after application of flow, the extent of crystallization is rather low. At the lowest applied strain of ε_H = 1.5, strong equatorial SAXS peaks reveal the formation of lamellae with normal directions pointing along the direction of

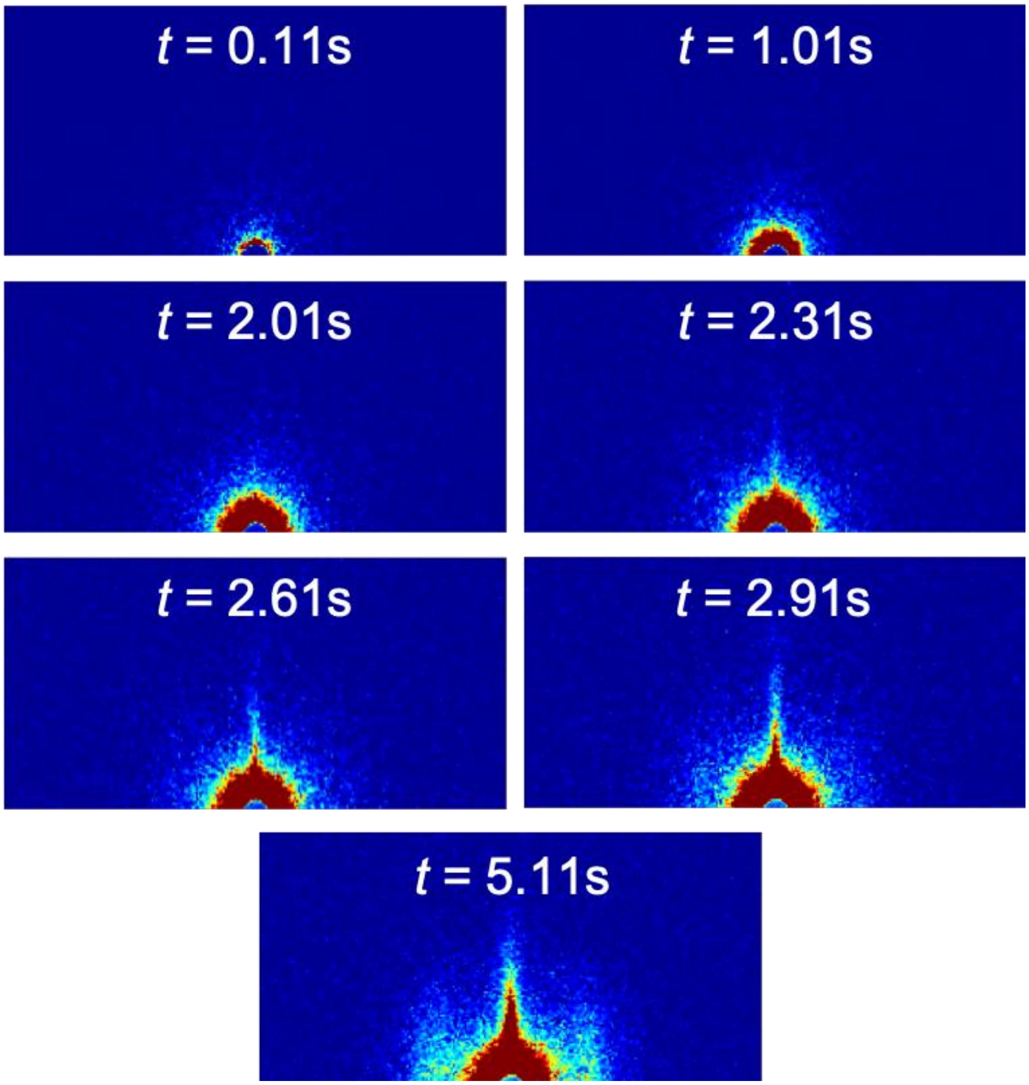

Figure 6.2: Representative SAXS patterns during and following flow at T_c = 127.5 °C, $\dot{\varepsilon}$ = 1 s^{-1}, and ε_H = 3. The beginning of flow is defined as t = 0 s. Flow direction is horizontal.

extension. This is consistent with the corresponding WAXS pattern where the diffraction from the (110) crystalline peak is more intense in the transverse direction, indicating that the c-axis of the unit cell is preferentially oriented in the flow direction. Increasing the Hencky strain to 1.7 leads to similar diffraction patterns in WAXS, but the SAXS image shows peaks along the flow direction as well as a very faint streak orthogonal to flow, conceivably suggesting the presence of a shish-kebab structure; however, the corresponding WAXS pattern does not show the highly oriented (110) peak perpendicular to flow that also accompanies shish-kebab morphologies. Scattering features associated with this extreme morphology are, however, clearly seen in experiments conducted at higher applied strains of ε_H = 2.3 and 3, as expected for strong flow conditions involving applied strains of $\varepsilon_H > 2$. In these experiments, the SAXS patterns display distinct streaks perpendicular to flow and concentrated lobes of intensities parallel to flow. In WAXS, the (110) and (220) are strongly concentrated along the meridian, indicating a very strong preferential alignment of the c-axis along the flow. These scattering patterns are in qualitative agreement with traditional shish-kebab SAXS and WAXS features. Comparison of images in experiments conducted to ε_H = 3 in Figure 6.2 and Figure 6.3 shows that, although substantial additional crystallization occurs in the 38 minutes following flow, the characteristic shish-kebab features remain.

In selected flow conditions, *ex situ* x-ray scattering images were collected on quenched samples after opening the oven to cool the melt-crystallized sample that was characterized using *in situ* SAXS/WAXS for ~38 min after flow. Figure 6.4a presents SAXS patterns of quenched samples from experiments at ε_H = 1.7 and 3 that reveal the emergence of SAXS peaks at a higher scattering vector (q) upon cooling. In both applied strains, the SAXS images show clear

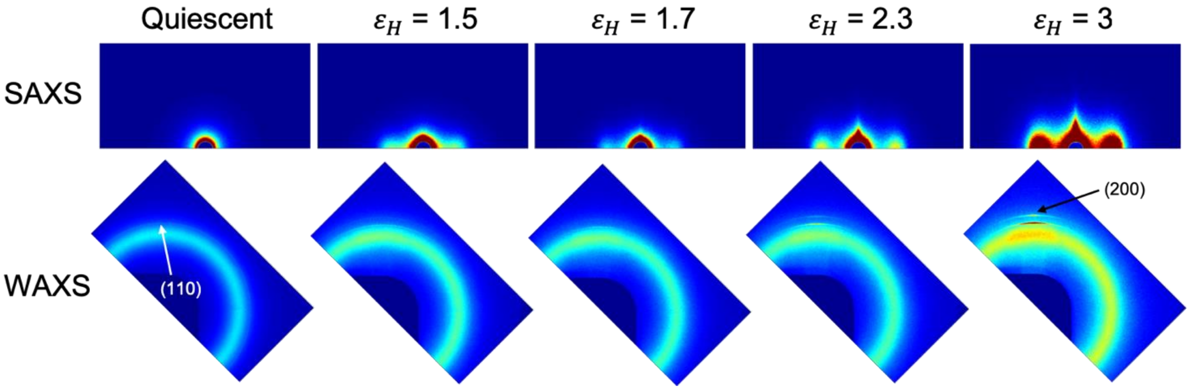

Figure 6.3: Representative SAXS and WAXS patterns from experiments at T_c = 127.5 °C at $\dot{\varepsilon}$ = 1 s^{-1} under various applied Hencky strains ~38 min after flow is applied. Flow direction is horizontal.

indication of “new” crystallites formed during the quench, together with the “old” formed at lower *q* during the preceding isothermal crystallization. The “new” peaks upon cooling dominate the over the intensity of peaks formed during isothermal crystallization at T_c = 127.5 °C (Figure 6.4b); even after 38 minutes in the melt, there clearly was plenty of polymer melt still available to crystallize upon quenching. The fact that crystallization produced by quenching leads to peaks at substantially higher *q* is consistent with expectations that thinner crystalline lamellae should grow during rapid crystallization under conditions of higher undercooling. The SAXS patterns of the quenched samples show that the new crystals continue to adopt the high orientation of the flow-induced crystals formed isothermally during/after the extensional flow, indicating that they were likely nucleated from the existing crystallites.

6.4 Discussion

While the series of scattering patterns in Figure 6.3 demonstrate a transition in the lamellar scale morphology with increasing applied strain—lamellae with normal direction along the flow direction at lower strains to shish-kebab morphology at higher strains—the main question of whether this is dictated by the absence/presence of crystallinity induced during flow remains ambiguous. Experiments at ε_H = 1.7 and of ε_H = 2.3 both seem to produce SAXS patterns corresponding to a shish-kebab structure towards the end of the observation window (Figure 6.3), but no signs of crystallization were detected during and immediately after flow in the former flow condition (Figure 6.5a), while a shish feature was apparent in the SAXS image immediately following flow in the latter (Figure 6.5b). Based on observations from Figure 6.2 that the onset of shish occurs at applied strains above 2, it is plausible that the sample stretched

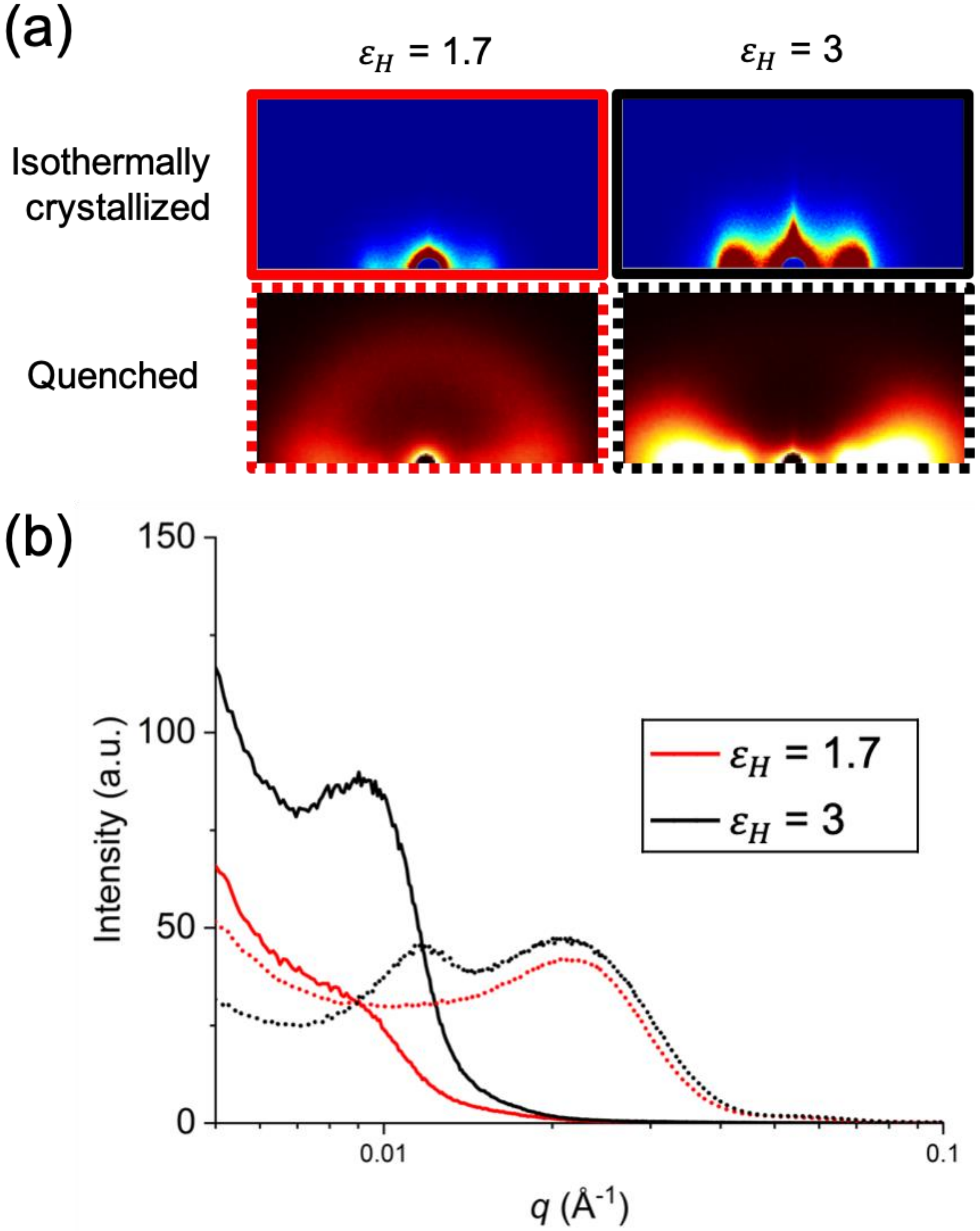

Figure 6.4: *Ex situ* SAXS patterns from experiments subjected to extensional flow at 1 s^{-1} to strains ε_H = 1.7 and 3, and then quenched to room temperature 38 min after flow. (b) Azimuthally averaged intensity profiles of isothermally crystallized samples prior to quenching (solid lines) and after the quench (dotted lines) samples.

to ε_H = 2.3 crystallized towards the end flow in the experiment, resulting in a SAXS pattern with a clear streak perpendicular to flow and peaks concentrated parallel to flow as crystallization proceeded. Contrary to this observation, the final SAXS pattern at ε_H = 1.7 may suggest the presence of shish-like structures that formed *after* the application of flow. However, the scattering feature is rather diffuse compared to that at higher applied strains and is dominated by the intensity concentrated along the flow direction, making it difficult to confirm the existence of a shish-kebab structure.

Although questions of detail remain unanswered, we notice a certain trend in the crystallization behavior. The scattering patterns from experiments in which crystallization occurred following flow (Figure 6.3; ε_H = 1.5 and 1.7) suggest that the absence of crystallinity during flow leads to oriented crystallization with lamellae normal pointing in the flow direction. On the other hand, if crystallization is induced during flow (Figure 6.3; ε_H = 2.3 and 3), the resulting structure is always a shish-kebab superstructure with shish and lamellar normal along the flow direction. In fact, this observation is in agreement with studies from the literature that utilize *in situ* synchrotron x-ray scattering to characterize extensional flow-induced crystallization. Liu and colleagues performed simultaneous *in situ* SAXS/WAXS measurements and extensional rheometry on a lightly cross-linked HDPE subjected to similar thermal histories used in our experiments.[68,69] In step strain experiments where samples were stretched to Hencky strains up to 2.5 under large extension rates of 10 s^{-1}, the authors monitored the structural evolution immediately following deformation and demonstrated that samples stretched to low strains (ε_H < 1.25) resulted in oriented crystallization at the end of crystallization (~6900 s after extension).[68] The final SAXS pattern is depicted by an anisotropic intensity distribution that is

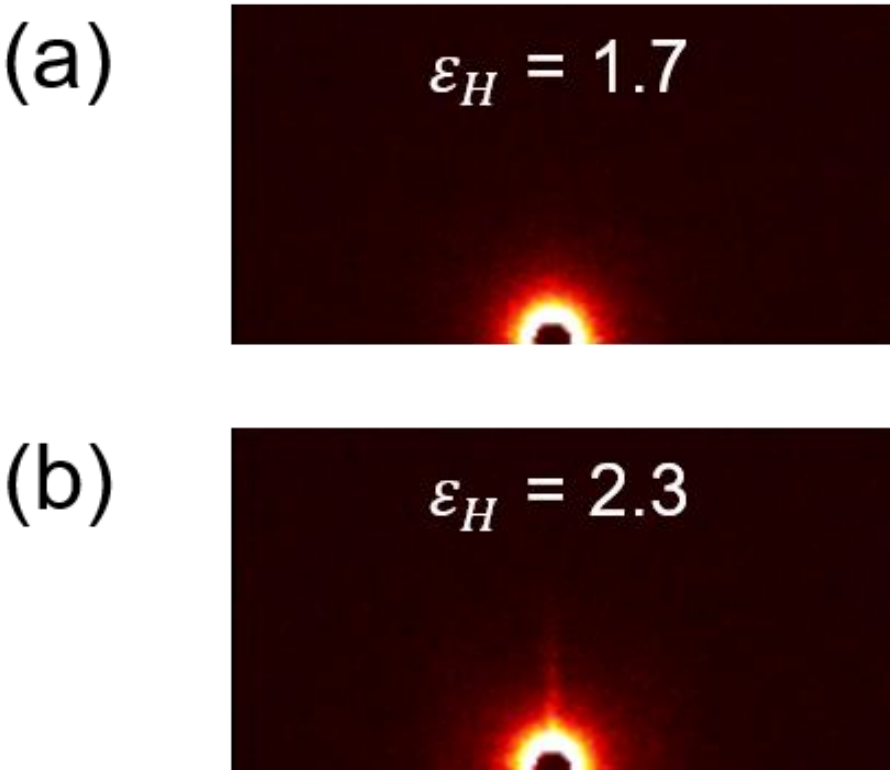

Figure 6.5: SAXS images collected immediately after flow from experiments at ε_H = 1.7 (a) and ε_H = 2.3 (b).

concentrated parallel to the direction of extension, indicating lamellar normal pointing along the flow direction. Experiments under higher strains (ε_H > 2), corresponding to the regime that resulted in strain hardening in the mechanical response, produced SAXS patterns associated with a traditional shish-kebab morphology. This work was followed by *in situ* structural characterization of the same material during extension at a strain rate of 0.02 s^{-1} and a Hencky strain of 2.8.[69] Experimental results verified that shish induced *during* flow as reflected in SAXS patterns was accompanied by strongly aligned (110) and (220) peaks along the meridian in WAXS images.

From a broader perspective, these overall observations agree with the robust trend seen across our flow-induced crystallization studies on various semi-crystalline polymers, summarized in Figure 6.6a. Short-term flow-induced crystallization experiments on PLA, iPB, and LDPE consistently led to induced anisotropy in SAXS patterns that indicated oriented crystallization with lamellar normal oriented in a preferential direction (Figure 6.6a). The corresponding WAXS images also showed anisotropic distribution in the diffraction peak intensities. While a range of lamellar scale morphologies were observed under various flow conditions, the characteristic signatures of shish-kebab morphology—SAXS streak perpendicular to flow, extremely anisotropic WAXS peaks—were not found. In continuous flow-induced crystallization experiments of LDPE where the applied flow was sufficiently strong to induce crystallization during extension, oriented SAXS patterns reflected the presence of a shish-kebab morphology (Figure 6.6b). These were complemented by WAXS patterns that showed a sharp diffraction peak perpendicular to flow, indicating strong alignment of the c-axis of the polymer crystal unit cell parallel to the direction of extension. Having studied a number of semi-crystalline polymers, the wide range of morphologies and phenomena observed across different materials is unexpected based on conventional viewpoints in flow-induced crystallization of coil-stretch transition or stretched network formation. In fact, neither of these ideas is invoked in flow-induced crystallization models that would anticipate such a broad and dissimilar behavior across different semi-crystalline polymers.

6.5 Conclusion

The morphology of melt-crystallized HDPE is strongly influenced by the absence/presence of crystallinity during flow. Short-term flow experiments in which crystallization proceeded following the application of flow demonstrated that the applied deformation leads to oriented lamellae with normal direction preferentially aligned parallel to flow. When the applied strain exceeds a Hencky strain of 2, we notice the onset of shish that serves as an indicator of crystallization developing during flow. SAXS patterns from experiments at ε_H = 2.3 and 3 reveal features associated with a shish-kebab morphology. This observation is consistent with the overall trend seen in other flow-induced crystallization studies of on PLA (Chapter 3), iPB (Chapter 4), and LDPE (Chapter 5).

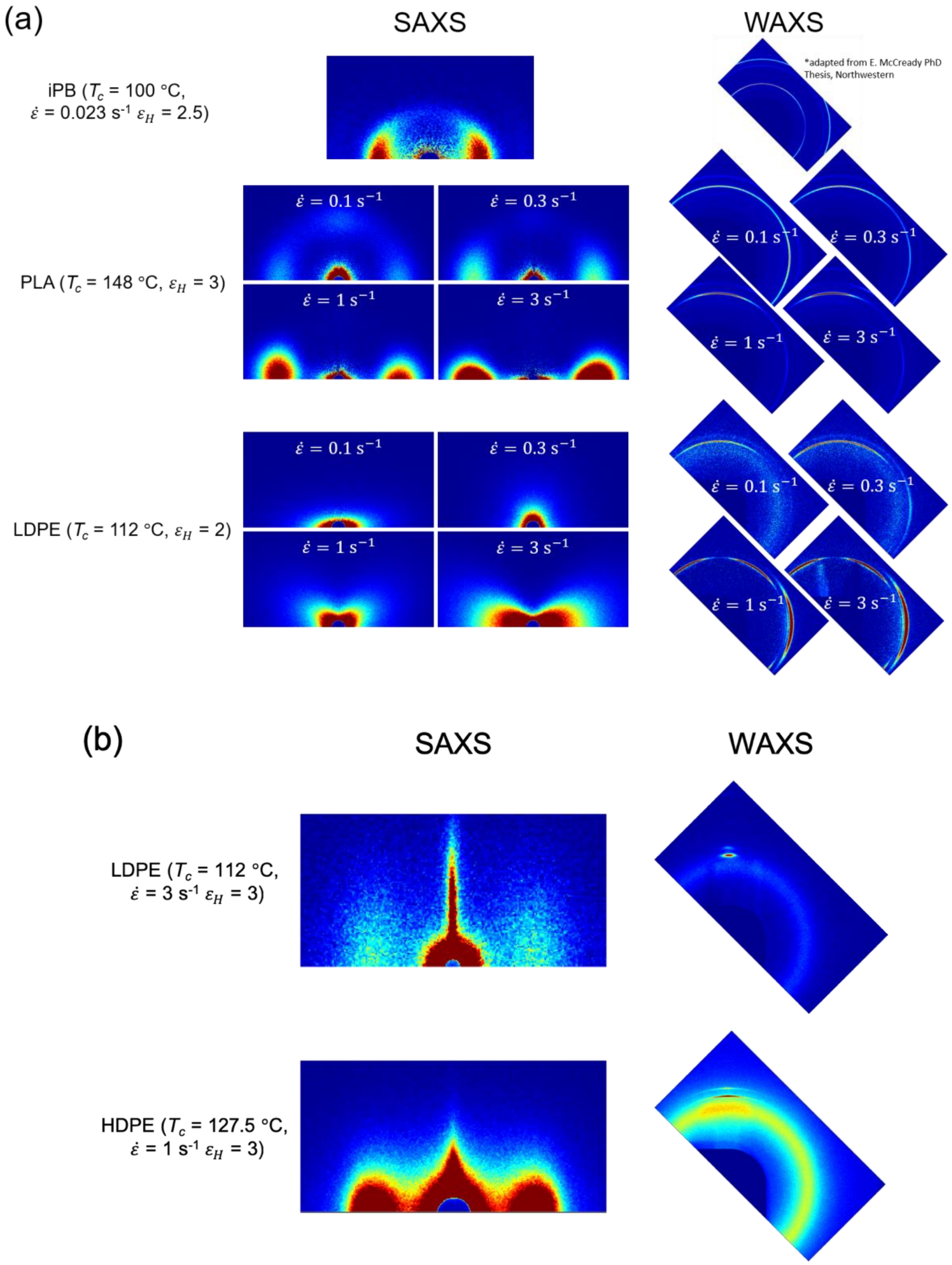

Figure 6.6: Summary of crystallization behavior observed in short-term (a) and continuous (b) flow experiments from various semi-crystalline polymers.

Chapter 7

Concluding Remarks

The work presented in this thesis was aimed to gain molecular insights into flow-induced crystallization (FIC) of polymer melts under extensional flow by capitalizing on *in situ* x-ray scattering techniques. A novel instrument was utilized to characterize the range of structures and morphologies induced by extension in a wide selection of semi-crystalline polymers, including polyolefins and bio-based polyesters. Time-resolved synchrotron-based x-ray scattering measurements provided direct information on the crystallization kinetics, developing crystallinity, and the evolving orientation distribution of crystallites. Coordinated studies of experiments and computational modeling directly tested a central assumption that underlie in flow-induced crystallization models and demonstrated the possibility of extending this general approach to different types of flow. These studies as a whole have provided an improved fundamental understanding of the phenomenon in polymers under extensional flow that has tremendous value and potential on the rational design of polymer processing and applications.

In Chapter 3, we have examined crystallization in a branched poly(lactic acid) (PLA) subjected to uniaxial extensional flow. This study has shown significant new contribution to the body of PLA crystallization literature, in which the crystallization behavior of PLA melt under extensional flow has never been reported. In general, small- and wide-angle x-ray scattering (SAXS and WAXS, respectively) data delivered consistent results for both the extent of crystallization and the degree of crystallite orientation. Increasing the extension rate at a constant applied Hencky strain generally led to faster crystallization kinetics as well as higher degrees of crystallite orientation. Similar qualitative behavior was observed with increasing the applied strain at a fixed extension rate. Unusual behavior in the crystallization kinetics and crystallite morphology was observed at intermediate extension rates and strain, which may be attributed to the complicated deformation history induced on a nonuniform sample. Overall, experimental results confirmed that accelerated crystallization kinetics is associated with higher degrees of orientation.

Chapter 4 presented designed strategies of flow-induced crystallization experiments guided by computational models. In this work, the underlying hypothesis that molecular orientation/stretching induced by flow leads to enhanced nucleation was interrogated by subjecting isotactic poly(1-butene) (iPB) to combinations of extension rates and Hencky strains that produced similar enhancements in nucleation. Experiments were designed using the model developed by Roozemond and Peters,[90] where the number density of flow-induced nuclei was calculated from the molecular stretch parameter during flow inception and following cessation, using predictions from a simplified Rolie-Poly model. Scattering data revealed accelerated crystallization kinetics and higher final degrees of orientation with increasing extension rate at a fixed Hencky strain. For experimental conditions that were expected to result in similar degree and kinetics of crystallization, discrepancy in both the kinetics and final orientation states among experiments was observed. The discrepancy between experimental data and modeling predictions do not necessarily imply that the model formulation is incorrect, considering the assumptions and simplifications applied to describe the complexities of flow-induced crystallization. Rather, this general experimental design strategy has shown great promise to be easily adopted to design flow-induced crystallization experiments employing different flow types that would lead to similar flow-enhanced nucleation.

In Chapter 5, short-term and continuous flow protocols were applied to low-density polyethylene (LDPE) to explore the different crystallization behavior when the material crystallizes isothermally *after* the application of flow compared to *during* applied deformation. WAXS patterns were generally consistent with each other and indicated alignment of the c-axes of unit cells along the flow direction in both short-term and continuous flows. SAXS images under short-term flow showed diverse and complex evolutions in the lamellar-scale morphologies; those under continuous flow revealed distinct features of shish-kebab morphology. These dramatic differences in morphology were manifested based on only moderate changes in temperature and applied strain. Based on a direct comparison between the quantitative results from continuous and short-term flow experiments, the extent of crystallization produced in the former was significantly higher than that from the latter at comparable times. Further, the absence of crystallinity during applied deformation led to a zoology of unusual lamellar-scale microstructures that are quite different from traditional stacked lamellae associated with oriented crystallization. Based on overall observations, we postulated that the formation of shish-kebab morphology hinges on crystallization induced during flow inception and thus may serve as an indicator of crystallinity detected during flow.

Finally, in Chapter 6, the hypothesis posed in Chapter 5 was further explored by studying the crystallization in high-density polyethylene (HDPE). This study confirmed that the structure and morphology of the isothermally crystallized polymer is strongly dependent on the presence/absence of crystallinity during flow, particularly as a function of applied strain.

Comparison across all flow-induced crystallization experiments on the polymers presented in Chapters 3 – 6 corroborates the recurring observations in these studies: (1) different semi-crystalline polymers exhibit a wide array of lamellar-scale morphologies that is not anticipated based on conventional flow-induced crystallization viewpoints and (2) crystallization detected during flow always leads SAXS patterns reflecting a shish-kebab morphology (characterized by a sharp streak perpendicular to flow and concentrated intensities parallel to flow) and WAXS patterns that show highly concentrated diffraction peaks that indicate extreme alignment of the c-axis along the direction of flow.

This thesis primarily features experimental studies of flow-induced crystallization with a heavy emphasis on quantifying the extent of crystallization and orientation state of microstructures on an absolute intensity scale. For studies employing scattering techniques (x-ray, light, or neutron), these quantitative analyses can be readily applied to provide a comprehensive description of the structural information in 3D reciprocal space when paired with the qualitative study of 2D scattering images. This is highly applicable to the study of anisotropic systems, which is directly relevant to flow-induced crystallization in which crystallites are highly oriented.

While the research presented here is at the forefront of flow-induced crystallization studies by exploiting *in situ* x-ray scattering methodologies under a well-defined uniaxial extensional flow, further work in this field can be pursued in multiple directions. One important avenue that deserves more attention is coordinating experimental studies with computational modeling, as demonstrated in Chapter 4. This is motivated by the challenges associated with verifying complete flow-induced crystallization models, as they require formulation in great detail as well as full-scale simulations spanning extremely long time scales. To alleviate some of these problems, it would be prudent to test existing flow-induced crystallization models of various descriptions using the strategy outlined in Chapter 4. This strategy not only pertains to molecularly-based constitutive equations used in the Eindhoven models, but is also applicable to other constitutive equations. In fact, regardless of the choice of the specific constitutive model, the main advantage of this test strategy is that the effect of flow on enhanced nucleation can be readily tested without having to formulate and simulate the entire crystallization process. This general approach allows researchers to explore various macroscopic parameters (e.g. deformation rate, strain, stress) and test comprehensive FIC models in great detail by designing flow protocols that would lead to similar enhanced nucleation and monitoring crystallization via *in situ* techniques. The strategy can be revisited as necessary with refined experimental conditions without any demand for computationally expensive, full-scale simulations.

Additionally*, in situ* structural studies on the extensional flow-induced crystallization behavior of a wider variety of semi-crystalline polymers (e.g. poly(ethylene terephthalate) or polycaprolactone) would add great value to the existing body of FIC literature. Further experimental efforts pursued along these lines would allow opportunities to revisit the hypothesis discussed in Chapter 6 and test the extent to which it is applicable. Exploring a fuller range of kinematics experienced by polymers under both shear *and* extension as well as expanding the range of parameter space (i.e., crystallization temperature, extension rate, Hencky strain) beyond the conditions explored in this work would also contribute to an improved understanding of the complicated phenomenon. These advances and future steps have the potential to more positively impact the rational basis for designing polymer processes.

References

[1] Geyer, R., Jambeck, J. R. and Law, K. L., “Production, use, and fate of all plastics ever made - Supplementary Information,” *Sci. Adv.* 25–29 (2017). doi:10.1126/sciadv.1700782

[2] American Chemical Council, “US Resin Production & Sales 2017 vs. 2016,” (2018). Available at: https://plastics.americanchemistry.com/Plastics-Statistics/ACC-PIPS-Year-End-2017-Resin-Stats-vs-2016.pdf.

[3] Piorkowska, E. and Rutledge, G. C., *Handbook of Polymer Crystallization Handbook of Polymer Crystallization* (2013). doi:10.1002/9781118541838

[4] Mao, R., Mccready, E. M. and Burghardt, W. R., “Soft Matter Structural response of an ordered block copolymer melt to uniaxial extensional fl ow,” *Soft Matter* **10**, 6198–6207 (2014).

[5] McCready, E. M. and Burghardt, W. R., “In situ SAXS studies of structural relaxation of an ordered block copolymer melt following cessation of uniaxial extensional flow,” *Macromolecules* **48**, 264–271 (2015).

[6] McCready, E. M. and Burghardt, W. R., “Structural response of a prealigned cylindrical block copolymer melt to extensional flow,” *J. Rheol.* **59**, 935–956 (2015).

[7] Maron, S. H., Nakajima, N. and Krieger, I. M., “Study of Entanglement of Polymers in Solution by Viscosity Measurements,” *J. Polym. Sci.* **37**, 1–18 (1959).

[8] Edwards, S. and Edwards, S. F., “The statistical mechanics of polymerized material Recent citations The statistical mechanics of polymerized material,” *Proc. Phys. Soc.* (1967).

[9] De Gennes, P. G., “Reptation of a polymer chain in the presence of fixed obstacles,” *J. Chem. Phys.* **55**, 572–579 (1971).

[10] Doi, M. and Edwards, S. F., “Part 1 - Brownian Motion in the Equilibrium State,” *J. Chem. Soc. Faraday Trans. 2* **74**, 1818 (1978).

[11] Larson, R. G., *The Structure and Rheology of Complex Fluids* (Oxford University Press, 1999).

[12] Meissner, J., “Rheometer zur Untersuchung der deformationsmechanischen Eigenschaften

von Kunststoff-Schmelzen unter definierter Zugbeanspruchung," *Rheol. Acta* **8**, 78–88 (1969).

[13] Meissner, J., "Development of a Universal Extensional Rheometer for the Uniaxial Extension of Polymer Melts," *J. Rheol.* **16**, 405 (1972).

[14] Meissner, J. and Hostettler, J., "A new elongational rheometer for polymer melts and other highly viscoelastic liquids," *Rheol. Acta* **33**, 1–21 (1994).

[15] Münstedt, H., "New Universal Extensional Rheometer for Polymer Melts. Measurements on a Polystyrene Sample," *J. Rheol.* **23**, 421 (1979).

[16] Matta, J. E. and Tytus, R. P., "Liquid stretching using a falling cylinder," *J. Nonnewton. Fluid Mech.* **35**, 215–229 (1990).

[17] Sridhar, T., Tirtaatmadja, V., Nguyen, D. A. and Gupta, R. K., "Measurement of extensional viscosity of polymer solutions," *J. Nonnewton. Fluid Mech.* **40**, 271–280 (1991).

[18] Tirtaatmadja, V. and Sridhar, T., "A filament stretching device for measurement of extensional viscosity," *J. Rheol.* **37**, 1081–1102 (1993).

[19] Rasmussen, H. K., Nielsen, J. K., Bach, A. and Hassager, O., "Viscosity overshoot in the start-up of uniaxial elongation of low density polyethylene melts," *J. Rheol.* **49**, 369–381 (2005).

[20] Sentmanat, M., Wang, B. N. and McKinley, G. H., "Measuring the transient extensional rheology of polyethylene melts using the SER universal testing platform," *J. Rheol.* **49**, 585 (2005).

[21] Macosko, C., *Rheology: principles, measurements, and applications* (VCH, 1994).

[22] Trouton, F. T., "On the Coefficient of Viscous Traction and Its Relation to that of Viscosity," *Proc. R. Soc. London. Ser. A.* **77**, 426–440 (1906).

[23] McLeish, T. C. B. and Larson, R. G., "Molecular constitutive equations for a class of branched polymers: The pom-pom polymer," *J. Rheol.* **42**, 81–110 (1998).

[24] McLeish, T. C. B., "Tube theory of entangled polymer dynamics," *Adv. Phys.* **51**, 1379–1527 (2002).

[25] Münstedt, H., "Dependence of the Elongational Behavior of Polystyrene Melts on

Molecular Weight and Molecular Weight Distribution," *J. Rheol.* **24**, 847 (1980).

[26] Derakhshandeh, M. and Hatzikiriakos, S. G., "Flow-induced crystallization of high-density polyethylene: The effects of shear and uniaxial extension," *Rheol. Acta* **51**, 315–327 (2012).

[27] Schrauwen, B. A. G., Breemen, L. C. A. V., Spoelstra, A. B., Govaert, L. E., Peters, G. W. M. and Meijer, H. E. H., "Structure, deformation, and failure of flow-oriented semicrystalline polymers," *Macromolecules* **37**, 8618–8633 (2004).

[28] Heimenz, P. C. and Lodge, T. P., *Polymer Chemistry* (CRC Press, 2007).

[29] Schultz, J. M., *Polymer Materials Science* (Prentice Hall, 1974).

[30] Pennings, A. J. and Kiel, A. M., "Fractionation of polymers by crystallization from solution, III. On the morphology of fibrillar polyethylene crystals grown in solution," *Colloid Polym. Sci.* **205**, 160–162 (1965).

[31] Mackley, M. R., "Shish kebabs; hydrodynamic factors affecting their crystal growth," *Colloid Polym. Sci.* **253**, 373–379 (1975).

[32] Schultz, J. M., *Polymer Crystallization: The Development of Crystalline Order in Thermoplastic Polymers* (Oxford University Press, 2001).

[33] Lagasse, R. R. and Maxwell, B., "Crystallization During Shear Flow," *Polym. Eng. Sci.* **16**, 189–199 (1976).

[34] Titomanlio, C. and Marrucci, G., "Capillary Experiments of Flow Induced Crystallization of HDPE," *AIChE J.* **36**, 13–18 (1990).

[35] Bove, L. and Nobile, M. R., "Shear-induced crystallization of isotactic poly(1-butene)," *Macromol. Symp.* **185**, 135–147 (2002).

[36] Koscher, E. and Fulchiron, R., "Influence of shear on polypropylene crystallization kinetics," *Polymer* **43**, 6931–6942 (2002).

[37] Kornfield, J. A., Kumaraswamy, G. and Issaian, A. M., "Recent Advances in Understanding Flow Effects on Polymer Crystallization," *Ind. Eng. Chem. Res.* **41**, 6383–6392 (2002).

[38] Somani, R. H., Hsiao, B. S., Nogales, A., Srinivas, S., Tsou, A. H., Sics, I., Balta-Calleja, F. J. and Ezquerra, T. a., "Structure development during shear flow-induced crystallization

of i-PP: in-situ small-angle X-ray scattering study," *Macromolecules* **33**, 9385–9394 (2000).

[39] Li, L. and Jeu, W. H. De, "Shear-Induced Crystallization of Poly (butylene terephthalate): A Real-Time Small-Angle X-ray Scattering Study," *Macromolecules* **37**, 5646–5652 (2004).

[40] Somani, R. H., Yang, L., Zhu, L. and Hsiao, B. S., "Flow-induced shish-kebab precursor structures in entangled polymer melts," *Polymer* **46**, 8587–8623 (2005).

[41] van Meerveld, J., Peters, G. W. M. and Hütter, M., "Towards a rheological classification of flow induced crystallization experiments of polymer melts," *Rheol. Acta* **44**, 119–134 (2004).

[42] Zhao, Y., Hayasaka, K., Matsuba, G. and Ito, H., "In situ observations of flow-induced precursors during shear flow," *Macromolecules* **46**, 172–178 (2013).

[43] Vega, J. F., Hristova, D. G. and Peters, G. W. M., "Flow-induced crystallization regimes and rheology of isotactic polypropylene: Effects of molecular architecture," *J. Therm. Anal. Calorim.* **98**, 655–666 (2009).

[44] Mencik, Z. and Fitchmun, D. R., "Texture of Injection-Molded Polypropylene," *J. Polym. Sci.* **11**, 973–989 (1973).

[45] Fujiyama, M. and Wakino, T., "Structure of skin layer in injection-molded polypropylene," *J. Appl. Polym. Sci.* **35**, 29–49 (1988).

[46] Liedauer, S., Janeschitz-Kriegl, H., Jerschow, P., Geymayer, W. and Ingolic, E., "On the kinetics of shear induced crystallization in polypropylene," *Int. Polym. Process.* **8**, 236–244 (1993).

[47] Hadinata, C., Boos, D., Gabriel, C., Wassner, E., Rüllmann, M., Kao, N. and Laun, M., "Elongation-induced crystallization of a high molecular weight isotactic polybutene-1 melt compared to shear-induced crystallization," *J. Rheol.* **51**, 195 (2007).

[48] Ma, Z., Steenbakkers, R. J. A., Giboz, J. and Peters, G. W. M., "Using rheometry to determine nucleation density in a colored system containing a nucleating agent," *Rheol. Acta* **50**, 909–915 (2011).

[49] Hamad, F. G., Colby, R. H. and Milner, S. T., "Onset of Flow-Induced Crystallization

Kinetics of Highly Isotactic Polypropylene," *Macromolecules* **48**, 3725–3738 (2015).

[50] Roozemond, P. C., van Drongelen, M., Verbelen, L., Van Puyvelde, P. and Peters, G. W. M., "Flow-induced crystallization studied in the RheoDSC device: Quantifying the importance of edge effects," *Rheol. Acta* **54**, 1–8 (2015).

[51] Elmoumni, A., Winter, H. H., Waddon, A. J. and Fruitwala, H., "Correlation of material and processing time scales with structure development in isotactic polypropylene crystallization," *Macromolecules* **36**, 6453–6461 (2003).

[52] Kumaraswamy, G., Issaian, A. M. and Kornfield, J. A., "Shear-enhanced crystallization in isotactic polypropylene. 1. Correspondence between in situ rheo-optics and ex situ structure determination," *Macromolecules* **32**, 7537–7547 (1999).

[53] Acierno, S., Palomba, B., Winter, H. and Grizzuti, N., "Effect of molecular weight on the flow-induced crystallization of isotactic poly(1-butene)," *Rheol Acta* **42**, 243–250 (2003).

[54] Baert, J., Van Puyvelde, P. and Langouche, F., "Flow-induced crystallization of PB-1: From the low shear rate region up to processing rates," *Macromolecules* **39**, 9215–9222 (2006).

[55] McHugh, A. J., Guy, R. K. and Tree, D. A., "Extensional flow-induced crystallization of a polyethylene melt," *Colloid Polym. Sci.* **271**, 629–645 (1993).

[56] Somani, R. H., Hsiao, B. S., Nogales, A., Fruitwala, H., Srinivas, S. and Tsou, A. H., "Structure development during shear flow induced crystallization of i-PP: In situ wide-angle X-ray diffraction study," *Macromolecules* **34**, 5902–5909 (2001).

[57] Hsiao, B. S., Yang, L., Somani, R. H., Avila-Orta, C. a. and Zhu, L., "Unexpected Shish-Kebab structure in a sheared polyethylene melt," *Phys. Rev. Lett.* **94**, 1–4 (2005).

[58] Keum, J. K., Zuo, F. and Hsiao, B. S., "Probing the flow-induced shish-kebab structure in entangled polyethylene melts by synchrotron X-ray scattering," *J. Appl. Crystallogr.* **40**, 48–51 (2007).

[59] Troisi, E. M., Portale, G., Ma, Z., Van Drongelen, M., Hermida-Merino, D. and Peters, G. W. M., "Unusual melting behavior in flow induced crystallization of LLDPE: Effect of pressure," *Macromolecules* **48**, 2551–2560 (2015).

[60] Bach, A., Almdal, K., Rasmussen, H. K. and Hassager, O., "Elongational Viscosity of

Narrow Molar Mass Distribution Polystyrene," *Macromolecules* **36**, 5174–5179 (2003).

[61] Bach, A., Rasmussen, H. K. and Hassager, O., "Extensional viscosity for polymer melts measured in the filament stretching rheometer," *J. Rheol.* **47**, 429 (2003).

[62] Chellamuthu, M., Arora, D., Winter, H. H. and Rothstein, J. P., "Extensional flow-induced crystallization of isotactic poly-1-butene using a filament stretching rheometer," *J. Rheol.* **55**, 901 (2011).

[63] White, E. E. B., Winter, H. and Rothstein, J. P., "Extensional-flow-induced crystallization of isotactic polypropylene," *Rheol. Acta* **51**, 303–314 (2012).

[64] Sentmanat, M., Delgadillo-Velázquez, O. and Hatzikiriakos, S. G., "Crystallization of an ethylene-based butene plastomer: The effect of uniaxial extension," *Rheol. Acta* **49**, 931–939 (2010).

[65] Yan, T., Zhao, B., Cong, Y., Fang, Y., Cheng, S., Li, L., Pan, G., Wang, Z., Li, X. and Bian, F., "Critical strain for shish-kebab formation," *Macromolecules* **43**, 602–605 (2010).

[66] Tian, N., Zhou, W., Cui, K., Liu, Y., Fang, Y., Wang, X., Liu, L. and Li, L., "Extension flow induced crystallization of poly(ethylene oxide)," *Macromolecules* **44**, 7704–7712 (2011).

[67] Cui, K., Meng, L., Tian, N., Zhou, W., Liu, Y., Wang, Z., He, J. and Li, L., "Self-acceleration of nucleation and formation of shish in extension-induced crystallization with strain beyond fracture," *Macromolecules* **45**, 5477–5486 (2012).

[68] Liu, D., Tian, N., Cui, K., Zhou, W., Li, X. and Li, L., "Correlation between flow-induced nucleation morphologies and strain in polyethylene: From uncorrelated oriented point-nuclei, scaffold-network, and microshish to shish," *Macromolecules* **46**, 3435–3443 (2013).

[69] Liu, D., Tian, N., Huang, N., Cui, K., Wang, Z., Hu, T., Yang, H., Li, X. and Li, L., "Extension-Induced Nucleation under Near-Equilibrium Conditions: The Mechanism on the Transition from Point Nucleus to Shish," *Macromolecules* **47**, 6813–6823 (2014).

[70] Yang, H., Liu, D., Ju, J., Li, J., Wang, Z., Yan, G., Ji, Y., Zhang, W., Sun, G. and Li, L., "Chain Deformation on the Formation of Shish Nuclei under Extension Flow: An in Situ SANS and SAXS Study," *Macromolecules* **49**, 9080–9088 (2016).

[71] Wang, Z., Ju, J., Yang, J., Ma, Z., Liu, D., Cui, K., Yang, H., Chang, J., Huang, N. and Li, L., "The non-equilibrium phase diagrams of flow-induced crystallization and melting of polyethylene," *Sci. Rep.* **6**, 1–8 (2016).

[72] Wang, Z., Ju, J., Meng, L., Tian, N., Chang, J., Yang, H., Ji, Y., Su, F. and Li, L., "Structural and morphological transitions in extension-induced crystallization of poly(1-butene) melt," *Soft Matter* **13**, 3639–3648 (2017).

[73] Schneider, W., Koppl, A. and Berger, J., "Non-Isothermal Crystallization Crystallization of Polymers (System of Rate Equations)," *Int. Polym. Process.* **2**, 151–154 (1988).

[74] Baig, C. and Edwards, B. J., "Atomistic simulation of flow-induced crystallization at constant temperature," *EPL (Europhysics Lett.)* **89**, 36003 (2010).

[75] Wang, M., "Hierarchical orientational relaxation inducing shish-kebab formations in polymer melt crystallization," *J. Phys. Chem. B* **114**, 3488–3493 (2010).

[76] Jabbarzadeh, A. and Tanner, R. I., "Flow-induced crystallization: Unravelling the effects of shear rate and strain," *Macromolecules* **43**, 8136–8142 (2010).

[77] Avrami, M., "Kinetics of Phase Change. I General Theory," *J. Chem. Phys.* **1103**, 1103 (1939).

[78] Avrami, M., "Kinetics of phase change. II Transformation-time relations for random distribution of nuclei," *J. Chem. Phys.* **8**, 212–224 (1940).

[79] Avrami, M., "Granulation, phase change, and microstructure kinetics of phase change. III," *J. Chem. Phys.* **9**, 177–184 (1941).

[80] Ziabicki, A., "Theoretical analysis of oriented and non isothermal crystallization," *Colloid Polym. Sci.* **252**, 207–221 (1974).

[81] Eder, G., Janeschitz-Kriegl, H. and Liedauer, S., "Crystallization processes in quiescent and moving polymer melts under heat transfer conditions," *Prog. Polym. Sci.* **15**, 629–714 (1990).

[82] Tanner, R. I., "On the flow of crystallizing polymers I. Linear regime," *J. Nonnewton. Fluid Mech.* **112**, 251–268 (2003).

[83] Zheng, R. and Kennedy, P. K., "A model for post-flow induced crystallization: General equations and predictions," *J. Rheol.* **48**, 823–842 (2004).

[84] Boutaous, M., Bourgin, P. and Zinet, M., "Thermally and flow induced crystallization of polymers at low shear rate," *J. Nonnewton. Fluid Mech.* **165**, 227–237 (2010).

[85] Zuidema, H., Peters, G. W. M. and Meijer, H. E. H., "Development and validation of a recoverable strain-based model for flow-induced crystallization of polymers," *Macromol. Theory Simulations* **10**, 447–460 (2001).

[86] Coppola, S. and Grizzuti, N., "Microrheological Modeling of Flow-Induced Crystallization," *Macromolecules* **34**, 5030–5036 (2001).

[87] Peters, G. W. M., Swartjes, F. H. M. and Meijer, H. E. H., "A recoverable strain-based model for flow-induced crystallization," *Macromol. Symp.* **185**, 277–292 (2002).

[88] Custódio, F. J. M. F., Steenbakkers, R. J. a, Anderson, P. D., Peters, G. W. M. and Meijer, H. E. H., "Model development and validation of crystallization behavior in injection molding prototype flows," *Macromol. Theory Simulations* **18**, 469–494 (2009).

[89] Steenbakkers, R. J. a. and Peters, G. W. M., "A stretch-based model for flow-enhanced nucleation of polymer melts," *J. Rheol.* **55**, 401 (2011).

[90] Roozemond, P. C. and Peters, G. W. M., "Flow-enhanced nucleation of poly(1-butene): Model application to short-term and continuous shear and extensional flow," *J. Rheol.* **57**, 1633–1653 (2013).

[91] Roozemond, P. C., van Drongelen, M., Ma, Z., Hulsen, M. a. and Peters, G. W. M., "Modeling flow-induced crystallization in isotactic polypropylene at high shear rates," *J. Rheol.* **59**, 613–642 (2015).

[92] van Drongelen, M., Roozemond, P. C., Troisi, E. M., Doufas, A. K. and Peters, G. W. M., "Characterization of the primary and secondary crystallization kinetics of a linear low-density polyethylene in quiescent- and flow-conditions," *Polymer* **76**, 254–270 (2015).

[93] Roozemond, P. C., van Erp, T. B. and Peters, G. W. M., "Flow-induced crystallization of isotactic polypropylene: Modeling formation of multiple crystal phases and morphologies," *Polymer* **89**, 69–80 (2016).

[94] Mao, R., "Rheo-X-ray Investigation of Structure Development in Polymer Melts Under Uniaxial Extensional Flow," (Northwestern, 2011).

[95] McCready, E., "In Situ X-ray Scattering Analysis of Polymer Melts Under Uniaxial

Extensional Flow," (Northwestern, 2015).

[96] Roe, R.-J., *Methods of X-ray and Neutron Scattering in Polymer Science* (Oxford University Press, 2000).

[97] Sentmanat, M. L., "Miniature universal testing platform: From extensional melt rheology to solid-state deformation behavior," *Rheol. Acta* **43**, 657–669 (2004).

[98] Somani, R. H., Yang, L., Hsiao, B. S., Agarwal, P. K., Fruitwala, H. a. and Tsou, A. H., "Shear-induced precursor structures in isotactic polypropylene melt by in-situ rheo-SAXS and rheo-WAXD studies," *Macromolecules* **35**, 9096–9104 (2002).

[99] Stadlbauer, M., Janeschitz-Kriegl, H., Eder, G. and Ratajski, E., "New extensional rheometer for creep flow at high tensile stress. Part II. Flow induced nucleation for the crystallization of iPP," *J. Rheol.* **48**, 631–639 (2004).

[100] Ito, H. J., Takimoto, T. and Koyama, K., "Elongational Flow and Crystallization Melt Polymer Behavior in Supercooled Melt Polymer," *Seikei Kakou* **7**, 576–581 (1995).

[101] Auras, R., Harte, B. and Selke, S., "An overview of polylactides as packaging materials," *Macromol. Biosci.* **4**, 835–864 (2004).

[102] Soppimath, K. S., Aminabhavi, T. M. and Kulkarni, A. R., "Biodegradable polymer nanoparticles as drug delivery devices," **70**, 1–20 (2001).

[103] Wiebe, J., Nef, H. M. and Hamm, C. W., "Current status of bioresorbable scaffolds in the treatment of coronary artery disease," *J. Am. Coll. Cardiol.* **64**, 2541–2551 (2014).

[104] Saeidlou, S., Huneault, M. a., Li, H. and Park, C. B., "Poly(lactic acid) crystallization," *Prog. Polym. Sci.* **37**, 1657–1677 (2012).

[105] Wang, J., Bai, J., Zhang, Y., Fang, H. and Wang, Z., "Shear-induced enhancements of crystallization kinetics and morphological transformation for long chain branched polylactides with different branching degrees," *Sci. Rep.* **6**, 1–13 (2016).

[106] Li, X.-J., Li, Z.-M., Zhong, G.-J. and Li, L.-B., "Steady-shear-induced Isothermal Crystallization of Poly(L-lactide) (PLLA)," *J. Macromol. Sci. Part B* **47**, 511–522 (2008).

[107] Zhong, Y., Fang, H., Zhang, Y., Wang, Z., Yang, J. and Wang, Z., "Rheologically determined critical shear rates for shear-induced nucleation rate enhancements of poly(lactic acid)," *ACS Sustain. Chem. Eng.* **1**, 663–672 (2013).

[108] Jalali, A., Shahbikian, S., Huneault, M. A. and Elkoun, S., “Effect of molecular weight on the shear-induced crystallization of poly(lactic acid),” *Polymer* **112**, 393–401 (2017).

[109] Xu, H., Zhong, G. J., Fu, Q., Lei, J., Jiang, W., Hsiao, B. S. and Li, Z. M., “Formation of shish-kebabs in injection-molded poly(L-lactic acid) by application of an intense flow field,” *ACS Appl. Mater. Interfaces* **4**, 6774–6784 (2012).

[110] Li, J., Li, Z., Ye, L., Zhao, X., Coates, P., Caton-Rose, F. and Martyn, M., “Structure evolution and orientation mechanism of long-chain-branched poly (lactic acid) in the process of solid die drawing,” *Eur. Polym. J.* **90**, 54–65 (2017).

[111] Liu, J., Zhang, S., Zhang, L. and Bai, Y., “Uniaxial stretching behavior of polylactide with long chain branching,” *Colloid Polym. Sci.* **295**, 297–306 (2017).

[112] Tang, H., Chen, J. Bin, Wang, Y., Xu, J. Z., Hsiao, B. S., Zhong, G. J. and Li, Z. M., “Shear flow and carbon nanotubes synergistically induced nonisothermal crystallization of poly(lactic acid) and its application in injection molding,” *Biomacromolecules* **13**, 3858–3867 (2012).

[113] Yang, I. K. and Wu, C. H., “Real-time SAXS measurements and rheological behavior of poly(lactic acid) crystallization under continuous shear flow,” *J. Polym. Res.* **21**, (2014).

[114] Ramachandran, K., Miscioscia, R., De Filippo, G., Pandolfi, G., Di Luccio, T. and Kornfield, J. A., “Tube expansion deformation enables in situ synchrotron X-ray scattering measurements during extensional flow-induced crystallization of Poly L-lactide near the glass transition,” *Polymers* **10**, 1–25 (2018).

[115] Li, H. and Huneault, M. a., “Effect of nucleation and plasticization on the crystallization of poly(lactic acid),” *Polymer* **48**, 6855–6866 (2007).

[116] Nofar, M., Zhu, W., Park, C. B. and Randall, J., “Crystallization kinetics of linear and long-chain-branched polylactide,” *Ind. Eng. Chem. Res.* **50**, 13789–13798 (2011).

[117] Najafi, N., Heuzey, M. C., Carreau, P. and Therriault, D., “Quiescent and shear-induced crystallization of linear and branched polylactides,” *Rheol. Acta* **54**, 831–845 (2015).

[118] Jalali, A., “personal communication,” (2019).

[119] Hu, W., Frenkel, D. and Mathot, V. B. F., “Simulation of Shish-Kebab crystallite induced by a single prealigned macromolecule,” *Macromolecules* **35**, 7172–7174 (2002).

[120] Lavine, M. S., Waheed, N. and Rutledge, G. C., “Molecular dynamics simulation of orientation and crystallization of polyethylene during uniaxial extension,” *Polymer* **44**, 1771–1779 (2003).

[121] Ko, M. J., Waheed, N., Lavine, M. S. and Rutledge, G. C., “Characterization of polyethylene crystallization from an oriented melt by molecular dynamics simulation,” *J. Chem. Phys.* **121**, 2823–2832 (2004).

[122] Wang, M., Hu, W., Ma, Y. and Ma, Y. Q., “Orientational relaxation together with polydispersity decides precursor formation in polymer melt crystallization,” *Macromolecules* **38**, 2806–2812 (2005).

[123] Graham, R. S. and Olmsted, P. D., “Kinetic Monte Carlo simulations of flow-induced nucleation in polymer melts,” *Faraday Discuss.* **144**, 71–92 (2010).

[124] Hadinata, C., “Flow-induced crystallization of polybutene-1 and effect of molecular parameters,” (RMIT University, 2007).

[125] Likhtman, A. E. and Graham, R. S., “Simple constitutive equation for linear polymer melts derived from molecular theory: Rolie-Poly equation,” *J. Nonnewton. Fluid Mech.* **114**, 1–12 (2003).

[126] Kimita, S., Sakurai, T., Nozue, Y., Kasahara, T., Yamaguchi, N., Karino, T., Shibayama, M. and Kornfield, J. A., “Molecular Basis of the Shish-Kebab Morphology in Polymer Crystallization,” *Science (80-.).* **316**, 1014–1017 (2007).

[127] Kanaya, T., Murakami, M., Maede, T., Ogawa, H., Inoue, R., Nishida, K., Matsuba, G., Ohta, N., Takata, S., Tominaga, T., Suzuki, J., Han, Y.-S. and Kim, T.-H., “Role of molecular weight in shish-kebab formation during drawing by small-angle neutron and X-ray scattering,” *Polym. J.* **49**, 831–837 (2017).

[128] Graham, R. S., Likhtman, A. E., McLeish, T. C. B. and Milner, S. T., “Microscopic theory of linear, entangled polymer chains under rapid deformation including chain stretch and convective constraint release,” *J. Rheol.* **47**, 1171–1200 (2003).

[129] Marrucci, G., “Dynamics of entanglements: A nonlinear model consistent with the Cox-Merz rule,” *J. Nonnewton. Fluid Mech.* **62**, 279–289 (1996).

[130] Doufas, A. K., Dairanieh, I. S. and McHugh, A. J., “A continuum model for flow-induced

crystallization of polymer melts," *J. Rheol.* **43**, 85 (1999).

[131] Wingstrand, S. L., Van Drongelen, M., Mortensen, K., Graham, R. S., Huang, Q. and Hassager, O., "Influence of Extensional Stress Overshoot on Crystallization of LDPE," *Macromolecules* **50**, 1134–1140 (2017).

[132] Huang, Q., Rasmussen, H. K., Skov, A. L. and Hassager, O., "Stress relaxation and reversed flow of low-density polyethylene melts following uniaxial extension," *J. Rheol.* **56**, 1535–1554 (2012).

[133] Hay, I. L., Kawai, T. and Keller, a., "A study on orientation effects in polyethylene in the light of crystalline texture," *J. Polym. Sci. Part C Polym. Symp.* **16**, 2721–2731 (1967).

[134] Cowking, A., Rider, J. G., Hay, I. L. and Keller, A., "A study on orientation effects in polyethylene in the light of crystalline texture," *J. Polym. Sci. Part C Polym. Symp.* **16**, 2721–2731 (1967).

[135] Keller, A. and Pope, D. P., "Identification of structural processes in deformation of oriented polyethylene," *J. Mater. Sci.* **6**, 453–478 (1971).

[136] POPE, D. P. and KELLER, A., "Deformation of oriented polyethylene," *J. Polym. Sci. Part B-Polymer Phys.* **13**, 533–566 (1975).

[137] Abou-Kandil, A. I. and Windle, A. H., "The development of microstructure in oriented polyethylene terephthalate (PET) during annealing," *Polymer* **48**, 5069–5079 (2007).

[138] Keum, J. K., Burger, C., Zuo, F. and Hsiao, B. S., "Probing nucleation and growth behavior of twisted kebabs from shish scaffold in sheared polyethylene melts by in situ X-ray studies," *Polymer* **48**, 4511–4519 (2007).

[139] Zhang, X. M., Elkoun, S., Ajji, A. and Huneault, M. A., "Oriented structure and anisotropy properties of polymer blown films: HDPE, LLDPE and LDPE," *Polymer* **45**, 217–229 (2004).

[140] Zuo, F., Keum, J. K., Yang, L., Somani, R. H. and Hsiao, B. S., "Thermal stability of shear-induced shish-kebab precursor structure from high molecular weight polyethylene chains," *Macromolecules* **39**, 2209–2218 (2006).

[141] Ugaz, V. M. and Burghardt, W. R., "In situ X-ray scattering study of a model thermotropic copolyester under shear: Evidence and consequences of flow-aligning

behavior," *Macromolecules* **31**, 8474–8484 (1998).

[142] Burghardt, W. R., Brown, E. F., Auad, M. L. and Kornfield, J. A., "Molecular orientation of a commercial thermotropic liquid crystalline polymer in simple shear and complex flow," *Rheol. Acta* **44**, 446–456 (2005).

[143] Rendon, S., Burghardt, W. R. and Bubeck, R. A., "Orientation dynamics in commercial thermotropic liquid crystalline polymers in transient shear flows," *Rheol. Acta* **46**, 945–956 (2007).

[144] Luo, B., "Structural Dynamics of Complex Fluids Subjected to Planar Extensional Flow Studied Using In Situ X-ray Scattering," (Northwestern University, 2018).

[145] Leheny, R. L., "XPCS: Nanoscale motion and rheology," *Curr. Opin. Colloid Interface Sci.* **17**, 3–12 (2012).

[146] Chung, B., Ramakrishnan, S., Bandyopadhyay, R., Liang, D., Zukoski, C. F., Harden, J. L. and Leheny, R. L., "Microscopic dynamics of recovery in sheared depletion gels," *Phys. Rev. Lett.* **96**, 3–6 (2006).

[147] Fluerasu, A., Moussaïd, A., Falus, P., Gleyzolle, H. and Madsen, A., "X-ray photon correlation spectroscopy under flow," *J. Synchrotron Radiat.* **15**, 378–384 (2008).

[148] Busch, S., Jensen, T. H., Chushkin, Y. and Fluerasu, A., "Dynamics in shear flow studied by X-ray Photon Correlation Spectroscopy," *Eur. Phys. J. E* **62**, 9 (2008).

[149] Fluerasu, A., Kwasniewski, P., Caronna, C., Destremaut, F., Salmon, J. B. and Madsen, A., "Dynamics and rheology under continuous shear flow studied by x-ray photon correlation spectroscopy," *New J. Phys.* **12**, (2010).

[150] Burghardt, W. R., Sikorski, M., Sandy, A. R. and Narayanan, S., "X-ray photon correlation spectroscopy during homogenous shear flow," *Phys. Rev. E - Stat. Nonlinear, Soft Matter Phys.* **85**, 1–7 (2012).

[151] Laurati, M., Egelhaaf, S. U., and Petekidis, G., "Plastic rearrangements in colloidal gels investigated by LAOS and LS-Echo," *J. Rheol.* **58**, 1395-1417 (2014).

[152] Rogers, M. C., Chen, K., Andrzejewski, L., Narayanan, S., Ramakrishnan, S., Leheny, R. L. and Harden, J. L., "Echoes in x-ray speckles track nanometer-scale plastic events in colloidal gels under shear," *Phys. Rev. E* **90**, 062310 (2014).

[153] Fuller, G. G., Rallison, J. M., Schmidt, R. L. and Leal, L. G., “The measurement of velocity gradients in laminar flow by homodyne light-scattering spectroscopy,” *J. Fluid Mech.* **100**, 555 (1980).

[154] Narayanan, T., Cheung, C., Tong, P., Goldburg, W. I. and Wu, X. L., “Measurement of the velocity difference by photon correlation spectroscopy: an improved scheme.,” *Appl. Opt.* **36**, 7639–7644 (1997).

Appendix A

In Situ X-ray Scattering Studies of Flow-Induced Crystallization in Poly(1-butene) under Shear Flow

A.1 Introduction

The rheology of polymers under shear is well-understood as shearing flows are relatively easy to generate by means of pressure-driven flow through a capillary channel or homogeneous shear using cone and plate geometries. The rheological behavior of polymers subjected to shear flow has also been extensively studied owing to its industrial relevance to polymer processing operations such as injection molding that primarily involves shearing flows. In this process, polymer resins are fed into a heated barrel through a hopper, and molten polymers are delivered to the mold by a screw.[3] The high shear rates experienced by the polymer melt lead to shear thinning, which allows the material to flow more easily due to its lowered melt viscosity. The application of flow has other consequences, in which the crystallization kinetics may be accelerated by orders of magnitude and the induced molecular orientation affects the final properties of the polymer product. This phenomenon, known as flow-induced crystallization (FIC), therefore is of significant industrial and scientific interest.

While shear flow is a dominant flow field in polymer manufacturing processes such as extrusion and injection molding, the kinematically stronger extensional flow dominates processing applications such as film blowing and blow molding. To gain a comprehensive understanding of FIC experienced by polymers during various processing applications, the effect of both shear and extensional flow on the subsequent crystallization behavior in semi-crystalline polymers has received tremendous attention over the past decades. Particular interest lies in gaining molecular/microstructural insight into the impact of alignment in polymer chains induced by the different types of flow on the crystallization process.

As reviewed in Section 2.1, x-ray scattering methods are powerful tools to probe the microstructural response to flow, especially in semi-crystalline polymers. The study presented in this Appendix section capitalizes on our experimental capability to perform *in situ* structural characterization under shear using x-ray scattering techniques[141–143] in order to characterize the flow-induced crystallization behavior in poly(1-butene) subjected to shear. Preliminary *in situ* x-ray scattering studies of shear-induced crystallization on this polymer demonstrated the feasibility of conducting such experiments.[144] This work is also largely motivated by the complementary FIC study employing uniaxial extensional flow on the same polymer of a different grade[95] to gain a broader understanding of the phenomenon in shear and extension.

This section presents time-resolved *in situ* small- and wide-angle x-ray scattering (SAXS and WAXS, respectively) measurements of shear-induced crystallization in poly(1-butene). A well-defined shear flow is applied using a modified Linkam shear cell. A short-term flow protocol is employed to explore the effects of shear rate and strain. The collected x-ray data are used to quantify the orientation distribution of crystallites and the extent of crystallization. A self-consistent method to calculate the volume fraction of crystallinity induced in the polymer during isothermal crystallization is presented. The quantitative analyses performed in this FIC study under shear has laid the foundation for applying these established methods to FIC studies under extensional flow, as presented in Chapters 3 – 6.

A.2 Material and Experimental Methods

The polymer studied in this work is an isotactic poly(1-butene), grade PB0300, donated by LyondellBasell. For linear viscoelastic (LVE) characterization, pellets were compression molded at 180 °C for 10 min into 1.5 mm disks that were loaded in 25 mm parallel plate fixtures in an ARES (Rheometrics Scientific) controlled-strain rotational rheometer. The melt rheology of the polymer is characterized by a broad distribution of relaxation times typical of a polydisperse polymer melt (LVE data presented elsewhere[144]). Based on molecular properties of the polymer obtained from literature,[90,124] the weight-averaged and entanglement molecular weights (M_w and M_e, respectively) were used to estimate the number of entanglements for this material (Table A.1). In addition to estimating the average relaxation time (λ_{avg}) determined from the relaxation spectrum obtained from a generalized Maxwell model fit to the LVE data,[144] the reptation (λ_{rep}) and Rouse times (λ_R) were estimated using the approach described by Roozemond and Peters[90] who attribute the slowest relaxation time to λ_{rep} and calculate λ_R using Eq. (1.6) (see Section 4.2.1). The estimated relaxation times were shifted to the experimental temperature (T_c) of 106 °C using the a time-temperature shift factor of 7.1 determined from an Arrhenius relation based on the melt rheology data at reference temperature (T_{ref}) of 160 °C.[144] The Weissenberg number (Wi), defined as the product of deformation rate and relaxation time, was estimated based on these relaxation times to characterize the strength of the flow (Table A.2). The estimated Weissenberg numbers indicate that the shear rates of $\dot{\gamma}$ = 1 s^{-1}, 2 s^{-1}, and 4 s^{-1} employed in the flow-induced crystallization experiments are strong flow conditions that lead to both alignment and stretching of polymer chains and are expected to lead to oriented flow-induced crystallization.

Table A.1: Molecular properties of isotactic poly(1-butene) used in calculating the Rouse time from the estimated reptation time. M_w is the weight average molecular weight,[124] M_e is the molecular weight between entanglements,[90] and Z is the number of entanglements per chain.

M_w (kg/mol)	M_e (kg/mol)	$Z = M_w/M_e$
347	18	19

Table A.2: Range of Weissenberg number based on estimated average relaxation time, reptation time, and Rouse time at 106 °C. The relaxation times obtained from LVE data at 160 °C are shifted to 106 °C using a shift factor of 7.1 extrapolated from an Arrhenius relationship.[144]

Relaxation Time (s)	T_{ref} = 160 °C	T_c = 106 °C	Wi Range at T_c ($\dot{\gamma}$ = 1 – 4 s^{-1})
λ_{avg}	1.6	11	11 – 46
λ_{rep}	6.9	49	49 – 196
λ_R	0.12	0.85	0.85 – 3.4

In situ x-ray scattering measurements were performed using a Linkam CSS-450 shearing stage that was modified to facilitate x-ray access (Figure A.1a). In this equipment, the polymer sample was contained between a pair of stainless steel inserts, and Kapton® was glued onto the inserts to provide windows that allow access for incoming and scattered x-rays (Figure A.1b). The instrument was integrated into the beam line at Sector 5ID-D of the Advanced Photon Source at Argonne National Laboratory and configured in a way that the incident x-ray beam traveled in the gradient direction of the shear flow field (Figure A.1c). A short-term flow protocol (Figure 2.6a) was employed to isolate the effect of flow on subsequent crystallization. The sample was first heated to an elevated temperature (180 °C), well above its melting temperature to clear its thermal history, and then cooled to T_c = 106 °C. Shear flow was initiated 1 minute after the sample was equilibrated at this temperature. Subsequent isothermal crystallization was monitored using *in situ* SAXS/WAXS measurements using an incident beam energy of 17 keV. No crystallization was detected in the image immediately following flow. Scattered x-rays were collected on Rayonix detectors with a resolution of 1920 x 3840 pixels (WAXS) and 3840 x 3840 pixels (SAXS) and with a 2 x 2 binning, positioned at a sample-to-detector distance of 0.21 m and 8.5 m, respectively. The first 45 images were collected at a 15 s interval between each frame. As the crystallization kinetics slowed down at later times, the intervals were increased to 60 s and then to 120 s, characterizing the structural evolution for a total of ~45 min after the application of flow. An exposure time of 0.5 s was selected. The applied shear strain ranged from γ = 4 to 16 and the shear rates from $\dot{\gamma}$ = 1 s^{-1} to 4 s^{-1} to explore both the effects of rate and strain on subsequent crystallization behavior.

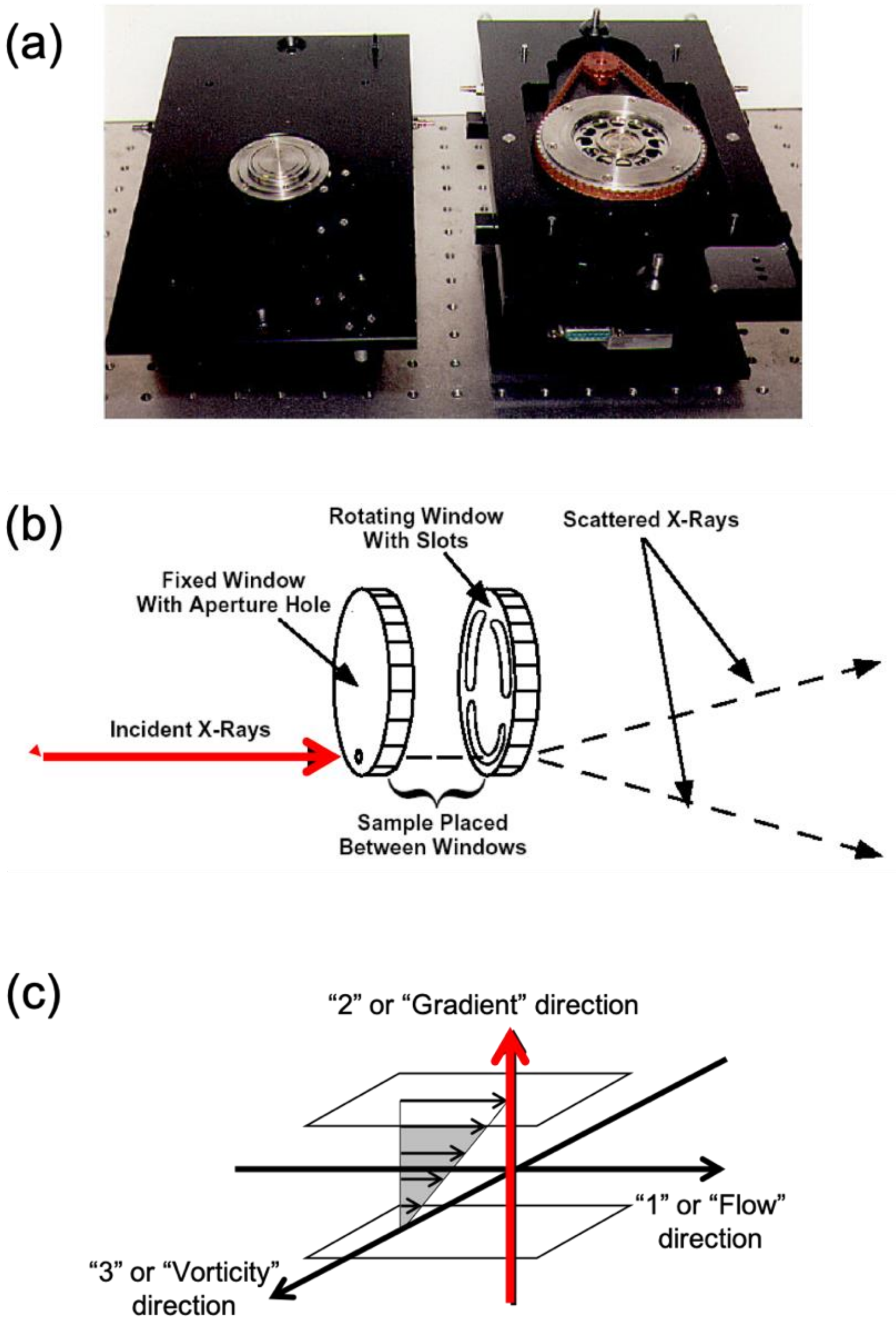

Figure A.1: Experimental instrumentation and setp for *in situ* x-ray scattering measurements under shear flow. (a) Photograph of the modified Linkam CS-450 shearing stage. (b) Schematic of the shear cell operation that facilitates x-ray scattering measurements. (c) Schematic illustrating the x-ray beam (red arrow) passing through the gradient direction.

A.3 Results and Discussion

A.3.1 SAXS/WAXS Image Analysis

Figure A.2 presents SAXS and WAXS patterns collected from an experiment conducted at T_c = 106 °C, $\dot{\gamma}$ = 4 s^{-1}, and γ = 16. Here, the image immediately after flow is defined as the time at which t = 0 min. In SAXS, the image at t = 0 min displays an isotropic intensity distribution, suggesting that there are no signs of crystallinity detected immediately following flow cessation. As time progresses, the patterns show a growth of anisotropically distributed SAXS intensity that is concentrated in the direction of flow. The data also show a peak intensity as a function of scattering angle, arising from the periodicity in lamellar structure. At t = 40 min, the concentrated lobes of intensities along the flow direction in SAXS indicate that the lamellae normals are preferentially oriented along the shearing direction. In WAXS, the image at t = 0 min shows no signs of crystallinity, which is consistent with the observation in the initial SAXS pattern. Over time, diffraction from the crystalline peaks appear and become more intense in the subsequent WAXS images. Towards the end of the monitoring window at t = 40 min, the diffraction from the (200) peak is strongly concentrated in the direction orthogonal to flow, indicating that the c-axis of the unit cell is preferentially aligned parallel to flow. The observations in SAXS and WAXS are consistent with the fact that the polymer chains aligning during flow lead to subsequent orientation of crystallites.

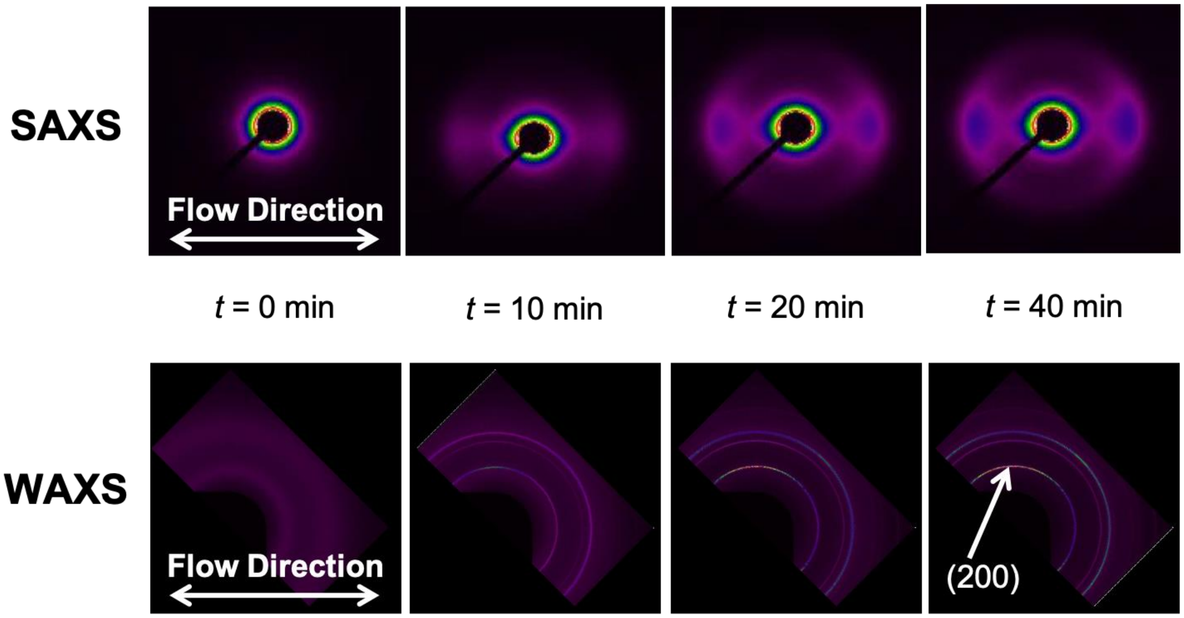

Figure A.2: Representative SAXS and WAXS images from an experiment at T_c = 106 °C, $\dot{\gamma}$ = 4 s^{-1}, and γ = 16.

A.3.2 Data Treatment for Quantitative Analysis

To allow quantitative comparisons across all experiments, the x-ray scattering data are converted to an absolute intensity scale. The data analysis procedures described in Chapter 2 require extrapolating the intensity from the two-dimensional (2D) patterns to three-dimensional (3D) scattering intensity distributions in reciprocal space. As in the body of the thesis, uniaxial symmetry is assumed about the flow axis. Since shear flow fundamentally does not promote uniaxially symmetric distributions of orientation, it must be recognized that this assumption is not appropriate; however, it is necessary to make any further quantitative progress, since otherwise 2D scattering patterns do not contain sufficient information to construct a representation of the growth and orientation of crystallites in 3D space. This assumption will be most suspect for weaker flow conditions (low rate and/or strain) in which the principal axis of molecular stretching will be rotated away from the flow direction towards the velocity gradient, but should become more appropriate at higher rates and strain where molecular stretching will increasingly align along the flow direction. In addition to assuming axial symmetry, a geometric correction for the curvature of the Ewald sphere is performed on the WAXS data (while it is negligible for SAXS data), as described in Section 2.1.

Under these necessary assumptions and corrections outlined in Section 2.4.1, the raw intensity from each of the 2D scattering image is extracted as a function of scattering vector q and apparent azimuthal angle φ' (true polar angle is φ), with an azimuthal binning of 1° increments (Figure A.3 and Figure A.4). A background subtraction is performed to isolate the scattering intensity contribution only from crystallization. The background correction process for SAXS is illustrated in Figure A.3a, in which the image immediate after flow ($t = 0$ min) is subtracted from all subsequent images. The resulting intensity after the background subtraction is shown in Figure A.3b, where the SAXS intensity shows a peak at q = 0.011 Å^{-1}. Based on the considerations described in Section 2.4.2.1, a q-range of 0.005 Å^{-1} to 0.04 Å^{-1} is selected for further analyses of scattering invariant and Hermans orientation factor, where the lower limit is selected to avoid any contributions from parasitic scattering near the beam stop, and the upper limit is selected such that the SAXS intensity approaches 0.

Unlike the SAXS background intensity that remains unchanged, the amorphous background in WAXS decreases as subsequent crystallization proceeds over time (Figure A.4a). Therefore, a polynomial is fit to the amorphous background in each image over the q-range spanning the primary peak is subtracted from the total intensity (Figure A.4b). Using this method, the intensity corresponding to the (200) peak is extracted from a q-range of q_1 = 0.775 Å^{-1} and q_2 = 0.9 Å^{-1}.

A.3.3 Quantifying the Crystallite Orientation Distribution

While recognizing that the applied flow does not fundamentally lead to a uniaxially symmetric orientation distribution, the orientation of crystallites is characterized from the 2D patterns using the Hermans order parameter $\langle P_2 \rangle$ assuming uniaxial symmetry:

$$\langle P_2 \rangle = \frac{3\langle \cos^2 \varphi \rangle - 1}{2}. \tag{2.14}$$

In the expression above, $\langle \cos^2 \varphi \rangle$ is the average of $\cos^2 \varphi$ weighted by the azimuthal intensity distribution $I(\varphi)$, which can be obtained by radially integrating the SAXS and WAXS absolute intensities over the specified q-range determined earlier, and given as

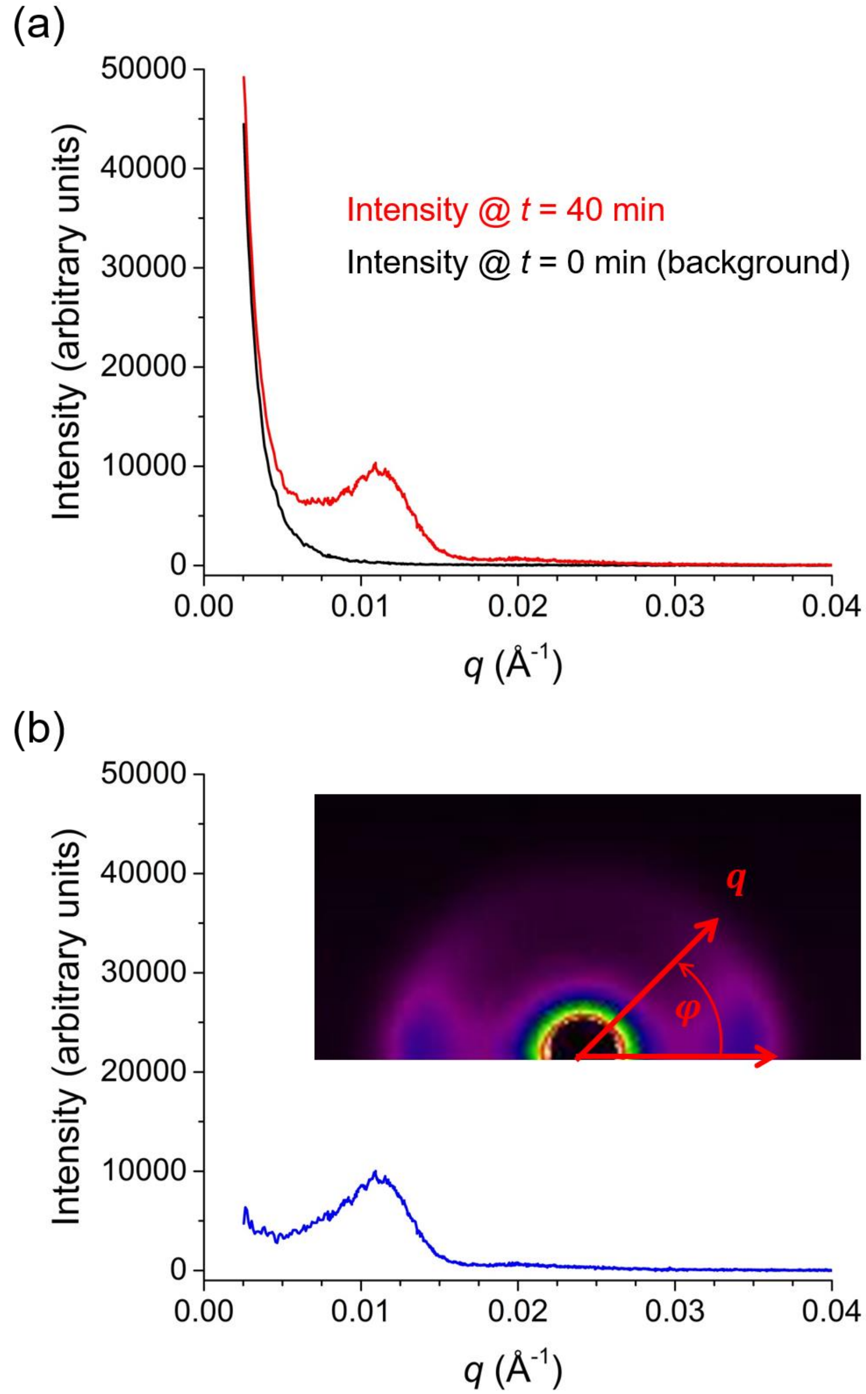

Figure A.3: Illustration of background subtraction process in SAXS. (a) The scattering intensity from the image immediately following flow (*t* = 0 min) is subtracted from intensities from the subsequent images. (b) The resulting intensity after the background correction. Flow direction is horizontal in the inset SAXS image.

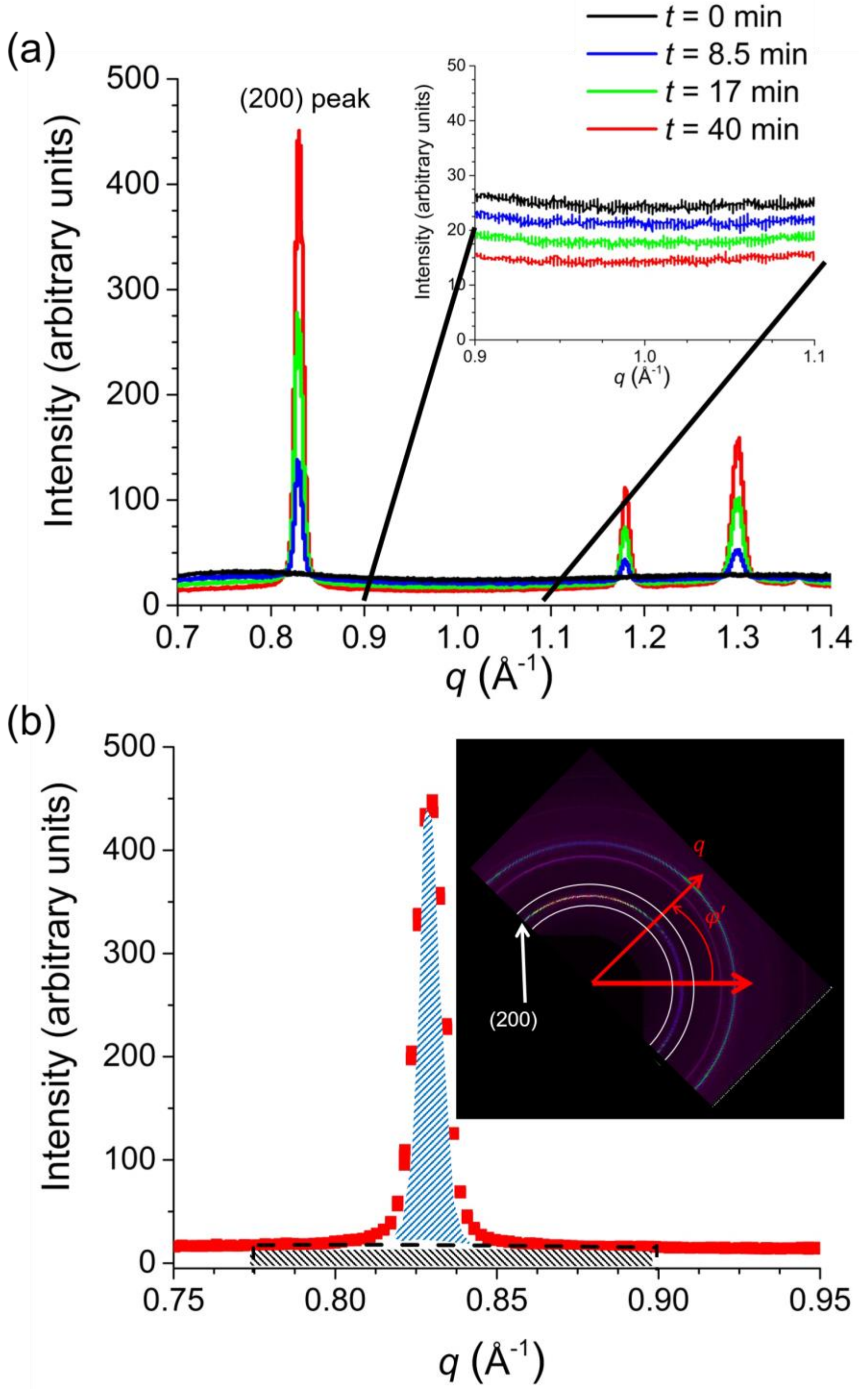

Figure A.4: (a) Change in WAXS intensity over time, highlighting the decreasing amorphous background in intensity. (b) Illustration of the background subtraction process involving the polynomial fitting to the amorphous background (black shaded area) to extract the intensity from the primary peak (blue shaded area) from the total intensity (red). Flow direction is horizontal in the inset WAXS image.

$$\langle \cos^2 \varphi \rangle = \frac{\int_0^{\pi} I(\varphi) \cos^2 \varphi \sin \varphi \, d\varphi}{\int_0^{\pi} I(\varphi) \sin \varphi \, d\varphi}. \tag{2.15}$$

As described in Section 2.4.3, the values of $\langle P_2 \rangle$ are normalized by the value about the angle of perfect alignment, such that $\langle P_2 \rangle$ always ranges between -0.5 to 1 and is analyzed with respect to the flow direction.

The degree of crystallite orientation is characterized from experiments at a fixed shear rate of $\dot{\gamma}$ = 4 s^{-1} (Figure A.5a) and from those at a fixed shear strain of γ = 16 (Figure A.5b). In both cases, SAXS and WAXS data show qualitatively similar trends in the evolution of $\langle P_2 \rangle$. In fact, the initial microstructures that crystallize are highly aligned, as reflected in the values of $\langle P_2 \rangle$ closer to 1 in both SAXS and WAXS at early times. As subsequent crystallization proceeds, the overall $\langle P_2 \rangle$ values decrease and reach constant values. Focusing in the final values of $\langle P_2 \rangle$, we notice that the final degrees of lamellar and crystal unit cell orientation are somewhat higher for higher applied strains; however, this strain dependence is rather weak (Figure A.5a; inset). Almost no rate dependence is observed in the final $\langle P_2 \rangle$ values from experiments at a fixed strain (Figure A.5b; inset). In general, little obvious rate or strain dependence is observed in both lamellar and unit cell orientations.

A.3.4 Quantifying the Extent of Crystallization

In SAXS, the volume-weighted SAXS invariant (*Q/V*) serves as an indicator of the extent of crystallization as it is defined as the total scattering power in all reciprocal space. The integration in Eq. (2.12) is performed over 0.005 Å^{-1} to 0.04 Å^{-1} as determined earlier. The extent

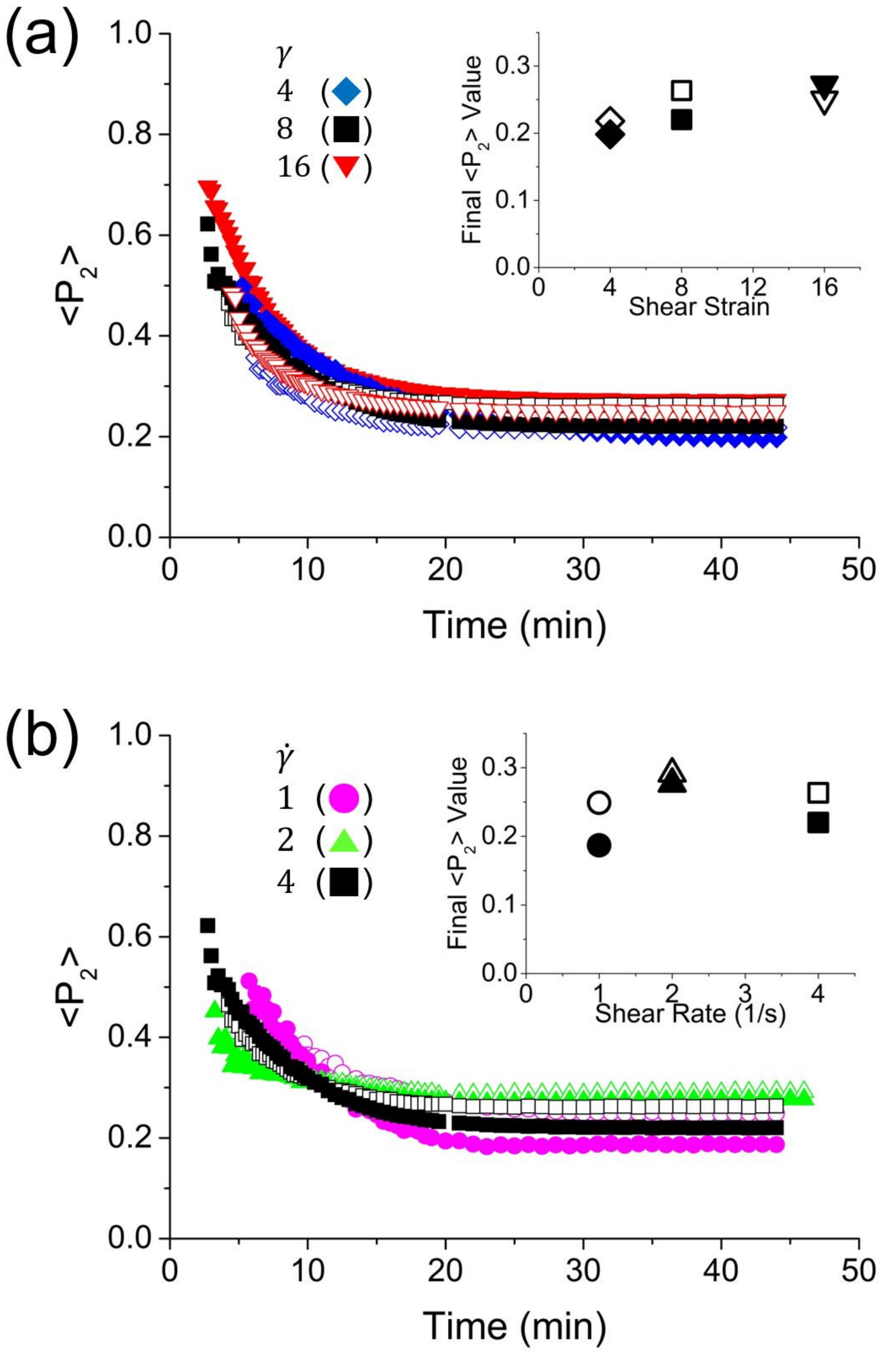

Figure A.5: Hermans order parameter from experiments at T_c = 106 °C at (a) $\dot{\gamma}$ = 4 s^{-1} under various strains and (b) γ = 16 under various rates. Open and closed symbols denote $\langle P_2 \rangle$ values obtained from SAXS and WAXS data, respectively. Inset figures show the final $\langle P_2 \rangle$ value plotted as a function of strain (a) and rate (b).

of crystallization from WAXS data is calculated from the intensity contribution only from the (200) peak as the following:

$$A_{200} = \int_{0}^{\pi} \int_{q_1}^{q_2} I_{200}(q, \varphi)\, q^2 \sin\varphi \, dq \, d\varphi \tag{A.1}$$

where $q_1 = 0.775$ Å^{-1} and $q_2 = 0.9$ Å^{-1}. Figure A.6 presents a comprehensive summary of the extent of crystallization calculated from SAXS and WAXS data from all experiments. At a fixed rate of $\dot{\gamma} = 4$ s^{-1}, the SAXS and WAXS measurements exhibit strong strain dependence, in which the crystallization kinetics is accelerated with increasing applied strain. We notice that both Q/V (Figure A.6a) and A_{200} (Figure A.6b) reach similar plateau values towards the end of the crystallization process. Calculations from SAXS and WAXS data are in good qualitative agreement with each other. Similar behavior is seen in experiments under different rates at a fixed shear strain, where crystallization kinetics is enhanced with increasing rate in both SAXS and WAXS calculations and similar trends in their growth are observed. However, both Q/V (Figure A.6c) and A_{200} (Figure A.6d) do not reach similar final values at the lowest shear rate of 1 s^{-1}; it appears crystallization has not yet been completed in the time over which crystallization was monitored.

The qualitative resemblance between the extent of crystallization calculated from SAXS and WAXS, particularly when varying strains, is quite clear. This raises an interesting question of how Q/V and A_{200} relate to the fractional degree of crystallinity ϕ_c, a more practical quantity, that is embedded in both of the calculated values. Although formulated differently, these indicators of the extent of crystallization should both reflect the same fundamental quantity—the

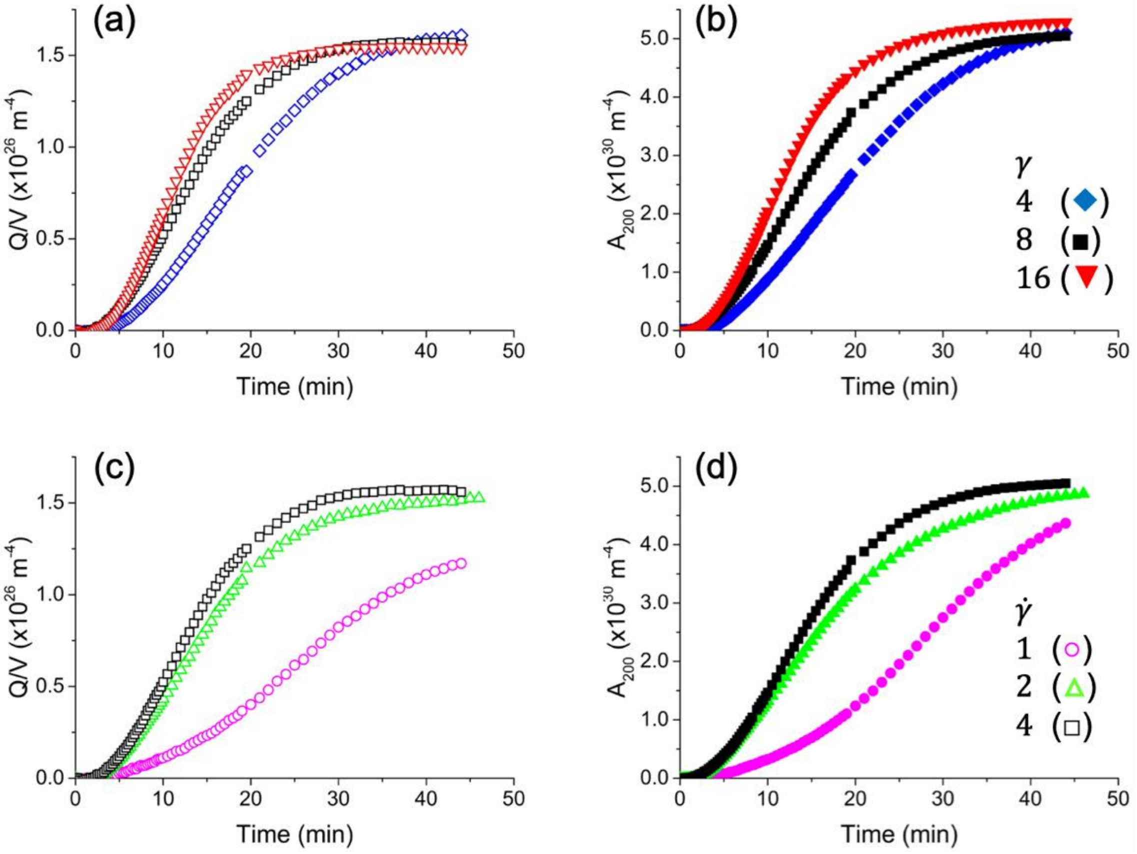

Figure A.6: Extent of crystallization from experiments at T_c = 106 °C at (a, b) $\dot{\gamma}$ = 4 s^{-1} under various strains and (c, d) γ = 16 under various rates. Open and closed symbols denote values of *Q/V* and A_{200} obtained from SAXS and WAXS data, respectively.

increasing amount of crystalline mass in the sample. This suggests that it would be possible to self-consistently determine the degree of crystallinity from SAXS and WAXS data by optimizing the consistency between the two, as described below.

In an ideal two-phase model, the SAXS invariant is related to ϕ_c through:

$$Q/V = (\Delta\rho)^2\phi_c(1-\phi_c) \tag{A.2}$$

where $\Delta\rho$ is the electron density difference between the crystalline and amorphous phases.[96] Based on the fact that the SAXS invariants reach similar plateau values towards the end of the experiment, the "plateau" *Q/V* values averaged from all experiments can be used to represent the final degree of crystallinity $\phi_{c,\mathrm{final}}$. In addition, since the invariant data in Figure A.6 do not pass through a maximum, ϕ_c must be less than 0.5 since Eq. (A.2) is symmetric about ϕ_c = 0.5. Using a range of possible $\phi_{c,\mathrm{final}}$ values between 0 and 0.5, a corresponding range of $(\Delta\rho)^2$ can be evaluated from Eq. (A.2). Each $(\Delta\rho)^2$ value can then be substituted into Eq. (A.2) to calculate the evolution of ϕ_c over time, or $\phi_{c,\mathrm{SAXS}}(t)$.

In WAXS, A_{200} is directly proportional to the degree of crystallinity:

$$A_{200} = C\phi_c \tag{A.3}$$

where *C* is a scaling factor. This implies that an error function (*E*) between $\phi_{c,\mathrm{SAXS}}(t)$ and WAXS in Eq. (A.3) (in the form of $\phi_{c,\mathrm{WAXS}}(t) = A_{200}(t)/C$) can be defined as:

$$E = \frac{\sum\left[\phi_{c,\mathrm{SAXS}}(t) - \phi_{c,\mathrm{WAXS}}(t)\right]^2}{\sum\left[\phi_{c,\mathrm{SAXS}}(t)\right]^2} \tag{A.4}$$

where the objective is to minimize *E* by changing *C*. This process (Figure A.7a) can be iterated with the updated *C* to "guess" what the final ϕ_c would be for a range of ϕ_c, until determining a ϕ_c value that produces the minimum in *E* (Figure A.7b).

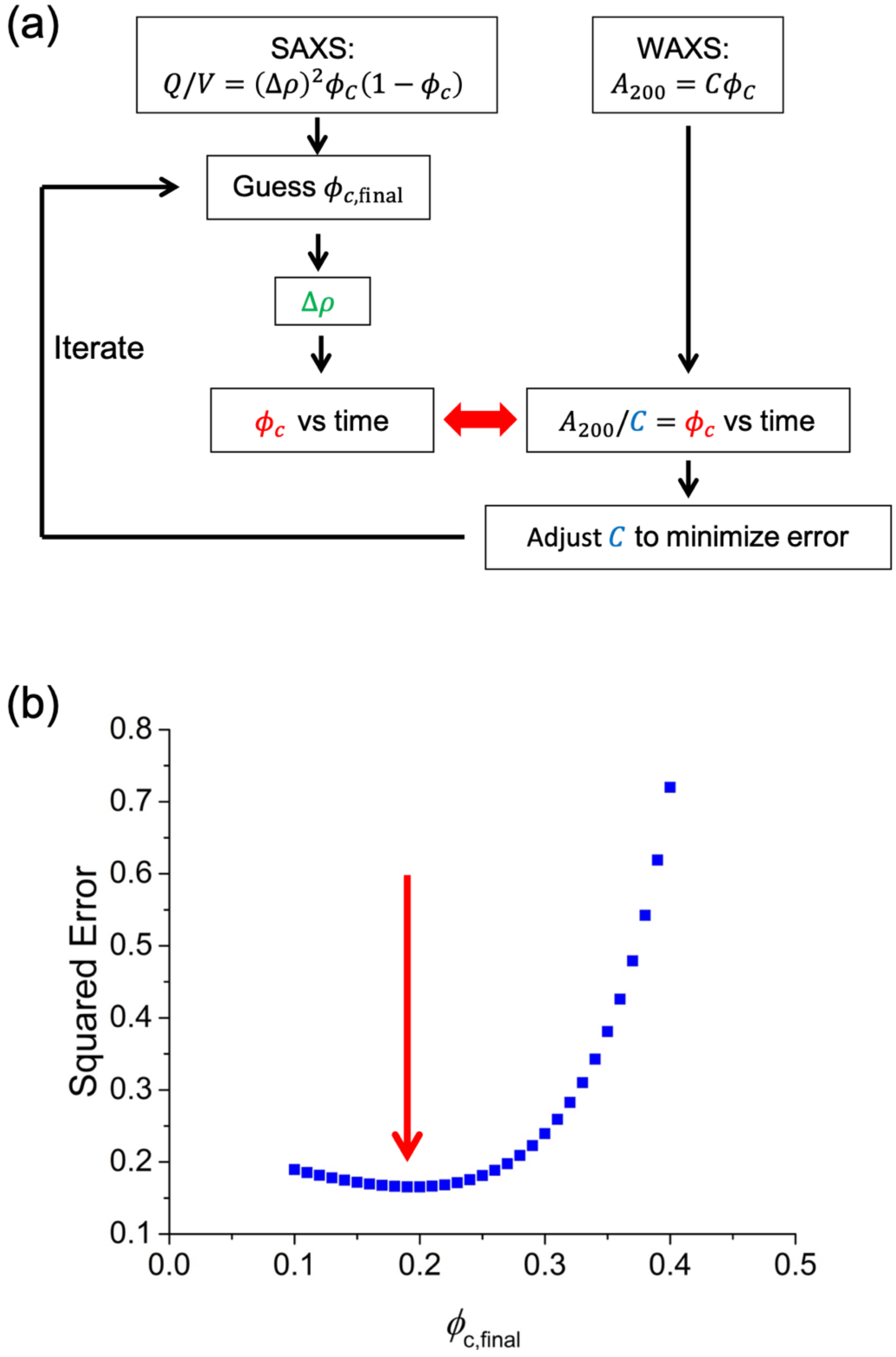

Figure A.7: (a) Optimization algorithm to self-consistently determine the fractional degree of crystallinity from SAXS and WAXS data. (b) Error minimization between the final degree of crystallinity (obtained from *Q/V*) and scaled A_{200} for a range of possible final degrees of crystallinity.

Figure A.8 presents the calculated degree of crystallinity via optimization strategy that seeks self-consistency between SAXS and WAXS. We notice that the method produces good overall agreement in the calculated fractional degrees of crystallinity, except at the slowest shear rate. This may be due to the fact that the largest errors associated with deviations from the assumed uniaxial symmetry around the flow direction are expected under weak flow conditions. SAXS and WAXS features are concentrated in different directions in reciprocal space (along and perpendicular to the molecular orientation direction, respectively), and hence would be affected differently by deviations from the uniaxial symmetry. The final degree of crystallinity of ~20% seems lower than what would be expected from a semi-crystalline polymer. One could speculate that this may be due to the failure in the ideal two-phase model that was used to calculate ϕ_c from the SAXS invariant. It is also possible that further crystallization will occur upon cooling the sample to room temperature, to reach the higher values that are typically quoted. A somewhat different approach to try to self-consistently extract ϕ_c from SAXS and WAXS data for a similar study of poly(1-butene) flow-induced crystallization following uniaxial extensional flow yielded similar values for the final degree of crystallinity.[95]

A.4 Conclusion

In this work, the flow-induced crystallization of poly(1-butene) under shear flow has been characterized using *in situ* x-ray scattering techniques. Simultaneous SAXS and WAXS measurements demonstrate that no obvious rate or strain dependence is observed in both lamellar and unit cell orientations. However, accelerated crystallization kinetics is observed with increasing deformation rate as well as total applied strain. An optimization strategy was proposed

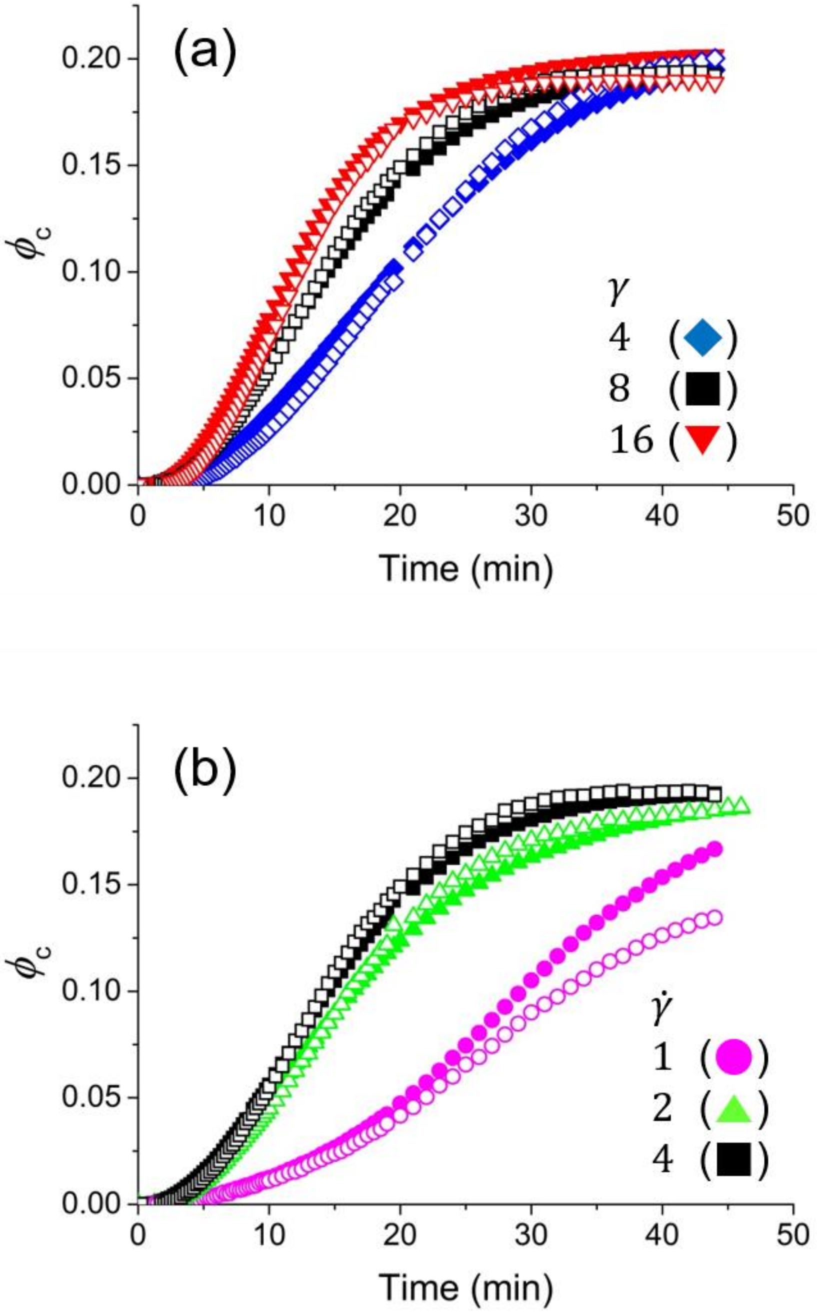

Figure A.8: Calculated fractional degrees of crystallinity from SAXS and WAXS data using the optimization strategy illustrated in Figure A.7. (a) Experiments conducted $\dot{\gamma}$ = 4 s^{-1} under various strains; (b) γ = 16 under various rates. Open and closed symbols denote SAXS and WAXS data, respectively.

to determine the crystalline volume fraction calculated from SAXS and WAXS self-consistently, which led to good agreement in the evolving crystallinity probed at the lamellar scale and unit cell level.

Appendix B

X-ray Photon Correlation Spectroscopy Studies of Structural Irreversibility in a Colloidal Gel under Oscillatory Shear Flow

B.1 Introduction

Soft solids exhibit solid-like elastic deformation under applied stress below the yield limit, or complex and nonlinear flow behavior under large deformations. These interesting mechanical properties arise from changes in their internal structure on mesoscopic length scales (10 – 1000 nm). However, in disordered soft materials, the lack of well-defined crystalline order on these small length scales makes it challenging to identify the microstructural features that give rise to such complex and nonlinear rheological behavior. This has naturally led to efforts to accurately probe the microscopic dynamics of amorphous solids to understand the connection between their microscopic structures and macroscopic mechanical properties.

In recent years, x-ray photon correlation spectroscopy (XPCS) has emerged as a powerful technique to probe the structural dynamics of soft materials including glasses, polymers, and gels. Similar in principle to dynamic light scattering which uses visible light, XPCS monitors speckle x-ray scattering patterns resulting from a partially coherent x-ray beam incident on a material.[145] The speckle patterns reflect the detailed instantaneous electron density distribution within the sample, while time-dependent fluctuations in the speckles contain information about its change in response to microscopic motions within the sample. Owing to the shorter wavelength of x-rays, XPCS is particularly suitable for studying materials in which the structural dynamics of interest lie within the range of length scales typically probed in the small-angle scattering regime. This provides XPCS the advantage of measuring dynamic processes on nanometer length scales and times scales of 0.01 – 100 s, which are length and time scales that coincide with the typical ranges that are relevant to the rheology of soft materials.

Motivated by this complementarity between XPCS and rheology, recent studies report XPCS measurements on soft materials subjected to shear flow. However, such measurements are not trivial to perform as the applied shear directly affects the measured intensity autocorrelation function, in which the change in microscopic dynamics in response to flow is manifested. Chung *et al.* decoupled the dominant effects associated with the applied shear from the autocorrelation function by inducing structural changes through pre-shearing and using XPCS following flow cessation to monitor the evolution of the dynamics of a depletion gel over an extended period.[146] While it was appropriate to impose a strong flow history on a sample with slow dynamics, the flow was poorly-defined as the sample was mixed and extruded into a chamber. Fluerasu and co-workers performed *in situ* XPCS measurements during shear and demonstrated that it was possible to measure the diffusive dynamics in the sample isolated from the effects of shear under specific conditions.[147–149] However, XPCS was applied under inhomogeneous shear (pressure-driven flows). As it is preferable to employ shear flow in which the velocity gradient is spatially uniform, Burghardt *et al.* explored the application of XPCS during homogeneous shear.[150]

Recent studies have proposed and demonstrated a strategy to apply oscillatory shear flow to a material that exhibits no internal structural dynamics and use XPCS to monitor the temporal evolution of the autocorrelation function dominated by shear. This concept relies on the fact that under small-amplitude oscillations, perfectly reversible deformation in the structure leads to "echoes" in the autocorrelation function that return to its initial value once every strain cycle. On the contrary, at large applied strains, irreversibility in structural dynamics contributes to decay in the echoes of the autocorrelation function. Laurati *et al.* adopted this principle to investigate the yielding behavior and plastic rearrangements of colloidal gels subjected to oscillatory shear flow by tracking the correlation function using diffusing wave spectroscopy—a light scattering analogue to XPCS.[151] A similar approach was employed by Rogers *et al.* who reported *in situ* XPCS echo peak measurements (as opposed to the entire waveform) on a colloidal gel under oscillatory shear that revealed a threshold strain beyond which irreversible particle rearrangements occur.[152] The study showed evidence of reversible microscopic dynamics at small strains below this threshold while the rheological mechanical response was nonlinear. In this Appendix section, we explore the application of simultaneous *in situ* XPCS and rheometry under oscillatory shear flow, thereby providing a comprehensive insight into the microscopic origins of structural irreversibility in a colloidal gel underlying its nonlinear rheological response.

B.2 Background

The theoretical and technical aspects relevant to XPCS are provided in detail in other works[147–149,153,154] Here, we present a brief overview of XPCS during homogeneous shear described in our previous work[150] and expand upon this to XPCS during oscillatory shear flow. In XPCS, temporal fluctuations of the scattering intensity are measured and expressed as the intensity autocorrelation function:

$$g_2(\boldsymbol{q}, t) = \frac{\langle I(\boldsymbol{q}, t_0) I(\boldsymbol{q}, t_0 + t) \rangle_{t_0}}{\langle I(\boldsymbol{q}, t_0) \rangle_{t_0}^2}, \tag{B.1}$$

where $\boldsymbol{q}$ is the scattering wave vector, *t* is time, and angled brackets indicate ensemble averages over points t_0 in the time series. The intensity autocorrelation function can also be written in terms of the intermediate scattering function $g_1(\boldsymbol{q}, t)$ through the Siegert relation

$$g_2(\boldsymbol{q}, t) = 1 + \beta |g_1(\boldsymbol{q}, t)|^2 \tag{B.2}$$

where β is a contrast factor that varies between 0 and 1 depending on the beam coherence properties and scattering geometry. The intermediate scattering function contains details about particle-particle movement correlations and thus is a key quantity that describes the underlying dynamics of a sample.

For colloidal suspensions subjected to shear flow, Fluerasu *et al.*[147] showed that the intermediate scattering function measured by homodyne XPCS can be described as

$$|g_1(\boldsymbol{q}, t)|^2 = \left|g_{1,D}(\boldsymbol{q}, t)\right|^2 \left|g_{1,T}(\boldsymbol{q}, t)\right|^2 \left|g_{1,S}(\boldsymbol{q}, t)\right|^2, \tag{B.3}$$

reflecting contributions from diffusive motion (*D*) of particles, from particle transit (*T*) through the scattering volume, and from shear deformation (*S*). In the absence of flow, the diffusive dynamics of the system governs the form of the intermediate scattering function since transit and shear terms do not come into play. For a sample that undergoes simple Brownian dynamics, the intermediate scattering function is then an exponential decay that involves a characteristic time $\tau_D \sim 1/(D_0 q^2)$ determined by diffusivity D_0 and the scattering vector. Conversely, diffusion effects can be neglected for samples that show slow structural relaxation (i.e. $\tau_D \gg 1$) within the relevant time scales, as is the case in this work.

In the presence of flow, the intermediate scattering function is determined by the transit and/or shear terms as some particles leave the scattering volume while other particles enter the path of the beam. The transit time effect arises when particles that move in and out of the scattering volume result in a loss of correlation, causing the intermediate scattering function to decay. This process involves a characteristic time scale $\tau_T \sim w/V$ determined by the width of the beam (w) and characteristic flow velocity (V) that is taken as the moving plate velocity. In other words, the particle transit contribution to the intermediate scattering function is determined by the flow condition, while its detailed functional form depends on the beam profile.[147] Under the experimental conditions used in this work, transit time effects are expected to be negligible.

The shear term can be determined given the velocity profile over the scattering volume. This process involves a characteristic time scale $\tau_S \sim 1/(q_{\parallel} H\dot{\gamma})$, where $q_{\parallel}$ is the component of the scattering vector parallel to the flow direction, H is the sample thickness, and $\dot{\gamma} = V/H$ is the shear rate. While the characteristic time for shear is shorter than that for transit in this work, transit time effects cannot be neglected at applied shear strains comparable to and above the characteristic strain for transit as the loss of correlation is driven by applied strain. Thus, it is important to note that the effect of shear can be isolated only when the sample exhibits no internal structural dynamics and is subjected to small deformations.

Burghardt *et al.*[150] showed that the intermediate scattering function measured under unidirectional shear flow, while neglecting the diffusion and transit terms, is given by

$$\left|g_{1,S}(\boldsymbol{q},t)\right|^2 = \frac{\sin^2(q_{\parallel} H\dot{\gamma}t/2)}{(q_{\parallel} H\dot{\gamma}t/2)^2}. \tag{B.4}$$

The intermediate scattering function under oscillatory shear can then be predicted by replacing the applied strain $\gamma(t) = \dot{\gamma}t$ with $\gamma(t) = \gamma_0 \sin(\omega t)$ such that

$$|g_1(\boldsymbol{q}, t)|^2 = \frac{\langle \sin^2[q_\parallel H \gamma_0 \sin(\omega t)/2] \rangle_\phi}{\langle [q_\parallel H \gamma_0 \sin(\omega t)/2]^2 \rangle_\phi}, \qquad \text{(B.5)}$$

where γ_0 and ω respectively are the magnitude and frequency of the oscillation, and angled brackets denote averaging over all phase ϕ. Figure B.1 illustrates the waveform of the intermediate scattering function as predicted by Eq. (B.5) using H = 0.2 mm and $q_\parallel$ = 0.00116 Å^{-1}, demonstrating that the scattering function is periodic and returns to its initial value at every strain period. It is also clear that only a small amount of shear strain is required to decorrelate the speckle patterns. The predicted waveform serves as a basis for comparison at smaller strains (where reversible dynamics are expected to result in measured autocorrelation functions qualitatively similar to Figure B.1) and at larger strains (where echo peaks are expected to decay with increasing applied strain and oscillation cycles).

B.3 Experimental Methods

A colloidal gel was prepared from a suspension of silica nanoparticles with diameters of ~32 nm dispersed in decalin with added polystyrene of molecular weight ~1300 g/mol. In the presence of a nonabsorbing polymer, the nanoparticles experience a depletion attraction to form a gel with final conditions of a colloidal volume fraction of 0.35 and polymer concentration of c_p/c_p^* = 0.194, where c_p^* is the overlap concentration. The depletion gel shows rheological properties typical of soft disordered solids: solid-like elastic properties where the storage modulus (*G'*) dominates over the loss modulus (*G''*) at low strains (Figure B.2a), and nonlinear

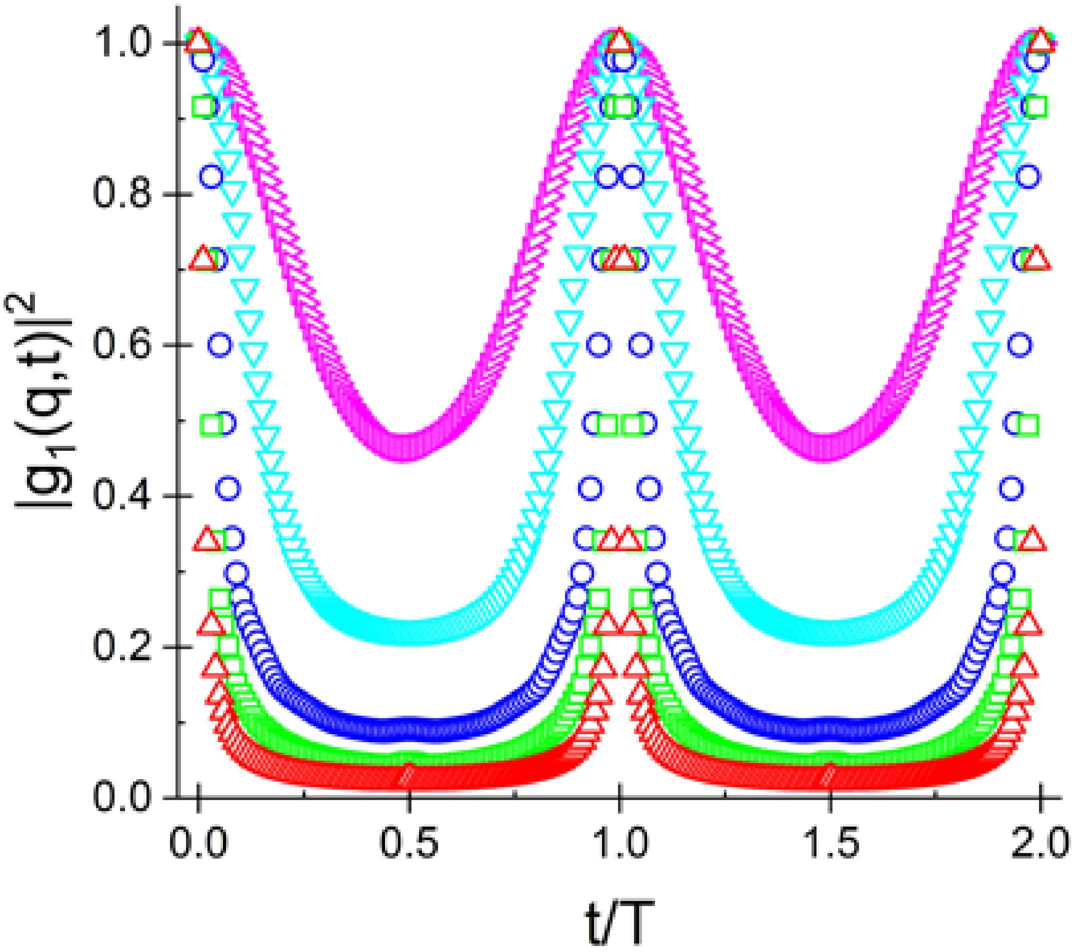

Figure B.1: Prediction of the intermediate scattering function subjected to small amplitude oscillatory shear in the absence of diffusive dynamics, using Eq. (B.5), H = 0.2 mm, and $q_{||}$ = 0.00116 Å^{-1}. At small strains, $g_1(\boldsymbol{q},t)$ periodically returns to its initial value every strain period (T), reflecting reversible dynamics at small deformations. Applied strains: 0.1% (▷), 0.2% (▽), 0.5% (○), 1.0% (□), 2.0% (△).

viscoelastic properties (decreasing *G'* that eventually crosses *G"*) at larger strains (Figure B.2b). The onset of nonlinear rheology in the mechanical response is at an applied strain of 0.1%.

Simultaneous *in situ* XPCS measurements and rheometry were conducted to study the onset of microscopic yielding process in the colloidal gel that is expected to correspond to its transition to the nonlinear rheological behavior. Small-angle XPCS measurements were performed at beamline 8ID-I of the Advanced Photon Source at Argonne National Laboratory, using a 20 x 20 μm x-ray beam of energy 7.35 keV. Data were collected using an SMD charge-coupled device (CCD) detector at a rate of approximately 200 frames/s in a series of 8000 data frames. Scattering intensity was measured over a 256 x 512-pixel region of interest to facilitate rapid data acquisition, but only a portion of these data were useable due to beam damage on the detector. Data collected under flow were analyzed using a series of smaller "bins" to compute autocorrelation functions using well-defined values of $q_{\|}$. Data presented here used $q_{\|} = 0.00116$ Å^{-1}.

Shear flow was applied using an Anton Paar MCR 301 rheometer. The colloidal gel was loaded in a polycarbonate Couette fixture consisting of a "cup and bob" with diameters of 19.9 mm and 19.5 mm, respectively, resulting in a sample thickness *H* of 0.2 mm (Figure B.3a). Oscillatory shear flow was driven by rotating the "bob" at 2.013 Hz to minimize the phase difference between the data collection rate (201.27 frames/s) and the oscillation frequency. A series of oscillatory shear flow was applied at strains ranging from 0.1% to 50%, with at least three selected strains per decade. The experimental setup is identical to performing a strain sweep experiment over an extended period of time, as illustrated in Figure B.3b. At each applied strain, the sample was exposed to two sequences of XPCS scans, in which the x-ray beam

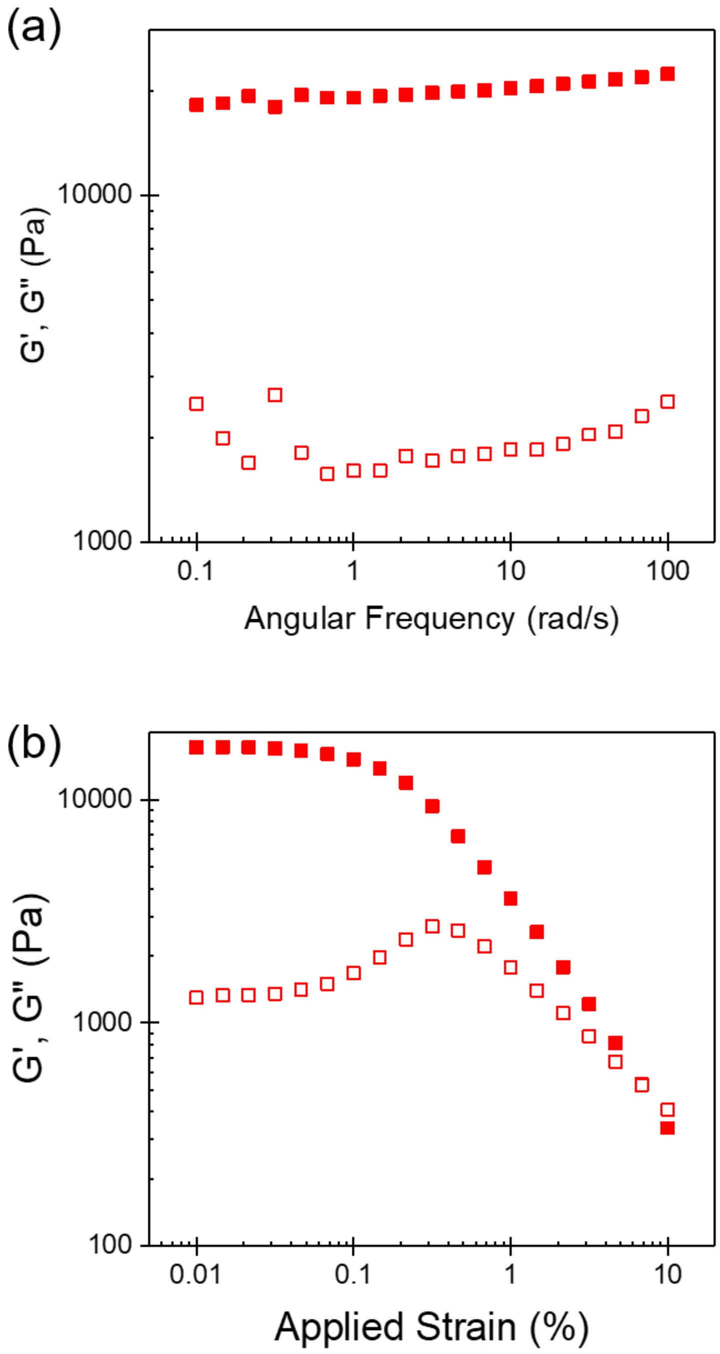

Figure B.2: Storage (■) and loss (☐) moduli measured at 0.01 % strain as a function of angular frequency (a) and at 10 rad/s as a function of strain amplitude (b). Colloidal gel shows elastic response at low strains, while transition from linear to nonlinear rheology starts to occur at $\gamma \geq 0.1\%$.

traveled in the gradient direction through the center of the Couette cell. The series of experiments were repeated at various sample locations by changing the vertical position of the x-ray beam while its path remained in the gradient direction.

B.4 Results and Discussion

Figure B.4a presents small-angle x-ray scattering (SAXS) data under quiescent conditions and reveals the limited q-range explored in this experiment. Within this narrow range, XPCS data were measured at $q_{||}$ = 0.00116 Å^{-1}where the sample scattered strongly enough to obtain reasonable data given the extremely short exposure times. XPCS experiments were also restricted to this low q value to ensure that the echoes in the intensity autocorrelation function were measurable, as Eq. (B.5) predicts that peaks become narrower with increasing q, leading to a possibility of the peak measurements being too narrow to resolve. Figure B.4b presents an XPCS scan of the sample under quiescent conditions, demonstrating that the colloidal gel does not undergo any structural relaxation over the experimental time of ~40 seconds. As discussed above, a sample with a long relaxation time is desirable as any change in $g_2(\mathbf{q}, t)$ waveform behavior can then be assumed to directly reflect the change in response to microscopic motion due to flow.

Under small deformations of $0.1\% \leq \gamma \leq 2.0\%$ (Figure B.5), the sample exhibits reversible dynamics and the shape of the correlation function is in qualitative agreement with the waveform described by Eq. (B.5). As the applied strain increases, the measured correlation functions reach a lower minimum value and the peaks get narrower while returning to the same

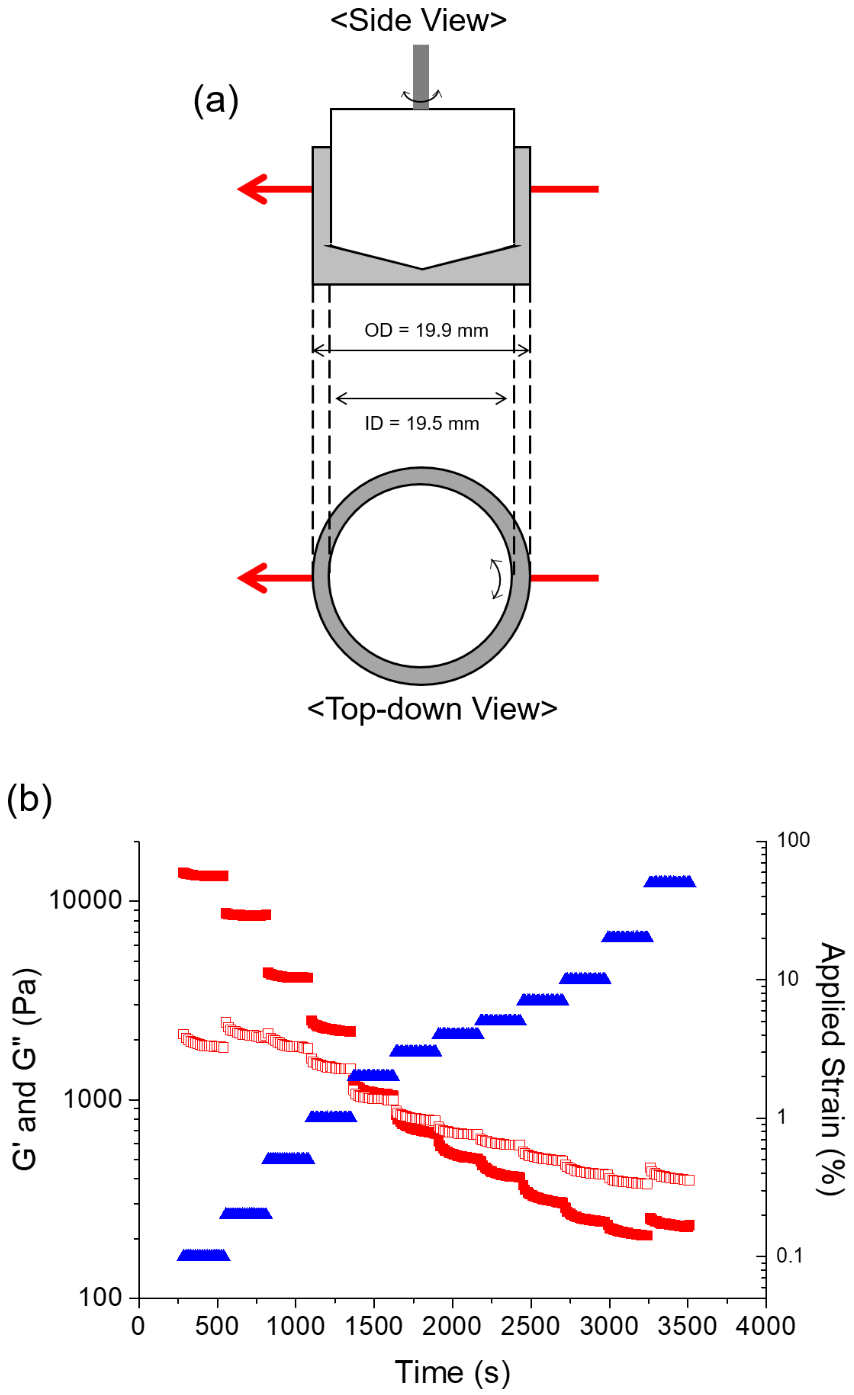

Figure B.3: (a) Overview of the experimental setup for simultaneous *in situ* XPCS and rheometry. Red arrow denotes the x-ray beam. (b) Storage (■) and loss (□) moduli were measured under oscillations at 2.013 Hz over applied strains (▲) ranging from 0.1% to 50%. At each strain, XPCS data were collected to capture the microscopic structural response while mechanical data were being measured simultaneously.

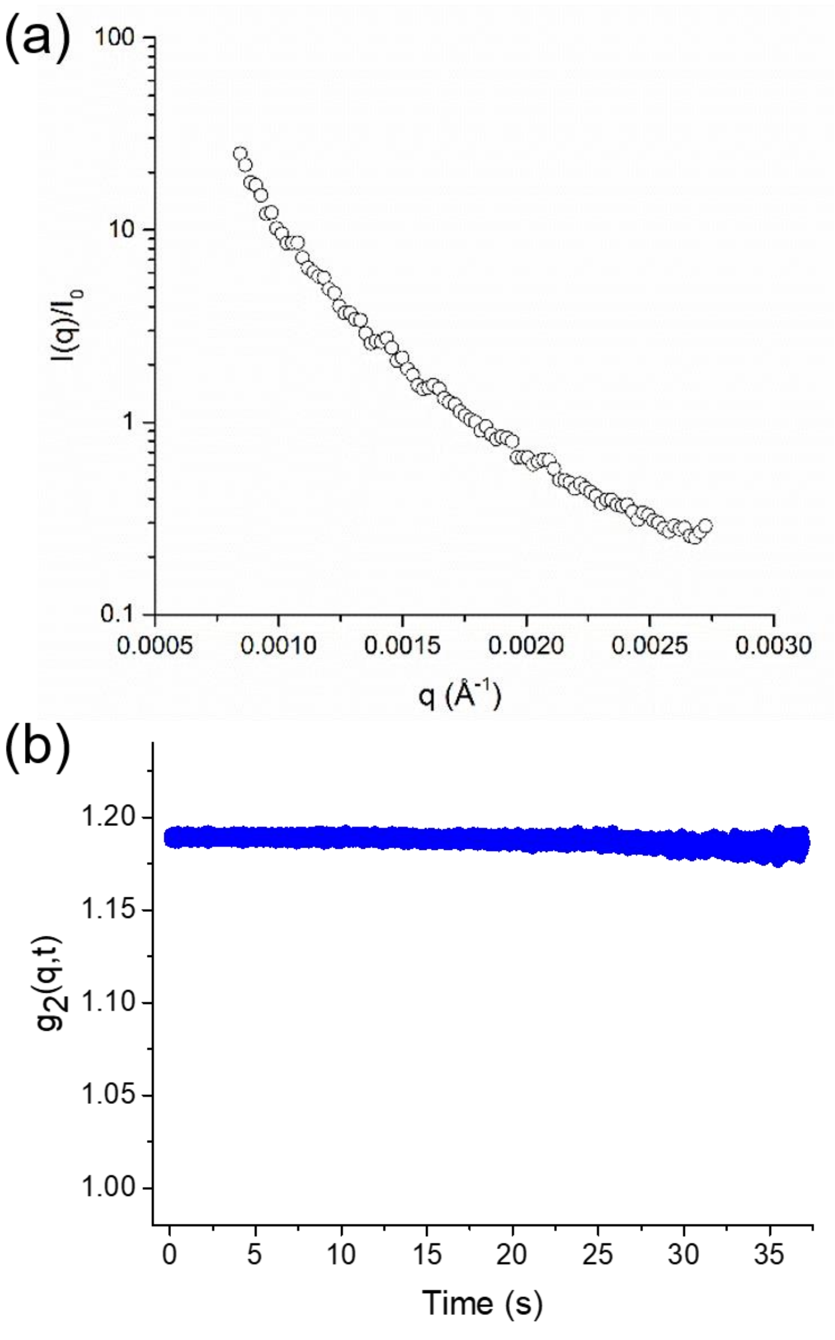

Figure B.4: Dynamics of the colloidal depletion gel in the absence of flow. (a) Static SAXS intensity was measured over a limited q-range due to damages on the CCD detector. This led to collecting XPCS data at $q_{||} = 0.00116$ Å^{-1} where the sample scattered strongly and exhibited slow dynamics. (b) XPCS scan under quiescent conditions shows that $g_2(\boldsymbol{q},t)$ remains constant for ~40 s, indicating no signs of intrinsic microscopic motion over the experimental time scale.

initial value every oscillation cycle, consistent with the predictions of Eq. (B.5). This qualitative behavior is observed at short times (Figure B.5a) and persists through long times (Figure B.5b). Figure B.5c demonstrates how structural reversibility is manifested in eight different sample locations, but it is evident that quantitative differences exist based on the dissimilar shapes of the waveform in detail. At a strain of 2.0%, the minimum of each measured correlation function falls short of the value of 1 by varying amounts, unlike the predicted waveform that reaches this minimum value at this applied strain. The primary assumption that leads to the waveform shapes predicted in Figure B.1 is that the velocity gradient in the shearing deformation is uniform; all other factors that influence this behavior are known and fixed. In the earlier study on a simpler material (dilute colloidal dispersion in steady shear flow), these same assumptions led to quantitative prediction of the autocorrelation function. The variability seen in Figure B.5c, and lack of detailed agreement with predictions of Figure B.1, thus suggests that the velocity gradient in these experiments may not, in fact, be uniform. Such heterogeneity would not be unexpected in a sample with complex microscopic structure like a colloidal gel, where local fluctuations in structure or particle density could lead to deviations from the assumed smooth and uniform deformation gradient (e.g., microscopic deviations from affine deformation). However, although spatial inhomogeneity in the details of the waveform is present across different detecting regions, the “echoes” reliably return to their starting value over the full duration of the experiment, indicating that the microscopic structural deformation, while probably complicated in detail, is still fully reversible.

Application of oscillatory shear at larger strains ($\gamma > 2.0\%$) causes the microscopic structural dynamics in the colloidal gel to become irreversible. Figure B.6a shows that decay in

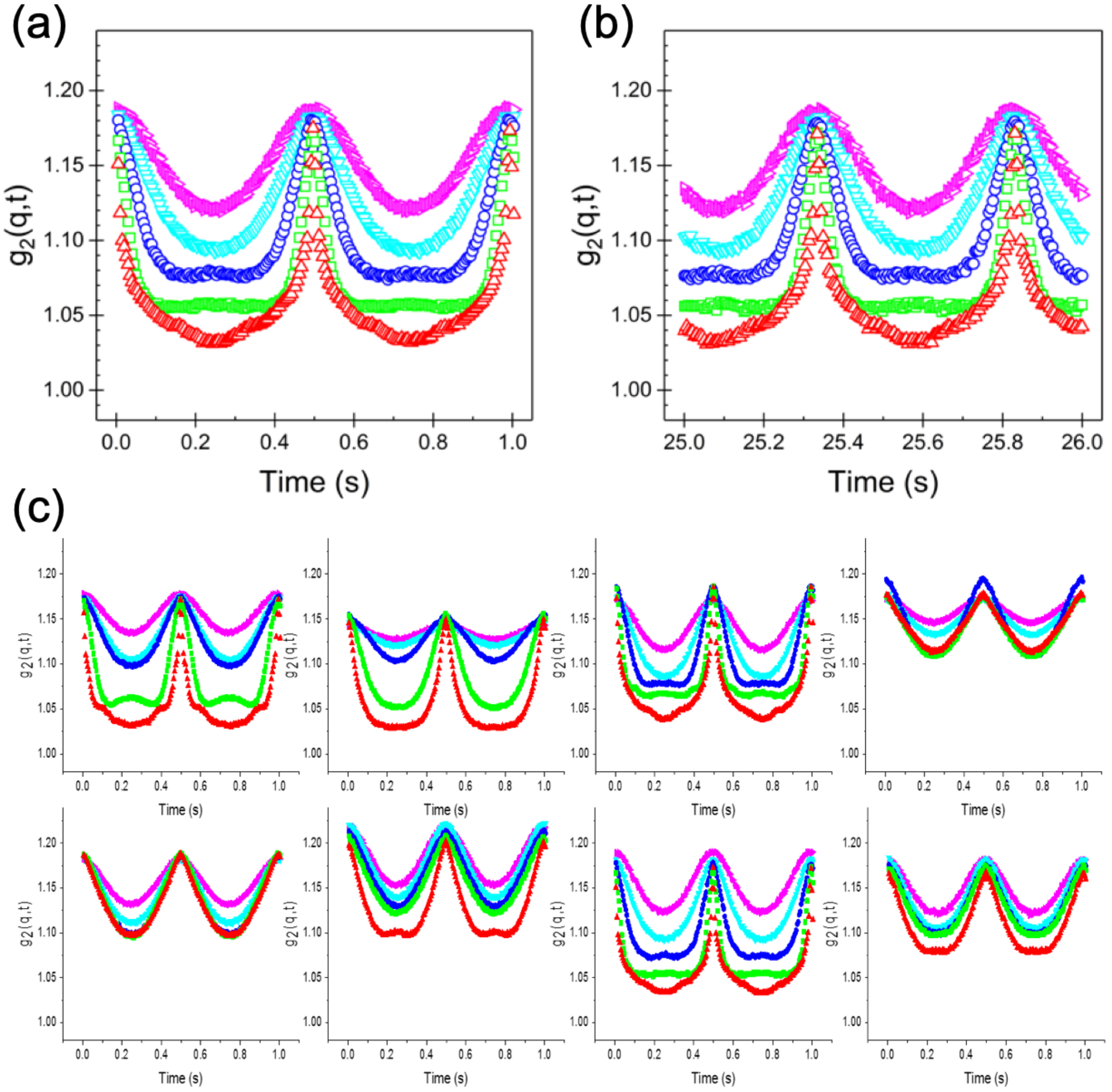

Figure B.5: Intensity autocorrelation functions measured at $q_{\parallel}$ = 0.00116 Å^{-1} in colloidal gel under small amplitude oscillatory shear flow. Applied strains: 0.1% (▷), 0.2% (▽), 0.5% (○), 1.0% (□), 2.0% (△). Under small deformations, reversible dynamics at short times (a) continue through long times (b), and waveforms measured at different vertical scanning positions show quantitative differences but qualitative agreement (c).

the measured autocorrelation functions is immediate after one or two oscillation cycles. Shortly after two periods, the echo peak values decrease with increasing strain. Structural irreversibility observed at short times continues through long times, as peaks no longer return to the initial value (Figure B.6b).

Manifestations of such microscopic irreversibility across different sample locations can be observed by tracking the echo peak value at each oscillation cycle as a function of the cycle number (Figure B.7). At small strains (0.5% and 2.0%), the maximum peak values remain constant throughout the entire experiment over all scanning regions. Decay in the echoes starts to occur at 5.0% strain across all locations except in one experiment. At applied strains above 5.0%, increasing strains accelerate the decay in the correlation function. It is evident that while spatial inhomogeneity is present among different scanning regions, the onset of microscopic structural irreversibility occurs between applied strains of 2.0 – 10%. Similar to the observations from Figure B.5c, experiments vary in detail quantitatively, but consistent qualitative behavior is robustly observed. However, comparing the onset strain of microscopic irreversibility to that of nonlinear rheological response in the bulk suggests that local deformation does not necessarily match the bulk response. The bulk rheology indicates that nonlinearity arises at a rather small strain of 0.1% relative to the onset strain of irreversible dynamics observed from XPCS measurements (Figure B.8). This suggests that homogenous affine deformation may not be easily assumed since local microscopic deformation is more complex.

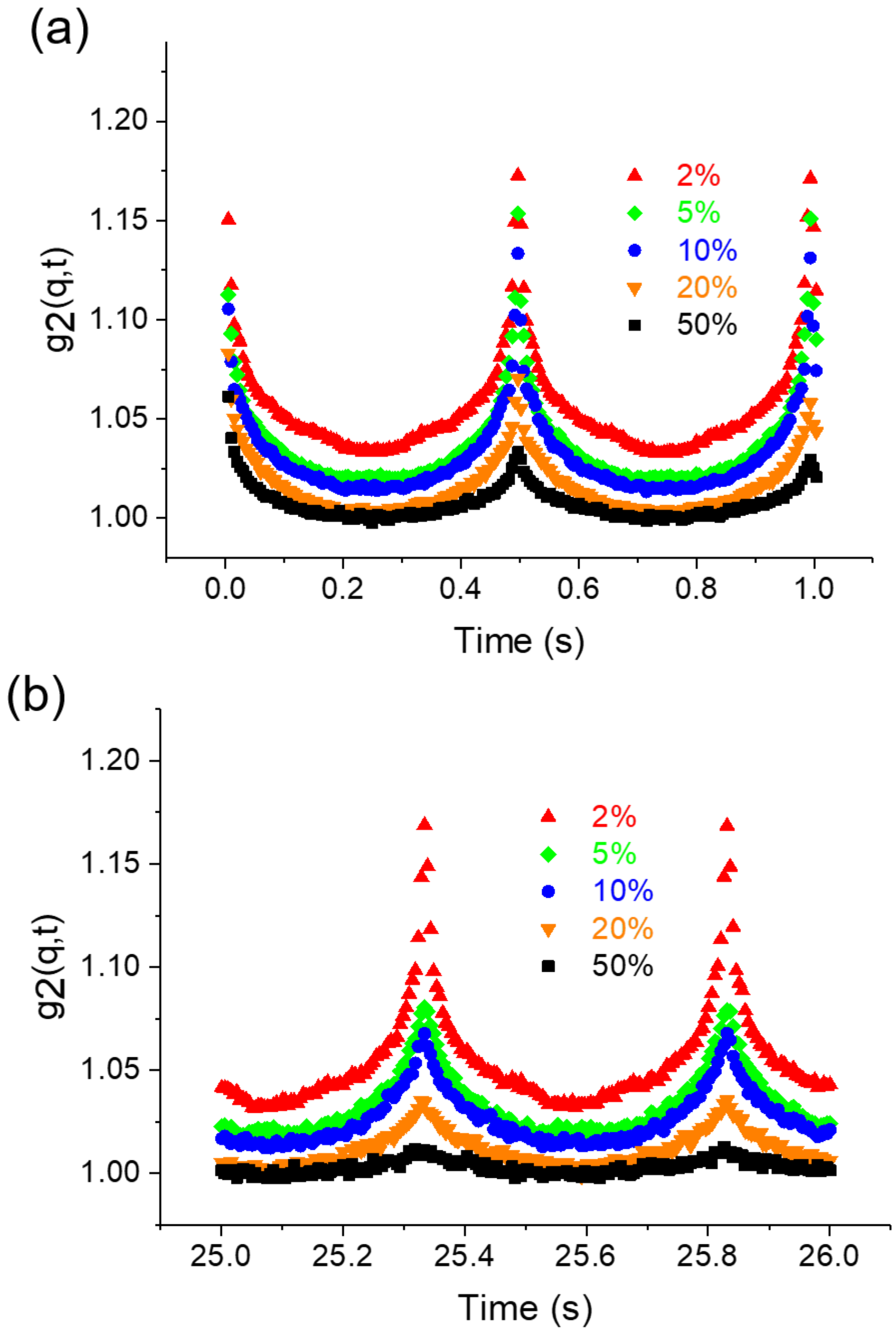

Figure B.6: Intensity autocorrelation functions measured at $q_{\|}$ = 0.00116 Å^{-1} in colloidal gel subjected to large amplitude oscillatory shear. At large applied strains, correlation functions decay immediately after two oscillation cycles (a) and irreversible dynamics continue through long times (b).

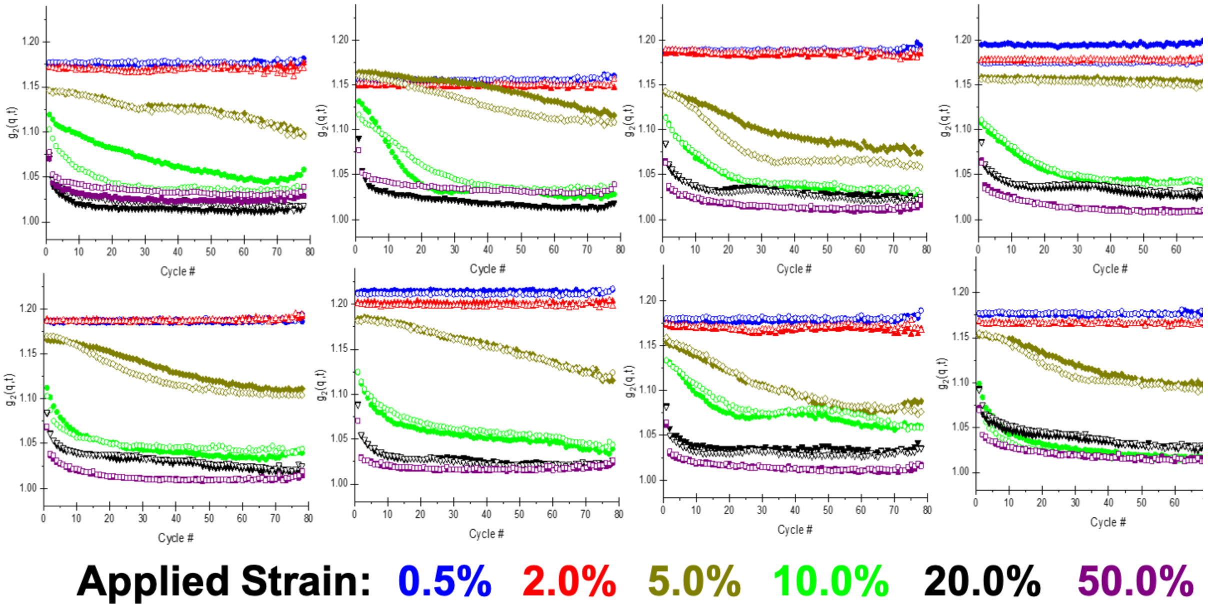

Figure B.7: Manifestations of irreversible dynamics in the sample across different scanning regions. Onset of structural irreversibility occurs between applied strains of 2.0 – 10%. The vertical axis displays $g_2(\boldsymbol{q},t)$ and the horizontal axis is the number of oscillation cycle.

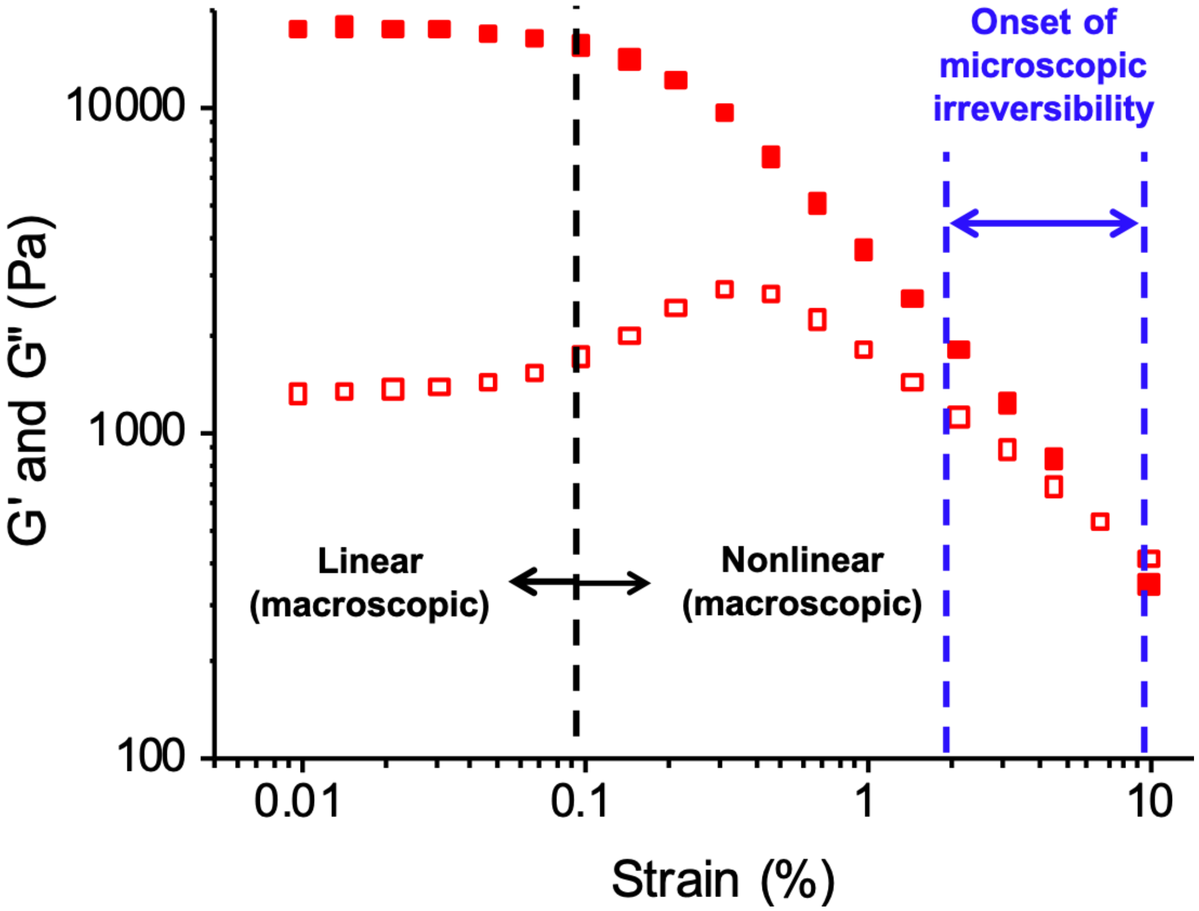

Figure B.8: Onset of nonlinear mechanical response in the bulk fluid in comparison to that of microscopic irreversibility observed from XPCS measurements.

B.5 Conclusion

Simultaneous XPCS measurements and rheometry under oscillatory shear have been successfully applied to study the microscopic origins of structural irreversibility in a colloidal gel. At modest applied strains from 0.1% to 2.0%, reversible dynamics were observed from the intensity correlation functions returning to the same initial value at each oscillation cycle throughout the experimental time scale of 40 s. However, variations in the quantitative response across different detecting regions disagree with predictions that assume homogeneous affine deformation. XPCS measurements of echo peaks at each oscillation period show that the onset microscopic irreversibility occurs at applied strains between 2.0 and 10%. This observation is in discrepancy with the bulk rheology, which indicates that macroscopic nonlinear response begins at strains above 0.1%. Upon analyzing data measured across different sample locations, it is evident that spatial heterogeneity is present as seen in both the details of the reversibility in waveforms and the onset of irreversibility. Such microscopic deviation from macroscopic deformation suggests that local deformation, although reversible, may be more complicated.